IMPROVED SELECTIVE LASER MELTING PROCESSING OF ALUMINIUM-SILICON-MAGNESIUM ALLOYS

Thesis submitted in accordance with the requirements of

The University of Liverpool

for the degree of

Doctor in Philosophy

By

Donal Lynch

February 2019

UNIVERSITY OF LIVERPOOL

Abstract

This thesis details the investigation of the cracking phenomenon of aluminium alloy AA6061 processed by Selective Laser Melting (SLM) and proposes a modified alloy composition which was proven to eliminate cracking.

High strength aluminium alloys are of commercial interest to the aerospace and automotive industries, in order to manufacture lightweight structural components. Current alloys that are regarded as processable through SLM are compromised by low strength, high cost or weight and this has led to an increased interest in developing high-medium strength aluminium alloys specifically for the SLM process. A thorough literature review was conducted to consider how different aluminium systems may perform when processed through SLM and subsequent heat treatments. From this, it was evident that alloys that can achieve appropriate mechanical properties are susceptible to cracking during the SLM process. AA6061 is an alloy within this category and it was selected for investigation due to its suitable mechanical properties, general use and availability in powder form. The potential sources of cracking are addressed in the literature review and a solution was proposed based on welding practices of AA6061. A powder blend of AA6061 powder and AlSi10Mg was made and processed by SLM. This imitates the practice of welding AA6061 with an Al-Si eutectic filler material. The blend ratio was selected to effectively adjust the silicon content of AA6061 by 1% and reflects the cracking susceptibility of binary Al-Mg_2Si and Al-Si alloys.

Optimisation of SLM processing parameters was performed on a Realizer SLM100 for AA6061, AlSi10Mg and the blend of the two materials. The process parameters, the density measurements methods and the design of experiments used for this study were scrutinised to contribute to the best practice for obtaining optimum densities. A high level of cracking was observed for every AA6061 sample that was produced. An unsuccessful attempt was made to influence the cracks through process strategies, namely reducing layer thickness and rescanning of each layer. SLM process parameter studies of the blended material demonstrated no cracking in any sample.

The causes of cracking were investigated, with a view to gain deeper understanding for alloy design and development for the SLM process. The microstructure of SLM built AA6061, AlSi10Mg and the blended material was studied using electron channelling contrast imaging, electron backscatter diffraction and chemical etching. This revealed that AA6061 and the blended material samples exhibited very similar grain structures, in contrast to the AlSi10Mg samples. The difference between AA6061 and the blended material was that pores could be found within the grain boundaries of the AA6061, which are likely the initiation points of cracks. The effect of the increased silicon content in the blended material was to provide enough silicon so

that no gaps were seen in grain boundaries. The cracks propagate through grain boundaries and this dictates the direction of crack growth.

Unidirectional samples were produced in an attempt to understand how the accumulation of stresses affects the direction and occurrence of cracks. These revealed no relation between cracks and principal stresses; rather cracks occurred at even spacings along scan directions irrespective of the part shape. The distance between cracks was ten times greater than the hatch spacing and is likely to relate to the weakest position within the microstructure due to grain misalignment.

Fractography was performed on the crack surfaces to examine if inclusions could be found that would weaken the material. High levels of oxygen were found on crack surfaces, but this formed after the crack surfaces open. Similar thick oxides are found on the top surfaces of samples and these were examined through energy dispersive X-ray spectroscopy. A reduction in surface oxides was observed with when the layer was rescanned. This reduction of surface oxide was not met with a reduction in oxygen content measured within the body of the samples. This study demonstrated that the surface appearance of the samples related to the level of oxides on the surface, which discolour the metal samples. A similar difference in discolouration was observed with samples produced with different laser beam diameters, but measurement of the oxide content was inconclusive due to the high amount of spatter on the surface of samples. The content and influence of oxides remains a concern for aluminium samples produced through SLM and deep etching of samples was used to examine the characteristics of the network of oxides within AA6061, AlSi10Mg and the blended material.

This study has therefore contributed to the understanding of aluminium alloys in SLM by; furthering understanding of the causes of cracking of an aluminium alloy in SLM, demonstrating a novel alloy with improved processability, and contributions to the knowledge of oxides within SLM aluminium specimen.

Acknowledgements

The author would like to acknowledge the contributions of Dr. Peter Fox, Dr. Robert Deffley and LPW staff, Dr. Matt Fulton and the centre for global eco-innovation, Dr. Karl Dawson and staff at imaging Centre at Liverpool, Mr. Dave Atkinson, Mr. Jack Carter-Hallam and staff in the engineering school office, Ms. Rebecca Garrard and family and friends for their support, without which this thesis wold not have been possible.

John 11:35

Contents

Abstract i
Acknowledgements iii
Contents v
Nomenclature ix
1 Background 1
1.1 Development of Selective Laser Melting 1
1.2 Applications 3
1.3 Materials Used in SLM 7
1.4 Aims and Objectives 9
2 Literature Review 11
2.1 Introduction 11
2.2 Aluminium Alloys in SLM 12
2.2.1 Cast Alloys in SLM 13
2.2.2 Wrought Alloys in SLM 15
2.3 Powders 19
2.3.1 Powder Production Techniques 19
2.3.2 Powder Characterisation and Specification 21
2.3.3 Powder Reuse 23
2.4 Gas 24
2.4.1 Process Atmosphere 25
2.4.2 Hydrogen in SLM Aluminium 25
2.4.3 Oxides in SLM Aluminium 27
2.5 Melting 30
2.5.1 Laser Interactions during SLM 31
2.5.2 Spot Size and Shape 32
2.5.3 Balling 34
2.5.4 Process Parameter Development Strategy 35
2.6 Solidification and Strengthening Mechanisms 36
2.6.1 Strengthening Mechanisms 40
2.6.2 Microstructure of SLM Aluminium 43
2.7 Thermal Stresses 57

2.7.1 Mechanisms of Thermal Stress 57
2.7.2 Accumulation of Stress with SLM 58
2.7.3 Cracking under thermal stresses in SLM 60
2.7.4 Mitigation Thermal Stresses 63
2.8 Cracking in SLM Aluminium 68
2.8.1 Mechanism of Solidification Cracking 69
2.8.2 Mitigation 73
2.8.3 Summary 75
3 Materials and Methods 77
3.1 Realiser SLM 100 77
3.1.1 Focus Test 80
3.1.2 Limits and Resolution of Hatch Exposure and Point Distance Inputs 84
3.1.3 Limits and Resolution of Hatch Distance 88
3.2 Renishaw AM 125 89
3.2.1 Spot Size Test 92
3.3 Scanning Electron Microscopy (SEM) 94
3.3.1 Secondary Electron Imaging (SEI) 95
3.3.2 Electron Channelling Contrast Imaging (ECCI) 95
3.3.3 Electron Backscatter Diffraction (EBSD) 96
3.3.4 Energy Dispersive X-ray Spectroscopy (EDX) 97
3.3.5 SEM Equipment 97
3.4 Optical Microscopy 98
3.5 Laser Size Diffraction (LSD) 98
3.6 Powder Characterisation 99
3.6.1 SEM and EDX Characterisation of Powders 100
3.6.2 Powder Particle Size Analysis 102
3.6.3 Powder Flowability 103
3.6.4 Powder Actual and Apparent Density 104
3.7 Design of Experiments for Optimising Density 105
3.8 Density Measurement Methods 107
3.8.1 Archimedes 107
3.8.2 Micrographic Density 111
3.8.3 Pycnometer 114
3.8.4 Comparison of Archimedes v Pycnometry 116
3.9 Etchants 116
3.10 Summary 117

4 Processing Al-Si-Mg Alloys in SLM 118
4.1 SLM of AA6061 at 50 µm Layer Thickness 118
4.1.1 Test A1: AA6061, 50 µm Layer Thickness CCD DOE 119
4.1.2 Test A2: AA6061, 50 µm Layer Thickness CCD DOE 123
4.1.3 Test A3: AA6061, 50 µm Layer Thickness CCD DOE 127
4.1.4 Test A4: AA6061, 50 µm Layer Thickness CCD DOE 130
4.2 SLM of AA6061 at 25 µm Layer Thickness 133
4.3 SLM of AA6061 with Double Scanning at 50 µm Layer Thickness 137
4.4 SLM of AlSi10Mg 144
4.4.1 Test B1: AlSi10Mg with AA6061 parameters 144
4.4.2 Test B2: AlSi10Mg, CCD DOE 147
4.4.3 Test B3: AlSi10Mg, CCD DOE 149
4.4.4 Test B4: AlSi10Mg, CCD DOE 153
4.5 SLM of AA6061 - AlSi10Mg Blended Powder 155
4.5.1 Test C1: Blended Material with AA6061 parameters 156
4.5.2 Homogeneity of blended parts 159
4.5.3 Test C2: Blended Powder, CCD 160
4.6 Summary 163
5 Investigation into Cracking in AA6061 166
5.1 Effect of Part Shape and Scan Direction on Cracks within AA6061 Parts 166
5.1.1 Fractography of All-Y Scanned Sample Crack Surface 169
5.1.2 Fractography of XY Alternating Scanned Crack Surface 174
5.1.3 Microstructure of Unidirectional Scanned Parts 180
5.2 Location of Cracks within Weld Tracks 184
5.3 Location of Cracks within Microstructure 186
5.3.1 Grain Structure of AA6061 at 50 µm layer thickness 186
5.3.2 Grain Structure of AA6061 at 25 µm layer thickness 193
5.3.3 Grain Structure of AlSi10Mg 196
5.3.4 Grain Structure of Blended Material 197
5.3.5 EBSD of AA6061, AlSi10Mg and Blended Material 200
5.4 Presence of Oxides with AA6061 samples and on Top Surface 204
5.4.1 Effect of Rescanning on Oxides on Top Surface 205
5.4.2 Effect of Rescanning on Oxides within the Bulk Material 210
5.4.3 Effect of Spot Size on Oxides 213
5.4.4 Deep Etched Samples 218
5.5 Summary 225

6 Conclusion 226
6.1 Future Work 229
7 References 231

Nomenclature

Roman Symbols

Ed	Energy density per volume	Jmm^{-3}
M_{body}	Mass of a density sample	g
$M_{buoyancy}$	Buoyancy force of samples suspended in liquid	g
$M_{submerged}$	Mass of sample suspended in water	g
P	Pressure	Nm^{-2}
P_{dist}	Point distance	µm
P_{laser}	Laser power	W
T	Temperature	°C
V	Volume	m^3
d	Grain diameter	nm
s_{point}	Point distance	µm
s_{hatch}	Hatch distance	mm
t_{eff}	Effective layer thickness	µm
t_{expo}	Exposure time	µs
t_{layer}	Layer thickness	µm
t_{sd}	Scan duration	s
v_{scan}	Scan speed	mms^{-1}

Greek Symbols

$\eta_{\lambda}(T)$	Laser absorptivity for given wavelength and temperature	-
λ	Wavelength	nm
$\rho(T)$	Electrical resistivity for given temperature	Ωm
ρ_{body}	Density of sample	gcm^{-3}
ρ_{water}	Density of water	gcm^{-3}
σ	Yield strength	MPa
σ_0	Peierls stress	MPa

1 Background

Additive Manufacturing (AM) is a group of manufacturing processes, whereby parts are constructed by the addition of material rather than its removal or by forcing a shape change by deformation or melting and freezing, as in conventional manufacturing. Selective Laser Melting (SLM) is an AM process, in which powder is laid as a thin bed and then selectively fused to the previous layer or substrate by the application of a laser [1]. Three dimensional parts are built through the successive layering of the powder and fusion of the relevant parts of each layer [2]. The key advantages identified for AM have been new design opportunities, increased complexity with reduced manufacturing steps, and reduced material waste [3] and potential to process new materials [2].

SLM is capable of producing metallic parts with high shape definition, density and high design complexity. These advantages are being utilised in the automotive and aerospace industries to reduce the weight of metallic components [4] and offer significant lifetime fuel savings as weight reduction is imperative to fuel efficiency. While lightweight components are being developed in SLM, there is a lack of suitable lightweight metals, with adequate strength, that can be processed.

The purpose of this project was to investigate potential lightweight alloys for processing with SLM and to propose new alloys for applications that are optimised for SLM use in the automotive and aerospace industries.

It was identified near the start of the project that age hardening aluminium alloys were a group of materials that offered significant potential within the chosen application areas because they are strong lightweight materials. However, age hardening aluminium alloys are not normally processed directly from the melt and their mechanical properties are developed by the application of often complex heat treatments. The conventional versions of most of these alloys are considered unweldable due to the formation of unsuitable microstructures and the development of cracks on cooling. It was considered possible that the smaller weld melt pool in SLM along with the rapid cooling may overcome these problems, and therefore their behaviour was thought worth investigating.

1.1 Development of Selective Laser Melting

The first AM technology is normally considered to be Stereolithography (SLA), patented by Hull [5]. This used photosensitive resins which polymerised in UV light, and by controlling the exposure of the polymer to the UV light a thin layer of solidified resin was formed. The final 3D object was constructed from a series of these thin

layers chemically bonded together [6]. This method of producing a solid object by bonding together layers of material has since been used in many AM techniques.

A later technique is Selective Laser Sintering (SLS) [7], which again utilised layer-wise manufacturing but with a thin layer of powder rather than liquid, and with the powder being sintered together by heat rather than by chemical bonding. This allowed a much wider range of materials to be processed giving a greater variety of properties [8]. SLS was originally used to process polymers such as wax [9], nylon [10] and polycarbonate [11], but later metals and ceramics were processed by adding a polymer binder which bonded the green part together, and the binder was removed later during sintering [12]. This allowed metal parts to be produced but these were not fully dense, although the density could be increased by infiltration or by hipping, although hipping is expensive, and infiltration used a different alloy to the original powder. The extra processing steps of removing the binding materials and increasing the density of the parts for SLS were not desirable [13] and limited the application of the technology.

The invention of Selective Laser Melting (SLM), patented in 1998 as "SLS at Melting Temperature" (Meiners, et al., 1998), was a modification of the SLS technology that raised the temperature of the powder layer to above its melting point. The technology of SLM systems are very similar to that of SLS but the microstructures produced are very different, the SLS microstructure being produced without melting (unless the part was infiltrated) while SLM produces a structure like many small weld beads. The advantage of SLM is that melting can produce a fully dense component but at the expense of changes in microstructure and the development of high thermal stresses due to thermal gradients. While problems with evaporation, weld splatter and oxidation make the design of SLM machines more challenging. Another significant difference is in the type of laser used, with SLS mainly using CO_2, while SLM typically uses solid-state fibre lasers [14]. The choice of the solid-state fibre lasers allows better coupling of energy into metals, because of the wavelength of light produced, and have a smaller spot size for finer features. The lasers used in SLS have a better coupling of energy to plastics and ceramics [14].

SLM has been used to process a wide range of materials but is primarily used for metals [15], where it can produce fully dense and functional parts with the design freedoms of layer-wise AM. However, there are significant problems including the high thermal stresses generated by the temperature gradients across the part. To reduce the effects of these stresses that can cause deformation, the parts are built on to a base plate normally via a support structure. The high thermal stresses and their effects are discussed further in the literature review.

Other AM processes that can build solid metal parts include laser engineered net shaping (LENS), electron beam melting (EBM) and laminated object manufacturing (LOM). Of these EBM is similar to SLM using powder bed layer wise fusion, while the others are very different. LENS delivers metal to a melt pool created by a laser as

either blown powder or wire rather than a layer, giving greater design freedom when building but at the expense of the accuracy compared to layerwise manufacturing [16]. The technique is often combined with machining to produce large complex parts. This technology is more successful in cladding and in surface repair than building stand-alone parts [17].

LOM is a metal AM system which builds parts by stacking sheets that are cut and bound to each other using thermal adhesive to build parts layer by layer to form the final part. As the layers are glued, they lack strength unless they are sintered together. The precision, resolution is controlled by the plate thickness [18].

EBM is very similar to SLM in concept but uses an electron beam rather than laser energy to melt the material. The electron beam can move at higher velocities than the laser beam, and when combined with a high beam current, large regions of the bed can be heated rapidly. This is used to heat and sinter the powder bed to reduce thermal stress, constrain parts within the powder bed and to prevent powder dispersing during processing. Feature resolution in commercial EBM machines are not as fine as can be achieved with commercial SLM lasers. They also use larger particle sizes than SLM increasing the minimum layer thickness (typically 100 μm) [19]. The uptake of EBM has been less than SLM, mainly because of the complexity of the vacuum systems and electron guns and also because there is currently only one manufacturer [20]. This situation may change as other manufacturers enter the market as the patents on this technology expire. This has limited the materials processed successfully, of which only titanium alloys can be considered a lightweight metal [19].

1.2 Applications

SLM has found a number of uses in aerospace and it is expected that the list of applications will grow with the maturation of the technology. Aerospace and automotive industries have been heavily investing in the development of SLM since 2011 [21] and investment is still increasing [22]. The UK government has acknowledged the role of additive manufacturing in advancing aerospace capabilities as has been made explicit by their awarding of funding [23].

The largest investor in metal AM has been General Electric (GE), who initially used the technology in its subdivision 'GE Aviation' but has since created a subdivision 'GE Additive'. GE has worked largely in secret, collaborating with metal AM company Morris Technology before buying them in 2012 [24]. GE also purchased controlling stakes in Arcam AB and Concept Laser when creating 'GE Additive' [25]. Arcam AB are the only manufacturer of EBM machines and Concept Laser are a prominent SLM

machine manufacture (estimated to have 4.6% and 18.1% of the AM metal market respectively [26], valued at $1.2bn in 2017 [27].

The incentives for GE and other aerospace companies to invest in the layer wise technologies lies in the design freedoms of the process combined with the ability to build functional metal parts. The allowable complexity can be used to greatly reduce the weight of some components and therefore save on fuel. For aviation each 1kg of reduced weight saves $3,000 in fuel in a year [21], which is the equivalent of 18 ton of CO_2 emissions [28]. As well as the reduced weight, the use of SLM may also reduce the cost of manufacturing especially where the number of parts needed is low or where parts can be combined to reduce the part count. Another possibility is by improving other manufacturing processes such as SLM produced investment casting moulds with conformal cooling channels [29].

The highest profile example of metal AM used in aerospace has been the use of fuel injection nozzles developed by CFM International, a joint venture between Safran Aircraft Engines and General Electric Aviation (Figure 1). The nozzles are used in LEAP engines which fly on a large variety of single aisle commercial aircraft, such as the Boeing 737. The nozzles are printed as a single piece where previously they were twenty pieces and required a difficult assembly. Metal AM allowed for improved performance, reduced cost and reduced the weight by 25% [30].

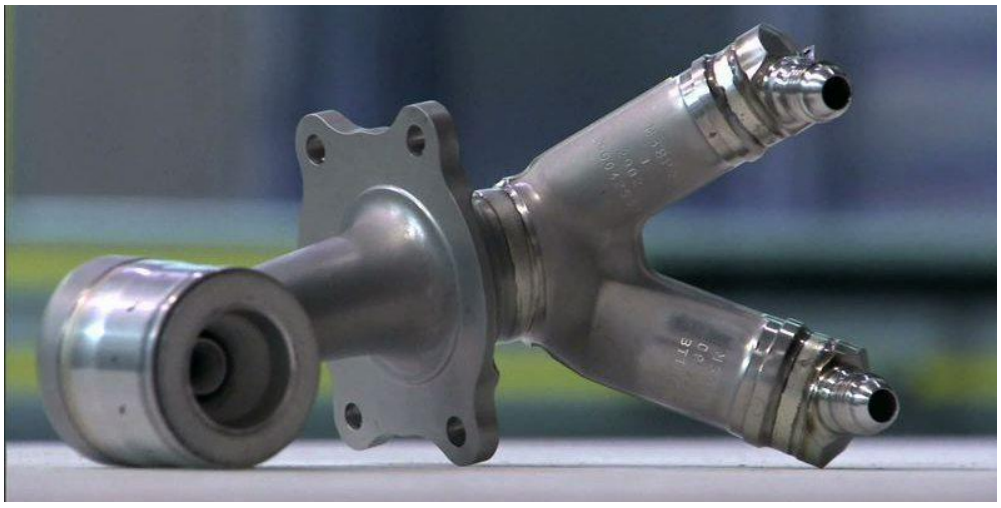

Figure 1 LEAP engine fuel nozzle created by CFM International (Petch, 2016)

GE has other metal AM parts in jet engines, such as a compressor inlet temperature housing, which was the first metal AM part certified by the U.S. Federal Aviation Administration [31] and have tested a turbo prop engine with 16 additively manufactured titanium parts [32]. 11 of those parts were a consolidation of 845 parts, such as frames, sumps, bearing housings and other stationary parts, from the previous design, with a reduction in weight and increase in power [33].

Metal AM parts are being included in many jet engine productions, including the Rolls-Royce Trent XWB [34] and Pratt and Whitney's PurePower PW1500G [35]. Jet engines

are high value items and in production runs in thousands, which gives a small indication of the economics of the technology, which does not offer much economy of scale [36]. The ability to produce one off parts or parts with low production runs, is being used with the development of rocket engines, such as with NASA [37], GKN [38] and Space X [39]. SpaceX has tested rocket engines with over 40% printed parts [22]. Metal AM is also being used for the production of satellites, which are low production run items. Airbus first started using metal AM on production of satellites in 2011 [40] but this has become more common recently. Boeing launched geostationary satellites with 50 metal titanium AM parts in 2016 [41] and SATRevolution, D-Orbit [42] and Space Systems Loral [43] all started producing satellites with metal AM in 2017. Space Systems Loral used metal AM to produce advanced antenna tower structures on their SSL 1300 geostationary satellites halving the weight and construction time of the antenna, as well as cost saving [44].

Beyond the use of metal AM within engines and in low production run items, there has been a trend from large aircraft companies, such as Boeing and Airbus, to increase the reliance on the technologies to produce structural parts that have manufacturing cost and weight savings. Boeing first started to use metal AM on military aircraft in 2003 and on civilian aircraft, the 787 Dreamliner, in 2017 [45]. The Boeing 787 Dreamliner will incorporate structural Ti64 components (Figure 2) manufactured through a wire fed AM system developed by Norsk Titanium AS [46]. The parts have poor surface roughness and require a lot of machining, but the advantages of reduced material waste and lead times remain. The adoption of metal 3d printing is projected to save $3m on the production cost of the planes [47] of which 136 were delivered in 2017 and 72 were delivered in 2018 as on 30th June [48] .

Figure 2 AM Components produced for the Boeing 787 Dreamliner by Norsk Titanium AS, as-built and after machining [49].

Airbus have also invested significantly into metal AM and have created a division, APWorks, for AM advancement in the company. The Airbus A350 XWB has over 1000 AM parts but most of these are polymer [50]. However, included on these aircraft are

titanium brackets with a lightweight design and built by SLM. The new bracket design not only reduced the weight of the part but reduced the waste from 95% for the original milled part, down to 5% [51]. Airbus is also working with Safran Landing Systems to use metal AM to produce hydraulic units for the A350 [52].

The Airbus A320neo, which uses the aforementioned LEAP engines, has many metal AM parts. Figure 3 shows a nacelle hinge bracket for the A320 aircraft, manufactured through SLM with a design optimised using Altair software and the previous hinge bracket produced using traditional techniques. The SLM design had a weight saving of 64% (592g).

Figure 3 Comparison between Airbus A320 nacelle hinge bracket designed and manufactured using traditional techniques to that of additive manufacturing [53]

Airbus have also designed a partitioning wall for the A320, between the seating and the plane galley, which uses SLM manufactured joiners with carbon fibre trusses. It is claimed that the use of SLM allowed a weight saving of 45% on the previous partition design [4]. The material used with the SLM parts is an APWorks patented aluminium alloy Scalmalloy [54]. This is an important step in weight saving in aircraft as previously titanium alloys have had to be used. This alloy has limited availability and it is yet to be seen what demand there will be, given the high cost of alloys containing rare earth elements. The material does not outperform Ti64 in specific strength or ductility and unlikely to be more cost effective per unit weight [54] but it does point to the need for an AM processable low cost age hardenable aluminium alloy [55].

Automotive industries are investing in metal AM, where it is proving beneficial in low batch scenarios such as high end models, spare parts for classic vehicles, rapid prototyping and rapid tooling [56]. Many car companies have been developing metal AM facilities and in 2018 BMW announced that it is investing over £10m in additive manufacturing facilities [57].

High end models such as Bugatti Chiron hypercar [58] and BMW i8 Roadster, both use metal AM in car production [59], while companies such as Porsche [60] and Audi [61]

are using the technology more for manufacturing spare parts on demand for classic vehicles. Research trends show an interest in greater use of the technology, but uptake is likely limited by cost of production (as well as a necessity for quality control assurances). Porsche have researched manufacturing differential housing with metal AM and demonstrated improved performance with weight savings was possible [62].

The flexibility and reduced tooling costs of SLM makes it economically competitive in low batch numbers. The optimum batch size while an advantage in aerospace may be a deterrent to automotive [51]. The fast production time and rapid modifications to design allow rapid part testing and optimisation, this is being used by Audi and BMW for rapid prototyping and rapid tooling [63] and is particularly advantageous in niche applications like Formula One motor racing [64].

The use in this area is shrouded in secrecy [56] but a few examples have shown reduced part weight [65]. It is predicted that 3D printing within the automotive industry will be worth $1.1 billion a year by 2019, though for large uptake the costs of AM must be reduced [66]. Patents expiring will help lower the costs of machinery by increasing competition, but the cost of materials must also be competitive.

A consideration for the continuing uptake of SLM in these industries is the potential weight reduction that can be achieved with the ability to produce high complexity structures, such as cellular lattices. These light weight structures have been a focus of research since 2006 [67] and many software packages exist to aid optimisation of designs [68]. Surface roughness is a regularly sited problem with SLM components, reducing tensile strength and fatigue life, and the proportionally high surface area of lattice structures may be an issue [2]. Machine performances continues to improve, and many researchers are focussed on improving the surface finish of SLM [69]. These structures do not alleviate the desire for lightweight materials but rather may be used in conjunction for further benefit.

1.3 Materials Used in SLM

The most common materials used in metal AM have been iron, titanium and nickel based [2], partially due to their conventional applications and partially due to the ease of processing. Iron based alloys have been investigated since 1993 [70] and are currently the most commonly used, as they are readily processable and competitively priced [71]. Nickel alloys are the basis for many high temperature superalloys and therefore of interest for aero-engines. The interest in titanium has largely been for medical implants as the alloys have good biocompatibility [2]. Of these materials, titanium is the least dense (Ti (4.51 gcm^{-3}), iron (7.83 gcm^{-3}) and nickel (9.81 $gcm^{-3)}$)) and alloys such as Ti64 have a high strength to weight ratio (243 MPa $kg^{-1}m^{3}$) and therefore more likely to be used in lightweight applications. Lighter structural metals,

such as magnesium (density of 1.74 gcm^{-3}) and aluminium (2.7 gcm^{-3}) are not yet seen as processable using SLM without concessions to mechanical performance [72], but there is significant drive within the industry to be able to process these materials

A number of attempts have been made to process magnesium and magnesium alloys [73] but there has been little success in achieving acceptable materials [74]. The main issue appears to be with the excessive evaporation of magnesium during processing. Magnesium has a similar melting temperature to aluminium at 650°C but has a very low boiling point of 1093°C, compared to aluminium (melting point of 660°C, boiling point 2470 °C). Alloying can be used widen the liquid range [75], as can the use of increased gas pressure [76] but in both cases excessive evaporation was still a problem and there was limited success [77].

Aluminium alloys are a more promising prospect, with some aluminium alloys, mainly near eutectic Al-Si, having been extensively researched, although some other alloys have been considered [78]. The main challenges of SLM processing involve poor flowability of powders, oxide formation, poor wetting, high reflectivity and low melt viscosity [79]. To overcome these problems more powerful lasers have been used that supply enough power to achieve higher melt pool temperatures. These seem to increase build quality by obliterating surface oxides, so that wetting is improved [80]. Some aluminium alloys are now regarded as processable and a new focus for many researchers is trying to process age hardenable aluminium alloys that will be functional in lightweight structural applications [78]. The challenge with all age hardenable aluminium alloys is that they require alloy specific heat treatments to form the correct microstructure and that these alloys are susceptible to cracking in cooling from the melt [72]. Extensive cracking of these alloys has been reported on SLM processing and one challenge is to understand the cause of the cracking and stop the cracks forming [81, 82, 83]. Questions about achieving age hardenable microstructures remain but are only worth addressing after cracking has been eliminated.

Aerospace is investing heavily into metal AM and functional light weight alloys will be important in weight sensitive applications. Conventional aluminium alloys are less expensive than titanium and there is an expectation that this is also true for AM parts, although this is not true at the moment. This thesis presents work that addresses the need to understand the behaviour of age hardening aluminium alloys during SLM processing and to explain the cause of cracking which is stopped these alloys from being useful. A major issue is that alloys currently used in SLM were designed to be processed by a different route and it is likely that new alloys will need to be developed to complement the SLM process. This development has already started with steel [84], titanium [85] and nickel superalloys [86]. Some attempts have been made with aluminium alloy design and development that will be addressed in the literature review. To develop new alloys, it is important to study and understand the

interactions between the SLM process, the microstructure formed and the mechanical properties.

Another indication of the importance of SLM to industry is the funding of specialist metal suppliers like LPW who have specialised in traceable and certified metal powder supplies. The work presented in this thesis was carried out in collaboration with LPW and supports their perceived need for low cost lightweight alloys for the SLM market. This PhD sets out to address the lack of understanding of the behaviour of light alloys in the SLM process and to develop understanding both of the process and microstructures, considering also how these work together to alter the mechanical properties.

1.4 Aim and Objectives

The aim of this project was to increase understanding of the behaviour of aluminium alloys during SLM processing, so as to improve the quality of components produced. This knowledge will lead in the future to the design and manufacture of environmentally friendly ultra-lightweight parts for application in the aerospace and automotive sectors.

To achieve this the following objectives were met:

1. Review of literature; To understand the current knowledge of light weight alloys and SLM processing a full review of the literature was carried out throughout the duration of the project, as the subject changed quickly. The review also considered the conventional processing of aluminium alloys and the interaction of alloy, processing and properties. It was identified that crack formation in aluminium alloys during SLM processing was a significant problem. Also identified was the complex relationship between the heat treatment and the properties of the alloys and this was taken into consideration when considering which alloys to study.
2. Investigation into the behaviour of alloys in the SLM process; three alloys were processed through SLM to understand how the composition affects processability and the microstructures were analysed and compared to those of conventionally produced materials to identify features that would affect the properties of the parts produced.
3. Analysis of oxides with SLM aluminium alloys; oxide formation is known to be a serious problem with conventional aluminium processing both in welding and casting. The literature review was therefore extended to consider oxide formation on aluminium alloys during other fusion processes as well as SLM. The presence of oxides on the surfaces and within the body of SLM built

samples, was analysed to further the knowledge of formation of oxides in the process and understand how these affect built parts.

4. Analysis of cracks formed with SLM aluminium; cracking is known to be a challenge to processing aluminium alloys. Literature on cracking within aluminium processed through conventional techniques and also how cracks are formed with SLM processing of other metals and considered, and this knowledge is used to examine and explain the cracking phenomena within SLM of aluminium.
5. Design and processing of bespoke aluminium alloy; the understanding of the behaviour of aluminium alloys during SLM was tested by the development and building samples with a novel alloy. The alloy was designed to reduce cracking based on the knowledge gained during the PhD and the predicted behaviour compared to the actual microstructure and cracking behaviour. This alloy was used to give a basis for advancing the understanding of the designing alloys for the SLM process.

2 Literature Review

2.1 Introduction

This section considers the current state of aluminium alloy processing, mainly focusing on SLM processing but also considering other alloys originally developed for other processing technologies. There is a clear trend for the desire for high strength age hardened alloys that can be processed by SLM, but all that have been attempted up until now have suffered from cracking defects. The challenges of processing aluminium alloys are reviewed, and the design of a suitable alloy to meet these challenges is developed from the information within the literature.

The challenges with processing aluminium alloys start with the powder materials. Handling aluminium powder is relatively difficult as it is light and often irregularly shaped and prone to poor flowability. The manufacture of powders and best practice for adequate powder flowability is evaluated in section 2.2.

The environment in which aluminium is processed is very important for the integrity of the materials as oxygen and hydrogen inclusions can cause porosity and embrittlement. The challenges with oxides are greatly felt as strong thick oxides may prevent bonding of materials or will create weak brittle areas. Tenacious aluminium oxides form and cover all unprotected surfaces, with deeper penetration of oxides forming at higher temperatures. All aluminium powders are encased in oxides. Hydrogen will also be attracted into the liquid material but is expelled during solidification forming internal pores. The best approach for dealing with these challenges will be discussed in this chapter.

To best understand the cracking phenomena that inhibits aluminium alloys in SLM, the effects of the SLM process are considered with focus on the heating cycles. This is addressed as three areas; the heating and melting of the powder material, the solidification of the molten materials, and the thermal cycles and generated stresses.

With the understanding of these areas it is possible to have a discussion on the potential cause of cracking and the predicted performance of alloys. Cracking in SLM and in other technologies which generate thermal stresses is not uncommon. Examples of other materials cracking during and after the SLM process and aluminium cracking within welding and casting are discussed and information is gleaned as to the potential cause of cracking with SLM aluminium. This is used as the basis for the design of the new alloy and hypothesise the cause of cracks, which is tested in chapter 5.

2.2 Aluminium Alloys in SLM

Comprehensive reviews of the aluminium alloys used in selective laser melting have been published by Olakanmi et al. [87] and Aboulkhair, et al. [79]. These reviews cover many of the challenges to processing aluminium alloys and they detail alloys that have been processed. They do not consider the full range of potential aluminium alloys, which could be processed through SLM. As this project has been to envisage novel aluminium alloys for SLM this review will consider alloys that have been developed for other processes. These will provide information on the benefits and pitfalls they may pose to processing by SLM.

Early work on aluminium has been focused on achieving fully dense parts with problems arising from the flowability of the powder, low absorptivity of laser energy, high thermal conductivity, relatively wide solidification range, high solubility of hydrogen, tenacious oxide films on surfaces inhibiting flowability wetting and embrittling parts [87].

Early research into SLM aluminium included work with medium-high strength alloy AA6061 [88], pure aluminium and aluminium-copper blends [89]. The best density results were found with Al-Si alloys, specifically AlSi12 and AlSi10Mg. These are near eutectic alloys with low solidification ranges, low coefficient of thermal expansion, low liquid viscosity and comparatively higher laser absorptivity [90]. The majority of research has been with these alloys [2].

Many of the problems facing SLM aluminium, such as the poor coupling of energy and heat loss by conduction, can be eased with high powered lasers, from 200W up to 1KW [80]. The higher powered lasers also improve liquid viscosity and hydrogen porosity by increasing melt pool temperatures and high density parts are achievable. The issues with oxides have not been fully solved and there are many questions about if and where oxide inclusions are formed and what effect they have on the final parts, which will be expanded on in section 2.3, but they are not a barrier to achieving sufficient densities. This has led to a more expansive view of processable alloys. The majority of SLM aluminium research has been with Al-Si cast alloys as they are seen as the easiest to process but now there is a growing consideration of mechanical properties. For this reason, an open view was taken to considering potential alloys.

Unalloyed aluminium, as defined as being at least 99% pure, is very soft and weak, with a yield strength below 100 MPa [72] and therefore it is always alloyed in structural applications. There are four mechanisms with which alloying elements can strengthen the materials (which are discussed in detail in section 2.5); solution strengthening, precipitate strengthening, cold working and, in certain processes, grain refinement. The majority of research in SLM aluminium has been with Al-Si alloys, which gain a portion of their strength from solution strengthening but this mechanism alone is insufficient to produce medium-high strength alloys. Considering the other

strengthening mechanisms; work hardening is inappropriate with a net shape manufacturing process, it is not clear how the mechanisms for grain refinement, such as nucleation and grain boundary pining, effect the SLM process [91] and while some grain refinement may be possible, the SLM process already produces fine grained parts in two dimensions, due to the steep thermal gradients within the melt pools. It is for this reason that SLM aluminium research has been increasing focus on precipitate strengthening alloys, and this is the focus of this literature review.

Aluminium alloys are conventionally classified into two groups, casting alloys and wrought alloys, as described in BS EN 573-1 [92] and BS EN 1706 [93] respectively. In general, casting alloys have higher alloying content and have a reputation of having low strength or toughness [72]. The high alloying content of casting alloys typically reduce the freezing temperature range which results in better flowability when molten and reduces thermal stresses when solidifying. These attributes are advantages in welding [90] and are equally advantageous in SLM. The disadvantage of these alloys is the comparative lack of strength compared to wrought alloys, but the method of processing the alloy plays a role in this.

2.2.1 Cast Alloys in SLM

As mentioned earlier, the majority of work on SLM of aluminium has been with Al-Si casting alloys. Early work on processing aluminium was with AlSi12 [94] which is a near eutectic alloy (eutectic point occurs at 12.6 wt% silicon, Figure 4).

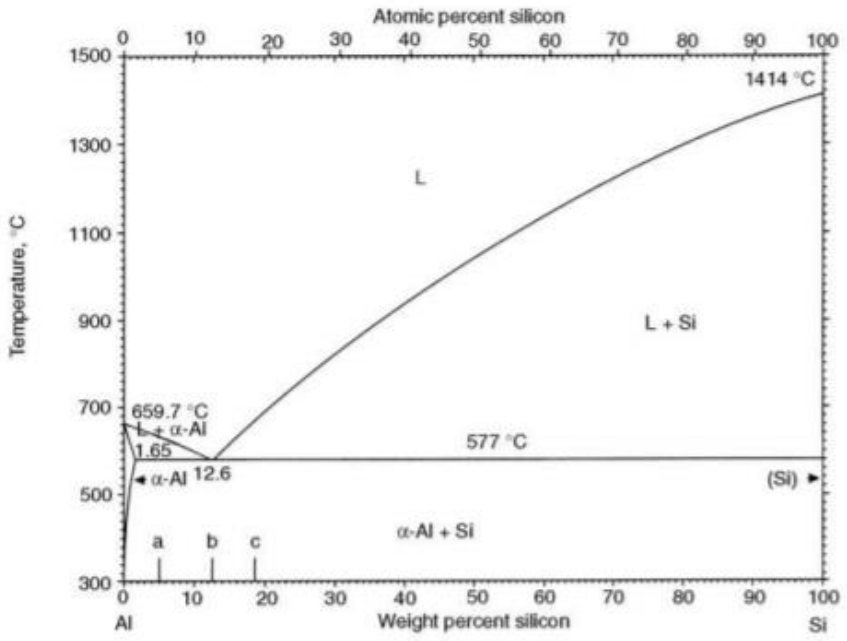

Figure 4 Aluminium-Silicon phase diagram [95]

The near eutectic alloy is used because it has low shrinkage, as well as a narrow freezing range, which reduces the risk of solidification porosity and cracking. Silicon can contribute to solid solution strengthening but most precipitates as a pure silicon

phase, often as plates and laths. The addition also improves the material wettability and flowability, which is why Al-Si alloys are the most frequently used casting alloys but are not used in wrought processing. Al-Si alloys are also used, for the same reasons, as filler materials for aluminium welding [90] . These properties also make these alloys easier to process successfully in the SLM [96].

AlSi10Mg is now more popular than AlSi12 as the addition of magnesium greatly improves the alloy strength while also having a positive effect on the material wettability and flowability [97]. More Al-Si casting alloys have been examined. Ma [98] investigated Al-Si20, Ullsperger et al [99] investigated Al-Si40 and A356 (Al-7Si-0.3Mg) and A357 (Al-7Si-0.55Mg) have been processed Kimura & Nakamoto [100] and Aversa [101] respectively. The alloys with much higher silicon content are typically used in high operation temperature range situations. A356 and A357 are very similar alloys, which exhibit greater strength than AlSi10Mg but have a much narrower process window [101].

In a study by Aversa [101], grain refiners were used with AlSi10Mg. TiB_2 is a grain refiner used in casting and welding as an inoculant to improve castability [102]. The use of a refiner reduces grain sizes but also avoids the growth of large dendrites that cause void formation. A greater solid volume fraction is reached before the grains interlock and hinder the feeding of liquid necessary to combat porosity (Figure 5). The alloys are useful in welding aluminium for the same reason. The inclusion of TiB_2 into AlSi10Mg had an effect on the processing window but not a considerable improvement on the already highly processable alloy. After only testing single scan tracks, Aversa et al., concluded that TiB_2, reduced the wettability of AlSi10Mg, this could be from the faster freezing time the nanoparticles induce. This could present a challenge with consecutive building in 3D. Li et al [103] showed the microstructure of AlSi10Mg with 7 wt% TiB_2 to have a finer grain structure then AlSi10Mg without and measured a corresponding increase in ultimate tensile strength, from 360 MPa to 530 MPa. There will be interest to see how this changes material properties of the alloy and if this could have a positive effect on alloys that are harder to process.

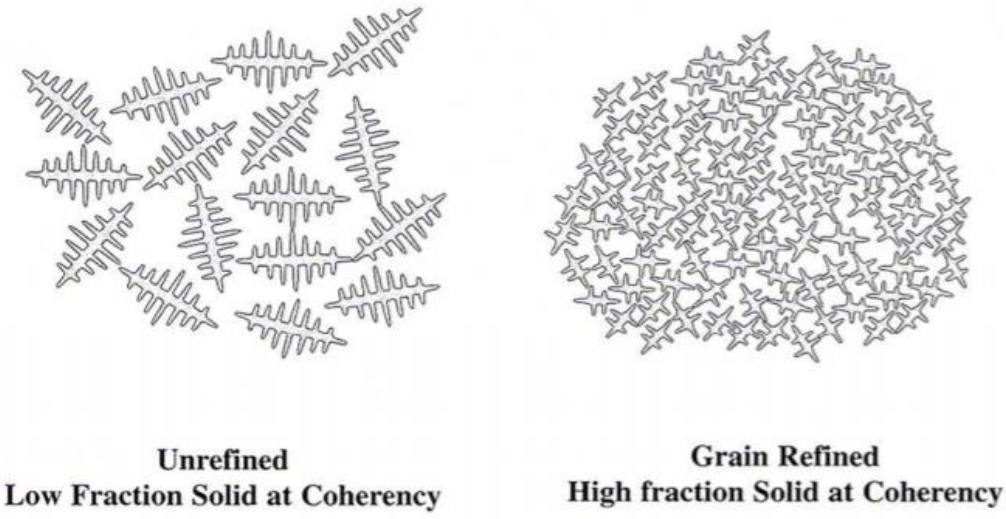

Figure 5 Effect of grain size on dendrite coherency and ability to feed liquid [102]

While research continues to try and find improved Al-Si alloys for SLM, a consideration must be placed on how they are used away from AM. They are not typically used for structural purposes as they are comparatively weak, with typical yield strengths below 200 MPa [72] (though SLM can achieve finer grain structures which double the yield strength but with reduced elongation). Stronger casting alloys include the addition of copper and nickel. A339 (Al -12Si -Mg -2.5Cu -Ni) and A336 (Al -12Si -Mg -Cu -1.5Ni) are used to make cast parts of motor engines which experience higher pressure, such as pistons. They have medium yield strength higher than 300 MPa, however, they are compromised by brittle failure, with <1% elongation to failure which could make them unsuitable for SLM processing [104]. It is for these reasons that higher strength wrought alloys are considered.

2.2.2 Wrought Alloys in SLM

Within the category of wrought aluminium alloys are higher strength heat treatable alloys. The compromise with these alloys is they are more challenging to process successfully with SLM, as they are known to be susceptible to cracking. The comparison exists between SLM and welding and most heat treatable aluminium alloys are only regarded as weldable with an appropriate filler material [90]. There are three main types of heat treatable wrought alloys; 2xxx series, 6xxx series and the 7xxx series.

The 2xxx series are Al-Cu alloys regularly have yield strengths above 400 MPa, after suitable heat treatment. The precipitate strengthening mechanisms of these alloys are very similar to the 6xxx and 7xxx series which will be discussed in greater detail in section 2.5. For precipitate hardening to occur a specific heat treatment regime is required. The first part of this allows the copper to dissolve into the aluminium matrix. The alloy is then quenched trapping the copper in solution. The final stage of the heat treatment causes the precipitation of copper rich particles throughout the aluminium

grains. At low temperatures these are nano sized copper precipitates only one or two atoms thick, called GP zones. At higher final stage treatment temperatures or longer times other phases are formed throughout the grains. The strength of the alloy comes from the even distribution of the small precipitates throughout the grains. If the precipitates become too large or form only at grain boundaries the alloy is significantly weaker. There are a range of different meta stable phases formed as the precipitates grow, the largest precipitates being the stable phase θ, which is tetragonal Al_2Cu. If the precipitates become too large (over aged) it can be difficult to get the precipitates to dissolve back into solution without remelting the material [72]. The heating, melting and solidification of material in SLM is a complex process, as is the heating and cooling of the solid as the subsequent layers are deposited. It is difficult to predict the phases that will form and to avoid overageing. Li et al, [105] studied the phase evolution in SLM processed Al-5Si-1Cu-Mg. Their results demonstrate the inconsistent heat-treatments that occur in different parts of the SLM sample and the evolution of larger more stable phases such as θ as the parts experience repeated heating and cooling cycles.

2xxx series are often regarded as unweldable due to either unsuitable phase formation or from solidification cracking. With regard to the latter problem, it was found that with a copper content above 4% improved weldability was observed [90]. The addition of copper decreases the materials corrosion resistance and 2xxx series alloys often require a protective coating [72]. The coating of complex part is very challenging, and this requirement may place a significant limitation on the design freedoms of AM.

Despite these problems there have been attempts to process Al-Cu alloys such as the work by Bartkowiak et al [106] who processed single scan tracks of various Al-Cu alloys without problems. Multiple layered samples of Al-Cu alloys were processed by Jerrard et al. [107], who blended AA6061 with pure copper particles and Zhang et al. [108] processed an Al-Cu-Mg alloy similar to AA2024. Both of these later alloys tested had higher copper content above 4% and didn't show any presence of cracking but it remains to be seen if the processed materials can be age hardened or if they are over aged in the SLM.

The 6xxx series alloys, which can be referred to as Al-Si-Mg alloys, gain their strength from Mg_2Si precipitates, which form similarly to Al_2Cu precipitates. The 6xxx series are not considered as strong as either the 2xxx or 7xxx series but are often preferred for other characteristics, such as good corrosion resistance [72]. A major reason for choosing the 6xxx series is that the alloys are easier to weld and attempts at processing these alloys in SLM have referenced their "weldability" [107]. However, they are not autogenously welded, as is the analogous scenario of SLM. It is well-established in welding that the cause of cracks is from solidification cracking, which is an issue relating to the material composition [109]. This can influence the choice of

material, such as 2022 compared to 2024 [110]. The 6xxx series alloys generally have a content of magnesium and silicon that coincides with the least favourable solidification cracking susceptibility (as can be seen on Figure 6). When sections are welded, they use a filler material either high in magnesium (5xxx series) or high in silicon (4xxx series) to avoid the concentration of magnesium-silicon that promotes cracking.

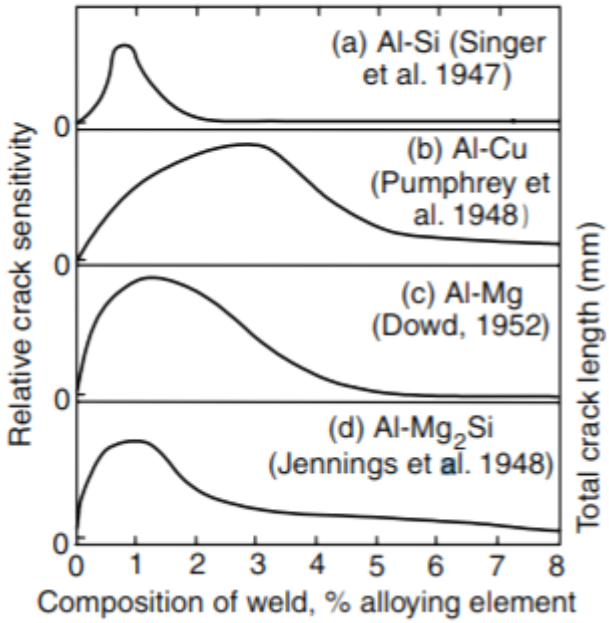

Figure 6 Influence of composition within binary aluminium alloys, on cracking susceptibility. Adapted by Kou [111]

AA6061 is a very popular alloy and attempts have been made at processing this through SLM without success since 2007 [88] and several other attempts have been made with limited success since [89] [112]. While not often cited in the literature for SLM, the big difficulty with processing this alloy is cracking (Figure 7), similar to welding [113]. The use of filler materials when welding 6xxx series is of interest to this project as it may be a way to avoid cracking. The filler materials used are very similar to the Al-Si alloys already used in SLM [114]. Braun [115] used AlSi10Mg as a filler when welding 6013 and found that the resultant material, with T6 heat treatment, recovered 90% of the original strength. This approach of blending a 6xxx series with AlSi10Mg is a potential way to improve SLM processing given the similarities between SLM and welding.

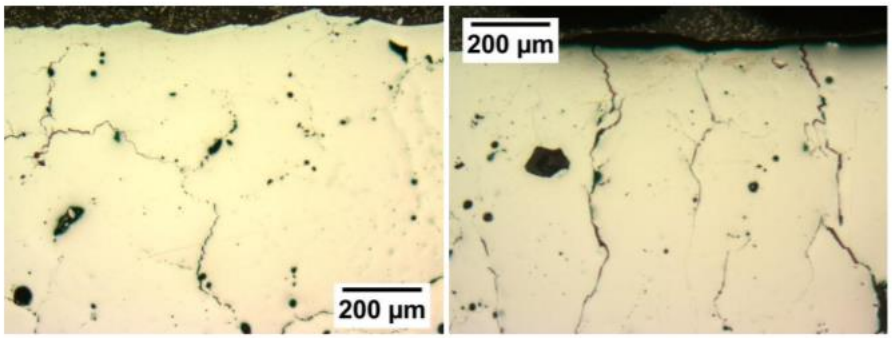

Figure 7 SLM As-built, polished AA6061, horizontal cross section (left) and vertical cross section (right) [81]

The 7xxx series are alloys that gain their strength from zinc and in some cases also from copper. The inclusion of copper speeds up the ageing process by creating copper GP zones, which might not be desirable in SLM if over ageing is a risk [116]. This series has some of the strongest aluminium alloys in common usage. The precipitation sequence can be more complex than the 2xxx or 6xxx series as several different precipitates form, such as $Al_2Mg_3Zn_3$, $MgZn_2$, and Al_2CuMg. Multiple stage heat treatments are often used to achieve peak strength but over ageing is less likely to be a major concern, unlike the 2xxx series [117]. The highest strength 7xxx alloys are not regarded as weldable and SLM processing has led to significant cracking in samples. Reduced cracking susceptibility has been observed with increased silicon content as in Al7075 where improved processability and reduced cracking was found [118]. Another consideration when laser processing Al-Zn-Mg alloys is the loss of Zn and Mg due to their low evaporation temperatures. This is known to be a problem when welding and there is evidence of significant material modification in SLM. Wang et al. [119] processed an Al-Zn-Mg-Cu alloy and the zinc content dropped from 11.90% to 9.10% and magnesium dropped from 2.72% to 2.33%.

Alternative aluminium materials have been processed in SLM. Dadbakhsh et al. [120] used aluminium powder blends to create metal matrix composites of Al with Fe_2O_3. Prashanth, et al. [121] processed an alloy that had a high content of rare earth elements, Al85-Nd8-Ni5-Co2. This material was designed to be used at elevated temperature up to 300°C. Rare earth elements can ease processing by providing a eutectic structure and the intermetallic phases can confine grain coarsening and dislocation movement at higher temperatures. For similar reasons Plotkowski et al [122] chose to process Al-Ce alloys as cerium is a relatively inexpensive rare earth element.

Another alloy of interest, mentioned in the background section of this thesis, is Scalmalloy, which is a Al-Mg-Si alloy with scandium and zirconium grain refiners first processed by Schmidtke et al in 2011 [123] and had gathered considerable interest by 2017 [124, 125, 126], with a high yield strength of 520 MPa being reported. Sc and Zr modified alloys have been in development since the 1970s, but use has been limited

due to the high cost [127]. The powder costs of Scalmalloy are an order of magnitude higher than other aluminium alloy powders. Scandium can be added to aluminium as a grain refiner and as a precipitation strengthener, Al_3Sc. It inhibits recrystallisation and grain growth allowing it to work at higher temperatures. Spierings at al [127] found reduced isotropy in strength, reasoning that the ultra-fine scandium-modified grain structure was more anisotropic [78].
The cost of scandium has motivated researchers to find alternative alloying additions, such as erbium [128]. Recently work has also shown that zirconium can be used to reduce cracking in Al-Cu alloys [129]. This suggests that grains refiners may be useful in SLM, and lower cost grain refiners such as TiB_2 may be effective.

2.3 Powders

Which materials are SLM processed is largely driven by their availability in a suitable powder form and Metal AM normally uses powders developed for other processes, such as pressing and sintering. The market for specialist AM powders is limited with only 1% of all powder production going into AM [26]. Many researchers use SLM's ability to alloy materials in-situ and use elemental powder blends [130] but this is not always appropriate. Smaller powder batch production techniques are being developed [131] but the majority of powders are produced in processes designed for larger batches [132].

2.3.1 Powder Production Techniques

The most commonly used powder production techniques are described by Dawes et al. [132] and the techniques and their characteristics are presented in Table 1. Aluminium powders are normally produced by gas atomisation (Figure 8). In gas atomisation the material is molten and pours from a tundish, which is a crucible like container, into the atomisation chamber. The stream of molten metal is broken up by jets of high speed gas, argon being used with aluminium to reduce oxide formation. Most gas atomisation produces particles within 0-500 µm size range, while some other designs achieve a size range 22–101 µm [133], this contains powders larger than the desired powder sizes for SLM which is typically 20-63 µm [134]. It is necessary, therefore, to sieve powders to a suitable size range. In theory, as the molten particles fall they will reduce their surface energy by forming spheres. However, gas atomised aluminium is often irregularly shaped. A potential reason for this is that solid aluminium oxides form even at very low oxygen levels and high temperatures, and this creates solid oxide films that stabilise the surface and resist the change in shape.

Table 1 Powder Manufacturing Process Characteristics (adapted from [132])

Manufacturing Process	Particle Size (μm)	Advantages	Disadvantages	Materials Processed
Water Atomisation	0-500	- High throughput, -Cost effective -Only requires feedstock in ingot form	-Reactive metal will produce oxides -Highly irregularly shaped particle -Low yield for <100 μm	Non-reactive materials, some steels
Gas Atomisation	0-500	-Can process reactive powders -High throughput -Only requires feedstock in ingot form -Spherical particles for most metals	-Irregular shaped aluminium alloys -Can leave satellites and internal porosity -Low yield for <100 μm	Al, Co, Ni, Fe, Ti
Plasma Atomisation	0-200	-Extremely spherical particles -Medium yield for <100 μm	-Requires wire or powder form feedstock -High cost -Can leave satellites and internal porosity	Cp Ti, Ti64
Plasma Rotating Electrode Process (PREP)	0-100	-Extremely spherical powder -Low size distribution -High yield <100μm	-Requires bar feedstock -Low productivity -High cost	Ti Exotics
Centrifugal Atomisation	0-600	-Narrow size distribution	-Difficulty in producing <50 μm powders for SLM	Solder pastes, Zinc of alkaline batteries, Ti and steel shot

Water atomisation operates similarly to gas atomisation, but the stream of molten metal is broken up by water. This method is cheaper than gas atomisation but produces less spherical particles, as the cooling rates are higher. This method is not suitable for producing aluminium powders as it will create a greater quantity of oxides [135]. Plasma atomisation uses a feed of solid material, in wire form, and melts and atomises the material using plasma torches. This method produces very spherical powder and in a narrow and appropriate size distribution. This method is costly and while it is used to create titanium powders, where it is used in high unit price medical applications with high regulation requirements, the cost does not appear to justify the demand for quality aluminium powders.

Centrifugal atomization uses the centrifugal forces of a rotating disc to break up the molten metal into particles. The particles are very spherical without satellites and in a narrow size distribution, however, the size range is larger than that needed for SLM. Plasma rotating electrode process (PREP) also uses centrifugal forces to atomise metals. In PREP, a rotating bar is fed towards a plasma torch where upon melting the liquid is pulled apart by the rotating force. This method produces a very narrow band of suitably sized powders, better than all other methods described but is also costlier.

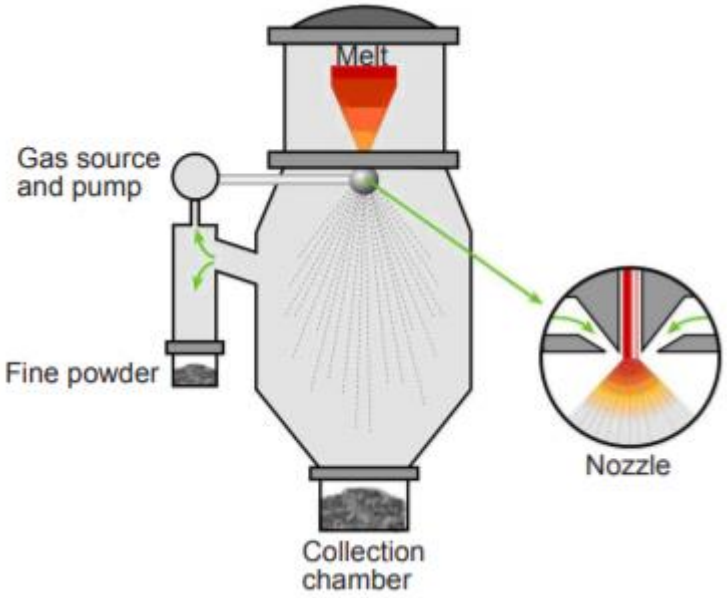

Figure 8 Schematic of gas atomiser for production of metal powders [136]

It is clear that powder costs are a consideration with the uptake of the technology and there is a desire to be cost effective in powder purchasing [137] [132]. Aluminium powders are produced by gas atomisation, because cheaper methods, such as water atomisation, are inappropriate, and better methods, such as Plasma atomisation and PREP, are too expensive. The needs of AM are inspiring new atomization processes [131] [138] and also improving the efficiency of the current systems. This includes considering powder characteristics, and if wider powder specifications could be used greater efficiency in production would be possible, lowering costs and having a positive environmental effect.

2.3.2 Powder Characterisation and Specification

As mentioned, there is a desire for spherical powder with a narrow size distribution. This relates to the ease of spreading powder layers [139], [140] and the consolidation of materials [96]. Irregularly shaped powder has poorer flowability than spherical powder and this reduces the handling ability, and can clog gravitational feed hoppers [141], reducing the ability to form a consistent layer and has lower layer densities (meaning there is more gas and less metal in the layer) [142]. Several studies have shown that irregular shaped aluminium powder is more difficult to process [87]. However, a study by Aboulkhair et al [143] comparing spherical and irregular shaped AlSi10Mg powders showed the increased difficulty in processing irregular shaped powder could be overcome by careful process parameter selection.

Narrow size distributions are desirable for improved powder flowability, but this is not practical for production and not ideal for layer density, which has an influence on part density [144]. A theorised ideal powder size distribution for layer density can be characterised as a multimodal distribution with finer powder particles occupying

interstices between large particles but in practice, even with powder blending, it is difficult to achieve densities above 70% [145].

The use of wider size distributions to increase packing density can be limited by the cohesive effect of fine powders. Powder “fines” can be characterised as powder particles with $1/7^{th}$ the diameter of the modal powder [142] but colloquially “fines” is used as a term for small powder particles that impede flowability. Fine powder particles have poor flowability as the force on the powder particles due to gravity is overcome by van der Walls forces, which is an attractive force between solid surfaces [146]. With aluminium’s light weight and the high surface area of the irregular shaped powder, the problem with fines is exacerbated and the typical lower size limit in specifications for SLM aluminium is 20 µm, which is larger than most other SLM powders [147].

A big influence on the specifications for powder size is the aperture sizes of the standardised sieve meshes, which are used to separate the powder into the appropriate sizes. The American society for testing materials defines sieve meshes for aperture sizes 45 µm, 53 µm, which are typical limits of SLM powder specifications [148]. Aluminium specifications use the next sieve size up, 63 µm, this is to include a larger yield of powder. This powder is used in conjunction with typical layer thicknesses of 50 µm or below. There is an intuitive and often speculated belief, but not conclusively tested, that if the powder size is larger than the layer thickness then the powder will not be deposited by the spreader. Abd-Elghany & Bourell [137] build samples with three different layer thicknesses (30 µm, 50 µm, and 70 µm) using powder with a wide size distribution (measured using sieve fractions, 46 µm mean size and 10% greater than 100 µm). Their results showed the thinner layer thicknesses produced denser parts and much reduced surface roughness. They concluded that these benefits were as a result of larger particles being removed by the wiper (Figure 9) and this is corroborated by work by Strano et al. [149] who showed that increasing powders sizes adversely affect surface roughness. This is supported by work published by Spierings et al [150] that showed surface roughness increased with increased powder size range. The effect was worse with powder that had a significant fraction greater than the layer thickness. This indicates that although the wiper may remove particles it does not do it effectively and without producing a rougher surface, possibly due to particles being caught under the blade scraping a line in the powder layer.

The importance of understanding the implications of using larger size powder particles not only relates to surface roughness as it could also have implications on the recyclability of the powder. With SLM unmelted powder within the machine gets recycled. If the powder is being separated with larger powder being removed from the bed, but remaining within the system, it could shift the powder size distribution up in size, which has an effect on the appropriate process parameters, unless suitable sieving is undertaken.

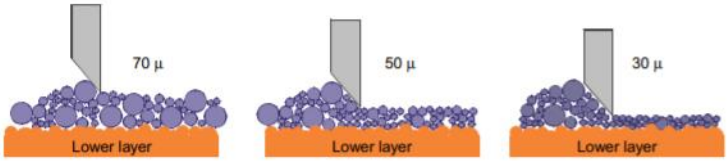

Figure 9 Schematic of the effect of layer thickness on what powder sizes are included in layers [137].

Another consideration observed by Spierings and Levy [151] is that the effective layer thickness when building in consecutive layers, is larger than piston movement (measured thickness), due to the powder layer being less dense that the solid layer of metal. As an example, when powder with an apparent/layer density of around 60% is spread into a 50 µm layer, that material reduces to 30 µm after consolidation. The subsequent layer of 70 µm will reduce to 42 µm, and this continues until the real volume of added material equals the piston movement. For this scenario, an 83.3 µm layer of powder with 60% density consolidates to 50 µm and this is defined by Speirings and Levy as the effective layer thickness, t_{eff}. This can be defined in the following equation:

$$t_{eff} = \frac{t_{layer}}{Powder\ density}$$

Equation 1 Effect layer thickness as a result of reduced density in consolidated powder material

This could mean that powder particles larger than the layer thickness could be allowed into the specifications for SLM aluminium, but it must be evaluated if the wiper separates the powders.

2.3.3 Powder Reuse

In SLM, the powder that remains unmelted within the machine is recycled and reused. As discussed above, the powder size has an effect on the processability and the appropriate processing parameters and therefore it is necessary that the powder is consistent. It is known that powder quality can “deteriorate”, which will affect the parts being produced [152], though it is does not always happen [153]. The causes of deterioration are likely to be loss of small particles, that can get airborne [145], or preferential sintering as smaller powders are significantly more likely to melt [150], powder separation due to handling [154] or from the wiper [137]. As such, the potential powder deterioration is specific to operating circumstance.

The change in the powder with recycling is not always detrimental. Seyda et al. [155] did experiments with Ti64, with 90% particles below 50 µm in diameter in 30 µm layers. Their results showed the powder size increased in use due to powder sintering, agglomeration, and the loss of fine powder particles. Another potential cause that was not considered in the paper was the separation and preferential building with smaller particles due to oversized particles being rejected from the bed by the wiper. The increase in powder size and size distribution improved the powder flowability and

packing density, which had a positive effect on the part density and mechanical properties. Similar results were found by O'Leary et al [156] with Ti64 and 40 µm layers, powder size increased from 18-41 µm to 21-50 µm after five builds. Neither study suggested a change in process parameters was needed and it may be that the improvements from packing density and flowability were more sensitive than a change in optimum processing parameters.

Efforts at measuring the reusability of AlSi10Mg powder were made by Del Re et al. [157]. They found that the powder sizes decreased in size and this caused a small reduction in yield strength and ultimate tensile strength (-4.22% and -3.19% respectively) (Figure 10). No information was presented regarding the layer thicknesses used. After each build, the powder was sieved through a 60 µm sized mesh and the efficiency of passing powder through these meshes may account for the reduction in larger sized powder.

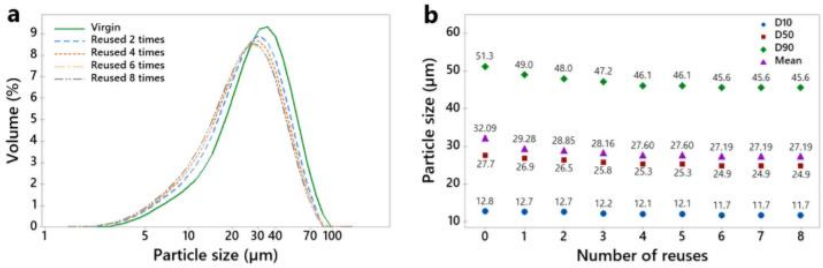

Figure 10 Particle size distribution of the AlSi10Mg powder with repeated reuse times, (a) particle size distribution as volume fraction, (b) Mean powder size and D10, D50, D90 percentiles.

While changing size is a concern with recycling powder, another is the presence of changing composition. Reduced processability has been found with recycled AlSi10Mg powder, with increased porosity being blamed on an increase of oxygen observable on the pore surfaces [158]. The powder can also pick up moisture from the atmosphere which then imparts oxides and hydrogen porosity into SLM parts, as observed by Weingarten et al. [159]. The challenges involved in avoiding moisture binding to the powders is not completely known, but for best practice, the powders are stored in argon filled containers.

2.4 **Gas**

As with welding and casting, aluminium alloys have an increased vulnerability to contamination by surrounding elements during heating and while in the liquid phase. In SLM, the processed metal should only be in contact with the gas in the build chamber and powder of the same composition, which, as mentioned above, could carry moisture into the chamber. This presents potential defects that arise from the presence of oxygen and hydrogen, which are known to have detrimental effects on welding and casting [72]. To limit the amount of moisture in the powder, careful

measures are taken during storage to reduce the amount the atmosphere can react with the metal. Most of the process is performed within an enclosed inert environment.

2.4.1 Process Atmosphere

SLM is performed within an inert atmosphere to reduce the rate of oxide formation on the heated metal. The process can be performed under vacuum [160], as with EBM , but the inert gas also has the function of removing spatter and evaporated metal fumes from the chamber as they interfere with the laser, as in welding [90], and also prevents build-up of condensate on the laser window. Oxygen cannot be completely removed from the chamber but it has been suggested that metal vapour behaves as a sacrificial material, reacting with the oxygen in the gas surrounding the melt pool, so reducing the amount of oxide within the built material [161]. This vapour phase reaction removes oxygen from the chamber as fine stable oxide particles that are trapped by the filters. This process is observed by the oxygen monitors that detect a drop in oxygen level during processing.

The choice of chamber gas is typically argon or nitrogen (for less reactive metals). Wang et al. [162] showed that there are no significant effects on processing AlSi12 in either argon or nitrogen compared with embrittlement when processed in helium. Nitrogen is generally avoided as it can react with many metals [163] [164], but Wang et al. argued that the reaction to form AlN is too slow for the fast melting within SLM, but this may not be the case for all SLM aluminium processing.

2.4.2 Hydrogen in SLM Aluminium

Hydrogen porosity is a widely reported problem in SLM processed aluminium [165] [166]) as with casting and welding (Figure 11). The issue arises as hydrogen has a high solubility in liquid aluminium and almost no solubility in the solid (Figure 12). Hydrogen dissolves into the molten aluminium and comes out of solution on solidification of the metal, however diffusion is restricted, and the gas is unable to pass through solid materials, and instead forms gas bubbles. The presence of hydrogen pores can be identified as they form perfectly spherical pores due to isostatic pressure. The gas pores are always expected to be hydrogen as it is the only gas with high solubility in aluminium liquid but not solid. Weingarten et al. [159] proved this is the case by fracturing samples within a vacuum and using mass spectroscopy to determine the escaping gas. Furthermore, Weingarten et al, proved that the main source of the hydrogen was from moisture brought in from powder and could be reduced by drying the powder before use in the SLM machine, by heating or by drying the powder inside the machine by pre-scanning. These two approaches have been tested with other aluminium powders with similarly positive results by Li et al [167] and Aboulkhair et al [166].

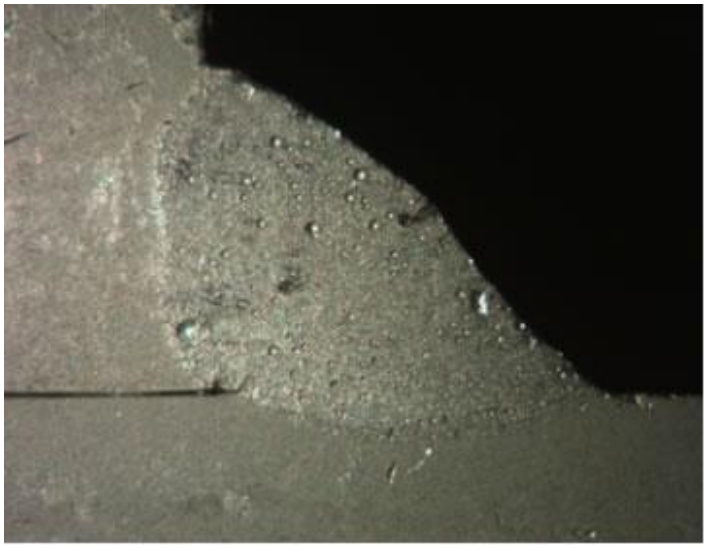

Figure 11 Hydrogen porosity present in welded joint of aluminium [72]

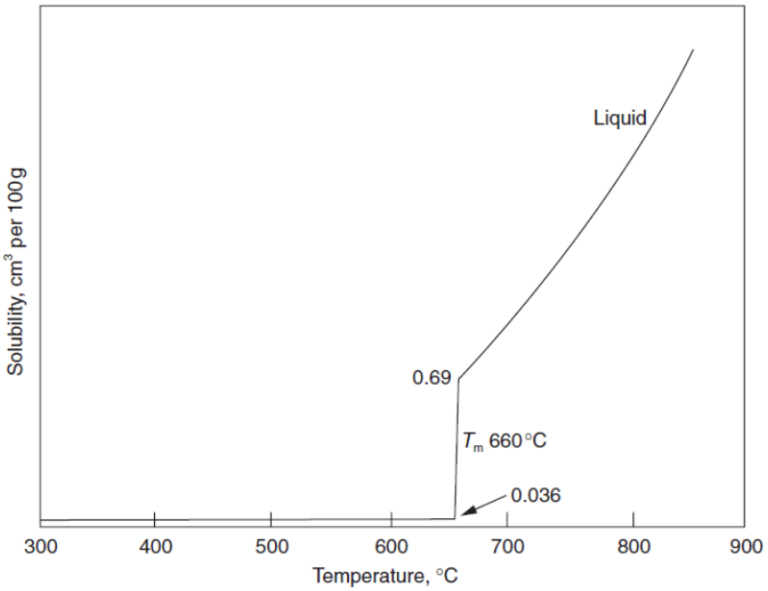

Figure 12 Solubility of hydrogen in aluminium [90]

It has also been shown that hydrogen porosity can be avoided with suitable scanning process parameters. In welding, it has been advised that hydrogen porosity can be avoided by increasing welding speed [168], while in SLM slower scanning speeds have seen reduced porosity [87]. The argument for speeding up scan speed is that there is less molten material and less time to absorb hydrogen. The argument for slowing the speed down is that the hydrogen has time to diffuse out of the solidifying metal, as the layer is very thin compared to welding. Weingarten et al. [159] showed that both arguments are relevant to SLM by testing a large range of scan speeds with varying beam diameter. They showed there was a least optimum scan speed for hydrogen porosity (Figure 13). The size of weld tracks are larger for welding, which is also in a less controlled environment than SLM and this informs the appropriateness of approach. The result found by Weingarten et al. was with a powerful and diffuse beam

(910W and 1mm beam diameter) and this may have created weld tracks more typical of welding in size than usually seen in SLM.

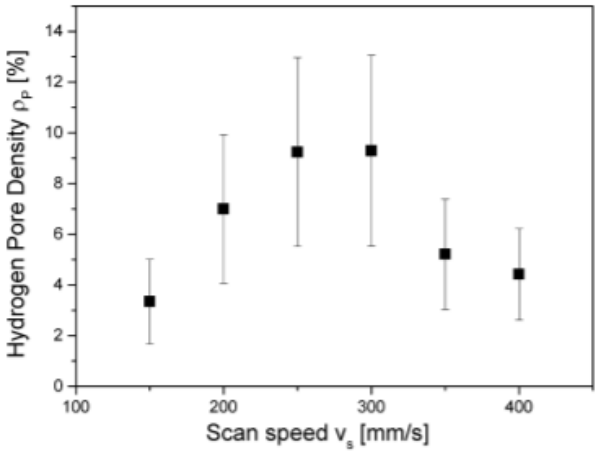

Figure 13 Dependence of scan speed on hydrogen pore density of AlSi10Mg SLM samples

Though it is not clear how the powder picks up moisture it is likely the moisture in the air chemisorbs on the powder due to the high surface energy. The moisture will cause both hydrogen porosity and oxides as it reacts with aluminium by the following equation:

$$3H_2O + 2Al \rightarrow Al_2O_3 + 3H_2$$

This implies that the presence of hydrogen indicates the presence of oxides and if powders pick up moisture this will cause both oxides and hydrogen porosity. Wang et al. [169] suggest that pores are more detrimental than oxides, provided the oxides don't cause pores, though the true effect of oxides in SLM aluminium is not known.

2.4.3 Oxides in SLM Aluminium

Oxides are known to form on all exposed aluminium surfaces and are very strong and stable. These oxides have melting temperatures of over 2000°C, much higher than the aluminium alloys and as such are difficult to remove. The presence of oxides prevents wetting of melt tracks [170]. Should two oxide fronts coincide there will be a weakness from the failed fusion. It has been observed in aluminium castings [171] that the oxides can fold over and leave pores between the meeting faces of the oxide. Even if the oxides do not cause pores and are wetted by aluminium on both sides their presence is not desirable as they are brittle and are a primary location for failure (Figure 14) and it has been suggested that they provide locations for hydrogen pores to nucleate [169].

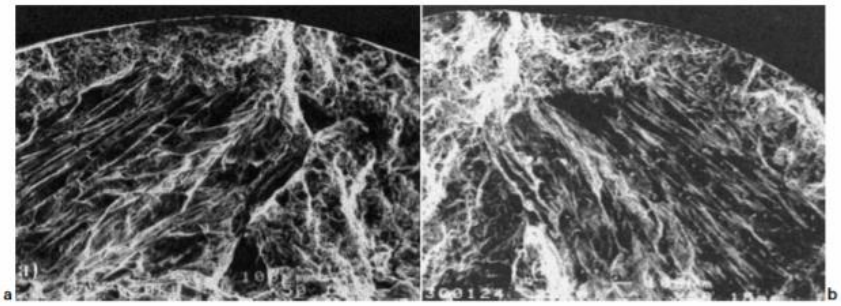

Figure 14 SEM image of corresponding fracture surfaces of sand cast Al-11.5Si-0.4Mg-0.57Fe-0.59Mn-0.17Ti showing extensive oxide films [171]

While it is strongly suspected that oxides form during SLM production it is not clear when they form and where they exist after production. The discolouration of the SLM aluminium surfaces is a strong indicator of thick oxides that form while the metal is at elevated temperatures [161] and the high level of balling indicates oxides forming at each layer [172](which is a result of the lack of wettability of the oxide coated surface). Thijs et al, [173] showed that the oxides on the top surface of steel samples were not uniform and the oxides were strongest at the sides of the melt tracks (Figure 15). The argument put forward for this is that the oxides float, and Marangoni convection direct the oxides to the sides, as well as the oxides growing strongest at the lower temperatures away from the centre of the melt pool. Marangoni convection is caused by a difference in surface tension where the liquid with higher tension has a stronger pull on the surrounding liquid. Surface tension is a function of temperature and a gradient is caused by the uneven heating of the melt pool. The highest temperatures are at the centre and this typically causes a reduction in surface tension and therefore the liquid on the surface is pulled to the sides, although this is affected by alloying elements and the gas composition.

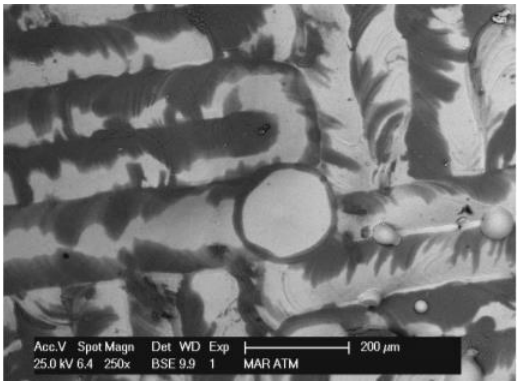

Figure 15 Back scattered Electron (BSE) graphs of the top surface of Maraging steel SLM part, where the oxides appear darker. A checkerboard scan strategy was used and is evident in the scan paths [173]

Marangoni convection is also suspected to play a role in the breakup of oxides within samples. Results from Louvis et al. [161], showed that oxides remained between scan

tracks but not between layers. It was proposed that Marangoni convection plays an important role in breaking up oxides to facilitate interlayer bonding (Figure 16).

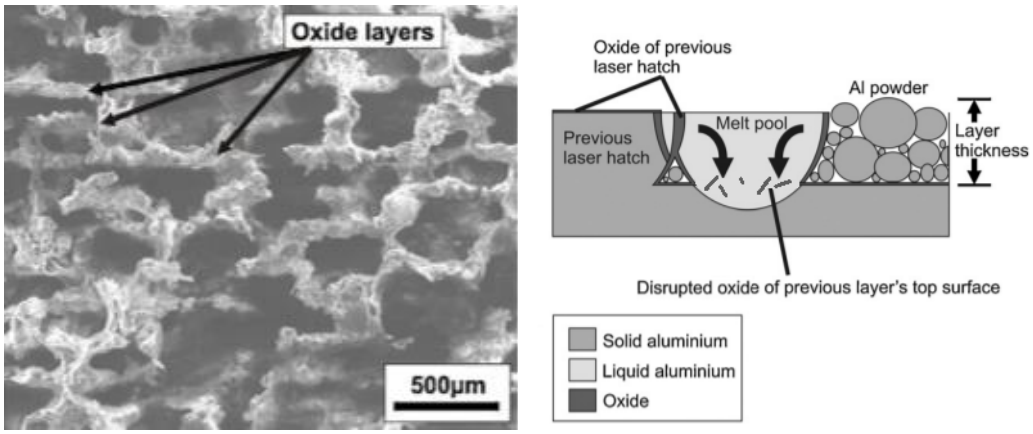

Figure 16 SEM image of SLM 6061 sample of oxides remaining after deep etching, removing all aluminium from the sample and (right) a reasoned explanation for the disruption of oxides allowing interlayer bonding [161]

Aluminium powder will contain oxides on the surface, and it must be considered how these affect processing and outcome. Olakanmi [96] tested powders with oxygen content varying from 2.8% to 15.9%. With the reasonable assumption that these oxides existed as a coating layer on the powder, concluded that changes in the thickness of the oxide film on the powder surface did not have a large influence on the melting and fusion of aluminium powders. Olakanmi suggested that the breakup of the oxide on the powder is as a result of the thermal expansion of the internal aluminium during heating and melting, Aluminium has a thermal expansion coefficient four times that of the oxide and the internal pressure of the aluminium causes the oxides to break, allowing the liquid metal to fuse. Fusion and formation of the weld pools has to occur faster than oxides form on the surfaces of the molten material. Another potential mechanism is that the oxide film directly under the laser beam is evaporated as suggested happens to the oxides on top of melt pools by Louvis et al [161]. This may be an inadvertent benefit to processing with higher powered lasers [80].

It has been demonstrated by Dadbakhsh & Hao [174] that increasing the layer thickness caused a reduction in the oxygen content in aluminium builds. The explanation for this was attributed to the increased energy required to create the larger melt pool, which may produce higher temperatures at the top of the weld pools. The powder size they used remained the same as that used in the typical 50 µm layer.

Assuming that oxide thickness is reasonably constant the amount of oxide on the powder per unit volume is a function of powder surface area, and it can be expected that larger powder particles carry less oxides into the system. How much the oxides on the powder contribute to the overall oxygen content of the final part is very hard

to determine as there are many other factors to consider such as oxide thickness, the oxygen content of the gas and where oxygen can enter the machine. Tang and Pistorius [175] calculated that the oxygen content was higher in the powder than in the built samples and judged that the samples' oxides were from evaporation and spatter of material rather than from unmelted oxides being pushed through melt pools. This conclusion was based on assessing the oxides as magnesium oxides which are most likely to be caused by evaporation from the alloy, than form on the surface of the powder. Though this does not rule out the possibility of both happening. Nyahumwa et al., [176] has suggested that oxides would be pushed through cast aluminium to remain within grain boundaries, and there is no evidence to support or refute this occurs within SLM aluminium.

The challenge of measuring and finding the location of oxides is that they are very thin, below 4 nm [175]. This can require TEM. Eddy-current testing (ECT) is another way of testing for oxides as the oxides have high dielectric conductivity in contrast to aluminium [177].

2.5 Melting

The primary criteria to classify the successful printing of a material in SLM is to produce a fully dense component, which is generally accepted as 99.5% dense or above [178]. The subject areas covered previously of powder characteristics and consistency, and contamination by gases are important to be able to achieve this consistently. Sufficient melting of the material is required to allow the liquid metal to wet and bond with adjacent solid without porosity or cracking. This is controlled by build parameters such as laser power, focus, exposure time, spot distance, hatch distance (where a hatched line is a line of spots) and layer thickness. The SLM process can be described as adding material through a sequence of welded spots (Figure 17); the first three parameters above control the size, shape and temperature profile of the spot and the second three are selected to ensure that spots have sufficient overlap to build fully dense parts.

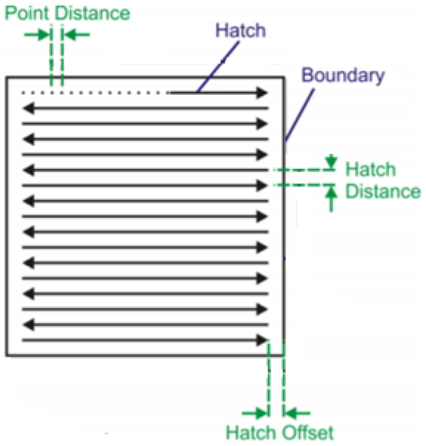

Figure 17 SLM parameters as defined by (MTT Technologies Ltd)

2.5.1 Laser Interactions during SLM

The spots are created as the laser interacts with the powder and any solid under the beam. A concern with processing aluminium, mentioned earlier, that also affects the welding of aluminium is that the material has a very high reflectivity and low absorptivity. Solid-state fibre lasers are commonly used in SLM applications for increased absorptivity in metals and finer spot size. The Bramson equation (Equation 2) can be used to calculate the absorptivity of materials for different laser light wavelengths. From this, aluminium has absorptivity of 5.6% for a source with 1.070 mm wavelength. This is very low, but three times higher than from a source with 10mm wavelength, similar to CO2, as typically used with laser welding.

$$\eta_\lambda(T) = 0.365\sqrt{\frac{\rho(T)}{\lambda}} - 0.0667\left(\frac{\rho(T)}{\lambda}\right) + 0.006\sqrt{\left(\frac{\rho(T)}{\lambda}\right)^3}$$

Equation 2 Bansom equation for calculating a metal's energy absorption coefficient for a laser for a given wavelength [179]

Where η is the absorptivity, λ is the wavelength of the laser, ρ is the electrical resistivity and T is the temperature.

The absorptivity is very low but improves with increased temperature. Rough surfaces are also a benefit as reflected photons are likely to interact with more surface. Powder beds are known to have high absorptivity as the beam reflects into the bed and interacts with multiple surfaces because of scattering (Figure 18). When the material melts and agglomerates it is expected that the absorptivity will drop. Trapp et al., [180], showed how the process parameters affect the absorptivity. They found that liquid aluminium has an absorptivity of 15% but this increases to 52% with keyhole-mode melting, where the laser ablates and bores into the materials, increasing material interactions of the reflected photons (Figure 19).

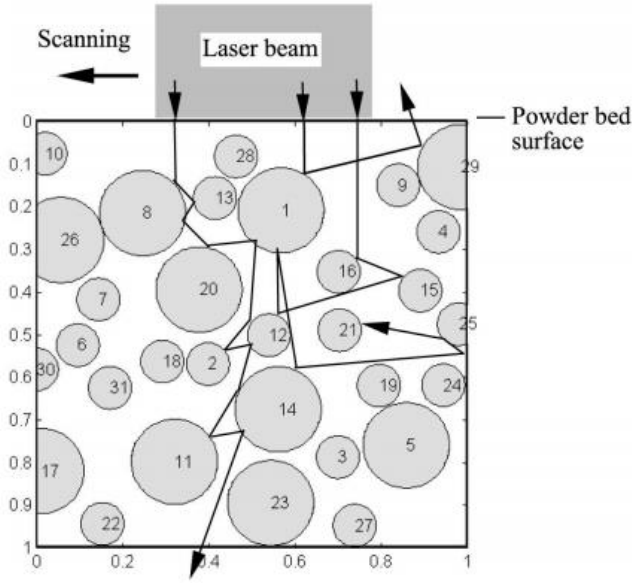

Figure 18 Illustration of laser interaction with powder particles (Zeng, et al., 2012)

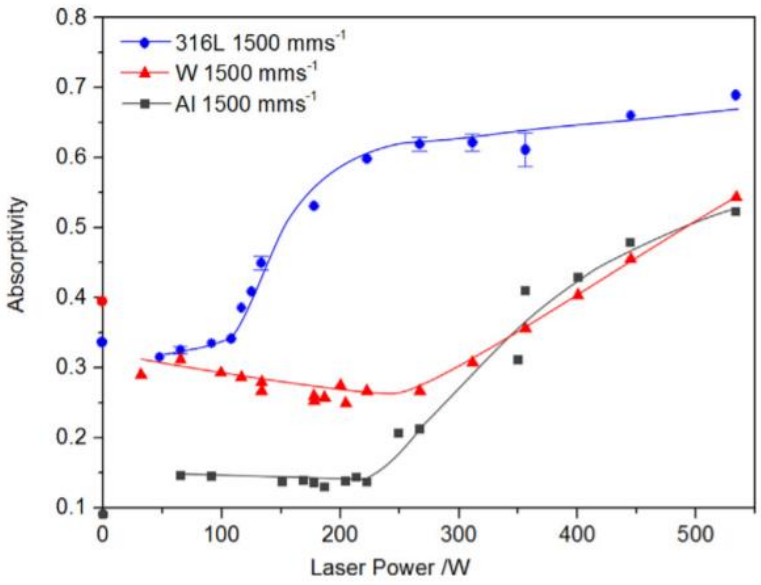

Figure 19 Absorptivity of aluminium alloy 1100, tungsten and 316L stainless steel as a function of laser power for a scanning speed of 1500 mms^{-1} [180]

2.5.2 Spot Size and Shape

The shape, size and location of the melt pool is important to the bonding of the new layer to the previously deposited material and to create a layer to which the next layer can bind [101]. Aversa et al., [101], showed that the shape of the weld tracks can differ greatly depending on the selection of parameters. Figure 20 shows a keyhole-mode melting scan track, which is conical in shape, with a penetration depth greater than the width of the melt track, and also an oval (or more accurately described as two semicircles, as symmetry is not a necessary feature) conduction-mode melting track, with greater width and sitting prouder of the substrate. Keyhole-mode melting is

created by evaporation of metal at the centre and the creation of a vapour cavity, which allows greater penetration of the laser. As the laser penetrates further into the metal the tracks have higher absorptivity, as mentioned above, but are less stable and are prone to porosity when the cavity collapses [181]. As such, keyhole-mode melting is not favoured compared with the more stable conduction-mode. The shape of the conduction-mode tracks are a function of the liquid/solid metal wettability and temperature gradients, which are affected by the conduction to surrounding material. Single scan tracks are often studied as a representative of the whole process, but the heat dissipation is much greater at this point than at the top of samples [105]. This may be why it is more often that keyhole-mode tracks are reported in single scan tracks [182] while the rounded melt pool boundary lines are more frequently observed in block samples [183].

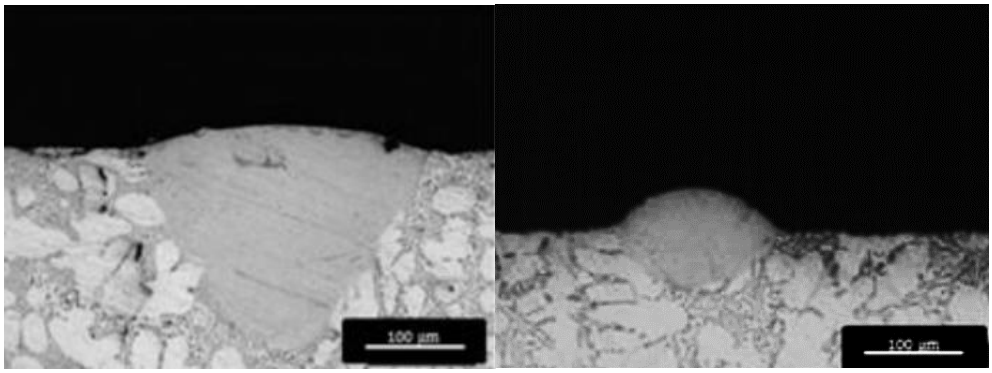

Figure 20 AlSi10Mg single scan track cross section optical micrographs showing (left) keyhole-mode melting (found with power = 185 W, scan speed 50 mm/s) and (right) conduction-mode melting (found with power = 190 W, scan speed 300 mm/s)

Spierings el al., [184] used a numerical model to simulate the temperature and fluid flow within an aluminium melt pool during SLM processing (Figure 21). Their calculations suggested that vaporisation takes place, as is observable during processing, but the vapour cavity is relatively shallow and therefore the shape remains wider than it is deep. This behaviour is further modified by the stirring of the melt pool, which appears to be largely driven by Marangoni convection.

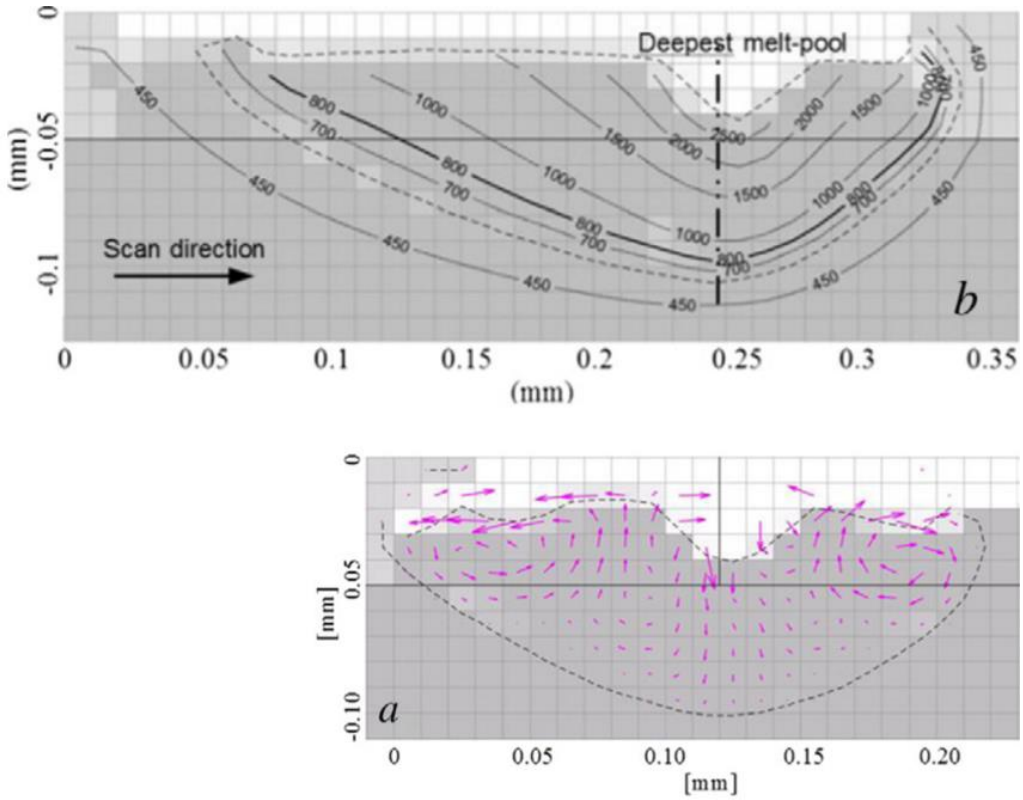

Figure 21 Simulated longitudinal cross-section at the centre of the melt-pool of SLM aluminium. Above shows the isotherms with boundary of 450°C where aluminium is 95% solid and dashed line at 635°C as the liquidus line. Below shows the calculated convection within the liquidus boundary [184]

2.5.3 **Balling**

The shape of the weld track above the substrate is influenced by the materials wettability. High surface tension can lead to balling, where the surface tension pulls the tracks into discontinuous balls [185]. Although aluminium is highly reactive and would be expected to have a high surface energy and tension, the presence of any solid oxide film modifies the behaviour by reducing the ability of the surface to flow and reducing the surface reactivity, lowering the chance of balling, but also reduces the wettability of the surface. Where balling occurs, it decreases the likelihood of subsequent melt tracks completely wetting the surface, which leads to porosity [172]. Balling can be described by the Plateau-Rayleigh instability, where surface tension disrupts a continuous stream of liquid, and a solution arrived at from this is to maintain a low ratio between molten track length to width [172]. This can be achieved by choosing scan strategies that keep low scan track lengths, such as a checkerboard scan pattern [186], or by widening the tracks width by increasing laser power or exposure time. Gu & Shen [187] reported that balling is less likely to occur with thicker layers as this also results in wider track width.

Increased exposure time and reduced scan speed are both considered to lead to increased balling by Rombouts et al [188], with a minimum time for which the material remains molten being required for balling to occur. This is similar to results found by Louvis [165] where increased time increased balling. However, the longer exposure

time and slower scan speeds are reported to reduce balling by increasing track width, as with the results from Li et al. (Figure 22). Furthermore, the slower laser travel speed should result in higher temperatures in the melt pools, which will lower the viscosity of the liquid metal, increasing wetting [189] This lessens the necessity for a flat building surface and could provide better recovery where balling occurs. The presence and strength of oxides on the molten aluminium may cause the opposite effect, as higher temperatures will create thicker oxides which will further impede wetting.

There is in the literature on this subject a tendency to consider the melt pool behaviour in a simplistic manner by only considering the molten metal, rather than the complex system that occurs in reality. This consists of solid surfaces covered with thin oxide films and molten metal also covered with thin solid oxide films. The surface reactivity and fluidity are controlled by the composition of the surface and so are controlled by any oxide films that form.

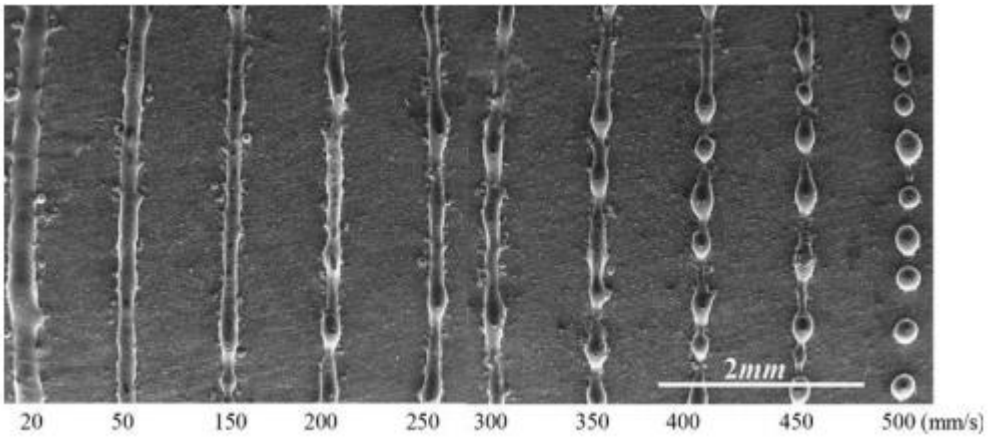

Figure 22 SEM images showing the balling characteristics of single scan tracks under different scan speeds [190]

2.5.4 Process Parameter Development Strategy

These issues inform the strategy to find suitable process parameters. In order to reduce testing time to find these parameters some researchers choose to use a material development strategy based on superimposing pool dimensions from single struts, or single scan tracks, to progress to walls and blocks (MTT Technologies Ltd). However, the melt pool is influenced by its surroundings and heat paths can be quite different when comparing very thin sections, as seen with parts below 1 mm by Takata et al. [191]. Morgan et al. [192] attempted to use this method with 316L where changing the spacing between fully dense walls could only produce 89% dense blocks. This approach is similar to a one-factor at a time approach, where the optimum parameters are found sequentially [165]. The problem with this approach is that the parameters are interdependent, e.g. the exposure time will change the track width and therefore influence the perceived optimum hatch distance.

These approaches originate from a desire to reduce the number of samples and builds required to find the optimum process conditions, but their shortcomings mean that an optimum density is not guaranteed, nor that satisfactory density will be reached.

Across these methods a common consideration is how much energy is imparted to the samples, with a belief that a threshold has to be reached to fully melt the tracks and fuse them with adjacent material [193]. A measurement of energy density is commonly used and can be measured as the amount of energy per line, per scan area, or per volume. The choice is reflective of the object being built. The choice between scan area or volume only varies with consideration of the layer thickness, which is least likely to be varied but it does influence the size of the melt pool and therefore it is included in this thesis. The equation for energy density for energy per unit volume is calculated by:

$$E_d = \frac{P_{laser}.t_{exposure}}{s_{point}.s_{hatch}.t_{layer}}$$

Equation 3 Energy density per unit volume [194]

Where E_d is the energy density, P_{laser} is the laser power, $t_{exposure}$ is the exposure time, s_{point} is the point distance, s_{hatch} is the hatch distance and t_{layer} is the layer thickness.

The measurements are crude as they do not consider the actual spot sizes, melt overlaps, absorptivity or heat loss to surrounds but are still used as a good "rule of thumb" [195]. Rescanning each layer is an approach that is often used to produce fully dense parts [196] and it is common to rescan the top layer to produce a better surface finish [197]. The energy density may not be able to be used when comparing these approaches as the effect of the parameters are likely to be quite different.

2.6 Solidification and Strengthening Mechanisms

Success when printing a material is dependent on successful melting and wetting between tracks and layers, but how well a material performs is dependent on solidification, as much of the alloys mechanical properties are controlled or limited by structures formed during solidification. In SLM, epitaxial growth is expected, where the crystals continue from the material below, and grains have competitive growth from the boundary toward the centre of the melt pool (Figure 23). This is similar to microstructure seen when welding aluminium, where epitaxial grains grow from the solid/weld boundary, although with welding equiaxed grains may nucleate in the centre. The absence of equiaxed grains in SLM is due to the individual layer thickness, with grains from the previous layer growing through the track before new grains can nucleate.

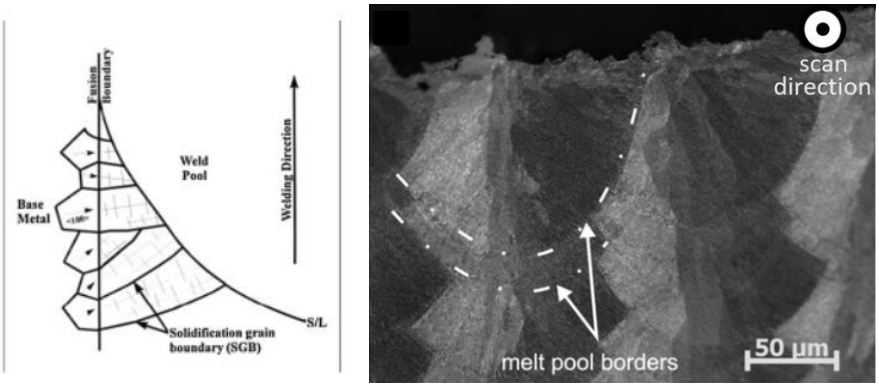

Figure 23 (Left) Schematic of grains growing during welding from underlying material in the direction of the weld [111]. (Right) Microstructure of SLM processed AlSi10Mg showing the grains direction from the melt boundaries toward the centre of the melt track [198].

The grain size and orientation are heavily influenced by the scan velocity [199], which alters the cooling rates [200]. With the fast scanning speed and high thermal gradients produced in SLM, the result is that a fine grain structure is produced with rotation of the growth direction altering with scan direction (Figure 24). However, because the grains grow from the previous layer as each new layer is applied the grain structure is elongated up through the build and this creates inhomogeneity in mechanical properties with SLM parts.

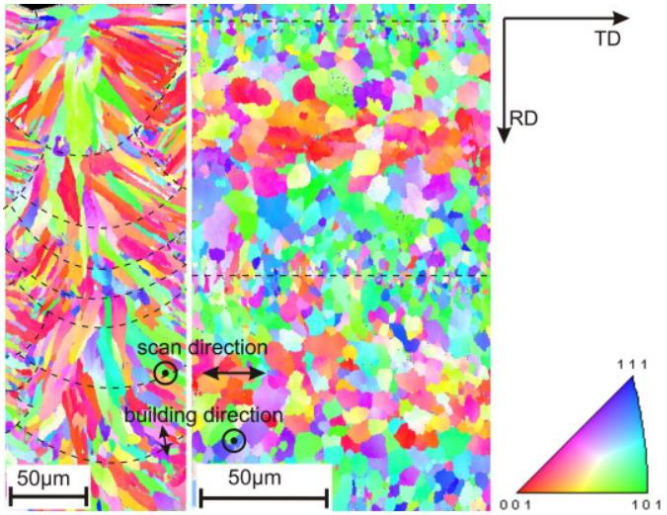

Figure 24 EBSD orientation maps in vertical view (left) and horizontal view (middle) of AlSi10Mg SLM part. SLM laser scanning direction is shown as well as melt pool boundaries denoted by the dashed lines. The grain orientation and EBSD scan direction are indicated on the right.

The direction of grain growth is controlled by the direction of movement of the heat source and therefore it is possible to have some control over the microstructure within the as-processed parts. Geiger et al. [201] used different scan rotation angles to alter the microstructure in SLM IN738LC and showed how the rotating scan angle of 67° improved the homogeneity of grain orientation (Figure 25). The scan strategy may also change grain sizes as scan tracks influence the thermal gradients within adjacent material temperatures [198]. Thermal gradients can also be manipulated

with double scanning, underbed heating, and using multiple heat sources. However, these are more often used in reference to thermal stresses, as will be discussed in section 2.7.

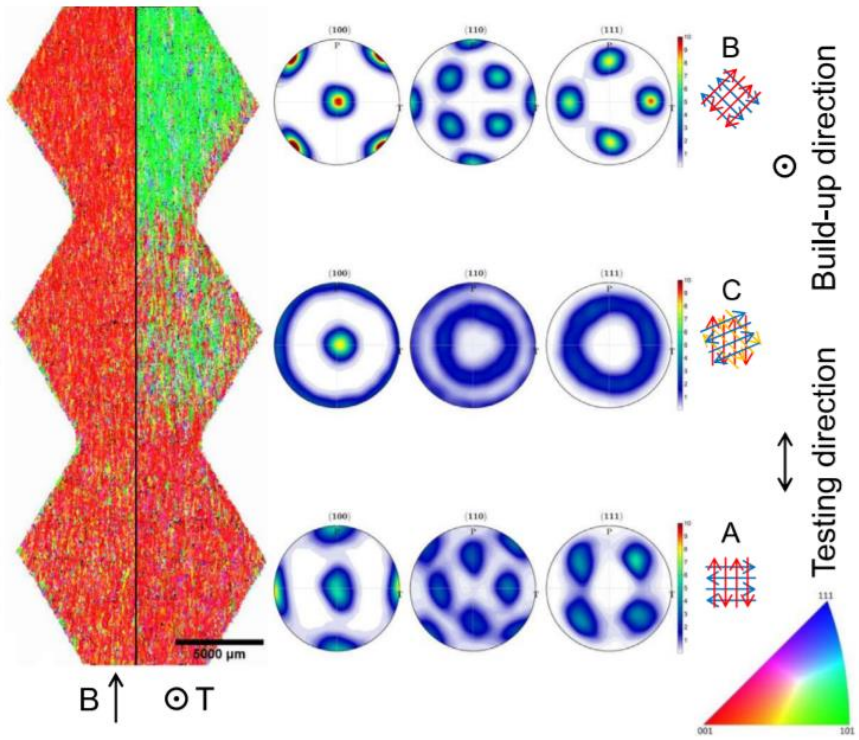

Figure 25 EBSD analysis of SLM built IN738LC triple tensile specimen built with varying scanning strategies A, C and B in as-built condition: Orientation maps (left), pole figures (centre) and scan strategies (right). The orientation map is split into half showing the crystallographic orientation by IPF colour codes with respect to the build-up direction and half the testing direction. The legend indicates contour levels in multiples of uniform distribution (MUD) [201]

The direction of the grain growth means that the grain size is not equal in all directions. It is challenging to precisely predict the microstructure of the parts produced by SLM as the material will not only experience non-equilibrium solidification after the initial melting but will also undergo remelting and reheating/cooling as more material is added. The cooling rates within the melt pools are very rapid at 10^5-10^6 °Cs^{-1} [158]. This reduces the diffusion of alloying elements compared to what would be seen in equilibrium phase diagrams. Subsequent heating and cooling with the addition of material complicates this further. Li et al. [105] processed Al-5Si-1Cu-Mg through SLM and found that the microstructure was location dependent with the larger grains near the bottom experiencing heating from the subsequent layers above, with more stable phases forming away from the top layers (Figure 26).

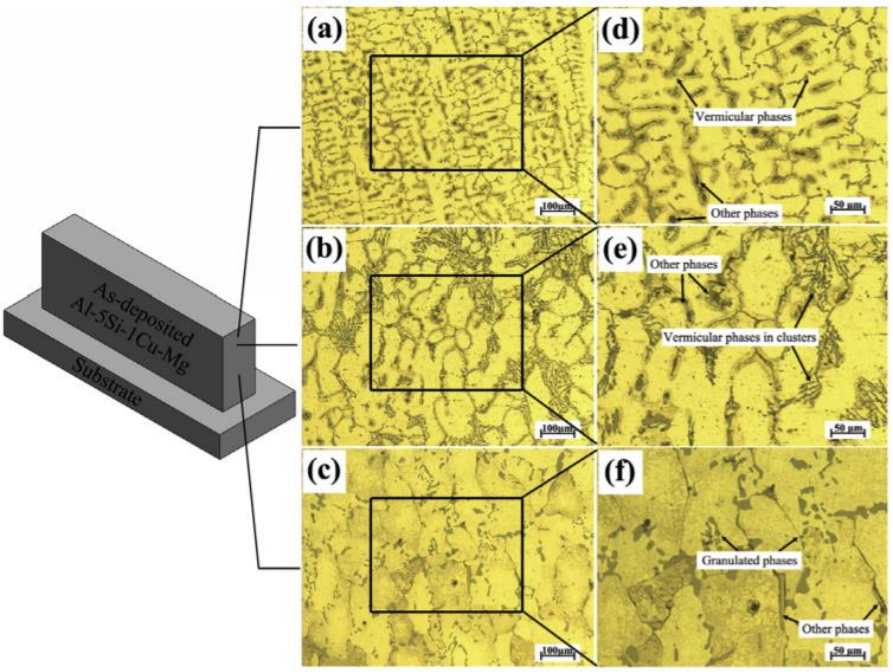

Figure 26 Optical images of the (a)(d) upper, (b)(e) upper middle and (c)(f) lower regions of a laser additive manufactured Al-5.32Si-1.19Cu-0.46Mg powder, build to be 200mm x 30mm x 25mm, processed with a 4.5 KW laser and 1000 mm/min.

Heat dissipation through samples is not consistent either and the solidification and reheating a location experiences is dependent on the shape of the part. Rangaswamy et al. [202], shown an example of this by calculating the isotherms of melt pools at different sections in thin wall samples (Figure 27). Takata et al. [191] analysed the effect on part width on the microstructure of AlSi10Mg. They found that parts with widths below 1 mm, would experience slower cooling rates and higher reheating from subsequent tracks, had finer, more abundant, silicon particles, equivalent to partial annealing. In alloys which are not easily solution treated, like some Al-Cu alloys, this could be a detrimental effect.

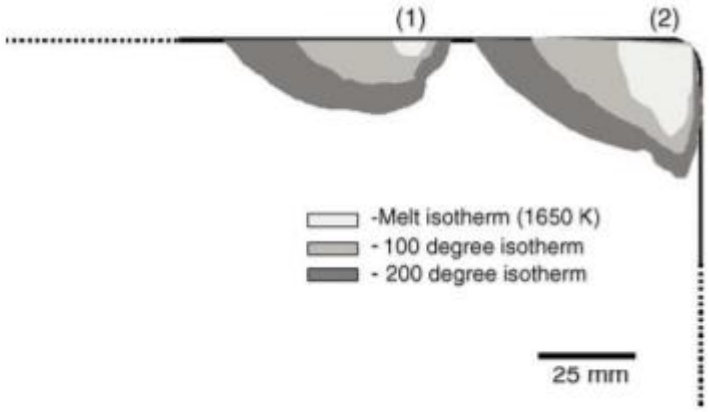

Figure 27 Schematic of the patterns of heat flow in a thin wall sample when the melt pool is (1) in the middle of the top edge and (2) when it is at the side edge of a thin wall plate (1mmx25mmx100mm) [202]

Outside laser parameters and part shape, there are many other factors that influence the microstructure. These include bed temperature, which will change the thermal gradients [203]. Similarly, layer thickness influences microstructure. Abe et al., [185] built tool steels with layer thicknesses of 30, 50 and 70 µm with the conclusion that the thinner layers produced denser parts, with higher tensile strength and hardness indicative of finer grained material. Similar results were found by Sufiiarov et al. [204], who compared inconel samples produced with layer thicknesses of 50 µm and 30 µm and found the narrower layer thickness increased the samples hardness and yield strength while reducing ductility. A caveat to this result is that the fusion defects were evident on the fracture surfaces of the 50 µm samples.

Initial powder state can also have an effect. Averyanova & al. [205] showed that different phases were present in SLM 17-4 PH, as a result of using powders from different sources that had different chemical composition, while still within ASTM standard specification.

Some efforts have been made to manipulate microstructures using these controls mentioned above. Huang et al. [206] employed electromagnetic vibration to create controlled microstructures in parts (Figure 28). For the aluminium samples, the optimum condition may be for the process to undergo annealing, solution treatment and ageing, and the main concern maybe that the alloy needs to avoid stubborn stable phases forming during processing.

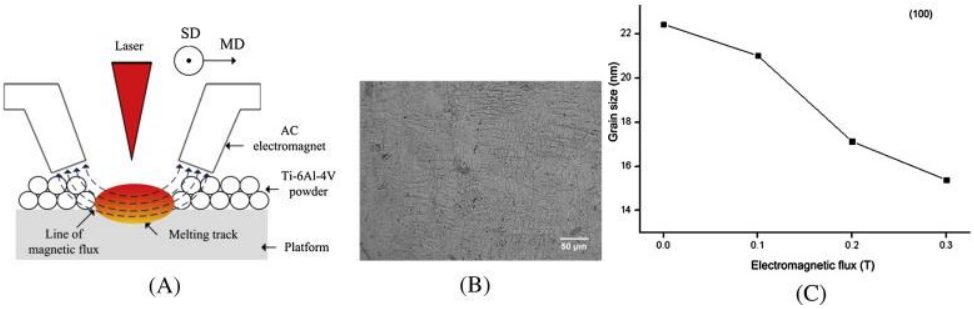

Figure 28 (A) Schematic of SLM experimental platform with dual-magnetic-pole AC electromagnet (SD is represents scan direction and MD is the movement direction of the electromagnet), (b) horizontal optical microscopy for Ti64 SLM part and (c) influence of electromagnetic flux on average grain size with orientation in XRD pattern. [206]

In this section, an attempt is made to understand the microstructure across various aluminium alloys processed through SLM and how that microstructure is influenced by the process.

2.6.1 Strengthening Mechanisms

First, it must be understood why it is important to control the microstructure and how it effects the mechanical performance of SLM parts. There are four ways in which aluminium alloys can be strengthened and all are variations on inhibiting the movement of dislocations, which are line defects the movement of which gives rise

to plastic deformation. Dislocations are surrounded by stress fields that can impede the movement of other dislocations upon slip planes in the crystal structure.

Grain Size

Grain boundaries are discontinuities in crystal orientation which impede the movement of dislocations. It is not possible with most grain boundaries for a dislocation to move from one grain to another. Therefore, finer grains, with more boundaries have higher strength and hardness. The relationship between the yield strength and the grain size is described in the Hall-Petch equation:

$$\sigma = \sigma_0 + k_1 d^{-m}$$

Equation 4

Where σ is the yield strength, σ_0 is the Peierls stress, k_1 denotes the strength of the cell boundaries, m is an exponent that varies from 1 to 0.5 and d is the grain diameter [72].

Solution Strengthening

Solid solution strengthening (SS) occurs where the crystal lattice is distorted by replacement of an atom with a vacancy or an atom of a dissimilar size, substitutional solid solution, or it can be distorted by an interstitial atom between atoms of the crystal lattice. The distortion in the lattice causes a stress field to form and thereby inhibits the movement of dislocations. This strengthening is capped by the solubility limits of the alloying elements, which is typically small for aluminium, and SS is not enough to produce medium to high strength alloys. The solubility limit of silicon in solid aluminium is 1.65% at 550°C and almost no solubility at room temperature.

The amount of solute in solution can be increased by the fast cooling rates seen in SLM, as the solute does not have time to diffuse and form a separate phase. This contributes to the increased strength of SLM processed Al-Si alloys compared to conventional methods [207]. However, this is not likely to be a preserved feature where post heat treatment, such as stress relieving annealing, is needed.

Precipitation Strengthening

As a solid alloy cools the solubility of alloying elements decreases and can cause a solid-solid phase transformation where elements will come out of solution during cooling of the solid material (Figure 29). In certain cases, these precipitates generate stress fields that form barriers to the movement of dislocations, this process is called age hardening or precipitation strengthening (PS). The precipitation sequence for Al-Mg-Si alloys under a conventional age hardening regime is as follows [208]:

$$\textit{atomic clusters (SSSS)} \rightarrow \textit{GP-zones} \rightarrow \beta'' \rightarrow \beta' \rightarrow \beta$$

Equation 5

The supersaturated solid solution is formed when the rapid cooling of the material traps solute atoms in solution within the solid. Within this supersaturated solution the solute atoms begin to cluster due to random motion and if this reduces the overall energy of the system, they become metastable in the form of GP zones. If the material is heated to a suitable temperature these GP zones can act as nucleation sites for other phases. Over time it is possible for a range of different phases to nucleate and grow, each being more stable than the previous one. This process is controlled by the difficulty in nucleation of the different phases and their relative stability.

This competition between the ease with which a precipitate can nucleate and its stability creates a sequence of precipitates that are controlled by alloy composition, temperature and time. For 2xxx alloys Guinier-Preston (GP) zones are the first to form and are fine clusters of copper atoms, below 10nm in size, formed throughout the grains. With Al-Mg-Si alloys the phase is also called GP zones but they are somewhat different being generally spherical clusters of Mg and Si with an unknown structure.

For AL-Mg-Si alloys, longer times at temperature allows new more stable phases to nucleate and diffusion leads to the growth of β″, which are the precipitates that give the maximum resistance to dislocation movement. β” are fine needle shaped precipitates of Mg_2Si with a monoclinic structure, they form when the alloy is aged at around 250°C.

With further aging β″ transforms into semi-coherent β′, which are rod shaped precipitates with a hexagonal structure, and finally into fully incoherent β platelets, which are the equilibrium phase in the precipitation sequence. At maximised strengthening, of the T6 temper, both β″ and β′ phases are present [209].

Should over ageing occur solution treatment can be performed to return the Mg-Si into solution by heating to 520°C for 1-1.5hrs [210].

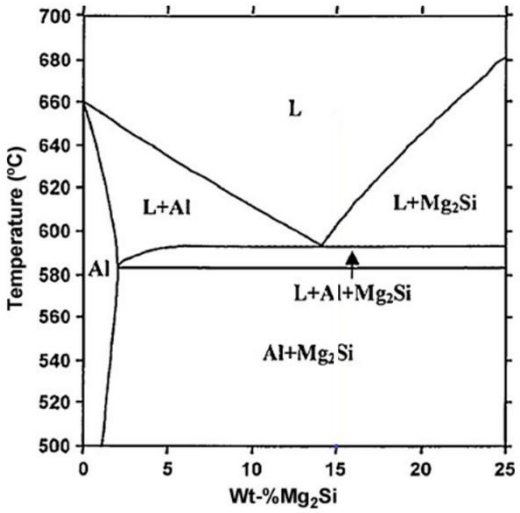

Figure 29 Al - Mg_2Si Binary phase diagram

The precipitation sequence for Al-Cu and Al-Zn-Mg alloys are similar. With Al-Cu, disk like GP zones are formed, which are replaced by the θ'' (Al_2Cu) phase at longer times. Over ageing creates semi-coherent θ' and finally the equilibrium phase tetragonal θ. The problem with using Al-Cu in SLM is the risk that over- ageing might occur producing an unsuitable microstructure, and the process is difficult to reverse with a simple heat treatment. Solution treatment is normally performed at 530°C for 2 hours, this is very close to the eutectic melting temperature of 548.2°C (Figure 30), but this cannot dissolve large blocky precipitates of θ.

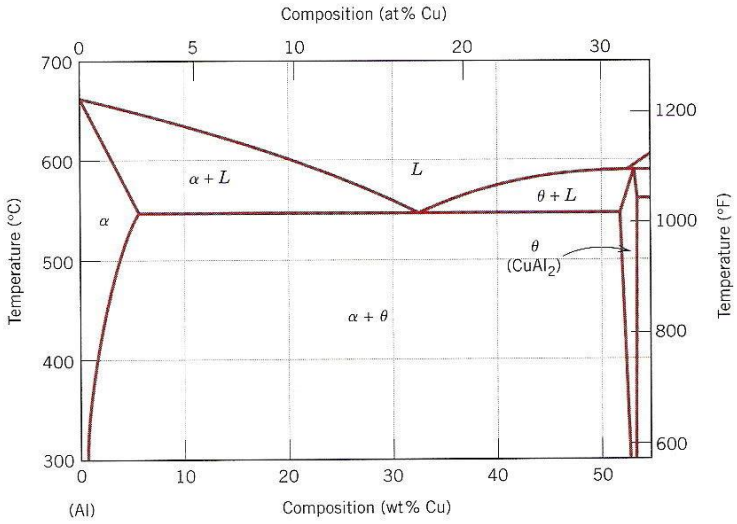

Figure 30 Al-Cu phase diagram

With the 7xxx series alloys, the precipitation sequence is not as simple, with more than one type of each precipitate forming, for example even with simple Al-Zn-Mg alloys two forms of GP zones are possible, along with other precipitates such as η' ($MgZn_2$). The composition of the precipitates can change depending on the copper content and ageing temperature [211]. The addition of copper increases the response to ageing, but this may not be desirable, and the copper also reduces the corrosion resistance of the material.

2.6.2 Microstructure of SLM Aluminium

The grain structure of many aluminium alloys processed by SLM have been analysed. Several examples exist of microstructures of SLM ALSi12 and AlSi10Mg, while examples of Al-Mg-Si, Al-Zn and Al-Cu are limited due to the limited success to print with these alloys.

SLM Al-Si Microstructure

Al-Si alloys are usually heavily alloyed, with near eutectic composition (Figure 4), and very narrow freezing ranges, 18°C for AlSi10Mg [212], which means a narrow band of transitioning material as the solidification front moves through the melt pool. Figure 31 shows how the short freezing range effects the solidification front compared to

larger freezing ranges typically seen with high strength aluminium alloys. Hypoeutectic Al-Si solidifies with pure silicon between columnar dendritic primary aluminium. The first material to solidify, at the melt track boundaries, typically has finer grains and is slightly different in composition. With AlSi10Mg and AlSi12, the melt pool boundaries are silicon rich and this means boundaries are easily identifiable (Figure 32), and more identifiable with increased silicon content [213].

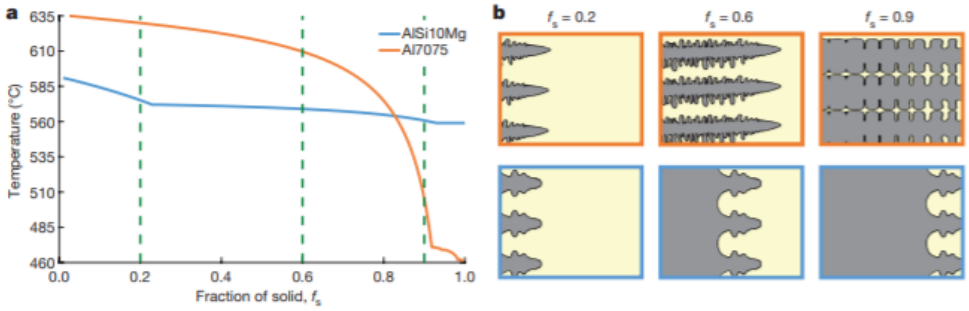

Figure 31 (a) Solidification curves for AA7075 (orange) and AlSi10Mg (blue) and (b) Schematic representation of solidification, indication how over a large temperature range leads to long channels of interdendritic fluid, whereas a narrower solidification range leads to a short interdendritic region with greater spacings [214].

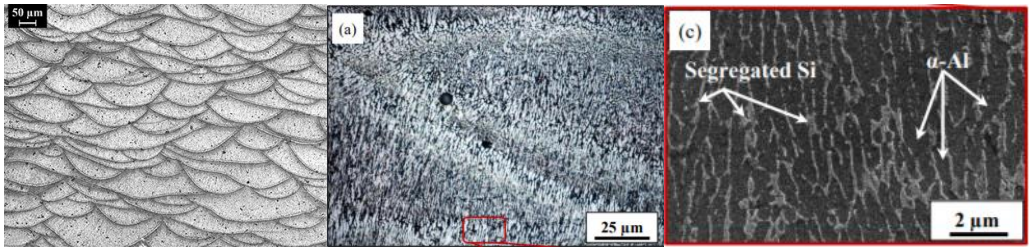

Figure 32 Microstructure of AlSi10Mg with silicon content identifying the melt pool boundaries [183] and structure of silicon and aluminium within the melt pool [215]

SLM Al-Si Mechanical Properties

A comprehensive list of recorded tensile stress-strain results for AlSi10Mg has been compiled by Tang & Pistorius [212] with UTS for as built samples ranging from 287MPa to 460MPa. SLM Al, as with other materials, has higher strength in the vertical direction than horizontal, as the grains are elongated, during freezing, toward the laser source (Figure 24). The tensile strength of SLM AlSi12 and AlSi10Mg in the vertical direction is far greater in the as-processed SLM condition than in cast, but the material has very low ductility (Figure 33). Similarly, hardness is much higher in the as-processed material [216]. This is a result of the fine microstructure produced from the fast solidification in SLM [217].

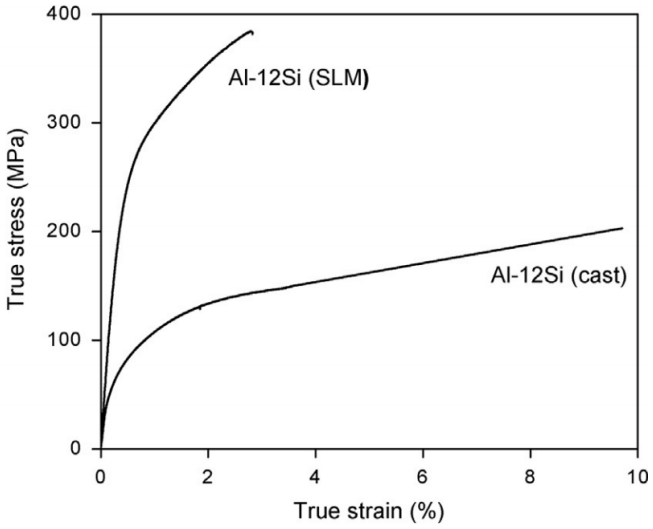

Figure 33 Tensile tests performed with cast and as-prepared SLM Al-12Si samples [218].

Part of the reason for the high strength and low ductility in SLM Al-Si alloys is due to the large amount of silicon at the melt pool boundaries, which is where failure occurs (Figure 34). Silicon is very hard and brittle and the presence of continuous films allow cracks to spread easily. The microstructure can be modified by longer heat treatments at quite high temperatures that allow the silicon phase to spheroidise removing the continuous phase and so improving ductility (Figure 35).

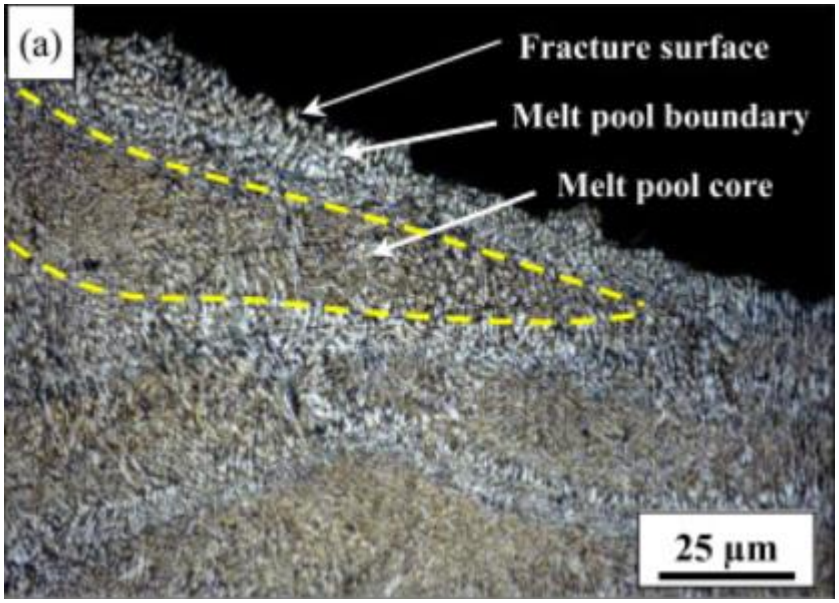

Figure 34 Cross sectioned fracture surface of tensile test sample showing failure along silicon rich melt pool boundary [215]

SLM parts are often annealed to reduce residual stresses. Some Al-Si alloys can be precipitation hardened, such as AlSi10Mg [158], and undergo solution treatment and age hardening. Figure 35 shows an SLM processed A356 (Al-7Si-0.3Mg), by Kimura & Nakamoto [100]. When it was annealed above 250 °C the microstructure was greatly changed. In this alloy, precipitation of β" occurs at this temperature. Kimura & Nakamoto [100] reported that the strength gained from ageing did not compensate

from the loss of strength from the other microstructure changes. Similar results have been reported for other Al-Si alloys. Li et al. [219] showed how the stress-strain curves of AlSi10Mg can be modified with heat treatment from high strength-low elongation to lower strength-high elongation, which is similar to the cast performance (Figure 36). Similarly, Ma et al [98] found that annealing Al-20Si at 400 °C reduced the UTS from 506 MPa to 252 MPa.

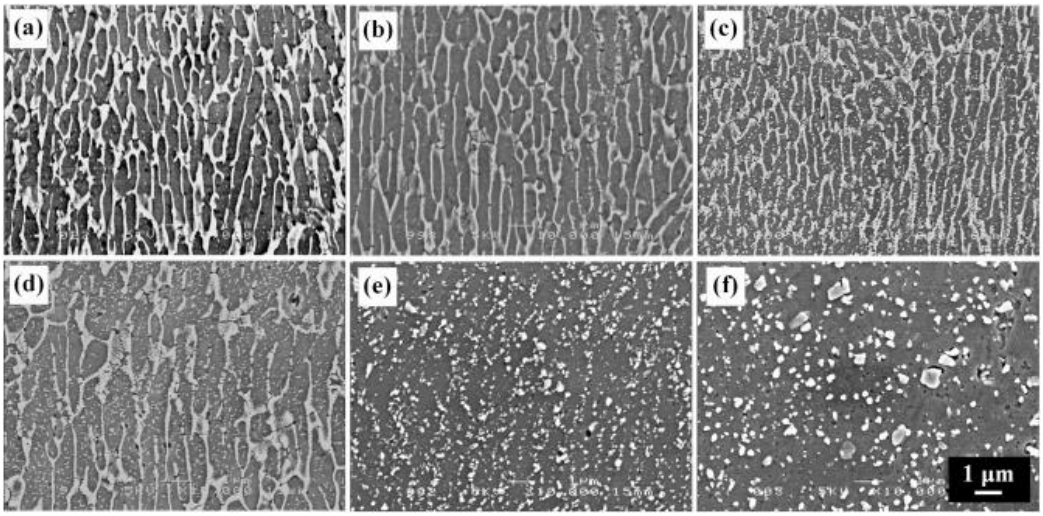

Figure 35 SEM images of the vertical cross sections of (a) an as-fabricated SLM specimen and T5 SLM specimens annealed for 5 hr at (b) 150 ℃, (c) 200 ℃, (d) 250 ℃, (e) 300 ℃, and (f) 350 ℃ [100]

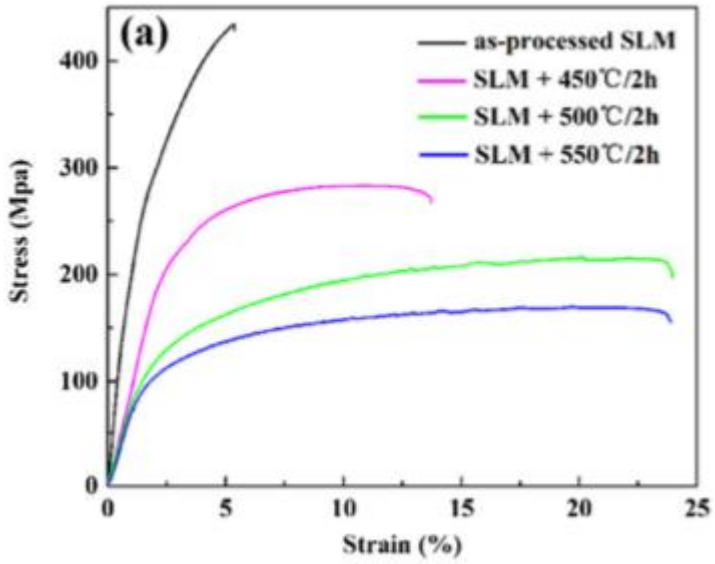

Figure 36 Tensile stress-strain curves of SLM AlSi10Mg samples that were heat treated at different temperatures [219]

A side effect of heat treatment is the density of built samples can drop as pores form [216]. The reduced density is caused by the diffusion of hydrogen held in solution of the aluminium lattice out of solution to form pores. Li et al [167] used XRM (X-Ray Microscopy) to view the evolution of pores in a single sample, before and after heat

treatment (Figure 37). The pores were spherical, and therefore identified as gas pores. They found that the pores increased in both number and size with heat treatment.

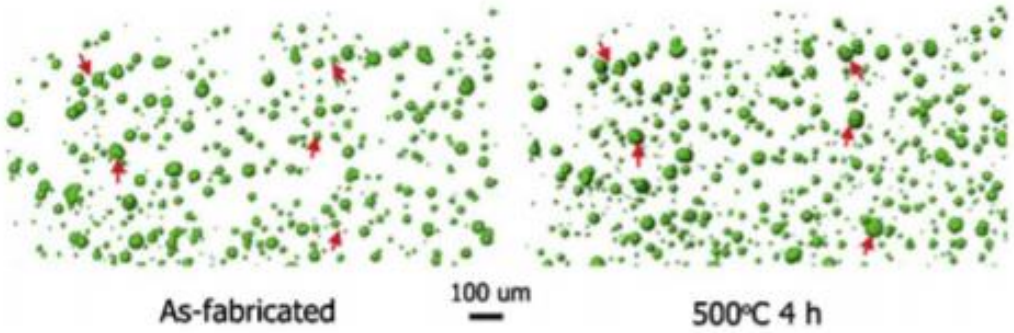

Figure 37 High resolution XRM results showing the evolution of pores in the AlSi12 cubes before and after heat treatment at 500°C for 4 hrs. Red arrows used to indicates corresponding pressurised pores.

SLM Al-Si-Mg Microstructure

The most commonly processed Al-Si-Mg alloy in SLM is AA6061 and this has had very little success. Fulcher et al. [81] used electrical etching to show the grain structure between cracks of AA6061 (Figure 38). The melt pool boundaries are not apparent, unlike in Al-Si alloys. This is due to the low alloying content of the alloy, which has less than 4% alloying elements. The freezing range of this material is 90°C and this causes a wider band of solidifying material than Al-Si alloys. This is likely to promote the grain growth to be consistent in direction and not as susceptible to the changes in direction of the laser.

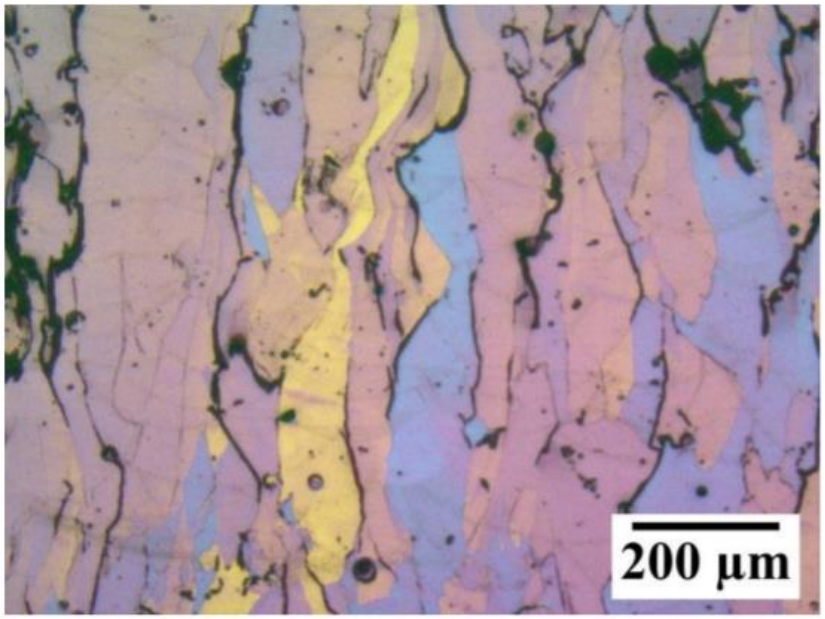

Figure 38 Optical micrograph of AA6061, vertical surface, as built and electrolytic etched

As the material cracks during processing the strength is low. Research has not been carried out to show evidence of precipitate phases in the processed material or post processing heat treatment. Fulcher et al. [81] used Charpy tests to test the facture

toughness of the material and this showed how the cracks weaken the material. SLM AA6061 fracture at the cracks, revealing the crack surfaces (Figure 39).

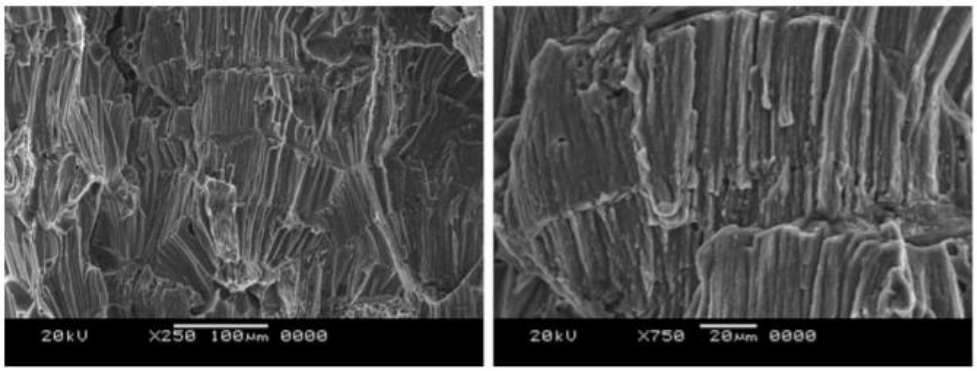

Figure 39 SEM images of AA6061 T6 vertical surface Charpy test fracture surface [81]

SLM Al-Cu Microstructure

Within the 2xxx series there are alloys ranging in weldability, with the highest strength alloys often the least weldable. In SLM, the limits of processability are not known, nor is there complete understanding of the ability to post-process age hardened alloys. Of the high strength alloys, research has shown severe cracking occurs in SLM processing. Koutny et al. [82] found with 2618 and Zhang et al [108] found with powder similar to 2024, that high density parts could be processed but always with the presence of cracks. Zhang et al [108] showed that the cracks are plentiful and propagate through the weld tracks (Figure 40).

Alloys with higher copper content (above 6%, as with casting Al-Cu alloys) are known to have better weldability. Karg et al. [220] processed 2219 (AlCu6Mn) with no reported cracks. They also reported no over ageing, however, the yield strength from as-build and T6 were low compared to conventionally manufactured material.

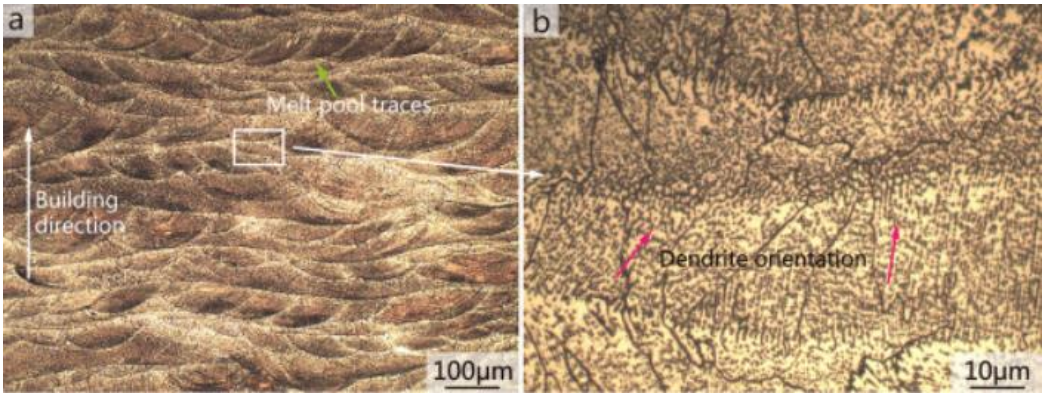

Figure 40 Optical microscopy images of etched dense SLM Al-Cu-Mg vertical cross sections showing detail of the melt pools [108]

An alloy of the composition Al-3.5Cu-1.5Mg-1Si was processed by Wang et al., [221] crack free. This content of copper is not typical of weldable al-cu alloys and is similar to unweldable alloys like 2007 and 2024, with the exception of higher silicon content.

The microstructure presented (Figure 41) is similar to that presented for AA6061 but without cracks between the elongated grains (Figure 38) (It should be noted that thin cracks may not be easily identifiable with this method).The composition responded positively to heat treatment and reasonably high tensile stress values were recorded (Figure 42).

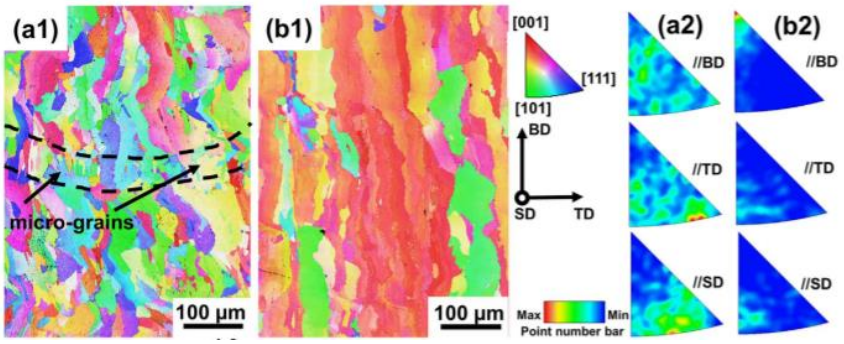

Figure 41 EBSD inverse pole figure maps: (a1) as processed and (b1) T6 heat treatment; texture intensity distribution: (a2) as processed and (b2) T6; Spatial orientation with respect to the build direction (BD), scanning direction (SD) and transverse direction (TD) and the colour code used for crystal orientation in the orientation maps are given in the top middle part of the figure [221].

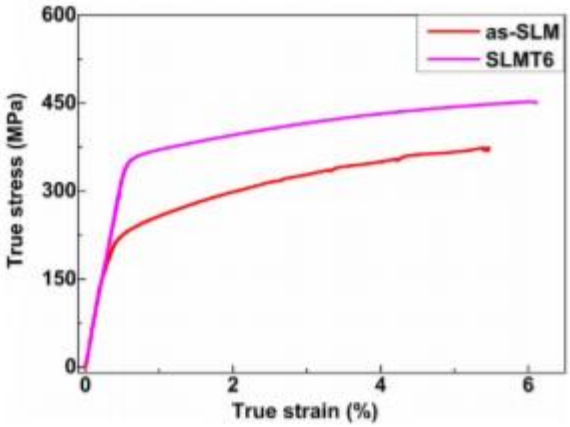

Figure 42 Tensile stress-strain curve of the as processed and T6 Al-3.5Cu-1.5Mg-1Si specimens [221].

SLM Al-Zn Microstructure

As with Al-Cu alloys, the 7xxx series contains high strength unweldable alloys and lower strength weldable alloys. Weldable alloys contain little to no copper and lower amounts of zinc and magnesium than the higher strength alloys. While there is a compromise on strength, many of these alloys still have high strength (such as 7003, 7046, 7039 and 7017 [72]) and may present a good route forward for SLM processing. However, to the authors knowledge, no efforts have been made to process these alloys, while considerable efforts have been made to process high strength and unweldable alloys such as 7050 and 7075.

Qi, et al. [83] showed the microstructure of SLM processed 7050 with both conduction mode and keyhole mode melting (Figure 43). As discussed before, conduction mode is preferential, and the microstructure appears similar to the age hardenable alloys

above. The microstructure of the keyhole mode part is very different, with much smaller grains, neither method was able to reduce cracking.

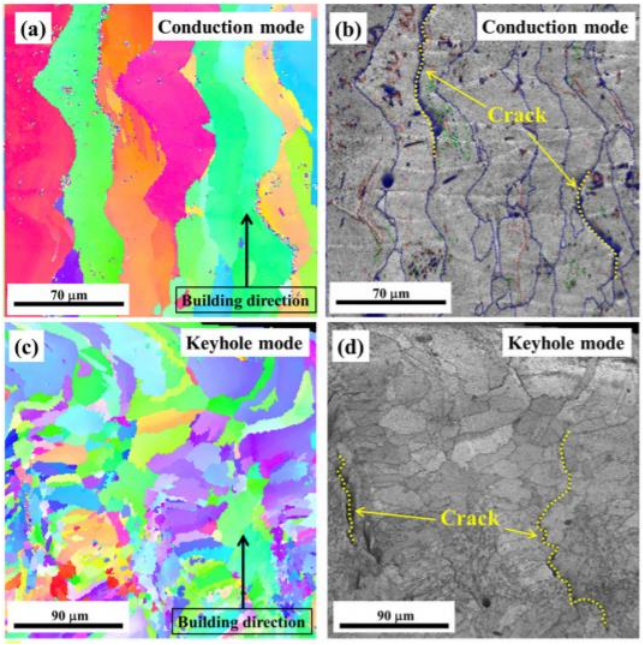

Figure 43 EBSD maps of SLM processed 7075 with two melting modes;(a) orientation image map and (b) grain boundary misorientation angle map in conduction mode, (c) orientation image map and (d) grain boundary misorientation angle map in keyhole mode [83].

One of the highest strength alloys is 7075 and this makes it very desirable for structural applications. This alloy is difficult to weld and efforts to build 7075 samples through SLM results in large amounts of cracking [222]. This has led to several attempts to modify the alloy for improved processability.

Montero-Sistiaga et al. [118] improved the processability with the addition of silicon. Silicon is known to improve the wettability and flowability of aluminium alloys by proving a low temperature eutectic that can heal forming cracks. Montero-Sistiaga et al.'s work shown that the addition of 3 wt% silicon significantly reduced cracking (Figure 44). EBSD results from this work highlight another possible reason for the reduction in cracks (Figure 45). The increase in silicon coincided with higher volume fractions of finer grained regions which could inhibit the growth of cracks.

The inclusion of silicon changes the phases that are formed with Mg_2Si, Cu-Zn-Si-Mg and Cu-Si-Mg-Al being present. Hardness values for as-processed SLM Al7075 +4%wt Si were above 90% of conventional 7075. The hardness has a significant drop in value with solution treatment that was not recovered with ageing attempts. The main reasoning for the higher as-processed hardness values was from the fine microstructure achieved with SLM and lost with solution treatment. Compression tests on the alloys were significantly below yield strengths of conventional AA7075 in all cases. This could present challenges with future use of the alloy.

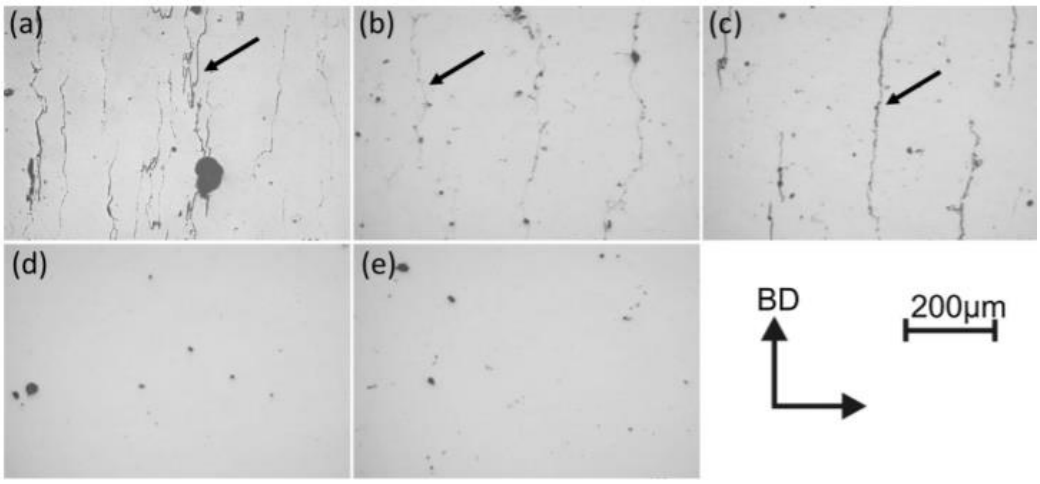

Figure 44 Polished vertical cross-section of 7075 with the following additions of silicon (wt%) (a) 0%, (b) 1%, (c) 2%, (d) 3% and (e) 4%. Cracks are highlighted with black arrows [118].

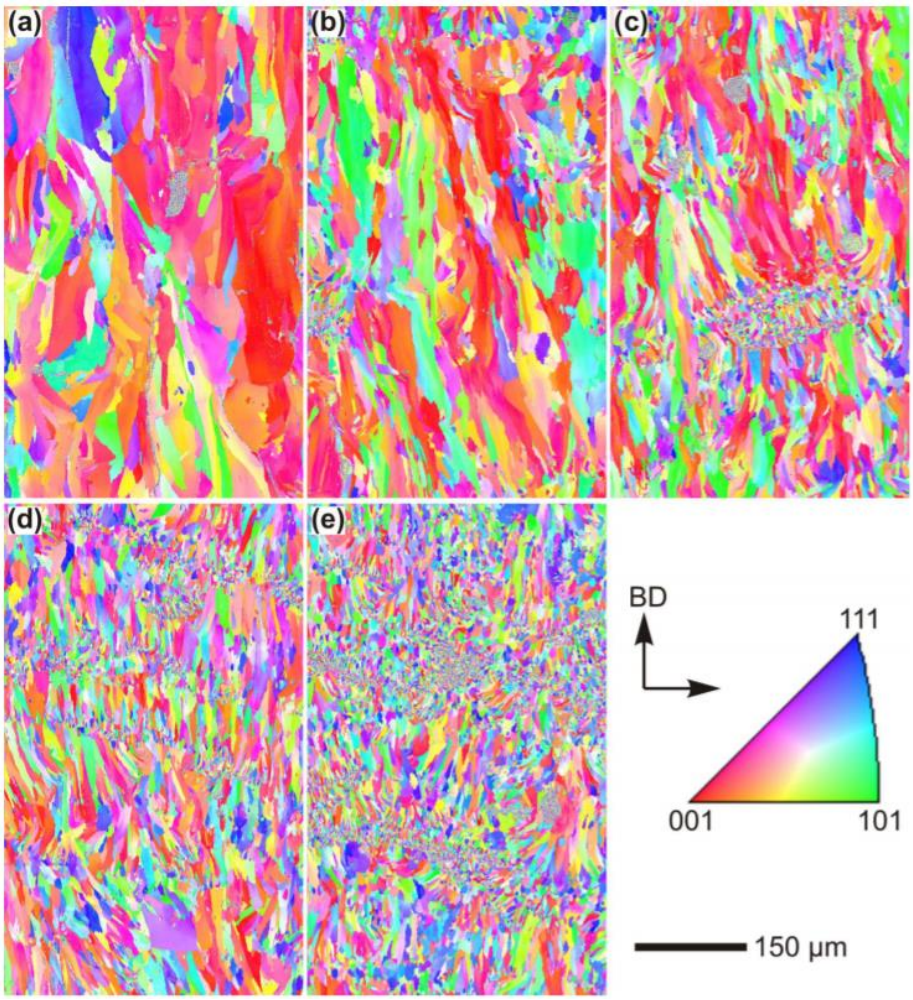

Figure 45 EBSD orientation maps of the vertical cross sections of 7075 with the following additions of silicon (%wt) (a) 0%, (b) 1%, (c) 2%, (d) 3% and (e) 4%. The crystallographic orientation is represented by the inverse pole figure for aluminium [118].

SLM Al Alloys with Grain Refiners

Grain refiners are often used with welding to improve weldability and increase strength and investigations have been carried out to see if the same benefits can be

achieved with difficult to process alloys in SLM. Scalmalloy, Al-4.5Mg-0.66Sc-0.37Zr [123], is an alloy, developed by Airbus [223], which uses both scandium and zirconium as grain refiners. These additions are often used together as scandium seeds grains while zirconium pins grain boundaries. These two additions have further benefits from age hardening though scandium has a far more potent response to age hardening.

The effect of scandium and zirconium on SLM microstructure is to produce a very fine and pronounced equiaxed grain structure at the melt boundaries, with elongated grains developing from this due to competitive growth (Figure 46). The fine microstructure increases the strength and homogeneity of specimen with the yield strength above 500 MPa for all orientations [123].

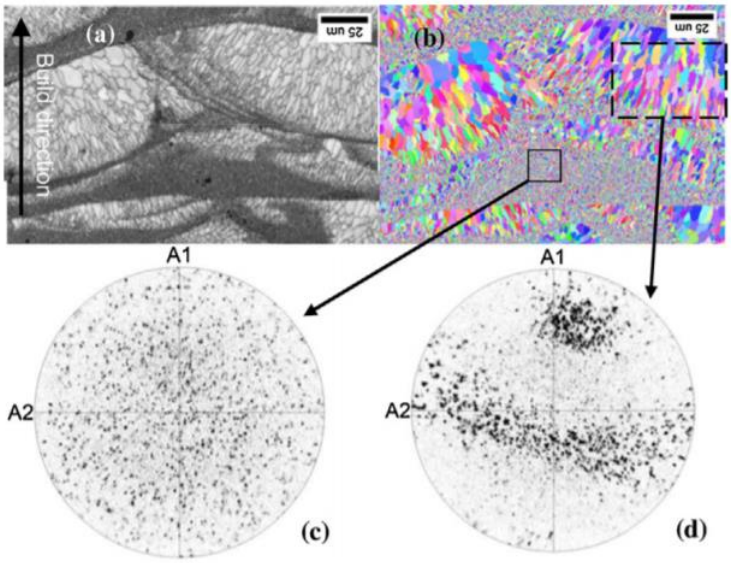

Figure 46 Microstructure of SLM Scalmalloy showing the fine grained and course grained regions. (a) Etched and (b) EBSD microstructure of the same region. [001] Pole figures for (c) fine grained region and (d) course grained region [127].

Work by Spierings et al, [224] had shown a high level of precipitation within the grain boundaries of the fine grained region (Figure 47). They identified these precipitates as consisting of oxides, mainly $MgAl_2O_4$ (spinel), with occasional Al_3(Sc, Zr) attached. The precipitation of Al_3Sc is expected to act as an inoculant for the fine-grained region and appear at the centre of grains but it is possible that some reaction with oxides occurs.

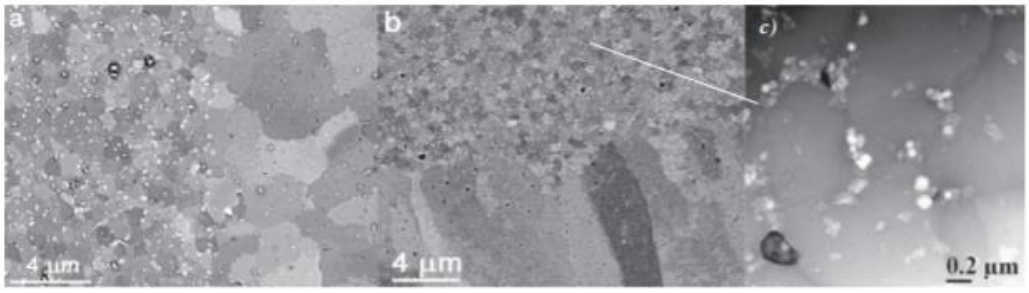

Figure 47 SEM images (a) and (b) of the SLM Scalmalloy showing FG and CG regions with grain boundary precipitates, (c) HAARDF-STEM image of oxide particles in FG material [224].

Other Al-Sc-Zr alloys have been researched. Yang et al. [125] processed Al-3.4Mg-1.08Sc-0.23Zr-0.5Mn through SLM, which has a higher content of scandium and reduce content of zirconium. EBSD results from this work (Figure 48) shows a similar structure to scalmalloy (Figure 46).

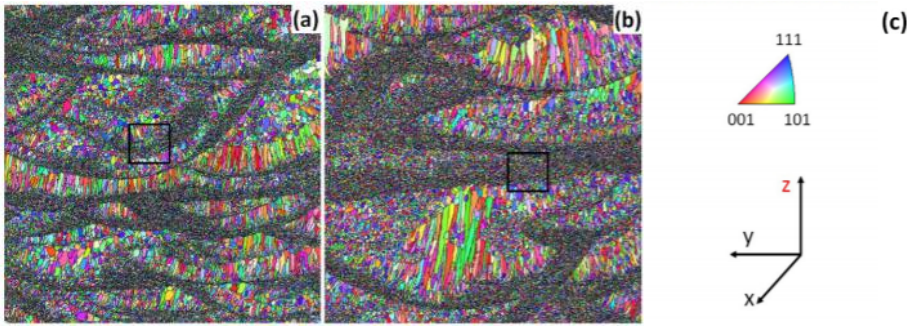

Figure 48 Microstructure reconstructed from inverse pole figures from EBSD measurement on Al-Mg-Sc-Zr alloy: (a)Energy density 77.1 Jmm-3; (b)energy density 154.2 Jmm-3; (c) pole map and part build orientation [125].

LI et al. [225] processed a similar material (Al-6.2Mg-0.36Sc-0.09Zr) and found the microstructure did not have as much of a fine grain structure (Figure 49). The content of scandium and zirconium were much reduced compared to the two previously mentioned compositions. Tensile tests were not presented with this material and therefore it is not clear how this change in microstructure effects the mechanical properties.

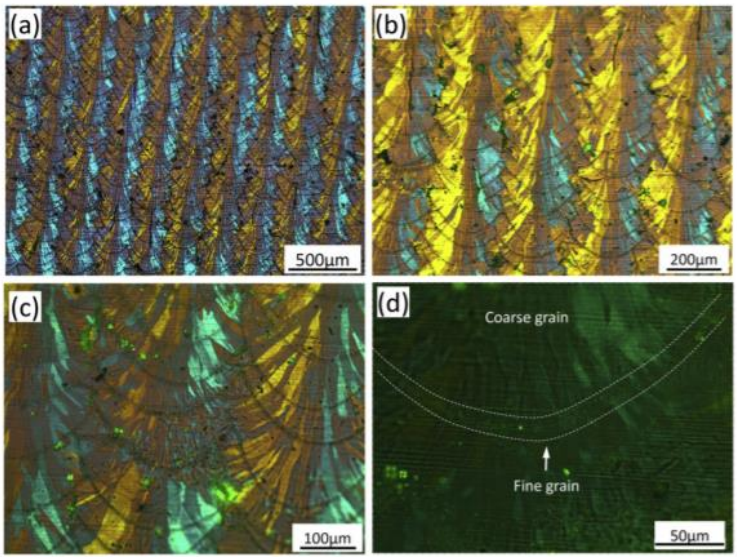

Figure 49 Polarizing micrograph of SLM Al-Mg-Sc-Zr sample showing microstructure of vertical cross section [225]

Awd et al [124] performed tensile tests on SLM processed Scalmalloy, with comparison to AlSi10Mg and blown powder Scalmalloy (Figure 50). The tensile properties for Scalmalloy are comparatively high for aluminium alloys, with high yield and ultimate strengths and reasonable elongation to failure. These results are cited as being homogeneous due to the fine equiaxed grain structure between melt tracks.

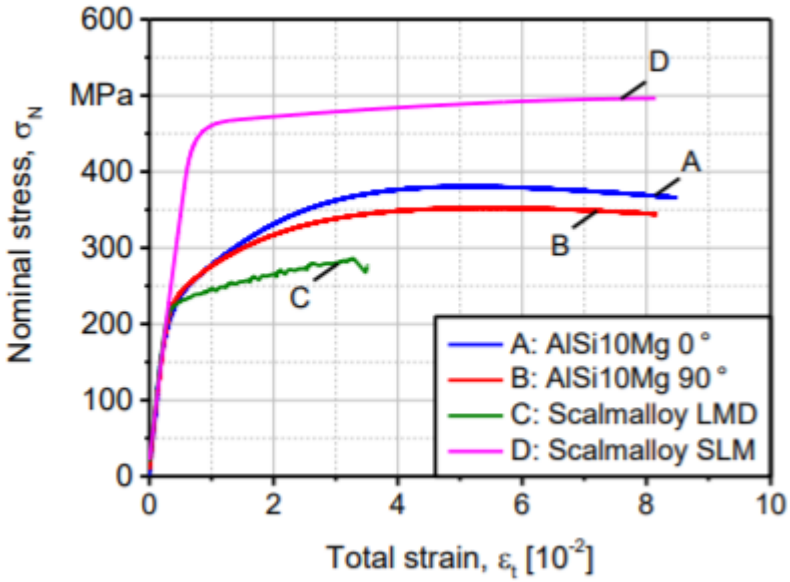

Figure 50 Tensile tests performed on Scalmalloy produced through powder bed and blown powder methods and on horizontal and vertical AlSi10Mg produced through powder bed AM [124]

Grain refiners are often added to existing alloys to improve weldability. Zhang et al. [129] added (2 wt%) zirconium to an Al-Cu-Mg alloy which had suffered from cracking during SLM processing. The effect of the zirconium was to create fine grained regions at the melt pool boundaries which inhibit crack growth and improve the strength and homogeneity of the specimen (Figure 51). Similar positive results were found by

Martin [214], who eliminated cracking in AA7075 by adding 1 vol% Zr. The strength of the AA7075+Zr was lower than what would be expected from conventional casting of AA7075 with the given possible reasoning being the loss of the main strengthening element zinc through evaporation.

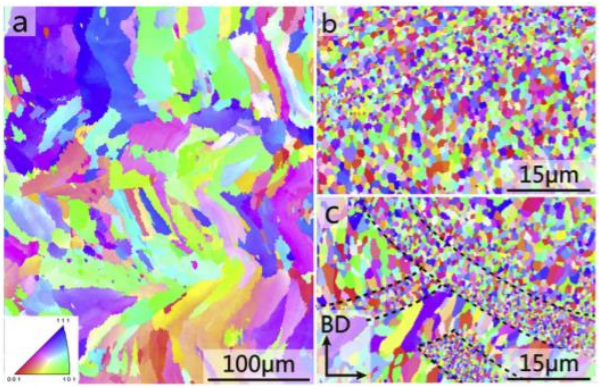

Figure 51 EBSD inverse pole figure maps of vertical cross sections of SLM produced (a)Al-Cu-Mg and (b and c) Zr/Al-Cu-Mg (Zhang, et al., 2017)

Prevention of cracking is not the only advantage of grain refinement and some researchers have tested alloy compositions with zirconium that would not be expected to crack without it. Croteau et al., [226] added zirconium to readily processable Al-Mg. The addition of zirconium created large regions of fine grains which improve strength and isotropy as the yield strength of these alloys measured along horizontal and vertical directions are always within 5% of each other, including in as-build and T6 conditions (Figure 52). Zirconium precipitates out to form cubic Al_3Zr, which help to strengthen the alloy. Evidence was shown that these precipitates form within grains and grain boundaries (Figure 53).

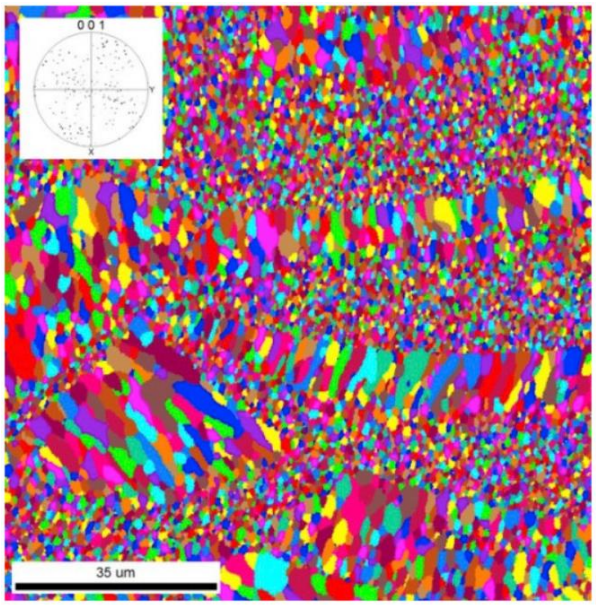

Figure 52 EBSD map showing a vertical cross section of Al-3.6Mg-1.18Zr wt% alloy produced through SLM. Build direction is from the bottom to the top and average grain size in fine-grain regions is 770 ±340 nm.

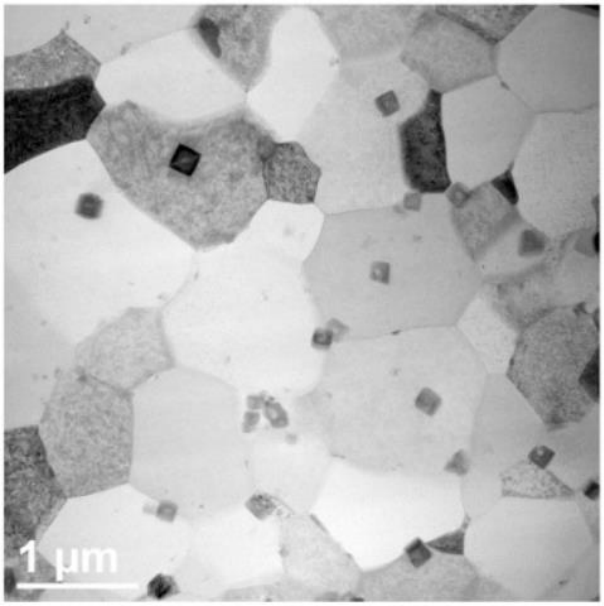

Figure 53 BF-STEM image of Al-3.6Mg-1.18Zr wt% alloy within fine-grain region showing primary cubic Al_3Zr precipitates both within the grains and at the grain boundaries [226].

Yang et al, [125], printed an Al-Mg-Zr alloy and did not achieve any noticeable grain refinement (Figure 54). The alloy composition was Al-4.5Mg-0.212Zr-0.17Si. The aim of their research was to compare the result with a similar alloy with scandium (Figure 48) and no extra addition zirconium compensating for the absence of scandium. The zirconium content is much less than the above alloys and may have been too meagre to note a contribution. Considerable cracking is evident in the EBSD images of the alloys which is surprising as cracking would not have been expected from composition without the presence of zirconium (Figure 6).

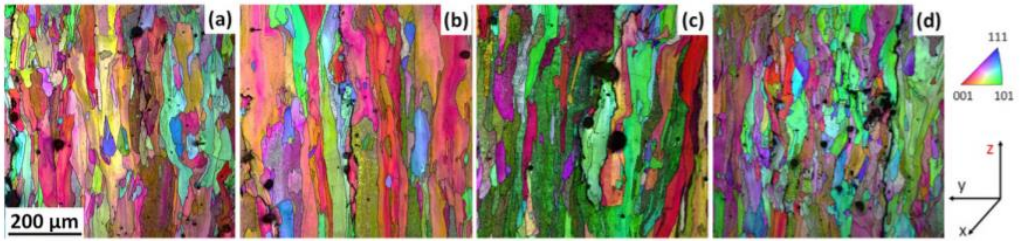

Figure 54 EBSD map showing microstructure reconstructed from inverse pole figures of SLM Al-Mg-Zr with various process parameters [125].

Evidence suggests that grain refiners can provide increased processability and isotropy of mechanical properties where sufficient grain refiners are added. More cost effective grain refiners, such as TiB, may be of interest as scandium and zirconium addition make a significant impact on the cost of the alloy composition, with a consideration on the quantity needed. Tang et al, [227] used TiB within welded AA5083. Their results found that welding speed influences the interaction of TiB with the alloy and increasing the speed required an increase in TiB. Li et al [103] added 11.6% TiB_2 to AlSi10Mg and produced parts with 530 MPa and 15.5% elongation, which is as strong as Scalmalloy with greater ductility. There has been sparse research

in the area of grain refiners in SLM aluminium with a potential for high performance alloys. There is also little knowledge of how they refine the grains in SLM, but it is necessary that they retard the growth of the pre-existing grains long enough to allow nucleation of new grains.

2.7 Thermal Stresses

The aluminium alloys that are processable through SLM have a fine grain structure and relatively high UTS, which is a result of fast solidification. This fast solidification generates large thermal stresses, and many materials are known to crack under stresses generated during SLM processing [228]. High strength aluminium alloys are known to crack in SLM, as they are in other processes where solidification and shrinkage occur, such as in casting and welding. These materials require post processing heat treatments to gain the majority of their strength and are therefore not as strong as high alloyed cast alloys. It is worth considering thermal stresses as a potential cause of this cracking as well as considering the influence the thermal stresses have on the crack propagation.

2.7.1 Mechanisms of Thermal Stress

There are two mechanisms of thermally induced stresses that occur in SLM [229]; contraction of cooling material, and thermal gradient mechanism (TGM). The former is caused by the contraction of material as it cools, with the melt pool fusing with surrounding material and then shrinking. The constriction of this shrinkage produces unrelieved stress. At the microstructural level, the stresses are primarily in the direction of grain growth [202], with greater mismatching of grain orientation resulting in higher stresses at the grain boundaries.

Within a single track, which are longer than wide, the greatest strain, and therefore highest stress, is along the scan direction [230]. The shape of the melt pool, mentioned in 2.4, alters the stresses in the track. Qi et al [231] observed that greater horizontal stresses were produced by conduction mode compared to keyhole mode melting. Within a layer, the shape of the scanned area has a considerable bearing on the direction of highest stress but when scanning a square surface, the highest stresses are still in the scan direction [186]. To distribute the stresses, and avoid the build-up of stresses in one direction, it is typical to rotate the scan direction on different layers.

TGM further adds to the tensile stresses in the top layer of material. This mechanism, which is used in laser bending of metals [232], describes the stress induced by heating a material where no melting takes place and is a result of the reduced strength of materials at higher temperatures. On heating, the solid material that surrounds the melt tracks expands and the yield strength lowers. This allows any stresses caused by

thermal expansion to be relieved. On cooling the material thermally contracts but because of the lower temperature is unable to plastically deform and this residual elastic strain leads to stresses within the material. (Figure 55).

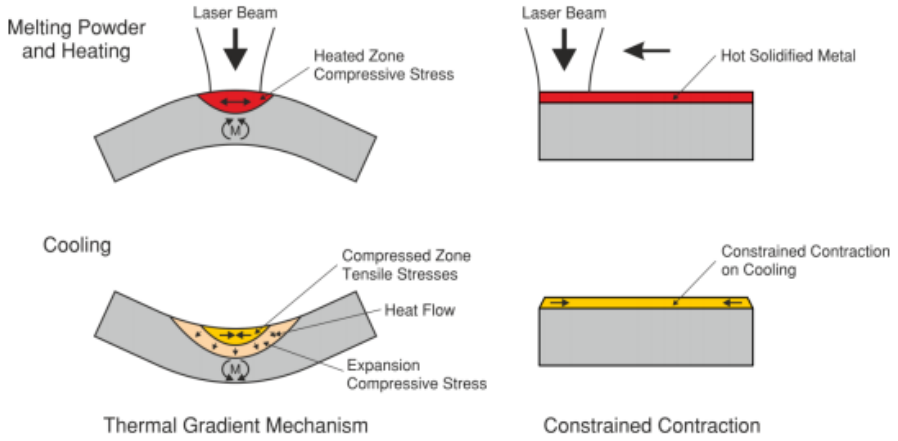

Figure 55 Thermal gradient mechanism causing deformation during SLM processing [186]

2.7.2 Accumulation of Stress with SLM

The effect these strains and subsequent stresses have in the horizontal and vertical directions are very different. The vertical strains are in a layer that is not restricted by the surrounding material as it is only on one side (below) and the shrinkage is largely unconstrained. In the horizontal direction with the scanned tracks fusing with already solidified material both to the side and below, the cooling scanned track experiences tensile stress because of differential cooling and this will generate balancing compressive stresses in the adjacent material. The colder material has higher yield strength and therefore the cooling melt track experiencing shrinkage will yield before the adjacent cold material. The result is that stresses accumulate, with peak compressive stresses at the centre of the scanned areas and with surrounding areas being subject to tensile stresses. As these stresses are in the build direction, the effect of accumulated layers is that the stresses build up, with tensile stress at the edge surrounding compressive stresses in the centre (Figure 56). When the part is removed from the build plate a certain amount of relaxation of these stresses occurs and the part deforms. The deformation is proportional to the residual stress and its distribution and measuring the deformation constitutes a means of measuring the stress (Figure 57).

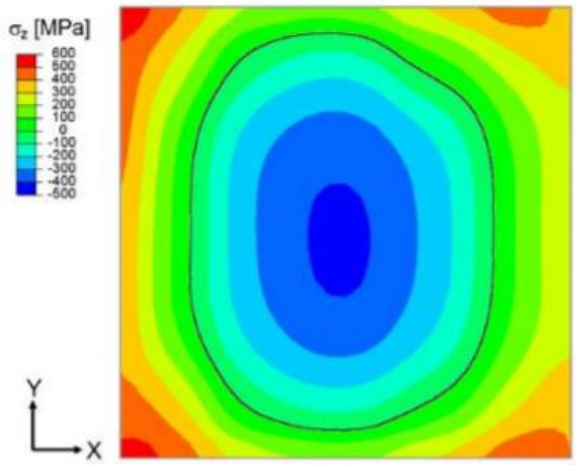

Figure 56 Stress map of the vertical stress in a 15x15x15 mm3 part, made with Ti64, at the interface of the part and baseplate. The black line indicates the boundary between tensile (+) and compressive (-) stress, [233]

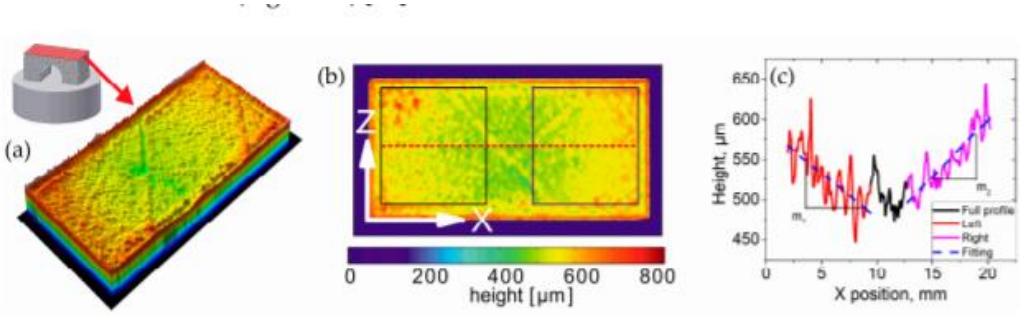

Figure 57 Determination of residual stress through measurement of deflection angle, α; (a) The surface profile was measured using a profilometer, (b) shows the centre line used for determining the deflection angle and (c) shows the angles of both legs with the deflection being 1.44° (slope m_1 = -0.61° and m_2 = +0.83°) [234]

The combination of the two stress mechanisms on the horizontal stresses is to produce a scanned surface under tensile stresses. The stress profile is such that the centre has the highest stress, while the top edges of the surface are not constrained and therefore have zero stress. The underlying surface inhibits the layer shrinking horizontally, and therefore the scanned layer exerts horizontal compressive stress on that surface. Subsequent layers further and to the accumulation of horizontal compressive stress. The result is that the top surface has the highest tensile stresses with progressively compressive stress beneath (Figure 58). The highest horizontal tensile stresses a section experiences are while it is the top layer. The stresses reduce with subsequent layers, eventually becoming negative. Upon removal of the baseplate, which exerts a compressive force, the stress profile changes to parabolic with tensile stresses at the top and bottom. The calculations by Mercelis and Kruth [229] suggest a relaxation of stresses and much lower stresses after removal, this is likely to be with deformation of the unconstrained part. Examination of different metals led to the conclusion that the stress profiles were the same, but the scale of the stresses altered with the mechanical stress-strain properties of the material.

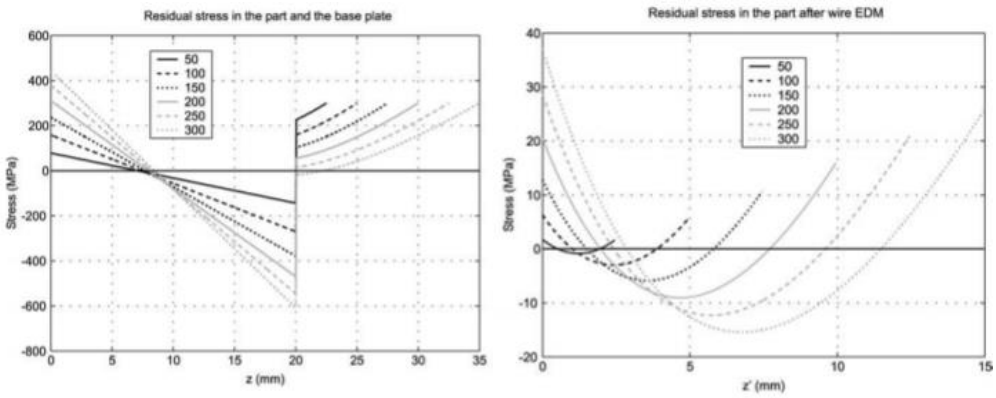

Figure 58 Influence of the number of layers on the residual stress profile with a baseplate and after the removal of the base plate, as calculated by [229].

This result is corroborated by analysis performed by Rangaswamy et al. [202] and Vrancken [233]. The stress map of the horizontal stresses (Figure 59) shows how manufacturing influences the compressive stresses at the centre of the part. The highest horizontal stresses are within the centre of the top and bottom of the part, the highest compressive stresses are in the centre of the part and there are low stresses near the side surfaces, where the material is less constrained.

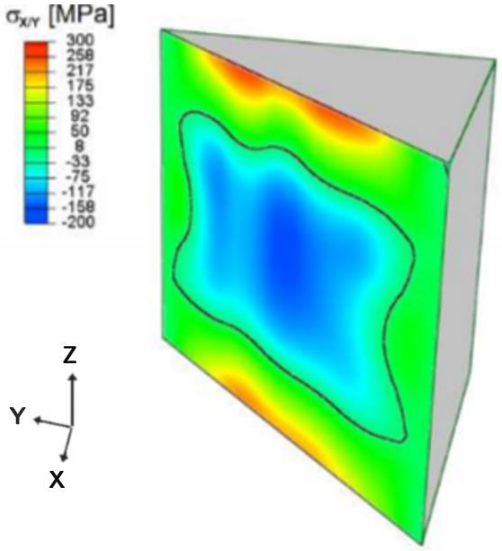

Figure 59 Stress map of the horizontal stress in a 15x15x15 mm3 part, made with Ti64, at the diagonal cross section. The black line indicates the boundary between tensile (+) and compressive (-) stress [233].

2.7.3 Cracking under thermal stresses in SLM

It is widely reported that cracking occurs in many metal parts that have been manufactured by SLM [228] and it is intuitive to connect this to high stresses that are experienced during processing. It may be important to understand that while the stresses evaluated in the previous sections are at room temperature, cracking due to stress may also occur at lower stresses at high temperature, as most materials are much weaker at elevated temperatures [235].

The cracking can occur due to either horizontal or vertical stresses with cracks appearing perpendicular to the direction of stress and providing some stress relief. The continuous accumulation of stresses was shown to take place under the action of vertical temperature gradients during cooling. Brittle metals, such as nickel-based alloys and tool steels, have been shown to be susceptible to horizontal cracks arising from these vertical stresses. Figure 60 shows the changes in cracking behaviour due to changing process parameters.

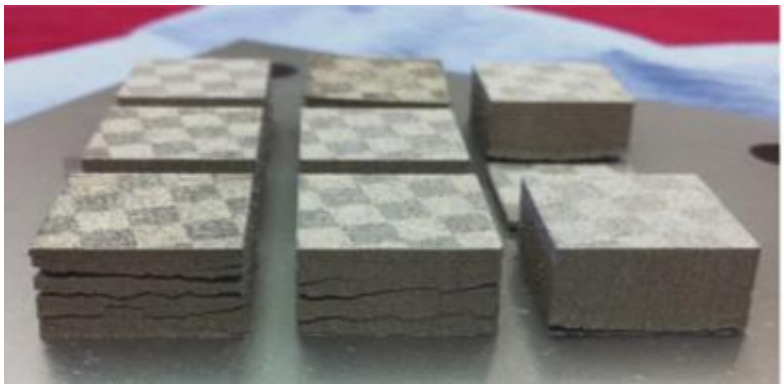

Figure 60 M2 HSS parts produced by SLM, showing cracks generated from thermal stress [236]

Horizontal stresses behave differently as the tensile stresses generated in a layer are not added to with subsequent layers. The maximum stresses are influenced by the area of the scanned surface and more cracks are known to appear on larger scanned areas [237]. No dependence on part height has been reported for the presence of vertically aligned cracks, nor would stress profiles in the previous section suggest that there would be.

The location of cracks will occur where the stress exceeds the UTS and this is affected by the inhomogeneity of SLM produced parts. Should cracking occur where the highest stresses are generated then the cracks should appear perpendicular to the scanning direction. However, weakness may be greater between scanned tracks or at the centre of tracks and this can result in cracks aligned with the scan direction. These two potential crack locations are perpendicular, one will not relieve stresses that cause the other. Figure 61 shows the presence of cracks on horizontal cross sections of two brittle materials. Cracks in Hastelloy C-276 appear solely in the direction of the highest stress, while stresses in tungsten appear most prevalently between the tracks with arcing cracks across them. As yet, no evidence has been presented as to the location of the cracks within SLM aluminium in relation to the scan track orientation. Examples in welding aluminium show that cracks in either direction can arise depending on welding circumstance (Figure 62).

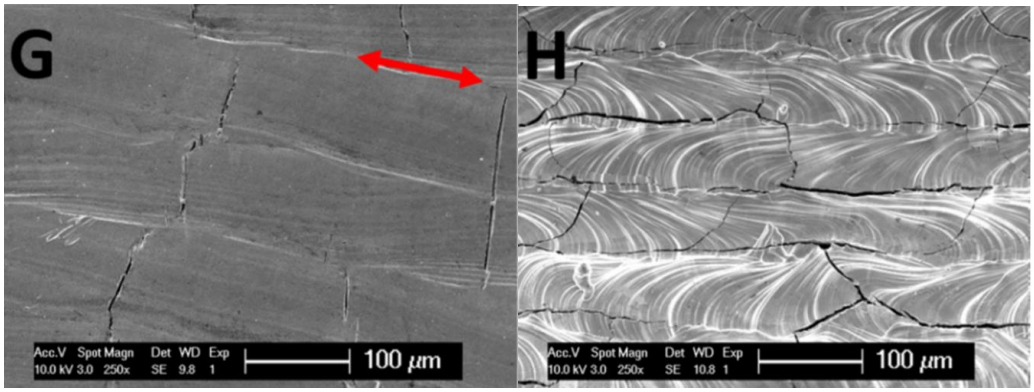

Figure 61 Top surfaces of cube specimen showing cracking in (G) Hastelloy C-276 and (H) Tungsten, red arrow on (G) shows scan direction and direction of principle stress

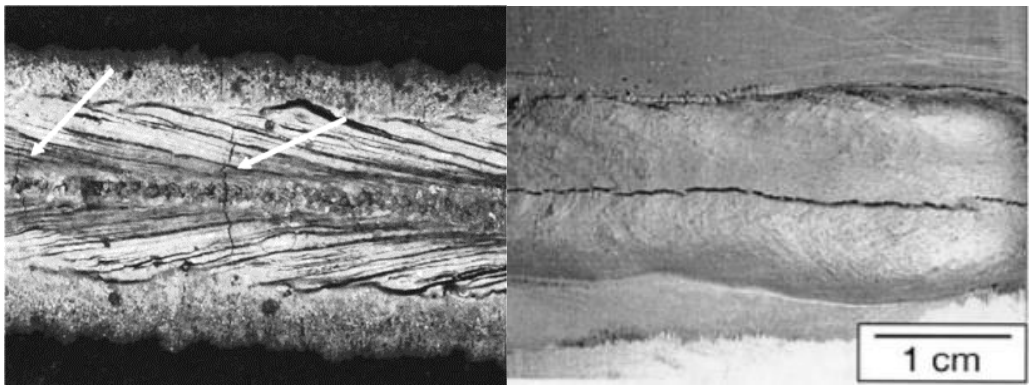

Figure 62 Transverse cracks found in AA7075 weld samples [235] and solidification crack running through the centre of the GMA weld of AA6061 aluminium

Part of the challenge in identifying the location of cracks within the structure is that it is common to rotate the scan direction for each succeeding layer. Cracks are a significant weakness and can easily propagate through layers, making the starting point of the crack more difficult to define. In samples built using a scan direction that rotates by 90° with each layer, (alternating scan direction in the x and y), it is commonly seen, in horizontal cross sections, that cracks are equally evident in both x and y directions. The pattern is sometimes referred to as mud-cracking [81]. If different scan strategies are used the orientation of the cracks alter accordingly, as with the use of a rotating scan angle of 60° used with Hastelloy C-276 (Figure 63), and with cracks observed with nickel superalloys scanned using the fractal pattern shown in Figure 64. The position of cracks in relation to scan tracks would be clearer with single direction scan strategies, but these are not popular as they exacerbate stresses in a single direction and are not good for producing high density parts [186]

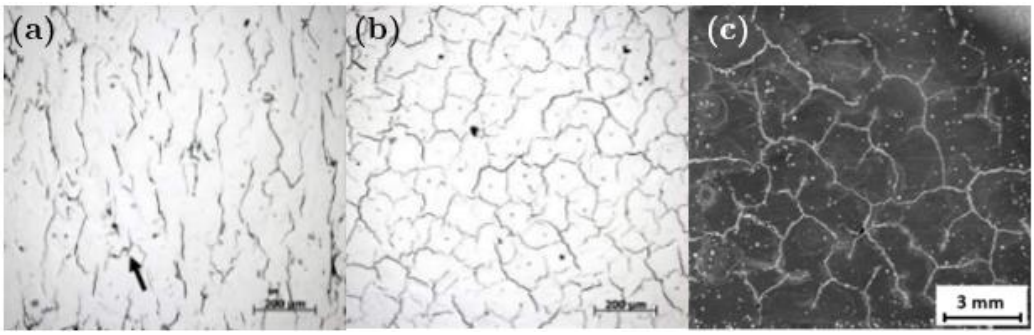

Figure 63 Mud cracks in SLM Hastelloy C-276 processed by Vrancken [228] with rotating scan angle by 60° each layer, (a) shows the vertical cross section and (b) shows the horizontal cross section, and aluminium alloy EN AW 2618, processed by Koutny et al. [237] using a X-Y alternating scan strategy (c) showing a horizontal cross section.

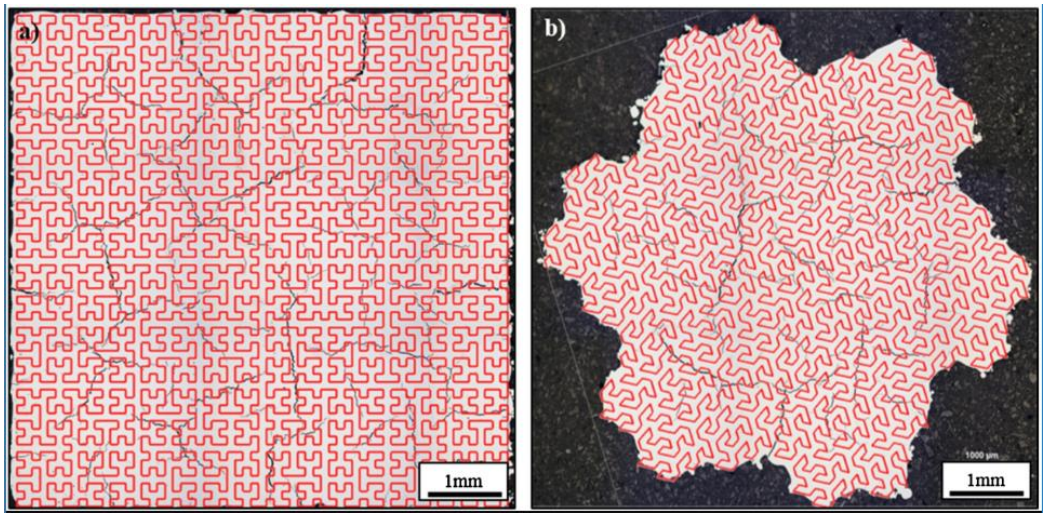

Figure 64 Cracks in SLM process Nickel-based CM247LC superalloy, using (a) Hilbert and (b) Peano-Gosper fractal scan strategies [238]

2.7.4 Mitigation Thermal Stresses

Some attempts have been made to reduce the number of cracks through mitigation of thermal stresses, with a view to eventual complete elimination. This has proved successful with brittle materials (Figure 60). Pure aluminium is known as a ductile material but as-processed SLM material, especially alloys, can be brittle. Research into the residual thermal stresses in aluminium suggests that they are significantly below the yield strength of the as-build material [239] at room temperature, however, the yield and ultimate tensile strength will vary with temperature and with local variations in composition that can occur in processing. As cracking is observed the stresses must locally exceed that required to nucleate a crack and then for it to grow. Several methods of alleviating cracks are performed in post processing, such as heat treatment [240] or shot peening [239], which are not appropriate if the cracks have already formed. It is necessary to reduce the stresses as they form, so the cracks cannot nucleate.

Scan strategies have a large influence on the generation of stresses within parts, and they have been widely researched. Laser parameters affect the size of melt pools and thermal gradients but they are selected primarily for optimising density. Thermal stresses are produced by steep thermal gradients and it is known in welding aluminium that faster scan speeds increase the probability of cracking [241]. Wider weld tracks typically increase cracking as there is a greater amount of material shrinkage which increases stress [90] and thinner layers may be expected to have a positive effect, but process parameters may be selected that reverse these expectations. Both Jansen [242] and Zaeh and Branner [243] showed that the residual stress increased with decreasing layer thickness for SLM steel alloys.

Alternating XY scan strategies are a commonly used scan pattern, whereby the scan direction rotates by 90° for each layer (Figure 65). This is preferred to unidirectional scanning which compounds issues with higher stresses along the scan direction [172]. Alternative scan rotation angles can be selected for furthering equal distribution of stresses. Many researchers and manufacturers prefer the scan rotation angle of 67°, as it is an integer value that has the highest number of iterations before it repeats. This is stated to improve homogeneity of the microstructure [201] but evidence suggests that it does not reduce the maximum residual stress. Kruth et al. [244], found that the optimum rotation angle was 90° (Figure 66) and this is further supported by tests by Ali et al. [245] and Robinson [186]. Part shape has an effect on the residual stresses, with longer scan lengths generating higher stresses [230] and it may be that the optimum scan rotation angle is part specific.

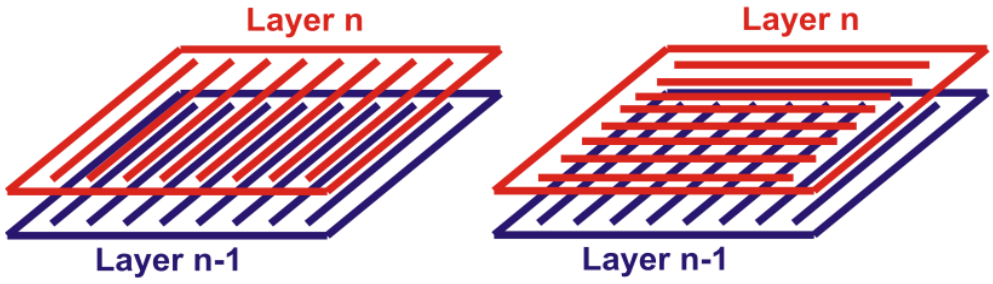

Figure 65 Scan patterns showing unidirectional scan direction (left) which results in aligning thermal stress and the XY alternating hatch pattern (right) which results in stresses alternating direction

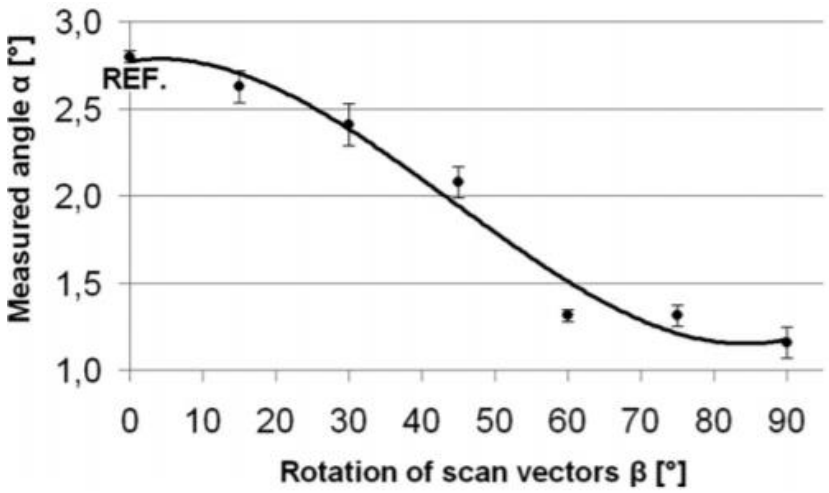

Figure 66 Influence on scan rotation angle (Rotation of scan vectors) on the deformation (measured angle) of SLM test specimen [244]

Checker board, or island, scan patterns (Figure 67) are often used in an attempt to reduce the thermal stresses [237]. It is known that longer scan tracks generate larger stresses because of the greater absolute shrinkage and greater thermal gradients, as tracks have more time to cool before the laser returns to scan the next track. The principle of the checkerboard strategy is to keep scan tracks short. Several different approaches can be made with this, such as including off-setting and rotating patches. This is to avoid the build-up of material, which tends to happen at the edges of each patch [246]. There are a number of variables that may be considered with this approach and the ability to reduce stress is not guaranteed. Research by Ali et al. [245], with Ti64 found that parts built with the checkerboard scan strategy had increased stresses compared to XY alternating.

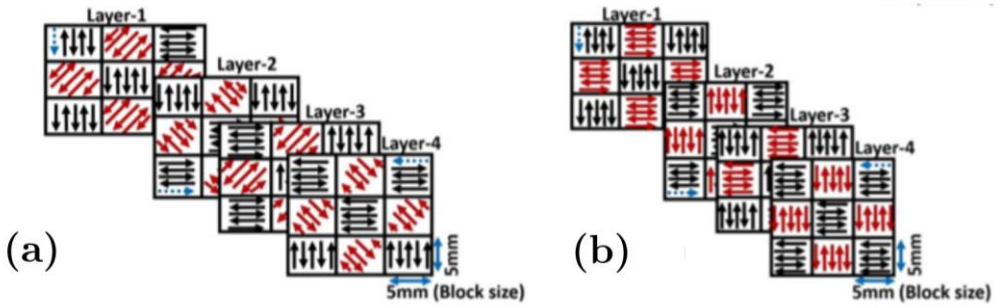

Figure 67 Schematics of checkerboard/island scanning strategies using adjacent islands rotating scan direction by (a) 45° and (b) 90° [245]

Another strategy to reduce stress is to scan layers twice, referred to as double scanning, rescanning or prescanning (depending on reference). Shiomi et al [240] and Ali et al. [245] demonstrated reductions in residual thermal stresses, of 55% and 33.8% respectively, when rescanning with 150% of the energy density of the primary forming layer. As well as reducing stresses rescanning has also been used in processing AlSi10Mg so as to achieve higher densities. Improved density has been shown with a secondary scan of 200% the energy density of the first scan [166].

However, rescanning is not guaranteed to have positive results. Ali et al. [245] found, while processing Ti64, a second scan at or below the energy density of the first increased the thermal stresses. Kempen et al [236] found rescanning was more likely to induce cracking in HSS tool steel, irrespective of energy density. The first scan has a big effect on the conditions of the second as the higher density that is achieved will increase conductivity of the surrounding material. This in turn may increase the cooling rate and thermal gradients, depending on scanning parameters, which increase the likelihood of cracking.

The ability to reduce stress through process parameters is limited. More effective methods of avoiding residual stresses can be achieved by modify the machine set-up. Using a second heat source has been found to be very effective at reducing stress and reducing cracking in welding aluminium. Abe et al. [185] used a dual laser system with a 1kW YAG laser and a 17W CO_2 laser (Figure 68). They found that by having the CO_2 laser follow the YAG laser they were able to reduce the stresses within the processed steel by slowing the rate of cooling and reducing the temperature gradients. Hu & Richardson [235] used a similar system in welding high strength aluminium and were able to remove transverse cracks, which are due to high stress. This method has proved successful at reducing stress in welding but has not been used to alleviate longitudinal cracks or solidification cracking. Yang et al., [247] used a heat sink rather than a second heat source to alleviate cracking in laser welding high strength 2024 aluminium (Figure 69). Their approach was to use a liquid nitrogen spray that followed the laser source. This does not reduce stress but strengthens the material and avoids temperature related weakness. Another consideration must be on how the heat sink changes solidification and growth of crystals. Usually in welding and in SLM the growth occurs at the melt pool boundary with the base material, but the heat sink will induce more growth from the top of the pool and a finer grain structure.

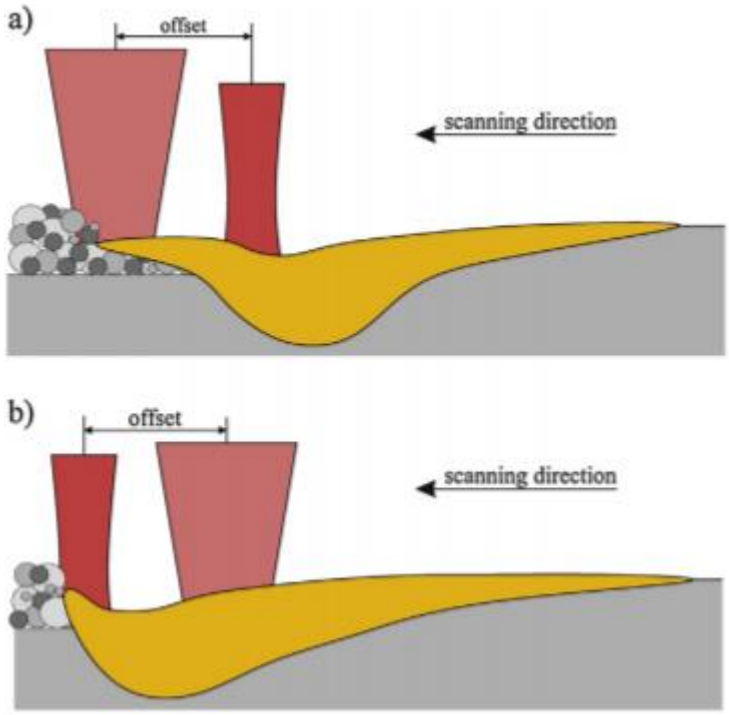

Figure 68 Dual Laser set-ups, using one high powered focused laser for melting and one defocussed laser for heating, depicting (a)preheating and (b)reheating, predefined by the beam offset [248]

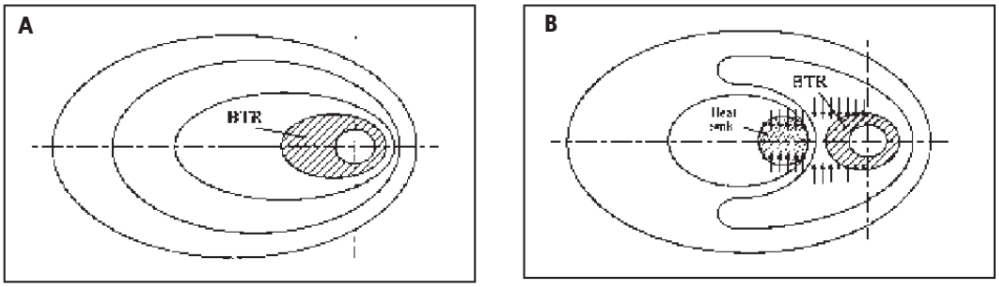

Figure 69 Schematic of the effects of a trailing heat on isotherms (A) conventional welding and (B) welding with a trailing heat sink [247]

The multi-beam system can provide localised heating to reduce cooling rates and relieve residual stresses. Another method of reducing thermal gradients is with heating the bed through the base plate [236]. This not only reduces the temperature gradient but also lowers the temperature drop during forming (shrinkage during the temperature drop from the base plate to room temperature should be consistent and therefore not generate residual stresses). Shiomi et al., [240] reduced the residual stress in a tool steel by 40% by heating the base plate to 160°C, 11.3% of melting temperature.

The heated base plates are more effective with aluminium due to the relatively low freezing temperature of its alloys. Siddique et al. [249] found, using x-ray diffraction to measure residual stress [250], that using a base heated to 200°C reduced stresses in AlSi12 by 77%. Bremen et al. [178] used the cantilever method, which measures the

deflection in parts after they are cut from the base plate, found no measurable residual stress in parts with base plate heating of over 200°C (Figure 70), though some stress is always likely to exist as the mechanisms of stress are still present.

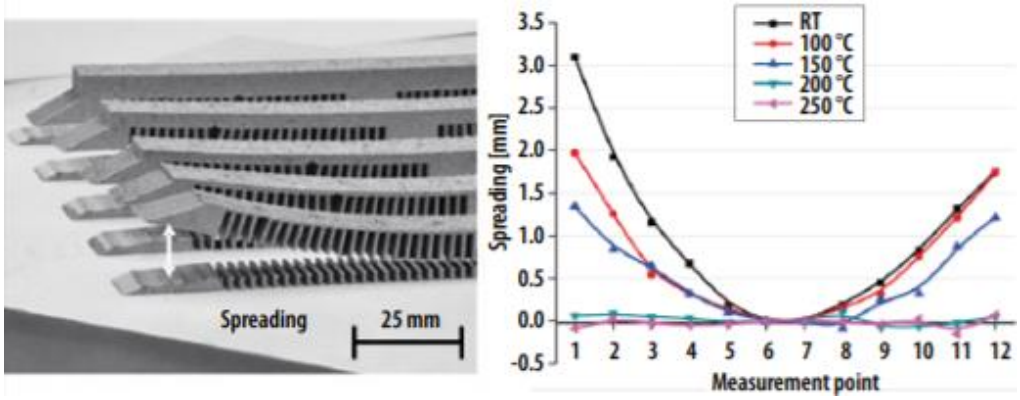

Figure 70 Effect of base plate preheating on deformation of AlSi10Mg cantilever (bar 2mm thick) [178]

Reducing stress has been effective at reducing cracks in many materials, particularly brittle materials. It has not been proven and it is not guaranteed to be effective at reducing cracks in SLM aluminium. The best method to approach this would be with machine modifications, and very positive results have been found with heating the base plate.

2.8 Cracking in SLM Aluminium

It is well established that high strength aluminium alloys are susceptible to cracking in SLM and it is often cited that the cause is the high solidification temperature range, high thermal conductivity, co-efficient of thermal expansion and solidification shrinkage [87]. The first relates to the extended mushy zone, which presents a point of weakness in the materials, which is reviewed later, while the rest relate to the development of stresses. Cracks appear where the local stress exceeds the local ultimate tensile strength and while the stresses generated in SLM are large, it is likely that cracks are related to a position of weakness within the material.

Oxides, which were reviewed in section 2.3, can be an unpredictable source of weakness that triggers cracks to form. The presence of oxides within SLM aluminium, specifically alloys AlSi12 and AA6061, was examined by Louvis et al., [161]. Cracking was not considered, and the densities may not have been high enough to observe cracking, but the presence of oxides forming between scan tracks could be a presence of weakness that initiates cracking (Figure 71). Oxides have been observed to be the location of initiated failures within aluminium castings [169]. A challenge with interpreting the presence of oxides at crack locations is whether the oxides preceded and initiated the crack or formed on the surface after the crack formed. SEM was used by Wang et al., [169] to differentiate “old” and “young” oxides, where thick

aluminium oxide films, formed at high temperatures, are observable due to "charging", where the charge of electrons impacting the oxides are not dissipated, while thin films formed at room temperature are not as visible. They argued that thick films formed during casting could be mixed into the melt and form a weakness, while thin films form with intersecting the part or cracks propagating through the cold material. Similar principles can be used with SLM, however where the cracks propagate during building, the crack surface could be exposed to form oxides while at high temperatures, despite attempts to remove all oxygen from build chamber (section2.4.3).

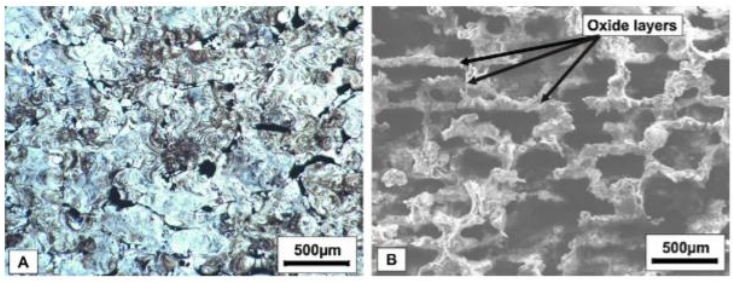

Figure 71 Optical and SEM micrographs of a AA6061 sample section: (A) after polishing and etching with Keller's reagent and (B) after deep etching with NaOH solution [161]

2.8.1 Mechanism of Solidification Cracking

High strength aluminium alloys are susceptible to solidification cracking during welding and it is suggested in this work that this is the most likely cause of cracking within SLM. Solidification cracks are identifiable within welding as they tend toward the centre of the tracks (Figure 72). This is more challenging within SLM where the tracks overlap and thermal cycles are complex.

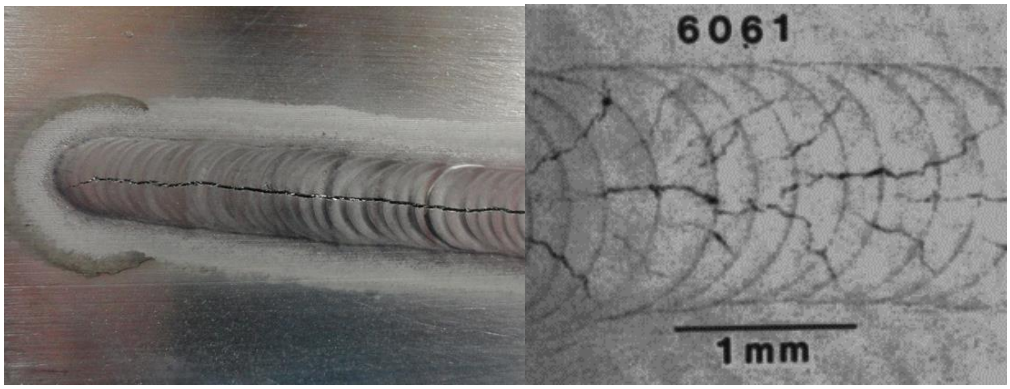

Figure 72 Solidification cracking observed in GTAW (TIG) weld of AA6061 [251] and exhibited on laser welded AA6061 plates [252]

Cracks in SLM aluminium tend to be vertically aligned cracks that can be described as "mud cracks" in appearance [81] (Figure 63). There are multiple reasons for the cracks to appear in this pattern, as mentioned in section 2.6, which includes solidification cracking.

Solidification cracking is an established cause of cracking in welding aluminium, however, there is not a complete consensus on the exact cause, or the mechanisms involved. Three of the most prominent theories are the shrinkage-brittleness theory, strain theory and the Borland's "General Theory" [109] and while crucial differences exist, there are many shared qualities, and all argue that cracking occurs as the final lower melting temperature liquid remains between the grains.

The shrinkage-brittleness theory, proposed by Pumphrey and Jennings [253], suggests that the material passes through a brittle temperature range during solidification, when dendrites start to interlock. Under contraction the intertwined dendrites can fail, and cracks appear. The strain theory [254] was a modification on this, whereby liquid films between dendrites provide a weakness where the cracks initiate. Borland's "General Theory" [255] of cracking suggests the location, quantity and wettability of the final liquid films are the defining factors. This theory suggests there is a worst case scenario where the wettability of the liquids allows a proportionally large area of dendrites to be coated in a thin liquid film, which cannot withstand the strain of the contraction, and backfill cannot occur [256]. In cases where the final liquid has poorer wettability the liquid will not be present surrounding the dendrites and higher level of solid bridging will occur, while liquid with better wettability allows greater backfill and healing where cracks start to emerge.

The above theories are often interpreted as the susceptibility of the material to solidification cracking, which is a process dependent on composition [109]. Where there is a pure aluminium, or is little alloying elements, there is not enough solute-rich liquid at the grain boundaries for solidification cracking to occur, while if the material is heavily alloyed there will be plenty of solute-rich low-freezing alloy to backfill and heal cracks as they form. Between the two extreme exists a composition where the solute-rich liquid can form a continuous film between grains before solidifying. This is reflected in the cracking susceptibility of common binary alloys (Figure 4Figure 6). Cracking in SLM aluminium does appear to follow this composition rule. Kimura [213] tested various Al-xSi binary compositions (x=0, 1, 4, 7, 10, 12). Al-1Si had heavy cracking while none was present in any other composition, which corresponds with the graph in Figure 6.

The solidification range is often described as synonymous with the cracking susceptibility, and features in the shrinkage-brittleness theory to describe the BTR (Brittle Temperature Range). Some researchers claim that cracking and solidification range are directly proportional with the highest cracking susceptibility occurring at the widest freezing range [257]. This is not the case. The peak cracking susceptibility for common binary aluminium alloys are; 1% Mg_2Si, 0.8% Si, 1-1.5% Mg and 1-3% Cu [258], while the maximum solidification range occurs at 1.91% Mg_2Si, 1.65% Si, 17.4% Mg, and 5.65% Cu [72].

Most alloys are not binary and some aluminium alloys with high cracking susceptibility have high solidification ranges, such as 2025, which has a solidification range of 131°C, and 7075, 160°C [259]. However, AA6061 has a similar solidification range to weldable alloys in the 5xxx series, such as 5456, which is used as a filler material during welding. There are alloys within the 6xxx series which have very low solidification range which have demonstrable cracking, namely 6005 [260] solidifies over 48 °C and 6063 [261], which has similar properties to AA6061, solidifies over 40°C.

Mushy Zone

The argument for the influence of the solidification range relates to the extension of the mushy zone, where the cracking occurs. Figure 73 shows a schematic of the advancing dendrites similar to material during welding or SLM processing. The weakness between the dendrites may be characterised, depending on solidification cracking theory, as a lack of strength from interlocking proportional to the stress from shrinkage, or lack of strength from liquid films preventing bonding and a lack of liquid backfill. Near eutectic alloys, like AlSi10Mg, have narrower mushy zones and less requirement for backfill. The size of the mushy zone is dependent on the solidification rate and the thermal gradients. Higher thermal gradients reduce the mushy zone but increase thermal stress. Faster processing speeds increase the thermal gradients, and reduce the mushy zone size, but cracking in 6xxx series alloys has been observed to increase with increased welding speed [241].

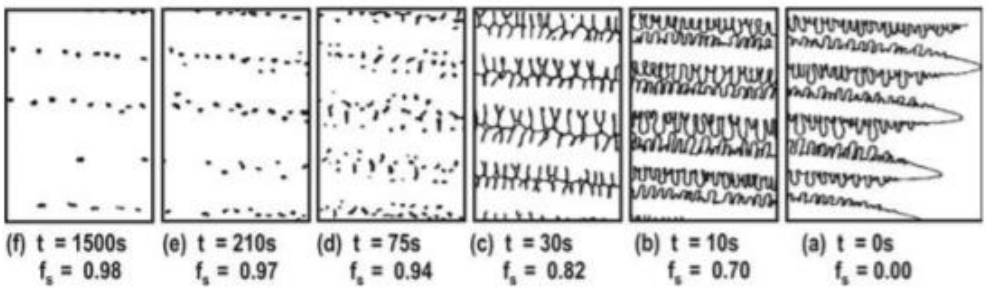

Figure 73 Schematic drawing showing progressive stages of dendritic solidification demonstrating regions of (a) dendritic growth, (b) liquid backfilling, (c) thin liquid films, (d)-(f) dendritic coherency [257]

Dendritic Coherency

The size of the mushy zone is a simplified view of how cracks are created, and as seen with solidification range and thermal gradients, it is not an altogether useful view. The point at which problems arise in the mushy zone is where dendrites become coherent and prevent backfilling of liquid between gaps created by the shrinking liquid and solid [262]. Smaller grains delay the point at which dendritic coherency occurs, raising the solid volume fraction (Figure 5). Cracking can be reduced in welding and casting by maintaining reduced grain sizes and grain refiners are a common component in aluminium welding filler material [263].

The size of the melt pool in laser welding is typically smaller than in other welding techniques and should be smaller in SLM. Cieslak and Fuersbach [252] found laser welding aluminium with continuous wave radiation could achieve crack free welds. The advantage of the small weld volume is that backfill and dendrite coherency is less likely to be an issue.

Kou [264] proposed a measure of crack susceptibility in welding by measuring the rate of transverse grain growth just before the final liquid solidifies, i.e. the rate neighbouring grains grow towards each other and interlock (Figure 74). The proposal is effectively measuring the solidification temperature range over an incremental volume fraction that is regarded as the most important. The arguments presented for the consideration of the solidification range and mushy zone are repeated, i.e. that the high temperature range will create large channels with restricted backfill, but with emphasis on the critical solid volume fraction.

The selection of $f_s^{1/2}$ as the denominator (f_s is the solid volume fraction) is due to this being proportional to the rate of transverse grain growth. Longitudinal grain growth is proportional to temperature and therefore the profile shown in T(°C) vs. $f_s^{1/2}$ represents the cross section of the grain. The changing rate of solidification highlights how considering the universal solidification range can oversimplify how the conditions for cracking can occur.

Non-equilibrium solidification takes place in SLM. This effects the solidification temperatures compared to the phase diagrams with phases changes occurring at lower temperatures, this changes eutectics behaviour and extends the freezing range, which increases the likelihood of cracking [265].

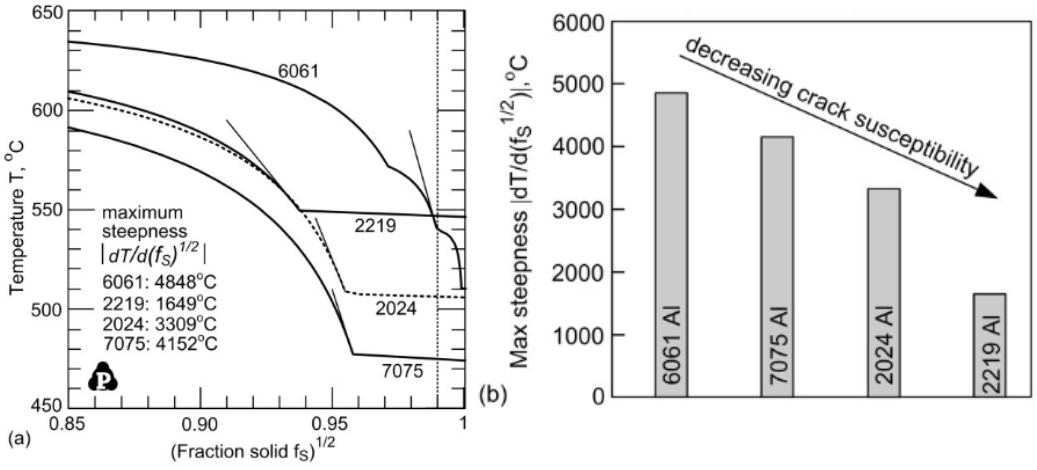

Figure 74 Crack susceptibility of wrought Al alloys 6061, 7075, 2024 and 2219: (a)T-$(fs)^{1/2}$ curves showing maximum steepness $|dT/d(fs)^{1/2}|$ to $(fs)^{1/2}$ = 0.99, beyond which extensive bonding is assumed to occur and end crack susceptibility; (b) predicted crack susceptibility based on the maximum steepness decreases in the order of 6061 Al, 7075 al, 2024 Al and 2219 Al [266].

Liquation Cracking

Liquation cracking and solidification cracking are two different sources of cracks in welding [267]. Liquation cracking occurs within the liquid/grain boundaries of partially melted zone (PMZ) near the weld pool (Figure 75).

In welding, liquation cracking can be differentiated from solidification cracking by location and shape, as liquation cracking does not show dendritic morphology. The distinction is important in welding, as liquation cracking occurs in the base metal and the use of composition altering fillers are ineffective [168], but the difference may only be academic in SLM due to the repeated remelting of materials and the inability to add location specific filler materials [265].

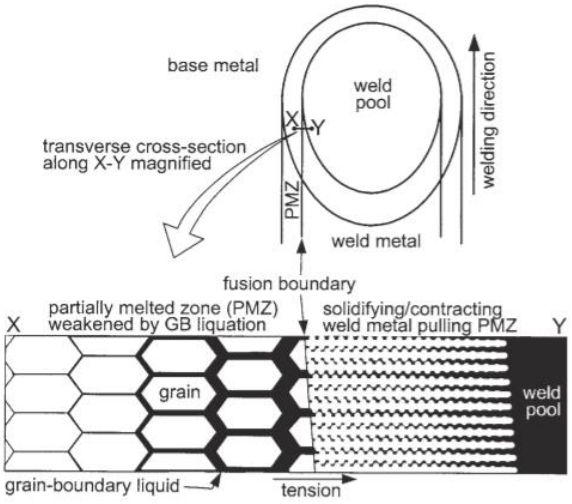

Figure 75 Mechanism of liquation cracking in the partially melted zone of an aluminium weld [109]

2.8.2 Mitigation

In welding aluminium alloys, there are several different approaches to resolving the issue of solidification cracking; these include compositional modification with filler materials, introducing grain refiners into fillers, reduction of stresses or physically constraining weld piece.

Compositional Modification

Filler materials can be used to modify alloy composition to avoid high cracking susceptibility levels (Figure 6) and some fillers, such as silicon rich alloys can provide healing to cracks as they form, as it is known eutectics compositions are the means of avoiding hot tearing [268]. Composition modifications are likely to weaken the material but tests with welding 6013 with AlSi12 have shown that over 90% of the strength can be recovered [115].

Many aluminium alloys that are regarded as weldable are only able to because of the compositional modification achieved using filler materials different from the base material. The selection of appropriate filler material is very well understood for

welding [90], however, the level of dilution of filler materials, and the necessary composition change is not highly considered.

The probability of cracking is altered with the level of dilution of the parent alloy with the filler material, but this is also dependant on welding conditions and therefore, in practice, the amount of filler material added is higher than an optimum to ensure a crack free weld. Coniglio, et al. [269], attempted to determine the critical levels of dilution for welding 6060 (Al-Si0.5si-0.5mg) using 4043 (al-5Si) as filler material. The weld piece was two coupons of 8mm thickness. The dilution was measured as the change in volume of the weld section, and variable loads were placed on the test pieces to determine how the critical dilution level varies with strain rate within the weld track (Figure 76). They found the necessary addition of filler material increases with the strain rate. The stresses that are present within a particular SLM part is not known, and while no external forces are applied during production, the building process itself creates significant stress levels, as discussed in section 2.6.

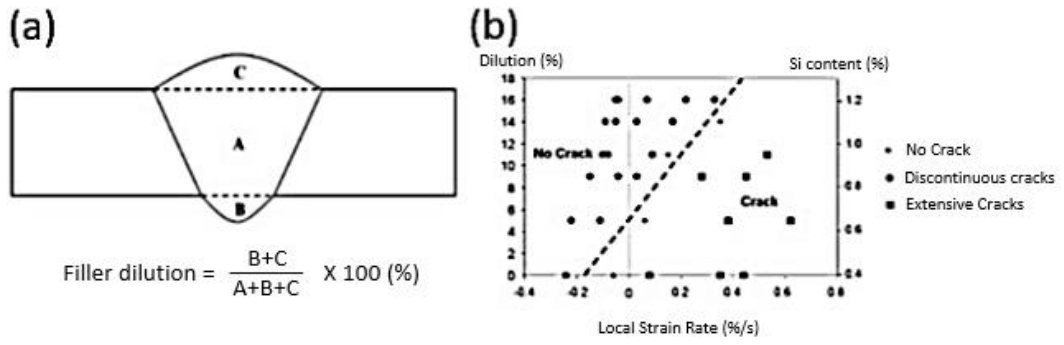

Figure 76 (a) Illustration of the dilution calculation from the weld cross section, (b)cracking susceptibility of alloy 6060 for variable 4043 dilution shown as a function of local strain rate across the weld section [269] .

Process Modification

Cracking within welded aluminium is often avoided by maintaining low stresses within the welded sections [270]. The generation of stresses within SLM was discussed in section 2.6, along with a discussion of methods to mitigate these stresses, such as scan strategies, double scanning, using multiple heat sources and heating the powder bed.

In the context of solidification cracking the effects of process parameters may not only be a question of the generated stresses. Olakanmi, et al. [87] suggested an optimum energy density exists to produce crack free parts. The argument put forward suggests that higher energy densities generate higher stresses and larger mushy zones, while lower energy densities have disorderly solidification fronts and less time for backfill when cracking occurs.

Beyond the energy density the selection of laser can influence solidification cracking. Cieslak & Fuersbach [252] observed that aluminium alloys are less susceptible to

cracking with continuous wave than with pulsed wave. Cao, et al. [258] noted that larger spot sizes reduced the cracking susceptibility.

Scan strategies have been developed in welding as a method to reduce cracking without altering material or laser parameters. Weaving tracks have been found to be effective at eliminating cracking with laser and arc welding. The weaving method is effective as it distributes the stresses and rather than shrinkage of grains concentrating stresses at the centreline, the centreline is discontinuous (as seen in Figure 77 (a) and (b)). An optimum wavelength exists for the optimum distribution of stresses. This method has been effective with reducing cracks in 6021 [271] and Al-5.6Mg [272].

It is not clear if this method would prove beneficial with SLM as it doesn't reduce stress but tries to avoid an over stressed centreline. The scan speeds in SLM are much faster and oscillating frequencies would need to be higher for any effect to be evident. Adopting this into SLM will have to deal with the extra challenges of avoid the accumulation of stresses, ensuring sufficient track melting and overlap, and potential lag from the mirrors.

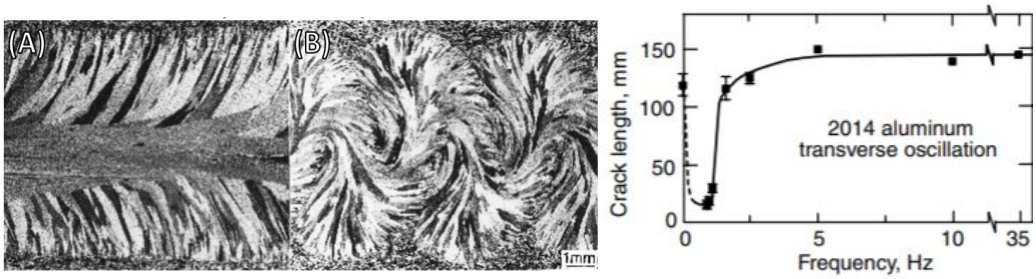

Figure 77 G-TAW welds of aluminium 2014 made with (a)no weaving and (b) weaving at a frequency of 1Hz, and (c) the effect of oscillation frequency on solidification cracking in G-TAW welds of aluminium 2014 [111]

2.8.3 Summary

As discussed in the background, the motivation for this project was to investigate high strength aluminium alloys processed through SLM with a view of proposing a novel alloy with improved performance. This review of literature was performed to gain a deeper understanding of the performance of aluminium alloys and how that affects and influences processing through SLM, this includes the characteristics of the aluminium powders and the effects of the processing environment.

It is clear that markets exist for high strength SLM aluminium alloys and there is an increasing trend of developing age hardenable wrought alloys for this. However, suitable alloys lack processability as they are susceptible to cracking during the process. To properly evaluate potential alloys, the predominant types of age hardenable alloys were discussed. The alloy that was selected to research in this project was AA6061, as this is a popular, medium-high strength alloy with a lot of

general use. Literature reveals that attempts at processing this alloy has been made since 2007 [88] but without success.

Different approaches to processing crack free SLM aluminium parts were discussed with many potential routes. The first attempts to reduce cracking in these alloys were made with altering process parameters and layer thickness and double scanning. Theses have been shown to have an influence on the generation of thermal stresses and therefore the presence of cracks. Other methods mentioned in the literature would potentially offer greater reduction in thermal stresses, such as installing a heated bed or a second beam, were outside the remit of the project.

Beyond reducing the stresses in SLM AA6061 parts, it was noted in the literature that modifying the composition could allow the material to process. Some success has been found with grain refiners to adjust the solidification dynamics and alter the cracking susceptibility of unweldable alloys, in SLM. Another solution based on welding of AA6061 is to adjust the silicon content to improve the weldability of the alloy [90]. Welding of AA6061 is performed using a filler wire with high silicon content which effectively alters the composition of the weld to reduce the cracking susceptibility without reducing the strength of the AA6061 alloy by more than 10% [115]. The attraction of this solution is that this should not increase the costs of the material and should not introduce phases not already present in AA6061.

The addition of silicon can be performed by blending AlSi10Mg into the AA6061. Both alloys are readily available in powder form and similarities in powder characteristics should make a homogeneous mixture achievable. Similar thermal properties of the alloys should make melting and mixing of the two alloys successful, with stirring occurring within the melt pools. Both of these alloys have been studied in SLM in the literature and therefore they provide a basis for mechanisms of cracking and the effect of the blended material can be studied.

3 Materials and Methods

This section details the manufacturing and measuring equipment, and materials and methods used for the completion of work presented in this thesis. Two SLM machines were employed during this research, a Realiser SLM100 and a Renishaw AM125. All SLM samples used in this project were manufactured with this equipment and the machine characteristics are described and process parameter used as variables during experimentation are evaluated. Three powders, AA6061, AlSi10Mg and a blend of the two, were processed to evaluate the cracking phenomenon in SLM aluminium and the proposed solution. In this chapter, these materials are characterised by their chemistry, powder size distribution, appearance, and flowability alongside descriptions of the methods used. Descriptions of all the equipment and methods used to analyse the SLM specimens is also presented, including the design of experiments (DoE), the approach to density measurements and a reasoning for the density measurement methods considered and used in later chapters.

3.1 Realiser SLM 100

The majority of samples analysed in this work were made in a Realiser SLM100 (Realizer GmbH, Germany) (Figure 78) with a YLR-200 laser (IPG Photonics, USA), which is a 200W continuous wave ytterbium doped fibre laser with a wavelength, λ =1070 nm.

Figure 78 Realizer SLM100 at the University of Liverpool with YLR-200 laser and modified gas filter system.

The optical system used to focus and direct the laser beam is shown in Figure 79. The beam that leaves the laser aperture passes through a Galilean beam expander (Sill

Optics, Germany) consisting of three lenses within a bespoke linear guide system. The process parameter “lens position” changes the position of a lens within this system and this is used to adjust the width of the beam, which changes the spot size of laser at the bed. The laser is said to be in focus at the minimum achievable spot size, which is 44 µm in this particular system. On passing the beam expander the beam is directed by two galvanometer scanner mirrors (Cambridge Technology, US) which deflect the beam through an f-theta objective lens (Sill Optics, Germany). This lens passively adjusts the focal length with respect to scanner angle such that the beam size is consistent across a flat plain, designed to be coincident with the chamber bed.

The build volume consists of the circular build plate, with diameter of 125 mm, and a maximum build height of 80 mm. The build plates used in this research were 10-15 mm thick AA2024 sections cut from 125 mm diameter bar.

To deposit powder during building, the powder is placed in a hopper, held on a rotating arm, which carries the hopper over the powder bed. At either side of the powder bed, as the hopper interfaces with the chamber walls, the slider designed with openings to transport a single dose of powder is moved between two locations with respect to the hopper. At one location the openings in the slider align with the opening of the hopper cassette and fill with powder. At the other location, the slider openings align with openings in the base of the hopper and deposit on the chamber bed. Silicone cord wipers attached to the rotating arm, either side of the hopper spread the powder across the build plate.

The process is performed in an argon gas atmosphere, as described in section 2.3, with a gauge pressure of 14 mBar. The overpressure is maintained to prevent air leaking into the system. The gas recycling circuit is represented in Figure 79. Gas flows over the build area to blow vapor and spatter away from the powder bed. The circuit carries highly reactive nano size condensate through a safe change filter, where it can be neutralised in post process.

The argon atmosphere is achieved prior to commencing processing, by purging the chamber with argon, with the lighter air escaping through an opened valve at the top of the chamber. Further reduction in oxygen is achieved with the gas recirculation pump. Processing does not begin until oxygen drops below 0.03% (300 ppm) and this drops further during processing, below the operating limits of the oxygen sensor, as sacrificial aluminium removes the oxygen through reaction. Oxygen in the chamber is measured with a lambda sensor (BOSCH GmbH, Germany) near the top of the build chamber.

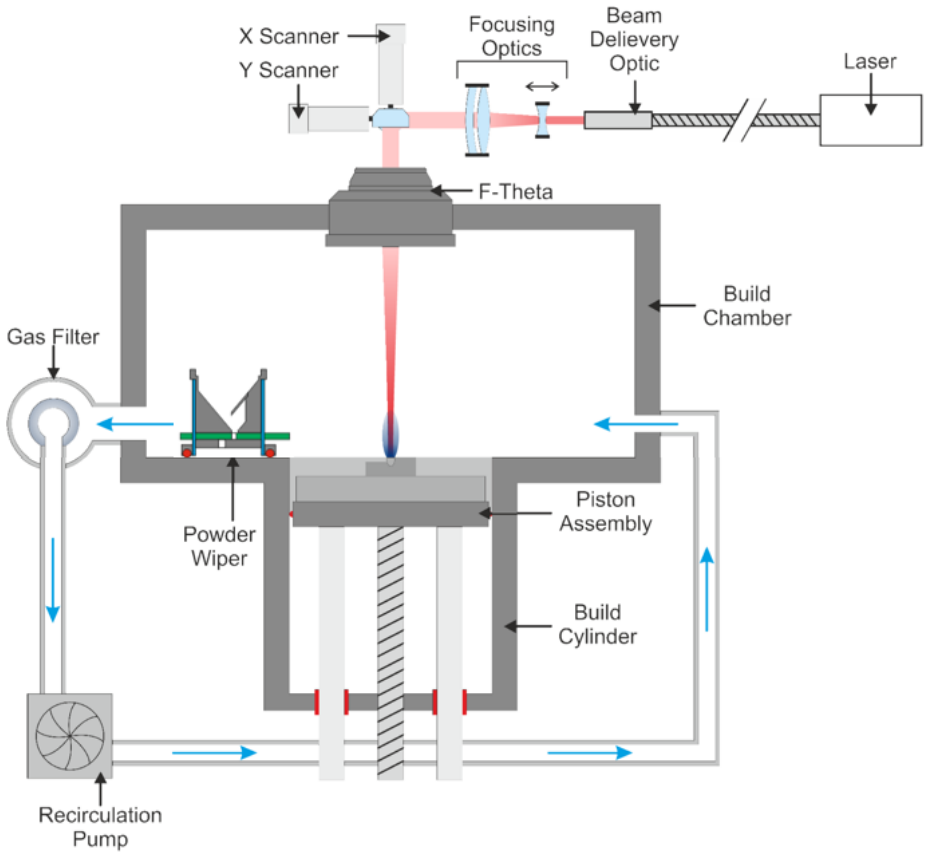

Figure 79 Schematic of optical system, gas recycling circuit and powder hopper and wiper in the Realizer SLM100

The build files for these machines are bespoke *.fas and *. f&s formats, which are hatch files and build files respectively, as these files describe the process parameters that make up a build part and part position in the bed. To generate these files first requires a stereolithography file (STL), which is the accepted standardised format for describing 3D parts in AM. STL files use connecting triangles, defined by three points and a vector, to approximate the surfaces of a part. Hatch files are generated by slicing the STL file at layer spaced intervals to define the scanned areas of each layer. The scanned areas are presented as scanned lines defined by the scan strategy, which is XY alternating for this project, and process parameters (Figure 17). Only internal density was considered for this project and therefore only point distance, hatch distance and exposure time for each point was used and boundary and contour parameters were discarded.

To make samples suitable for measuring density in all methods, described in 3.8, samples were designed to be rectangular with dimensions 8 mm x 8 mm x 17 mm (x, y, and z). The samples were built on four pyramid feet for ease of removal from the build plate with sample numbers printed on top for identification (Figure 80).

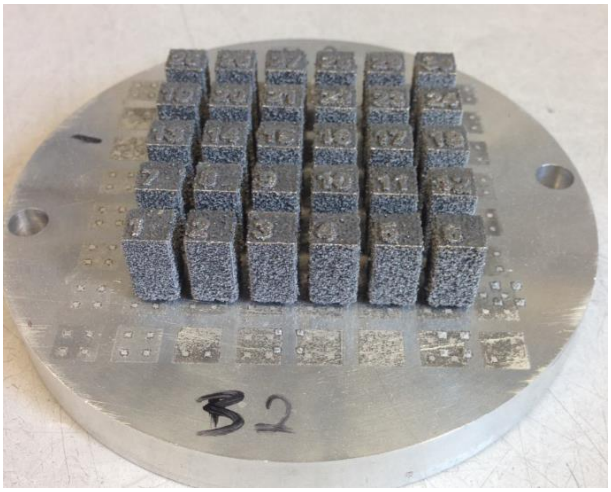

Figure 80 Realizer SLM100 build plate with aluminium samples for density measurements

The parameters that were changed during experimentation were, lens position, exposure time, point distance, hatch distance and laser power. Tests were carried out to understand the effects and limits of these inputs. This was important to determine that the intended change had a real change during processing.

3.1.1 Focus Test

Lens position was a variable within the tests to achieve optimum density of processed alloys. This parameter alters the beam size, by adjusting a focusing optic within the beam expander along a linear track (indicated on Figure 79). The parameter input allows the lens position to be modified between 8 and 28 mm (as far as was tested) in increments of 0.01 mm.

The beam is in focus when the smallest, most concentrated beam occurs on the plain of the chamber bed. The value of lens position to focus the beam was determined by measuring the size of spots printed on a build plate covered with thermal sensitive paper at the bed height. The beam scanned an array of spots with varying values of lens position; the smallest spot indicating the finest beam and therefore the focal point. The spots were captured using a DSLR camera and measured using imageJ [273]. The beam power and exposure time, 20 W and 50 µs respectively, were selected to expose but not burn the laser paper. The spot sizes were too small to capture in a single image with sufficient resolution but were stitched from nine images into a mosaic, 3x3 array. The laser paper was also marked with a boundary and labels, to ease stitching. A stitched image of the plate is presented in Figure 81.

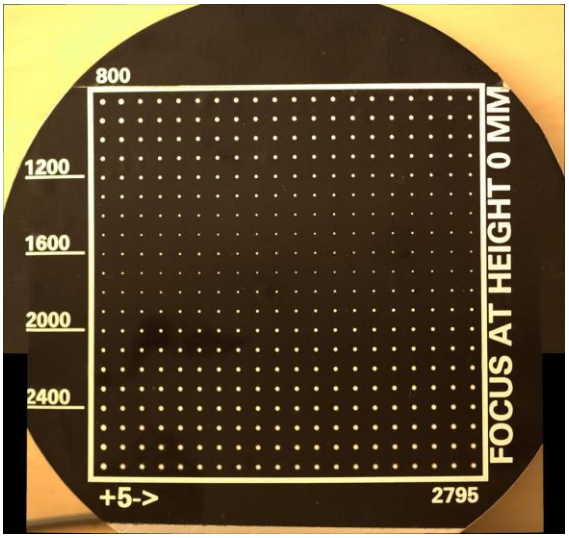

Figure 81 Stitched image of focus length test for SLM 100

The results of spot size analysis are presented in Figure 82. This shows that the spot size reduces to a minimum between lens position 15.00 mm and 17.50 mm. The shape of the rise between these may be due to excessive heating at the spot, as the beam becomes more concentrated. The thermal sensitive paper may also be altered by the heat dissipating from the adjacent spot and not the incident rays themselves. It is most likely the focus is at the highest point within this region, with 16.20 mm at the peak of this rise.

The shape of the weld pool is influenced by the size of the laser beam with the finer beams more likely to produce keyhole mode melting [189]. The finest beam can be used to achieve better surface finish [178], and this can be considered when processing a boundary on parts but only bulk densities are considered in this thesis. Defocusing the beam can have a significant improvement in part densities [274] and was utilised in this work. Focusing above and below the bed can have matching effects on spot size but it has been suggested by previous studies that better results are achieved focussing below the bed then above [186]. The spot test was repeated with the build plate raised 5 mm above the chamber floor. This showed that the lens position values above 16.20 mm focus the beam above the bed. The tests in Chapter 4 to find the optimum parameters will operate in the region up to and below the focus point.

The two furthermost left spots on each line have a larger spot size that does not fit the trend of the other spots on the plate, though the effect is reduced nearer the focus position, this could be a design flaw in the machine and may result in errors if tests are performed with parts built in this area. Another issue could be with beam shape; as the beam is defocussed, a trend emerges with the aspect ratio showing a dependence on position on the plate. This can be seen in the sawtooth trends that appears in Figure 83, where it is most pronounced on the lens positions from 18.00 mm to 22.00 mm.

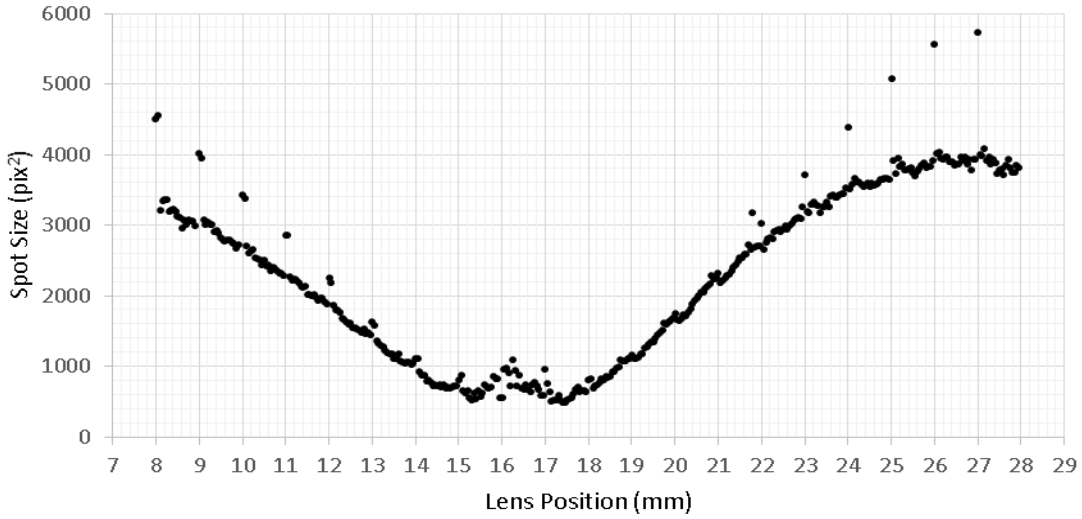

Figure 82 Focus test for SLM 100, lens position vs. spot size

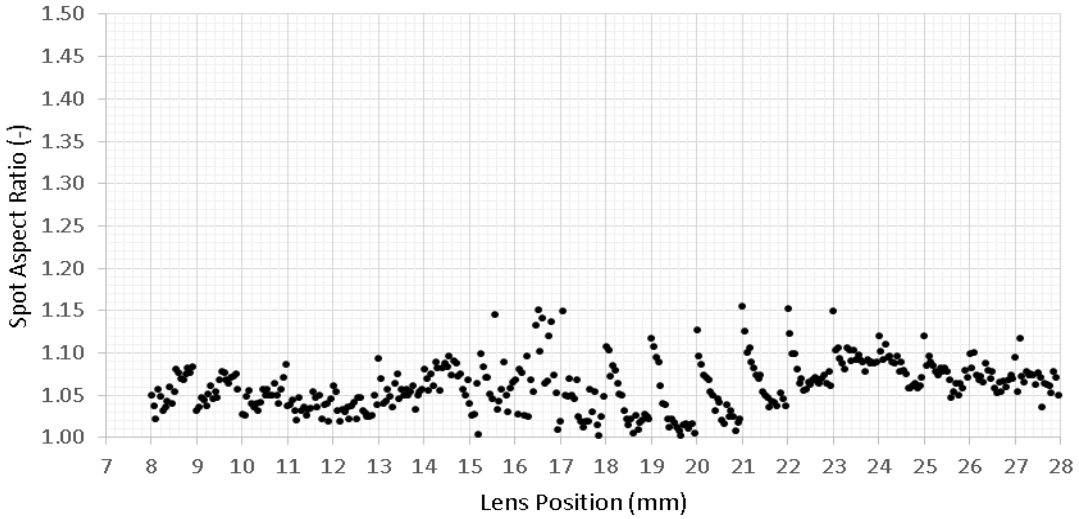

Figure 83 Focus test for SLM 100, lens position vs. spot aspect ratio

The consistency of laser spot size across the bed was tested; an array, 20 x 20, of spots was scanned across the bed, with the lens position fixed at 15.00 mm for all spots, as this lens position is typically used for material parameters in this machine. The layout of the spots was the same as with the previous test. The spots were numbered according to their location in order reading left to right, and from top to bottom. There is no pattern evident in either spot size (Figure 84) or aspect ratio (Figure 85). The scatter that is seen could be from the discretisation of the spots into pixels or from the process itself, as the spots are not scanned onto a perfectly flat surface and surface roughness, including bubbles or dirt between the plate and the thermal sensitive paper could alter the spot size.

Some beam inconsistency will be permissible and there are no known specifications for beam consistency to be met. The beam will change the temperature profiles in the material and therefore the effect will be material dependant. As such, improving the beam consistency would only be considered if the inconsistency was evident in the built parts. As no problem was ever discovered the beam can be consider sufficiently consistent.

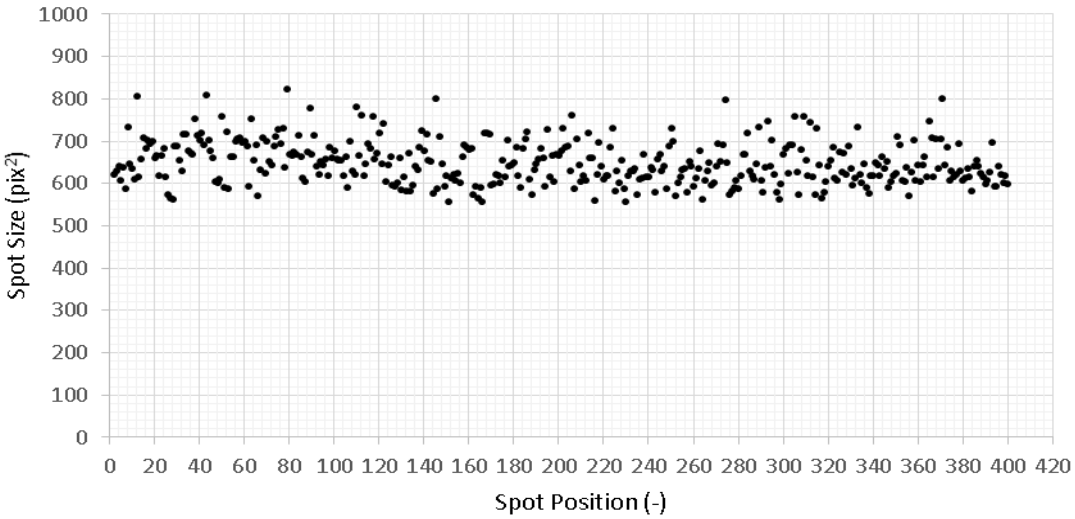

Figure 84 Spot size consistency test for SLM 100, spot position vs. spot size

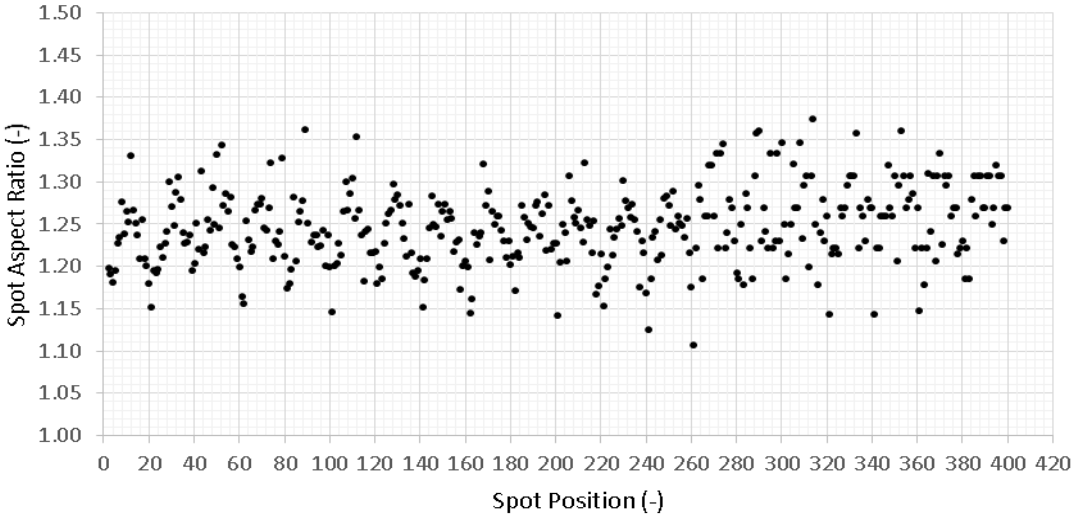

Figure 85 Spot size consistency test for SLM 100, spot position vs. aspect ratio

3.1.2 Limits and Resolution of Hatch Exposure and Point Distance Inputs

A scan track in the SLM 100 comprises of a series of discrete points, with the controlling parameters being the distance between the points and dwell time at each point, called point distance and exposure time, respectively. The laser remains on during the entire track and heats material between spots. This is seen in Figure 86, though the point distance is exaggerated, compared to values used during processing experiments, to show the scanning between spots. An experiment was carried out to learn the limits of these two parameters by measuring the time to scan a line with varying inputs. Alongside this, images were taken of various scanned lines (Table 2).

Each line ends with a larger shallower spot, possibly indicating a defocussing at the end of a hatch. The spot appears only as the final point in a scanned area, not on each hatch line. The thickness of the lines changes with heat input but this did not affect the final spot size. The discrete positioning of the spots is only evident where the point distance is at least 200 µm, while optimised density tests found the best results were with point distance below 100 µm. It may be the scanner mirrors cannot move fast enough to allow a complete dwell time and are always in motion. The mirrors will have periods of acceleration and deceleration between spots and these may alter the speed-time profile but it appears that up to 100 µm point distances can be interpreted as a continuous moving beam rather than the series of discrete points it should be. The implication of this would be that within this range altering both point distance and exposure time would be redundant. It was not clear if this interpretation could be extrapolated to higher exposures. The optimised density test found the best exposure times were above 500 µs, for all three materials.

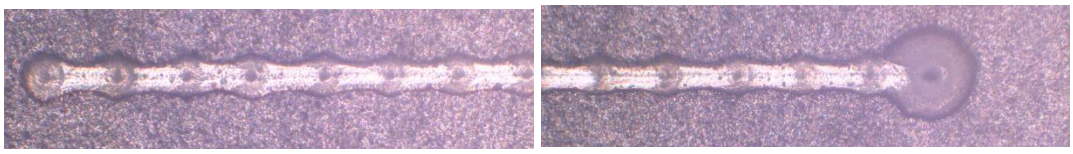

Figure 86 laser scan on thermal sensitive paper, exposure 200 µs and point distance 500 µm

The time duration of the line scans was recorded by connecting an oscilloscope to the laser control unit. The scan line length was set to be 10 mm for all scans; hatch exposure and point distance were varied to examine the limits of response of the laser control unit to test the machines sensitivity to these parameter changes. Various values were chosen to examine where the limits of these inputs are. Figure 87 shows that exposures below 20 µs and point distances below 10 µm do not affect the scan duration. These limits appear to be independent of each other, so tests with holding one variable constant will suffice to get the resolution and minimum value of the other.

Table 2 Images of scanned tracks across varying exposure and point distance

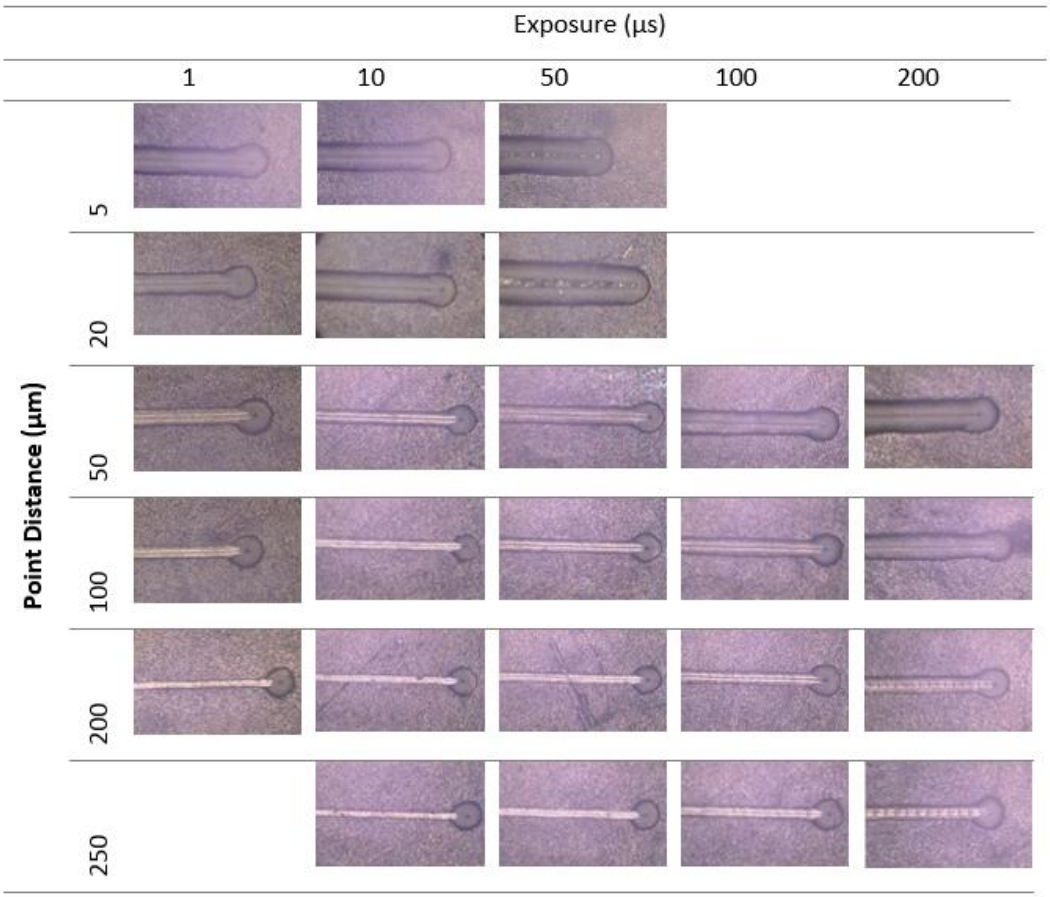

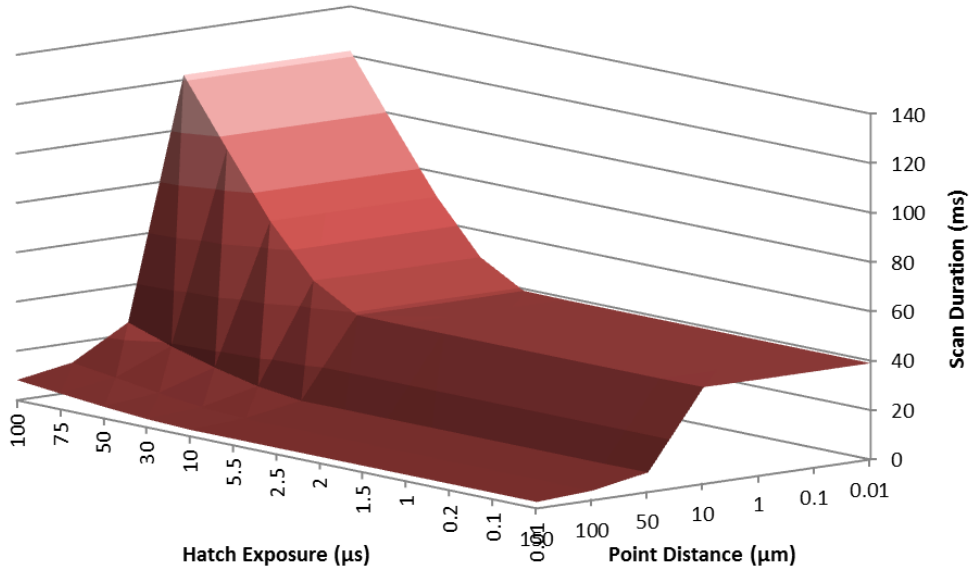

Figure 87 Effect of hatch exposure and point distance on the scan duration of a 10 mm line using hatch scan strategy.

The lower limit of point distance was found using 50 µs exposure time. The smallest increment of change in point distance is 10 µm and smallest value that can be input is 10 µm. The limits of exposure were found using 50 µm point distance. The smallest

increment of change in exposure is 1 µs and smallest value that can be input is 20 µs. These values inform the parameters tested in chapter 4, to find the optimised density.

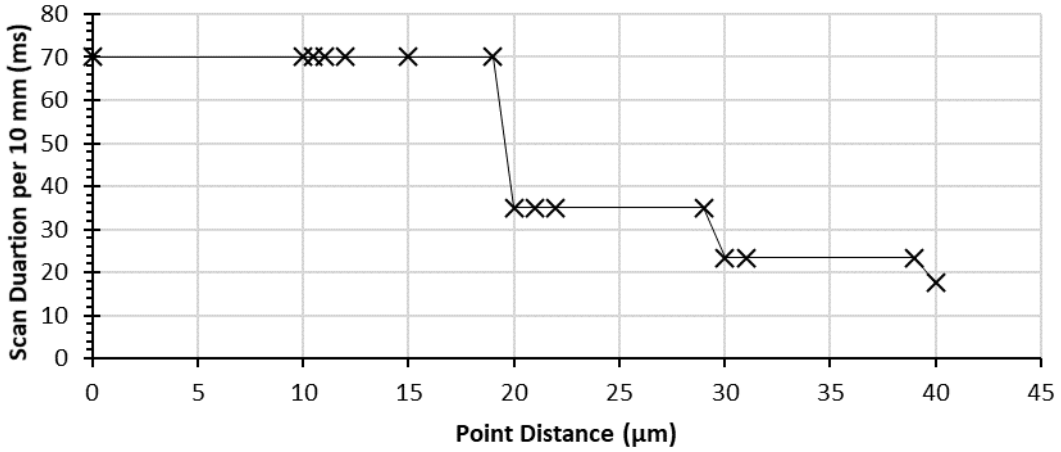

Figure 88 Point distance resolution and minimum input test

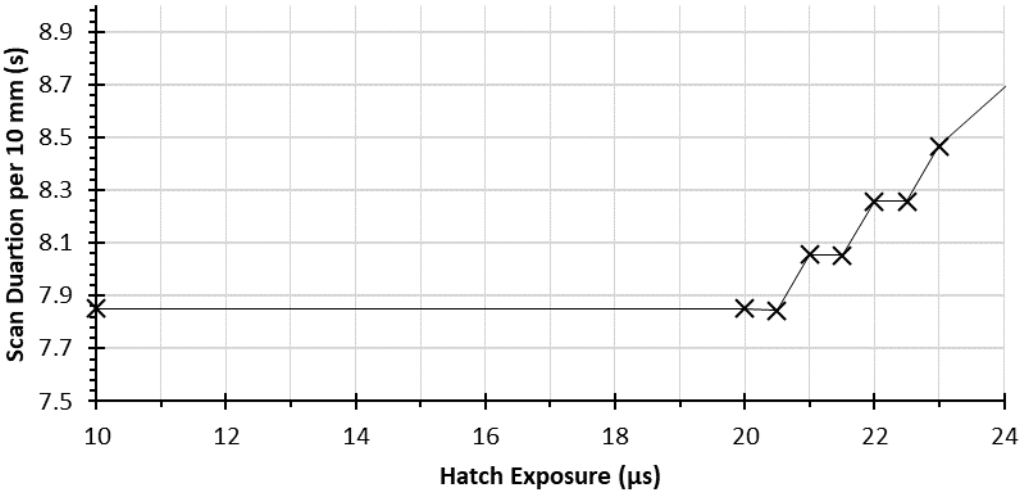

Figure 89 Exposure resolution and minimum input tests.

By understanding the limits of the parameters, it is possible to test how scan duration can be altered. If point distance is held constant then exposure has a proportional response to scan duration, and if exposure is constant then point distance has an inverse response to scan duration. These relationships were used to formulate an equation:

$$\boldsymbol{Scan\ Duration}, t_{SD} = C_1 \frac{t_{expo}}{P_{dist}} + C_2\, t_{expo} + C_3\, P_{dist} + C_4$$

Equation 6

Where; t_{expo} is exposure time, P_{dist} is point distance and C_1, C_2, C_3 and C_4 are constants. Minitab was used to find the equation that best fitted this form:

$$\boldsymbol{Scan\ Duration}, t_{SD} = 10.25 \frac{t_{expo}}{P_{dist}} + 4.25\, x10^{-4}\, t_{expo} + \frac{186.75}{P_{dist}} + 0.02$$

Equation 7

Figure 90 shows the fit of the predicted scan duration compared to the measured values. The errors show that all predicted values are within 2% of the measure value.

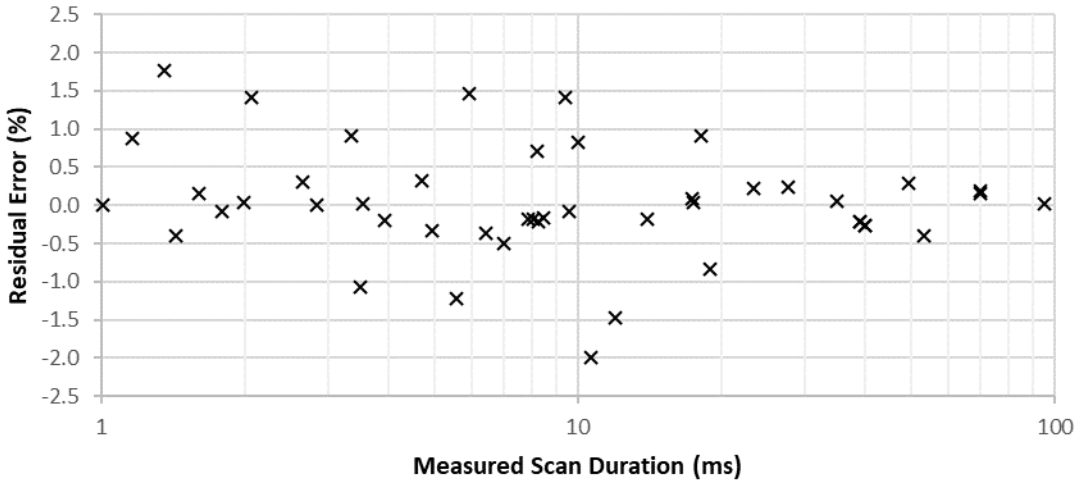

Figure 90 Measured scan duration vs. residual error in scan duration as predicted by Equation 7.

Error in generating this equation could have arisen from the accuracy of the readings from the oscilloscope and the truncation of readings to three significant figures. The first constant C_1 is likely to be the length of the line in mm, the second and fourth, C_2 and C_4, are insignificant. The relationship was not tested across lines of different length which could influence these constants. Dividing the line length by the scan duration gives the scan speed of the line. Using these values, scan speed can be expressed as:

$$\textbf{Scan Speed}, v_{scan} = \frac{P_{dist}}{t_{expo} + 19.67}$$

Equation 8

The predicted scan speeds are compared to the measured scan speeds in Figure 91. The errors have increased compared to Figure 90, as minor terms have been omitted but all errors are still within 5% of the measured value.

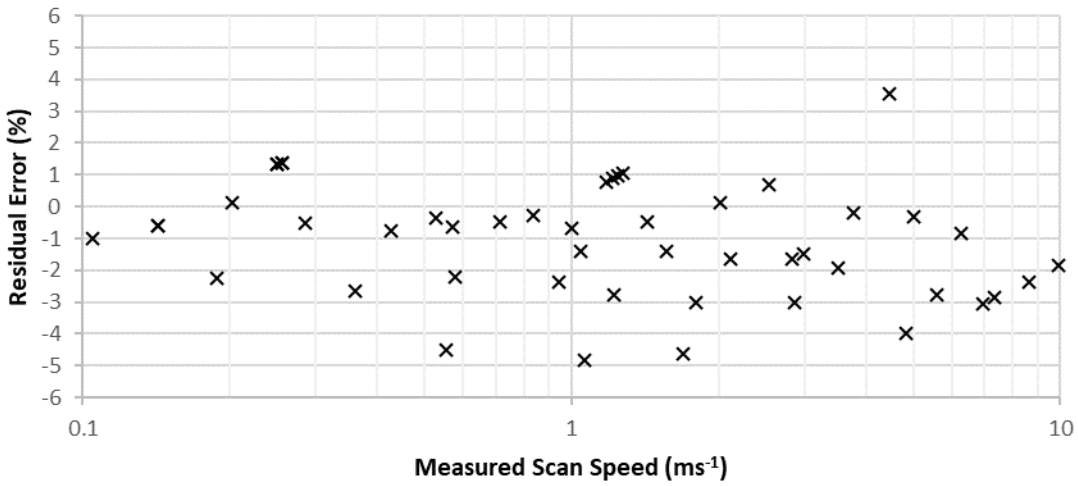

Figure 91 Measured scan speed vs. residual error of the scan speeds as predicted by Equation 8

This shows a different relationship then expected, as theoretically the denominator should only be the exposure time. It was not tested how geometry of the scan affects this relationship. It is possible that the denominator could be influenced by line length or by hatch spacing. The main conclusion from this investigation is that one must be aware that point distance and exposure time do not have the same influence on the scan lines, and so were not simplified to a scan speed parameter.

3.1.3 Limits and Resolution of Hatch Distance

The purpose of this test was to test if changes of 1 µm in hatch distance had a real effect on the space between hatches and if inputs to hatch distance had a minimum value.

To test the limit and resolution of hatch distance, hatch files was made for 5 mm cubes with different hatch distances. A single layer of these cubes was scanned onto thermal sensitive paper, impart the laser scan path for that layer (as in 3.1.1). The point distance, exposure time, laser power and lens position were 50 µm, 50 µs, 20 W, and 15.00 mm, respectively. The lines created by these parameters are roughly 105 µm in width (104.8 ±0.6 µm measured from a single line at five points with imageJ), therefore hatch distances below this will have overlap and only distinguishable at the rounded ends of the line. Figure 92 shows two of the parameters used to create the hatched patterns. In all the hatched bocks, the hatches start at the top left with successive scan lines altering direction. Figure 92 show that the hatches start 300 µm away from the starting point, consistently across all hatched areas. During the transition between scan lines the laser switches off. The kink at the start of each line show the scan line starts before the y-axis mirror is at rest. This is caused by the mirrors being underdamped.

Rather than requiring a precise measurement between two lines and precision imaging, the approach was taken to measure across several lines with the reasonable assumption that hatch spacings are equal between them. The hatched blocks were 5 mm square, and the hatching software is designed to place as many hatched lines up to but not matching or exceeding the designed boundary and no offsets are included. As such the number of hatch lines within the 5 mm boundary should change with hatch distance inputs.

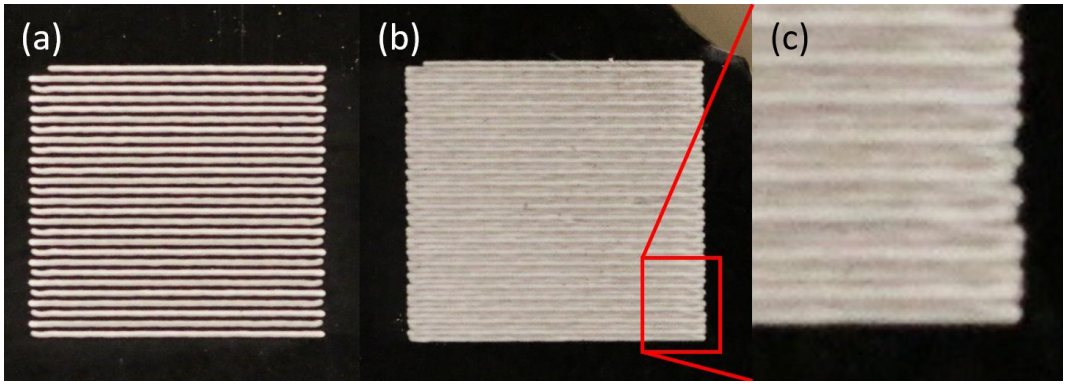

Figure 92 Hatched layer of 5mm square from hatch distance test; (a) 180 µm hatch distance sample showing separation of hatch lines, showing their width and direction, (b) 100 µm hatch distance sample used to measure real changes in hatch spacing and (c) close-up of 100 µm hatch distance sample's hatch lines, showing how they were counted to measure the change.

The number of hatches within the 5 mm square changes inversely to the hatch distance. Hatches distances of 98 µm, 99 µm and 100 µm had 51, 50 and 49 hatch lines respectively, within the 5 mm area. The area of these blocks measured 4.932mm, 4.870mm, and 4.808m, respectively, are shorter than what was expected but this could be from tilting in imaging. This confirms that the hatch distance resolution is at least equal to 1 µm.

The narrowest hatches caused overheating and melting of the build plate, with the greatest overheating occurring with hatch distance of 1 µm, the smallest value tested. This value is smaller than would be needed as the nominal beam diameter is 44 µm and melt tracks are around 150~200 µm wide. This confirms that all hatch distances input as whole numbers in microns will have a real change on the machine.

3.2 Renishaw AM 125

The second SLM machine (Figure 93) used for this experimental work was a Renishaw AM125 (Renishaw, UK) with a R4 RedPOWER laser (SPI Lasers, UK), which is, similar to the Realizer's YLR-200 laser, a 200W continuous wave ytterbium doped fibre laser. Optical tracks for the two machines are identical in configuration but the Renishaw has a nominal beam diameter of 35 µm.

The build plate is a 125 mm square area with rounded corners (Φ = 20 mm) and the maximum build height is 125 mm. The build plates used in this research were 10-15 mm thick plates of aluminium supplied by Renishaw AMPD. The powder deposition system is similar to the SLM100, though the hopper is fixed in position and the slider to release a dose of powder is triggered by the wiper, which moves on to rails linearly across the build plate.

The process performs in an overpressure argon atmosphere, with a similar gas recirculation system. Air is removed from the chamber by vacuuming the air from the chamber and refilling with argon.

Figure 93 Renishaw AM125 at the University of Liverpool

The intention of using this machine was as a replacement while the Realiser SLM100 was requiring repair. No density samples built in this machine are included in this thesis as a problem with focus was discovered. Initial tests observed that the top surface finish of parts showed variation with location on the build plate. (Figure 94). This variation was radial and centred on the middle of the plate. It was expected, and proved by results shown in section 5.4, that the more reflective surface was an indication of lower surface oxides, and therefore the parts built by this machine were included in the study of oxides in SLM aluminium. Tests described in section 3.2.1 proved that the cause of the discrepancy was with the focus, which was not sufficiently altered to flat field focus. The problem is likely to have been with the f-theta and should the system be repaired, it would be expected that the range of spot sizes would still be achievable in the system, manufacturer permitting.

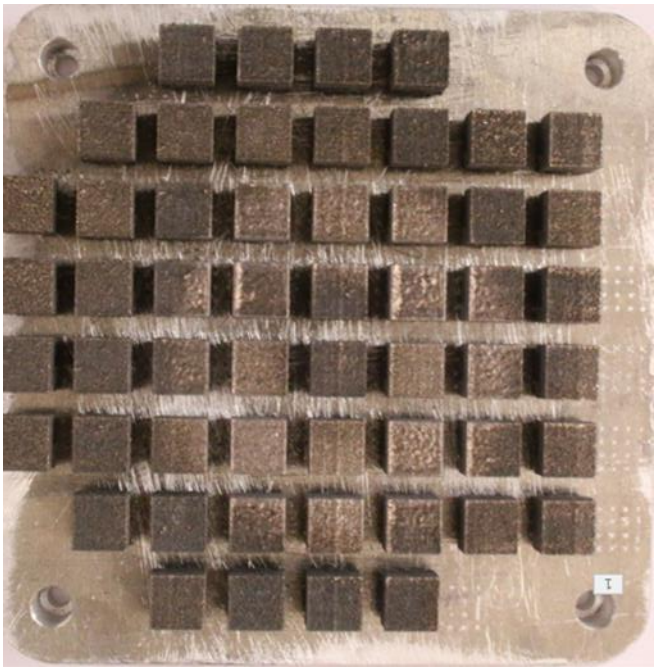

Figure 94 Density optimisation parameter test for AlSi10Mg build in the Renishaw AM125

It was important to understand if the location, and the appearance, has an effect on the build quality. A build was made with 6x6 array of parts all with equal parameters. The sample density was measured in the Archimedes method (Figure 95). The optimum parameters for this material in this machine are not known and the more porosity the greater the scatter in results would be, as porosity is a random occurrence. It is clear from the Figure 95 that the location has an effect on part density, similar in pattern to the surface appearance. The highest densities are in areas where the top surface appears darker and the lowest densities are in areas with more reflective surface.

97.21	96.46	97.13	96.97	96.92	97.58
96.55	96.26	96.62	95.66	97.41	97.15
96.29	95.14	97.07	96.35	95.20	97.49
96.04	95.71	97.30	98.24	94.88	97.13
96.24	97.15	96.70	95.41	96.90	97.14
96.18	96.29	96.92	96.71	96.19	97.80

Figure 95 Renishaw AM125 part consistency build, the gravimetric density colour gradient applied to aid identification of relative densities, with dense parts in darker colour.

3.2.1 Spot Size Test

Spot size tests, same as were used in section 3.1.1, were carried out test the hypothesis that spot sizes were changing across the bed and this was affecting the surface finish and part density. If the f-theta lens failed to correct the varying focal length across the bed then the effect would be similar to what is being seen in Figure 94 with a ring where the beam comes into focus and focal point above and below the bed at other locations. The spot size would not alter the energy input to the parts but would alter the temperature profile of the melt pool, with a finer focal point causing a steeper temperature gradient. The high temperatures could cause increased vaporisation and spatter, which are believed to act as sacrificial material for oxygen removal and therefore reduce the oxides in the build parts but may also be detrimental by defocussing the beam.

To study the focus of the AM125 machine, the same methodology as section 3.1.1 was used. An array of spots was marked onto thermal sensitive paper. The spots were scanned with focus at 0 (which is a machine parameter designed as the focal distance to the build plate), 200 µs exposure, and 100 W power. The parameters were selected to maximise the marked spot size without excessive heating or burning the paper. The size of the spots was measured by photographing the thermal paper (using the same DSLR camera as section 3.1.1), with many spots captured per image to reduce the amount of time required. The entire array of spots could be captured within two images which showed an annular trend in the spot size.

A plate, with thermal sensitive paper, was scanned with an array of 80x80 spots with focus input at 0. Figure 96 shows the spot sizes in this array. The plot shows a trend comparable to the top surface of the parts (Figure 94) and the density of the build parts (Figure 95). The finer spots appear to coincide with the location of reduced density and reflective surface and are as a result of the beam nearing focus, with minimum spot size at focus. The finer spots increase the energy intensity at the centre of the beam, which will increase the temperature at the centre of the weld pool, possibly increasing the amount of vaporisation and creating more plasma. The higher reflective surface could be a result of increased obliteration of oxides, as theorised by Olakanmi et al. [87]. Alternatively, metal vapour and spatter are suspected to reduce the amount of oxygen present by reacting with preferential reaction with the present oxides [161]. The dependence on location prevented density optimisation with this machine but the results from this build were used to test if spot size could be used to reduce oxides in section 5.4.

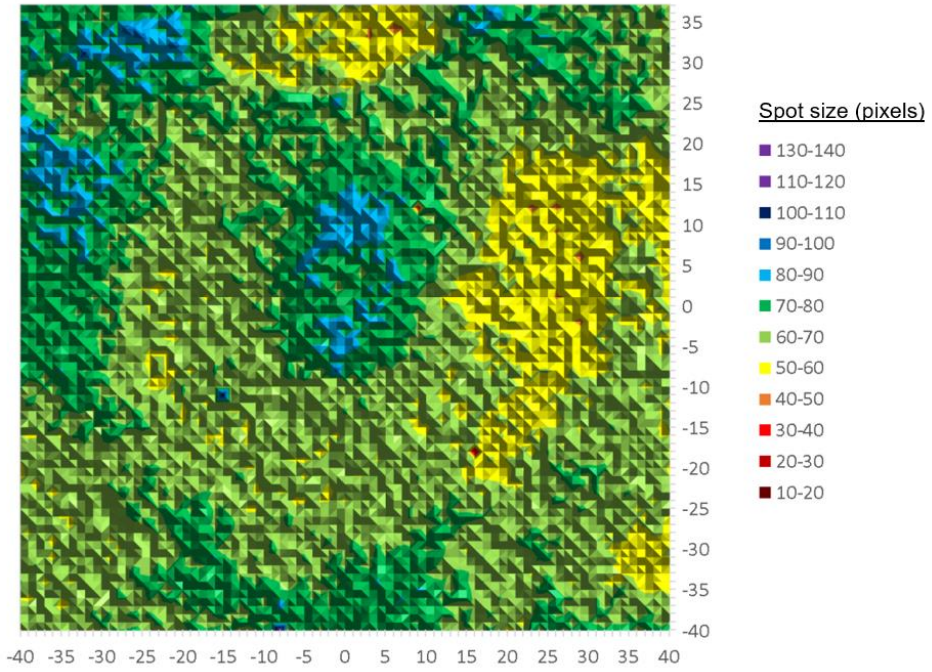

Figure 96 Renishaw AM125 focus test captured with two images.

An experiment was undertaken to see if dynamic changing of the focus parameter with position could homogenise focus and spot size. The pattern in spot size can reasonably be assumed to have ellipses of consistent spot size and spot size changing with distance from an origin (Figure 96). By changing the focus position with angle, every ellipse of constant spot size was tested across the range of focus values. The lens position in the Renishaw AM125 has discrete increments of change, and the smallest increment was tested in Figure 97.

An attempt was made to capture all spots in 24 images stitched together. At intersections between images there is often a sudden change in spot size. All images were captured under the same conditions with the camera and plate held at constant distance. There are several possible reasons for variation in apparent spot size between images. Image contrast could be affected by external light sources which were not controlled. The amount of light reflected from the plate could also affect contrast; This would affect the boundaries the most.

It was decided that there was enough of a size effect in changing the focus parameter that correcting for discrepancies between images was not necessary. It was expected that, if the focus could be changed to produce smaller spots then there would be a spiral as the smallest spots in each segment alter in radial distance. This appears to happen at a few locations but not across the entire range and it is clearly not possible to achieve a small spot near the centre of the plate. From machine focus of 4 to -2, the spots with size 1100-1250 pix^2 are present nearer the centre. Below -2 the change in focus changes the spot size but the smallest spots remain around 25 mm from the centre of the ellipses. This establishes that a satisfactorily consistent spot size cannot

be achieved by changing the machine settings and required physical repair that was not time permitting in this project. This machine was not used for producing density test samples.

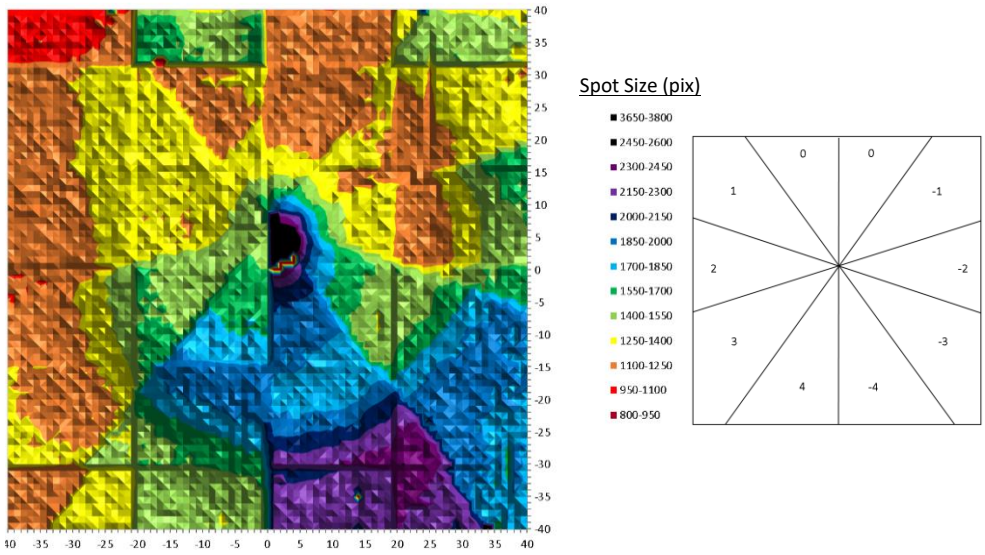

Figure 97 Renishaw AM125 annular focus test. Focus values are presented on the right with the resultant spot size record left

3.3 Scanning Electron Microscopy (SEM)

SEM uses a focussed electron beam to scan and interact with a conductive sample. The beam interaction causes many emissions, including electrons and radiation, from the sample (Figure 98) and can be used to characterise the material in various ways. The emissions used for analysis in this thesis are secondary electron (for surface imaging), backscatter electrons (for electron contrast channel imaging and electron backscatter diffraction) and characteristic X-rays (for energy dispersive X-ray spectroscopy). This section explains the emissions and the methods that were used for imaging and analysis.

The interaction zone between the electron beam and target is controlled, in this work, by the accelerating voltage and current of the beam. The beam current controls the number of electrons bombarding the target. The accelerating voltage influences the penetrative depth of the beam. Accelerating voltages of 5 kV and 20 kV were used in this work. Assuming the material is mostly aluminium, the depth of the interaction zone is estimated as 2.08 µm from a 20 kV beam and 0.206 µm from a 5 kV beam (as calculated from Kanaya and Okayama [275]). This value changes with oxide films thickness and composition. Surface oxides thickness is likely submicron and is likely shallower than the expected penetrative depth [212]. Penetrative depth is only one aspect when considered the source of emissions. Secondary electrons are generated throughout the interaction zone but due to their low energy, they are less likely to

pass through as much material as the higher energy backscatter electrons, and therefore are more likely to have been generated near the top surface. Similarly, x-rays can be generated throughout the interaction zone, but x-rays generated deep within the material are more likely to be absorbed as they pass through the material.

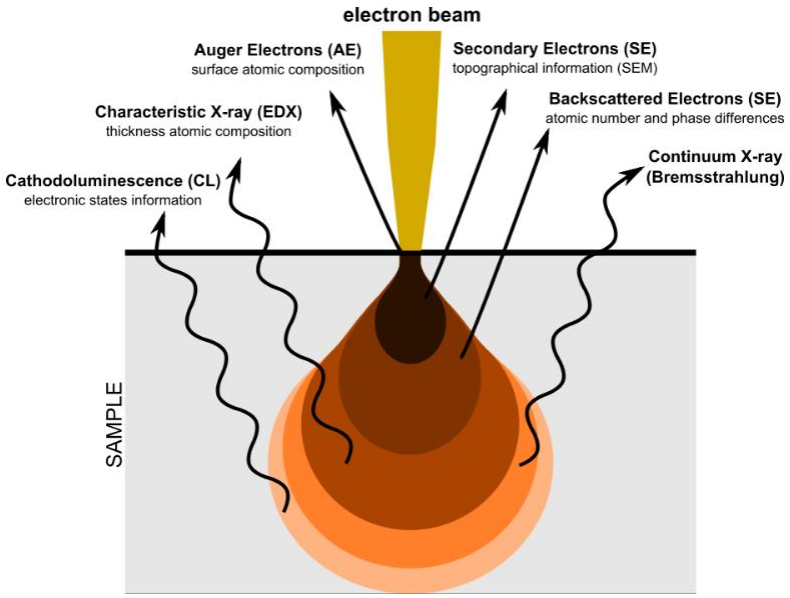

Figure 98 Electron and radiation emitted from different interaction zones from a focussed electron beam (adapted from Claudionico [276])

3.3.1 Secondary Electron Imaging (SEI)

Secondary electrons (SE) are low energy electrons produced from excited atoms and emitted from the sample when they acquire sufficient energy. As low energy electrons, they can be absorbed by interactions with surrounding material and only SE near the surface will exit the material and can be detected. A positively biased grid is used to deflect these secondary electrons away from higher energy backscatter electrons to be detected separately. The intensity of SE reaching the grid is a function of the incident angle and therefore an image of the target surface can be generated.

Secondary Electron Imaging (SEI) was used for topographical imaging. The advantage of this method over optical imaging is the higher depth of field and higher resolution achievable with the ability to focus the electron beam, as the wavelength of visible light restricts the maximum possible resolution to above 0.2µm. The disadvantage is that there is greater restricted access to the equipment and longer operating time as the electron beam requires a vacuum to operate and high resolution images can require relatively slow scanning speeds.

3.3.2 Electron Channelling Contrast Imaging (ECCI)

Electrons undergo multiple interactions with the target atoms and the electrons from the fired beam that deflected back out the sample are referred to as backscatter electrons. The level of backscatter is a function of the atomic weight of the target

material as heavier atoms in the target material scatter the electrons more efficiently and images with contrast in material composition can be produced. Similarly, but less efficiently, the grain orientation has an effect on the deflection and scatter of the electrons. Backscatter electrons have higher energy than secondary electrons and the interaction zones from which backscatter electrons can be produced is bigger as the electrons are less likely to be absorbed by the material.

Electron Channelling Contrast Imaging uses the dependence of backscatter on grain orientation to view grain structure of the samples.

Backscatter is not generated from the surface and in order to limit the depth of the measurement to only identify grains at the surface, a low accelerating voltage is used, 5 KeV and to increase the number of electrons for the measurement, the current of the beam was increased to 10 nA from 0.1 nA.

3.3.3 Electron Backscatter Diffraction (EBSD)

The backscattered electrons previously described can be used to obtain crystallographic orientation information about individual grains in a target material. As described backscatter electrons are scattered dependent on the orientation of the impacted crystal. In EBSD, the planes of atoms in the crystal act as a diffraction grating resulting in electron diffraction which gives patterns known as Kikuchi bands (Figure 99).

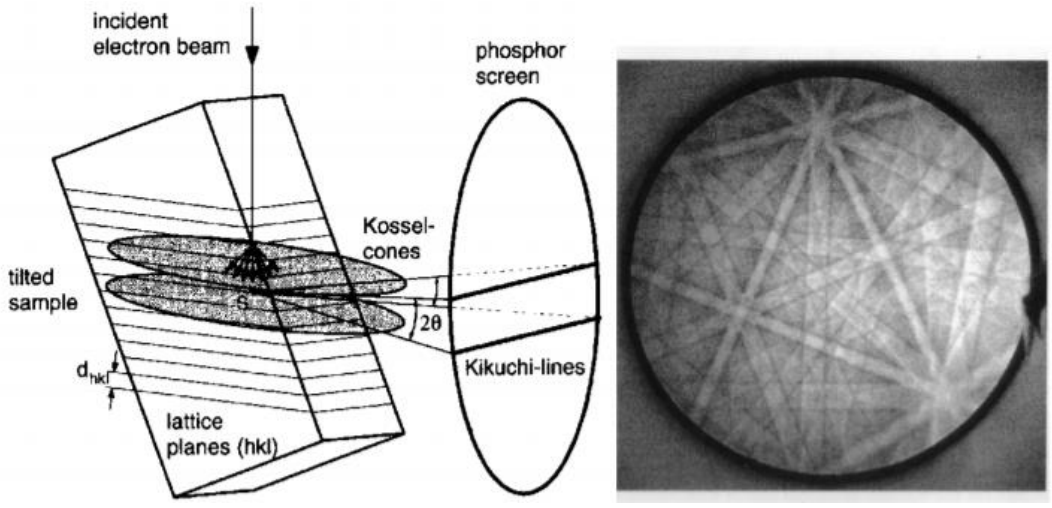

Figure 99 Origin of Kikuchi bands and example of a Kikuchi pattern [179]

The Kikuchi band pattern is used to determine the grain data as some of these arrive at the Bragg angle for each lattice plane [112]. The scattering source is between two planes hence two beams are produced (one for the upper and one for the lower plane) to give the typical band image, multiple bands are observed which represent each plane in the crystal and each band has a distinct width and corresponds to a particular orientation. A band is indexed by identifying the crystallographic indices of the bands

and poles (where the bands intersect), the pattern has all the information about a crystal's unit cell's angular relationship relative to a known reference axis.

EBSD allows for specific data of every grain and grain boundaries to be acquired, unlike ECCI which just produces contrast between grains but cannot be used to determine orientation.

3.3.4 Energy Dispersive X-ray Spectroscopy (EDX)

X-ray emission occurs when the inner shell electrons in the target are excited by the incident beam move into a higher, unoccupied level. The vacancy left by this process is filled by a higher energy electron from a higher energy level and x-rays are emitted to conserve energy. Each atomic element has a unique x-ray spectrum, defined by the different energies from the atom's electron shells, making identification of constituent elements possible.

Detection of light elements is difficult for a number of reasons including, the x-rays have low photon energies that can be absorbed within the target material reducing yield, few or single x-ray peaks, as smaller atoms have fewer shells, and low energy peaks are positioned near electronic noise of the detection system. This was a problem for studying the oxygen content within samples in section 5.4.

This method was used to analyse surface oxides on aluminium samples. EDX does not measure only the surface but from an interaction volume beneath the surface (Figure 98). Thickness of surface oxides was of interest and to differentiate the oxides at the surface from oxides within the sample, different accelerating voltages were used, with different interaction depths. A comparison of oxygen found with accelerating voltage of 5 kV and 20 kV shown how the lower accelerating voltage, which has shorter penetration depth, detected a higher ratio of oxides and therefore informs about the quantity and position of oxides.

3.3.5 SEM Equipment

Three Scanning Electron Microscopy (SEM) machines were used for imaging and analysis in this research; Hitachi TM4000Plus (Hitachi Ltd, Japan), JOEL JSM-6610 and JOEL JSM 7001f (Joel Ltd, U.K.). The Hitachi TM4000Plus is a fast use tabletop microscope with accelerating voltages of 5-15 kV and was used for SE surface imaging. The JOEL JSM-6610 is a field emission SEM and therefore can provide higher resolution images than the Hitachi TM4000Plus. It is a larger system and requires longer set-up time. This machine was used for SE imaging and EDX analysis, as it has an Oxford Instruments INCA X-act EDX detector. Accelerating voltage can be selected in the range of 0.3-30 kV and different accelerating voltages were used depending on the requirement.

This study used the oxford instruments EDX equipment on the JEOL JSM-6610 for measuring oxide content within SLM samples and due to overcounting of oxygen and

a benchmark standard piece of cold rolled and polished AA6061 was analysed which has close to zero oxygen content but the system reported a count of 2.17%. Overcounting of oxygen affected the result throughout this analysis but this gave a benchmark of acceptable oxygen and comparative analysis was used.

The JOEL JSM 7001f is also a field emission SEM but has a more powerful beam than the JOEL JSM-6610. This machine was used to generate ECCI as the more powerful beam increased contrast. Accelerating voltage can be selected in the range of 0-40 kV.

EBSD was performed on a FEI Helios Nanolab 600i SIB/SEM with an EDAX Octane Pro EDX detector.

3.4 Optical Microscopy

Optical microscopy (OM) was performed with an axioplan 2 (Zeiss, UK) operated in reflected light with various objective lenses. Stitching of images was performed with imageJ [273], where large areas and high resolution are required for analytical purposes, such as micrographic density.

3.5 Laser Size Diffraction (LSD)

Laser Size Diffraction (LSD) was the method used to measure powder sizes. In this method powders, carried by a liquid or gas, are passed between a laser beam and detector and cause the beam to diffract (Figure 100). The angle of the scattered light is dependent on the size of the particle, with smaller particles causing greater diffraction, and intensity and angle of light on the detector is translated into particle size. The method does expect the powder to be spherical and calculates the size perpendicularly to the beam direction, which due to powder aligning with the carrier flow is most likely to be the largest axis of each particle.

LSD was performed with a Malvern Mastersizer 3000 MU (Malven Instruments Ltd, UK). The Fraunhofer method was used, as the powder is opaque. The system is capable of calculating the equivalent spherical diameter of the particles to an accuracy of ±1 µm. To describe the powder size distribution three dimensions are used; D10, D50 and D90 represent the 10^{th}, 50^{th}, and 90^{th} percentiles of the particle size distribution.

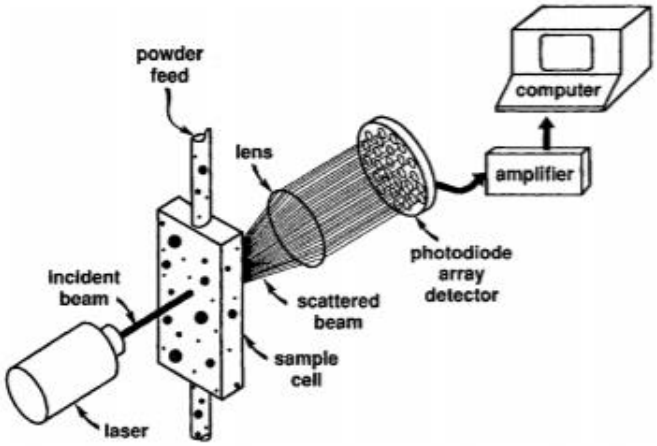

Figure 100 Schematic of particle size analysis with laser size diffraction [277]

3.6 Powder Characterisation

Two powders, AA6061 and AlSi10Mg, which were used during this project were purchased from LPW technology. Both were produced by argon gas atomisation and sieved to size 20-63 µm. The chemical compositions measured by LPW are presented in Table 3. A blend of the two powders was made to process as a new material. The powders were blended in the ratio 9:1, and the material composition can be assumed to be a weighted average of the two constituents.

Table 3 Chemical composition of AA6061 and AlSi10Mg powders reported by LPW (%wt)

	AA6061	AlSi10Mg	Powder Blend (weighted average)
Aluminium	Balance	Balance	Balance
Silicon	0.764	10.41	1.728
Magnesium	0.861	0.338	0.809
Iron	0.112	0.137	0.115
Copper	0.191	0.002	0.172
Chromium	0.175	0	0.158
Oxygen	-	0.089	0.009
Manganese	0.017	0.006	0.016
Titanium	0.007	0.008	0.007
Zinc	0.004	0.004	0.004
Nickel	-	0.004	-
Nitrogen	-	0.002	-
Lead	-	0.001	-
Other	<0.15	<0.05	<0.14

The purpose of the powder blend was to alter the alloy composition of AA6061 by increasing the silicon content by ~1% without significantly altering the rest of the material or material characteristics. The mixing of the powders was performed by passing the two powders through a sieve five times. There was no previous mixing protocol within the research group and a lack of access to specified mixing equipment [278, 279] so this method was devised based on intuition. The two components of the blend had similar size distribution, material density and flowability and therefore this method was expected to lead to good mixing. The number of passes may have been excessive but that was more favourable then risking failed mixing. Powder characterisation in this section testifies to the standard of mixing.

Powders were characterised by size using laser size diffraction (LSD), shape using scanning electron microscopy (SEM imaging), flowability using angle of repose (sheer cell) and chemistry using energy dispersive spectroscopy (EDX), as described above.

3.6.1 SEM and EDX Characterisation of Powders

SEM and EDX of powders was performed on a Hitachi TM4000Plus (Figure 101, Figure 102 and Figure 103). SEM images were taken to evaluate the shape of the powder particles and EDX was used to evaluate composition and mixing of blended powder. The composition measured with EDX is more surface sensitive, less accurate with light weight elements, and with less sampled material than the techniques used to determine the compositions presented in Table 3, therefore not as authoritative. The EDX measures a higher oxygen content, as the powder will have surface oxides. EDX mapping was used to show the location of elements within the powder. X-ray spectrums and calculated composition of each material is also presented.

SEM images show that the powder particles are very similar, of irregular shape, often elongated with few satellites and no fine powder particles. The EDX maps of AA6061 and AlSi10Mg show reasonable consistency of elements throughout the particles. The silicon map of the blended material shows the differentiation of AlSi10Mg, which has higher silicon content, and AA6061. The oxygen maps show concentrations of oxygen at the edges of the powders. This is because the oxygen is on the surface of the material and the angle of incidence will affect the ratio of x-rays produced from the surface oxides to those from the bulk material.

The similarities in powder shape and size is important for mixing as it is an indicator that the powders should not separate through vibration as can occur during use, e.g. while within the powder hopper during wiping process. The EDX showed satisfactory distribution of AlSi10Mg particles within the AA6061 powder. The calculated change in silicon content was below what was expected but this could be from inaccuracies of EDX measurement, as mentioned above.

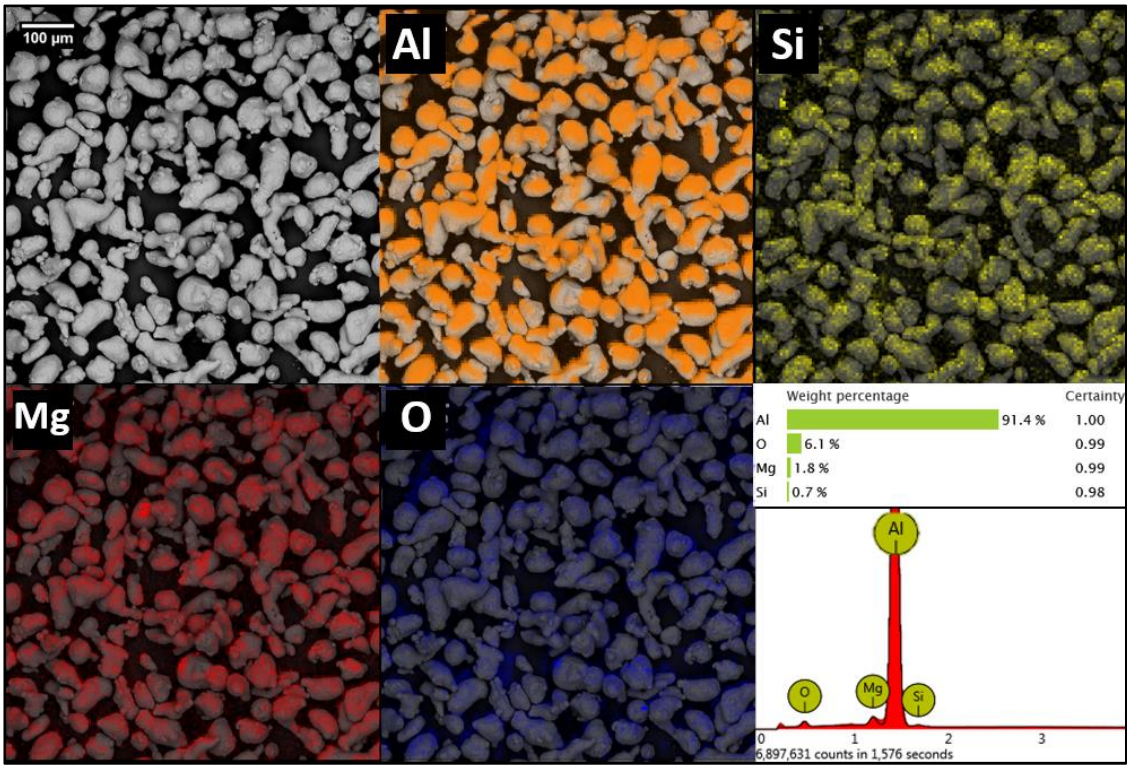

Figure 101 SEM and EDX results from AA6061 powder. The images, in reading order from top left, are the SE image of powder, EDX elemental maps for aluminium, silicon, magnesium and oxygen, and, bottom right, quantified presence of these elements and energy spectrum

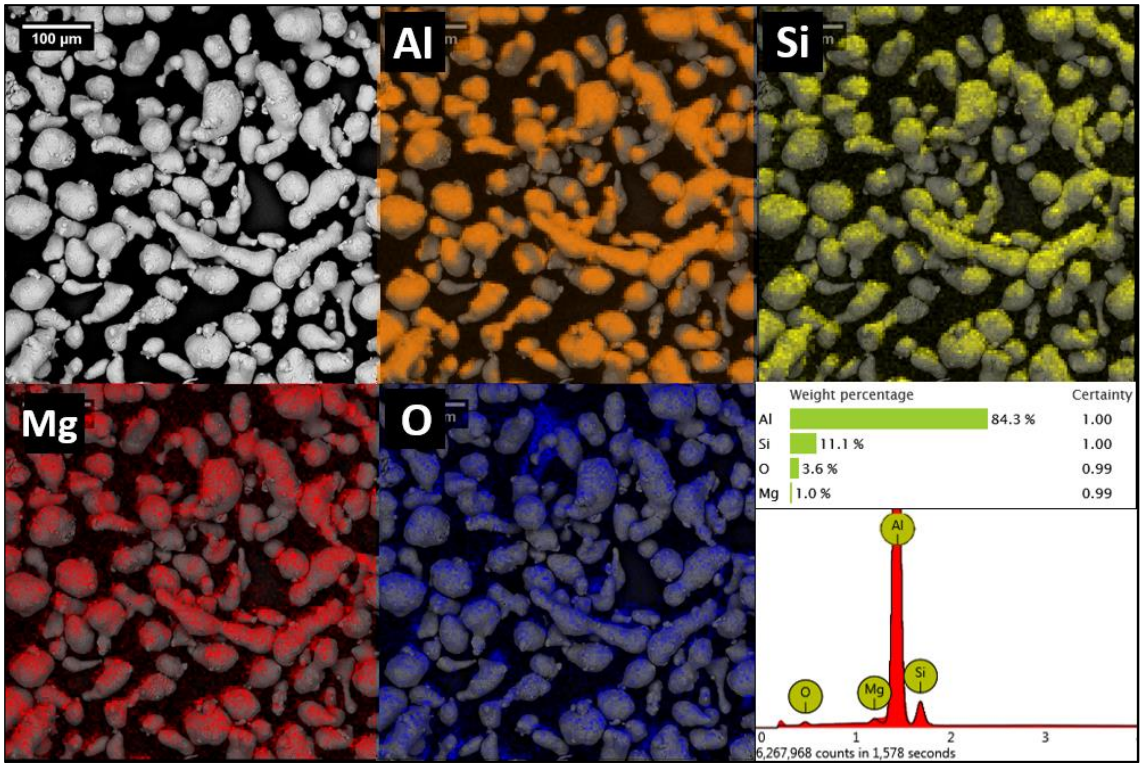

Figure 102 SEM and EDX results from AlSi10Mg powder. The images, in reading order from top left, are the SE image of powder, EDX elemental maps for aluminium, silicon, magnesium and oxygen, and, bottom right, quantified presence of these elements and energy spectrum

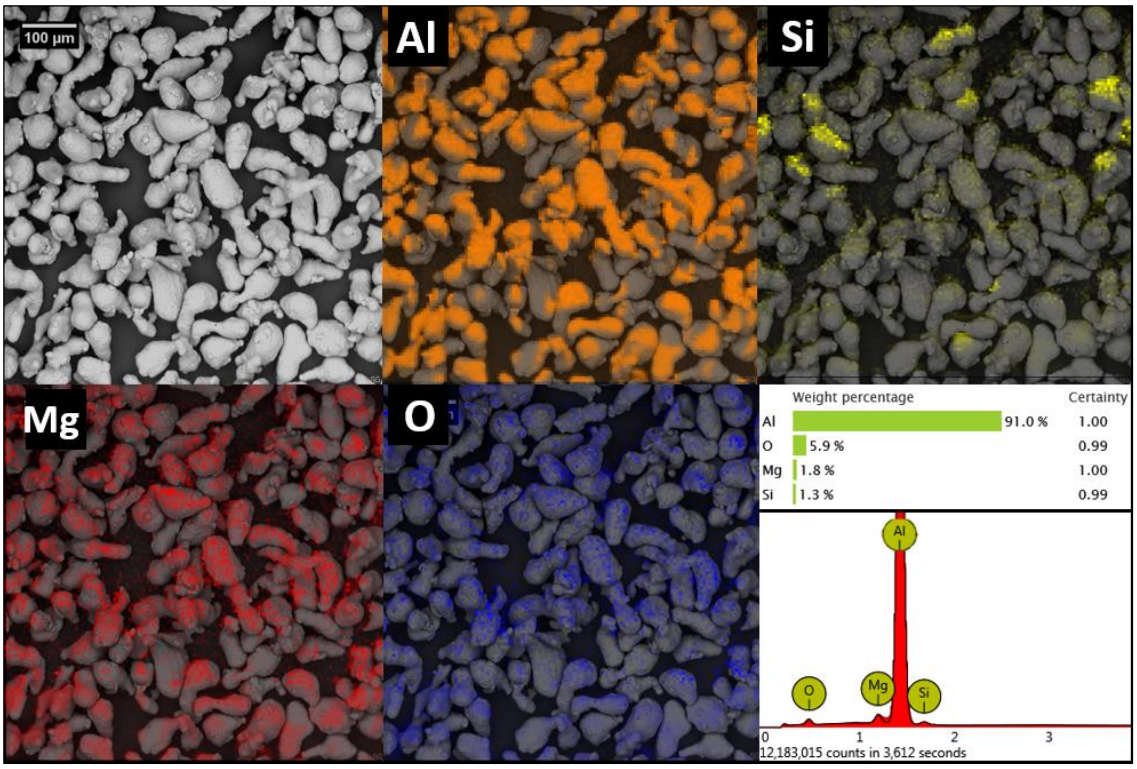

Figure 103 SEM and EDX results from blended powder. The images, in reading order from top left, are the SE image of powder, EDX elemental maps for aluminium, silicon, magnesium and oxygen, and, bottom right, quantified presence of these elements and energy spectrum

3.6.2 Powder Particle Size Analysis

Powder particle size was measured using LSD, these results are shown in Table 4 and Figure 104. The powders are similar in size, with AA6061 having a larger mean size and narrower distribution. The blended powder resulted in a narrower size distribution and a D50 higher than either of its constituent parts. This is not the predicted change in distribution from adding the smaller and wider-ranging AlSi10Mg to AA6061. Combining the distributions, weighted to the ratio of the blend, would result in a D10 of 34.1 µm, D50 of 53.4 µm, and D90 of 83.0 µm. Two possibilities for this discrepancy could be that the samples used do not truly represent powder populations or that the blended powder is not truly made up of powders as represented in the size distributions. To get representative samples the powder containers were stirred and the samples were made up from three separate locations. The same care was not taken to blend the powders. Larger powder particles are known to rise as the powder vibrates. The powder from both were likely taken from the topmost powder in their respective containers. It is possible that this powder was larger than the average and not represented by the LSD results. The differences between the sizes of the powders is small and not expected to have a significant influence on processability.

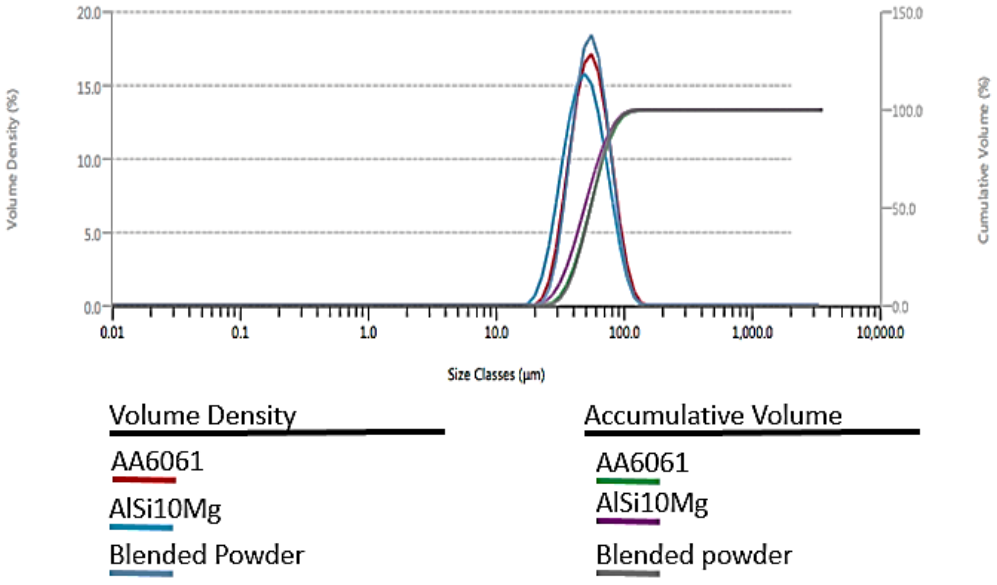

Figure 104 Powder size distributions AA6061, AlSi10Mg and blended powder as recorded through laser size diffraction

Table 4 Size of AA6061, AlSi10Mg and blended powder as recorded through laser size diffraction (µm)

	D10	*D50*	*D90*
AA6061	34.7 ± 1.1	53.8 ± 1.3	83.3 ± 1.6
AlS10Mg	30.2 ± 0.3	48.6 ± 0.2	78.0 ± 0.3
Blend	35.9 ± 0.6	54.0 ± 0.7	81.3 ± 0.8

3.6.3 Powder Flowability

Several methods exist to measure powder flowability, including the Hall flow test, carney funnel, Hausner ratio with tap density test and angle of repose [280]. A method of measuring the angle of repose includes the use of a Hele-Shaw cell to give a planar view of the angle of repose [281]. The angle of repose, in accordance with standards [282], is measured by pouring a powder into a conical pile and measuring the radius and height, which can be tricky without disturbing the pile. With the Hele-Shaw cell the base and height are easily measured.

With a need to measure the flowability of the powders and without immediate access to equipment a modified Hele-Shaw cell was designed and build from three laser cut pieces of acrylic adhered with chloroform (Figure 105). The cell also had a base that could be levelled with adjustable feet. The design included a platform of known length hence only the height needed to be measured.

Figure 105 Angle of repose cell, CAD model of cell (left) and the cell being used to measure the flowability of AA6061 powder (right)

Table 5 shows the results from the flowability of the three powders. The angle of repose is higher for aluminium than most other powders used in SLM, for reasons mentioned in section 2.2 but no flowability problems were observed during processing. The blended powder had a marginally lower flowability than AA6061 or AlSi10Mg. The trend in flowability matches the trend in powder sizes (Table 4) with the smaller powder having higher flowability.

Table 5 Flowability of aluminium powders measured by angle of repose

	AA6061	*AlSi10Mg*	*Blended Powder*
Angle of repose (°)	33.2 ±0.2	32.0 ±0.8	34.7 ±0.5

3.6.4 Powder Actual and Apparent Density

Attempts were made at measuring the actual density of the powder material through pycnometry, as described in section 3.8.3 (Table 6). It was expected that the density of the powder material would be equal to the theoretical ideal density of the SLM samples. Values for the density of AA6061 and AlSi10M are recorded in literature [72] and are presented in Table 6 as the expected ideal density of the SLM samples. The pycnometer measurement for AA6061 is near the value from literature, but the measurement for AlSi10Mg is significantly below the expected ideal density. Density measurement of AlSi10Mg samples built through SLM were found to be in accordance with the value from literature and not the measured pycnometry density. This could have been caused by internal porosity within the powder.

The density of the blended powder, measured by the pycnometer, was near that of a weighted average of the two powders, 2.6891 gcm^{-3}, which is expected. However, as

with AlSi10Mg samples, the density of samples produced through SLM was higher than this measured density. An expected density was calculated through the weighted average of the density of the two constituent materials. This density is also below the highest density that was recorded for the blended samples, which was measured through the Archimedes method as 2.7139 ± 0.0065 gcm^{-3}.

Apparent density was measured using a hall flow funnel and density cup according to ASTM B212-99 [283]. The relative density of AA6061 is 55.6%, which is higher than that of the AlSi10Mg which is 49.4% of the pycnometric density.

Table 6 Density measurements of aluminium powders (gcm^{-3})

	AA6061	*AlSi10Mg*	*Blend*
Expected Ideal Density	2.70	2.67	2.693[ŧ]
Pycnometer Density	2.6955 ± 0.0010	2.6319 ± 0.0021	2.6855 ± 0.0012
Apparent Density	1.5 ± 0.1	1.3 ± 0.0	1.4 ± 0.1

[ŧ]*Calculated as a weighted average of AA6061 and AlSi10Mg density*

3.7 Design of Experiments for Optimising Density

To appreciate the behaviour of materials processed through SLM it is important that the samples have an adequate density, of 99.5% or higher [178]. Design of experiments (DOE) was used for best practice at finding appropriate processing parameters. DOE is a systematic approach to experimentation for solving engineering and scientific problems. The underlying principals are to improved efficiency in data gathering and analysis over 'one variable at a time' methods by reducing the number of experiments required to generate sufficient data. Central Composite Design (CCD) was utilised as the most appropriate method to attain optimised process parameters [207], [284]. The following details the steps involved in performing this analysis.

The factorial design is the first issue that has to be planned, which considers the number of factors (i.e. variables to be scrutinized) at a given number of levels (a level is the number of values attributed to the factor being scrutinised). The number of tests/samples needed to complete the factorial is N^k, where k is the number of factors and N is the number of levels. Five factors were considered for affecting the density of built parts; laser power, exposure time, point distance, hatch distance and lens position. The number of levels should reflect the possible order of the response and requires a minimum of three for non-linear responses. Five levels were scrutinized, which would require 3125 samples for a full factorial study. A one factor at a time approach reduces the number of samples to 25 by testing each of the five factors without changing the others. This is not appropriate for SLM process parameters optimisation as the factors have a high amount of interdependence.

A Central Composition Design (CCD) is the most commonly used design for fitting second order models. The CCD consists of a 2^k factorial, 2k axial or 'star' points and n_c centre-points (where n_c is the number of repeated trials at the centre of the design), which gives five levels of each factor. For a three-factor experiment the CCD has 14 samples plus n_c centre points (as see in nodes of Figure 106). Density optimisation experiments used four-factor and five-factor CCD DOE with 6 repeated centre points, which required 30 samples and 54 samples respectively, which are not easily represented with 3D images.

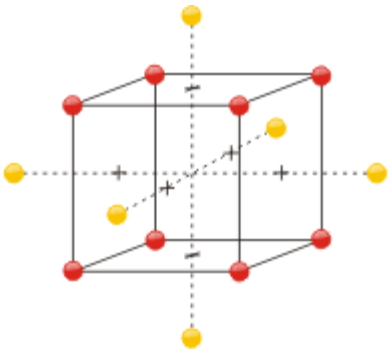

Figure 106 A three factor central composition design, with 2^3 factorial array in red, 2x3 axial or "star" point in yellow, and n_c, centre points in white

To visualise the factorial responses, Response Surface Methodology (RSM) was used, where the data generated is fit to an empirical model and is an estimate of the true factorial influence. An example of a response surface of a two factor study is shown in Figure 107. This representation is more difficult with greater than three factors. The representation available with software used in this study allowed cross sections of the response surface for each factor to be viewed with fixing the values of the other factors, e.g. in the example of Figure 107, the response curve of pressure could be viewed with setting temperature at a fixed value and vice versa.

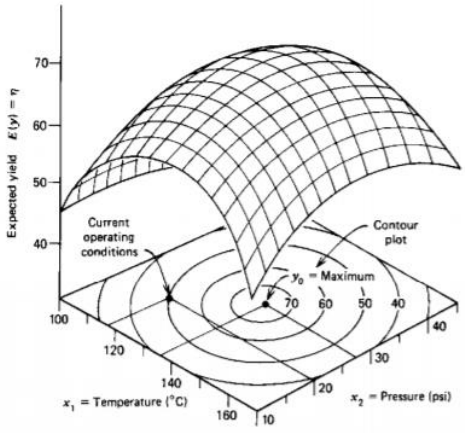

Figure 107 Example of a response surface from a two-factor study showing the interdependence of two key variables, temperature and pressure, on a result [179].

RSM factorial experiments can be used to find an optimum within a "region of operability" should the region contain an optimum, though the exactness of the result

could be compromised by the wide range between levels. Another approach is to examine a 'region of interest', which might not contain the optimum parameters but could direct the study to further regions of interest nearer the optimum parameters. This approach uses CCD as an appropriate design to model the input influence with the response surface. Minitab 16 (Minitab Inc, USA) was used to generate the appropriate tested parameter value and to perform the data interpretation to create the RSM graphs.

3.8 Density Measurement Methods

Three methods of quantifying part density were considered; pycnometry, Archimedes method and micrographic density. Archimedes and micrographic are the two most frequently cited methods for measuring density of SLM parts, with comparisons made in literature, it is known that they can give very different results [285]. In this thesis, the Archimedes method was used for measuring the density of all samples, with micrographic density only used for a selection of the highest densities from each build and the reasoning is presented here.

Alternative methods for measuring part density are available and one of these, pycnometry was considered. The principles of pycnometry are very similar to that used in the Archimedes method, as will be discussed below, but has the potential for higher accuracy. A comparison between sample density measurements made with the different methods was performed to contribute to the selection of the methodology and are presented here. The advantages and disadvantages of each method are discussed.

3.8.1 Archimedes

The Archimedes method for measuring gravimetric density was performed in accordance with ASTM B311 – 17 (Density of Powder Metallurgy (PM) Materials Containing Less Than Two Percent Porosity). The method is based on the principle that a body suspended in liquid experiences a reactionary force equal to the weight of liquid displaced. When the body is completely submerged then the volume of liquid displaced is equal to the volume of the body. The difference between the weight of the body in air and suspended in liquid is called the buoyancy force and equals the weight of the displaced liquid (Equation 9). This derives the equation which is used to calculate the density of the body.

$$M_{water} = M_{buoyancy} = M_{body} - M_{submerge}$$

Equation 9

$$\rho_{body} = \rho_{water} \cdot \frac{M_{body}}{M_{body} - M_{submerge}}$$

Equation 10

Where M_{water} and ρ_{water} are the mass and density of the displaced water, M_{body} and ρ_{body} are the mass and density of the specimen being measured and $M_{submerged}$ is the weight of the specimen while submerged in water.

The apparatus was set up in accordance with ASTM B311-17, as see in Figure 108. Distilled water was used as the reference liquid. An analytical balance was used, with precision of 0.0001 g. A nichrome wire, with diameter of 0.1 mm, was used to hold the specimens. The specimens were 8 mm *x* 8 mm blocks with 17 mm height, however, builds often did not reach this height and were stopped early. This is reflected in the errors calculated for each specimen. The blocks were built with a support structure comprising four trapezoidal feet for ease of building and removal from the build plate. Before measuring the sample density, the samples were cleaned to remove all loose surface powder using ultrasonic baths, run at room temperature for 60 minutes.

Figure 108 Analytical balance measuring the weight of a sample in water

To calculate the error of the density, the error from the readings were recorded and the propagation of errors for Equation 10 was calculated in Equation 19. The derivation of this equation was based on equations for error propagation from NIST/SEMATECH [286]. The propagation of error from an equation in the form of Equation 11 is shown in Equation 12, and the error for Equation 13 is shown in

Equation 14, where B and C are theoretical inputs to calculate A and δB, δC and δA are the errors associated with these values.

$$A = B + C$$

Equation 11

$$\delta A = \sqrt{\delta B^2 + \delta C^2}$$

Equation 12

$$A = B.C$$

Equation 13

$$\delta A = A\sqrt{\frac{\delta B^2}{B^2} + \frac{\delta C^2}{C^2}}$$

Equation 14

The equation to calculate the Archimedes density from the mass of a body in water and in air is shown in Equation 10. This equation can be written in the form of Equation 15 to simplify the error propagation to Equation 16, with factors altered to the form of Equation 17. The error of these factors can be calculated as in Equation 18 which combine to form Equation 19.

$$\rho_{body} = A.B/C$$

Equation 15

$$\delta\rho_{body} = \rho_{body}.\sqrt{\frac{\delta A^2}{A^2} + \frac{\delta B^2}{B^2} + \frac{\delta C^2}{C^2}}$$

Equation 16

$$A = \rho_{water}$$

$$B = M_{body}$$

$$C = M_{body} - M_{submerge}$$

Equation 17

$$\delta A = \delta\rho_{water}$$

$$\delta B = \delta M_{body}$$

$$\delta C = \sqrt{\delta M_{body}{}^2 + \delta M_{submerged}{}^2}$$

Equation 18

$$\delta\rho_{body} = \rho_{body} \cdot \sqrt{\frac{\delta\rho_{water}{}^2}{\rho_{water}{}^2} + \frac{\delta M_{body}{}^2}{M_{body}{}^2} + \frac{\delta M_{body}{}^2 + \delta M_{submerged}{}^2}{(M_{body} - M_{submerge})^2}}$$

Equation 19

Advantages and Disadvantages of Archimedes Method

The Archimedes method is a non-destructive method of measuring the absolute density of samples built through SLM and is the most time and resource efficient way of obtaining sample densities that was considered for this project.

The Archimedes method is considered highly accurate and has been compared favourably in literature to micrographic density [287]. Even with light samples, of 1 g, the contribution of errors generated from the scales is very low. The readings can be wrong where surface roughness prevents wetting the surfaces of the samples or where the water can infiltrate the surfaces. This can be indicated by the appearance of bubbles on the surface as the sample is submerged or where bubbles grow as air leaves cavities of the sample. With the former issue, shaking the submerged samples releases the surface bubbles allowing the wetting of the sample to improve. The latter problem highlights a failure in the methodology. A similar standard, ASTM B962 – 17, exists for PM parts with greater porosity which requires immersing the samples in oil to prevent water infiltrating the samples, this was not considered necessary as pores are less likely to appear near the surface of SLM samples as was empirically evident during the project, except where samples had very high levels of porosity (>10%). Where very high levels of porosity occur, there is also a risk of internal trapped but loose powder, which should not contribute to the density of the sample.

Water has high surface tension, which causes meniscus to appear at the beaker and at the wire, which causes a small error. To avoid this, many researchers use ethanol or acetone as the reference fluid.

The density of water is another source of error in the experiments, as it varies with temperature. In this work the temperature of the room is recorded but not the temperature of the water. It can be expected that water temperature is stable during recording the results of each set of experiments but variations in temperature are more extreme with seasonal changes, which has potential implications in direct comparison of results. If the density of the water is recorded incorrectly, it will introduce a bias error, which compromises absolute results but does not affect the observed trends.

With the aim of minimising porosity, the important measure is not absolute density but relative density. This can only be done with the Archimedes method where the ideal density is known. This value is known for AA6061 and AlSi10Mg but not for the blended material. An attempt was made to measure the ideal density by measuring

the density of the powder but the Archimedes density of the blended material SLM samples regularly recorded values higher than this.

For the reasons highlighted with errors from water density measurements and knowing the ideal density of the materials, the Archimedes method was used to measure the trend of densities from each build, while micrographic densities were used to evaluate the relative densities, which is only required of the highest density samples.

3.8.2 Micrographic Density

Micrographic density is a method where micrographs of cross sectioned parts are analysed to calculate the proportion of area that is regarded as a defect. Cross sectioning parts is useful for analysing the microstructure of the sample and the nature of defects. These qualitative advantages of cross sectioning have contributed to the popularity of the micrographic density despite the method being compared unfavourably to the Archimedes method [287].

In this project cross sections were produced by grinding and polishing mounted samples, to a 40 nm finish, using silicon carbide paper, diamond polished cloth discs and colloidal silica cloth. The parts need to be suitably polished to show the defects as they can be hidden from smearing caused by cutting or grinding. The 40 nm surface finish was needed to identify the fine cracks that were otherwise hidden. With the equipment available for this project this process taken 3 hours per sample. Where possible samples were sectioned using an IsoMet 4000 (Buehlar, USA) to allow both the vertical and horizontal cross sections to be analysed.

Optical images of the cross sections were taken using the axioplan 2 or with the optical camera within the Hitachi TM4000Plus. SEM images were taken with the Hitachi TM4000Plus, but it was apparent that different imaging techniques resulted in differing results, as seen in Figure 111.

To differentiate pores and solid, the image is converted to a greyscale bitmap and a threshold is applied with darker pixels identified as pores. The level of thresholding is not always obvious, as gradients of pixel darkness exist at the edge of pores. Uneven illumination of the surface causes inconsistencies with identifying a threshold across a sample, this was particularly evident with thin cracks that are not as dark as pores and more susceptible to local conditions. To correct for this a localised threshold was applied. To perform this correctly a local background value was needed. All the localised threshold generators that are available on imageJ do not discount the pores when calculating the background shade. A python script was written that could first differentiate large pores from bulk material and then use localised threshold that could identify cracks.

Large pores can be differentiated by examining the image histogram. Typically, two peaks are observed. The brighter of these being the mode shade of bulk material. The second peak is the mode shade of the pores and is usually near or at zero. A threshold can be made between these two peaks. It was decided that the value of this threshold would be at the lowest frequency of shades between these two peaks. The reasoning for this is that the frequency of shades of the materials will fit a normal distribution and continue decreasing until the normal distribution of shades of pores appear.

The next step is to use localised linear regression to calculate an expected value for each pixel and if the pixel was darker than the expected value by a selected local threshold, then it was regarded as a defect. By identifying pores beforehand, they can be discounted from estimating the background values. The inconsistency in lighting which causes the problem with global thresholding is radial, and so the image is sectioned into different areas where they can be interpreted as linear.

Figure 109 and Figure 110 show how the program identifies defects in two different samples and why the two-step process was necessary for the highly cracked samples. In the images below the porosity identified through the histogram are coloured white while those identified with localised linear regression are coloured black. Figure 109 shows a sample with large pores and cracks that are mostly identified with the general thresholding from the histogram. A similar histogram is apparent with Figure 110 but little of the porosity is identified with the global threshold and most is identified with the local thresholding.

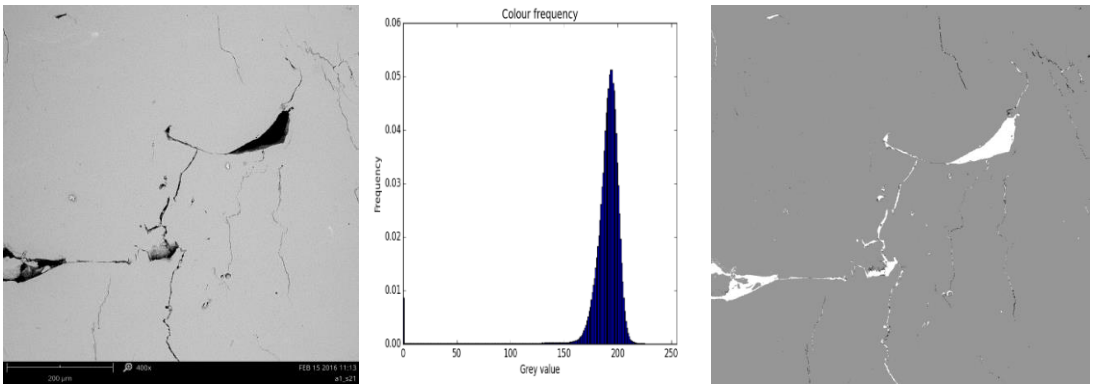

Figure 109 Example of cross-sectional density analysis. Bulk density = 97.69%, Porosity identified by histogram = 1.98% and defects detected by localised linear regression = 0.33%

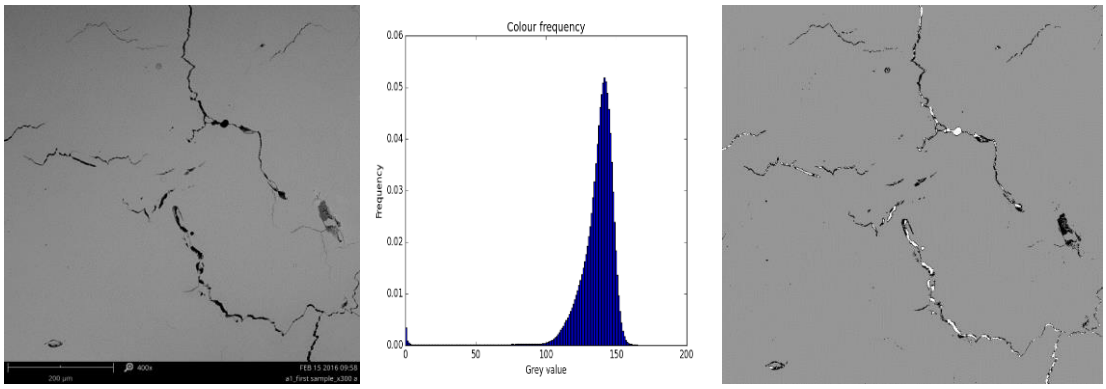

Figure 110 Second example of cross-sectional density analysis. Bulk density = 98.2%, Porosity identified by histogram = 0.55% and defects detected by localised linear regression = 1.25%

Advantages and disadvantages of Micrographic Density in Comparison with Archimedes Density

Figure 111 shows a comparison between Archimedes density results and micrographic densities recorded using OM and SEM images from vertical and horizontal cross sections. The main finding from these results is the lack of agreement between results.

The difference in results from the cross sections being imaged by optical microscopy or SEM highlights the influence that imaging has on the results. In general, the densities calculated from the optical microscopy (OM) images suggested a lower density than that calculated from the SEM images. This could be from reduced resolution around cracks and pores. Cracks appear thicker in OM images and this discrepancy may also occur with pores. This error will always be present with the discretisation of the images into pixels.

A major disadvantage of this micrographic density method is that it relies on the image cross section being representative of the bulk. Typically, only a single cross section is viewed, as grinding and polishing are resource consuming. With the samples measured in Figure 111, samples are measured in both the horizontal and vertical cross sections and there is a significant difference between the two cross sections for many samples. Using the two surfaces will increase the accuracy but it is not known how many cross sections would be required to appropriately represent the sample.

The sampling error is caused by the non-uniform distribution of defects, an example of which is gas porosity that can appear near the base of parts where moisture within the build chamber that cannot be removed through purging gets consumed through reaction with the metal, or fusion pores can appear between layers or near the boundary scan. It has been observed that the greater the number of pores, the less accurate this method becomes [287].

The Archimedes method and the micrographic method both add information to understanding the samples but do not validate each other. Sample A1 21 and A1 10

have very high Archimedes densities and low micrographic densities. During the analysis of the samples in section 4.1 it was determined that sample A1 21 was likely to have a low density that allowed the infiltration of water causing an error in the Archimedes density, while the Archimedes density sample A1 10 was consistent with parts with matching or similar parameters and therefore the micrographic density was in error. As discussed above, Archimedes densities are likely to have errors where the part densities are very low, and it was decided that the best approach to spot these errors was to also consider both the micrographic density and the trend with energy density. The lack of agreement between the horizontal and vertical cross sections show the potential risk of large sampling errors with the micrographic method and therefore the trends and analysis to achieve optimum density are more reliable with the Archimedes method. Cross sections are valuable for qualitative analysis of the samples and it is worth calculating the micrographic density of samples that are produced, it was decided that the highest density samples should be cross sectioned and polished, whereby the defects are analysed and micrographic density can be calculated.

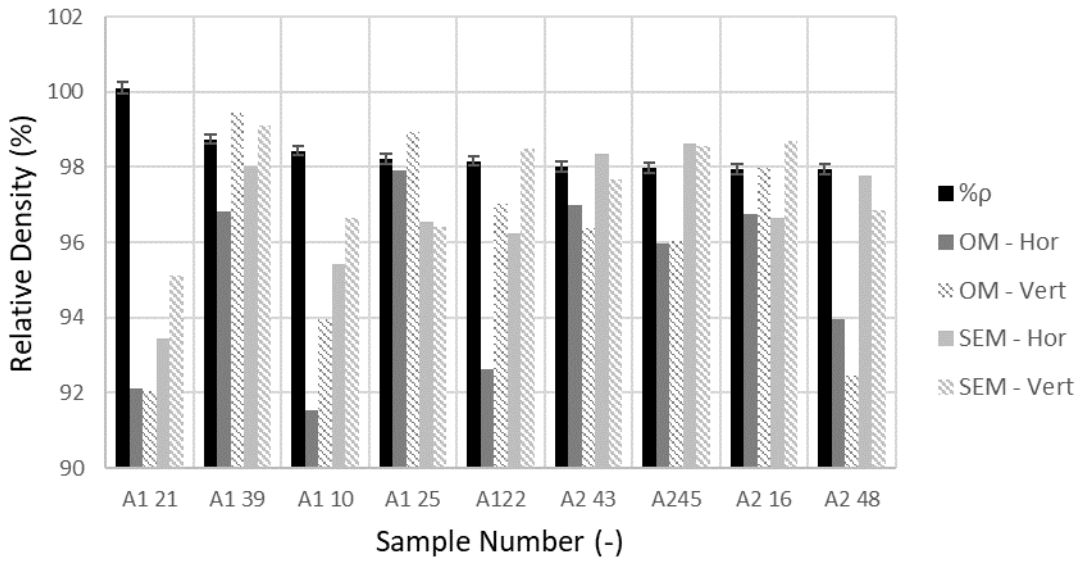

Figure 111 Comparison of Archimedes density with micrographic densities of horizontal and vertical cross sections, imaged by both optical (OM) and scanning electron microscopy (SEM)

3.8.3 Pycnometer

A micromeritics' AccuPyc II 1340 pynometer was used to measure the density of powder and SLM samples. The principles of pycnometry are based on Boyle's law where the volume and pressure of an ideal gas are inversely proportional. The AccuPyc II is a constant volume pycnometry, whereby the change in pressure that results from a known change in volume can be used to calculate the volume of the specimen inside the chamber. This can be expressed as:

$$\frac{P_1}{P_2} = \frac{V_1 + V_c}{V_1}$$

Equation 20

Where P_1 and V_1 are the pressure and volume of the initial condition, V_c is the change in volume and P_2 resultant pressure.

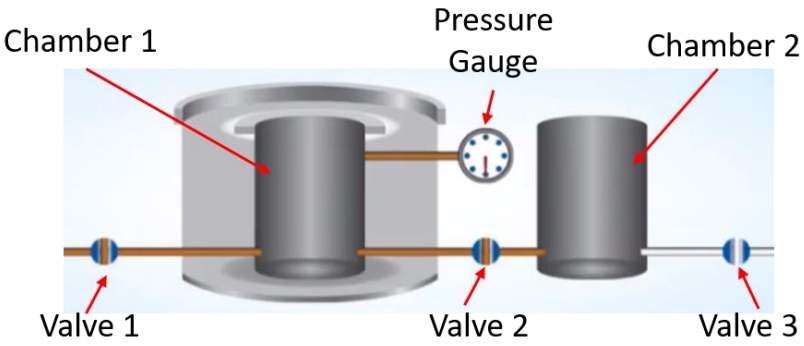

Figure 112 Schematic of gas pycnometry [288]

The pycnometer has two chambers with three valves to isolate them (Figure 112). The first chamber contains the specimen and the second is only to cause a known change in vloume. The first step is opening valve 1 and pressurising the first chamber, while it remains isolated from the second. When the first chamber reaches a set pressure valve 1 closes, so the mass of gas remains constant before valve 2 opens. The increase in volume results in a drop in pressure. This pressure is recorded before valve 3 opens to evacuate the gas. This method can be used to calculate the volume of the first chamber when empty and when a specimen is loaded. The equation to calculate the volume of the specimen is presented as:

$$V_{specimen} = V_{chamber\ 1} - V_{chamber\ 2} \cdot \frac{P_2}{P_1 - P_2}$$

Equation 21

Where $V_{specimen}$ is the volume of the specimen, $V_{chamber1}$ and $V_{chamber2}$ are the volumes of the two chambers, P_1 is the initial pressure of chamber 1, and P_2 is the final pressure of both chambers.

The AccuPyc II takes the mass of the specimen as an input and presents the result as a density value. The test is run ten times and the mean value and standard deviation are calculated. Helium gas is used as it behaves similar to that of an ideal gas. Helium can permeate metals, primarily along grain boundaries, but at a slow rate and so internal pores can contribute to the specimen volume. The big advantage of this method over the Archimedes method is that there is no issue with surface wettability nor errors arising from surface tension from the water such as a meniscus forming at the wire or at the beaker.

3.8.4 Comparison of Archimedes v Pycnometry

Twenty-six AA6061 samples produced through SLM with different porosities were measured with both Achimedes and pycnometry (Figure 113). The results of the pycnometry were always higher than the Archimedes densities and near the ideal density. The lowest density recorded by pycnometry was 2.655 gcm^{-3}, 98.33% of the ideal density.

Neither method attempted to fill pores accessible through the surface, as the pores were expected to be internal. From viewing all the cross sections across this project this did seem to be a reasonable assumption except possibly for the fine cracks. The cracks may reach the surface and provide a network connecting internal pores which the helium could permeate, but water could not. This would explain the near perfect density calculated from pycnometry.

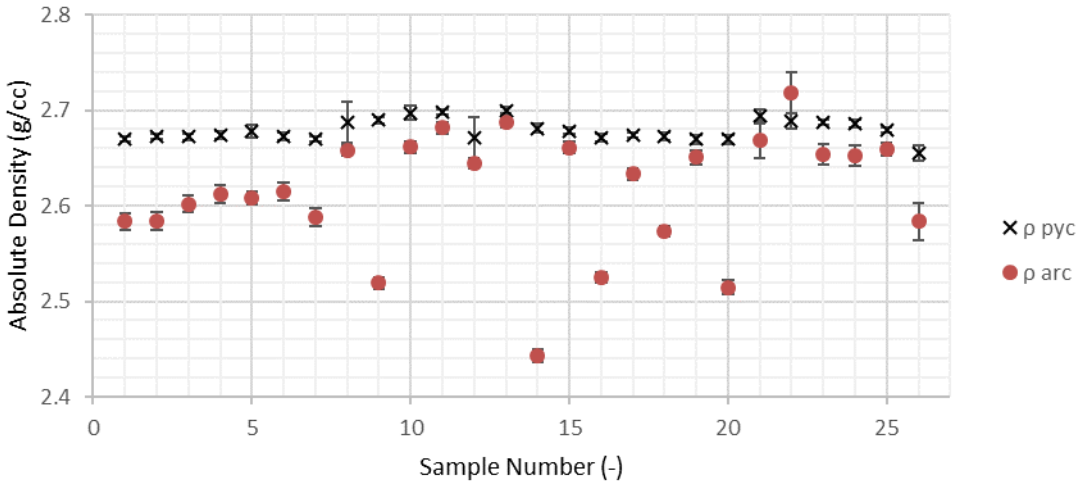

Figure 113 comparison of density measurements through Archimedes (ρ arc) compared with pycnometry (ρ pyc)

3.9 Etchants

To look at the effects of solidification on grain growth and identify weld track boundaries the materials were chemically etched with 1% NaOH solution for 30s. Figure 114 shows powder particles that were etched during the optimisation of the etching conditions.

Deep etching was also performed to view the oxides within SLM samples through removal of aluminium. The deep etching conditions were to submerge the samples in 40% NaOH for 12 hours, in accordance with work by Louvis et al., [161].

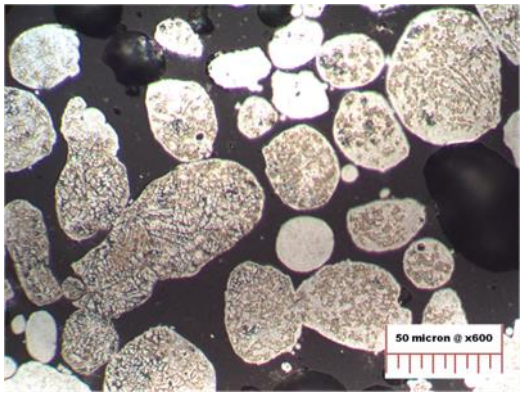

Figure 114 ALSi12 powder samples etched with 1%NaOH

3.10 Summary

In this section the materials and methods used to complete the work detailed in thesis are considered. All material samples produced by SLM were built with the Realizer SLM 100 apart from where stated in section 5.4.3, where samples built on the Renishaw AM125 were examined for oxygen content. In chapter 4, process parameter tests were performed to improve the density of samples, in order to achieve densities above 99.5%. The process parameters that are used to improve the densities of samples were characterised and these informed the resolution and limits of the input parameters. The design of experiments and the method of measuring the densities have also been detailed in this section. A comparative study was made between the three methods of measuring part density; Archimedes method, micrographic and pycnometry. The conclusion from this analysis was that all three methods had flaws relating to the intended use in this project, but the Archimedes method was the most appropriate for measuring each sample. Micrographs should be captured for cross sections of the highest density samples in order to assess the defects that remain in the samples and alongside these the micrographic densities can be measured.

In chapter 5, the microstructure of the three materials is characterised by optical microscopy and SEM analysis, using SEI, ECCI, EBSD and EDX as described in this chapter.

4 Processing Al-Si-Mg Alloys in SLM

In this section, the processability of AA6061, AlSi10Mg and a blended powder mixture were examined. A surface response design of experiments was utilised to identify process parameters for optimised part density, as described in section 3.8.

AA6061 is an alloy selected in this project as having desirable characteristics for light weight structural applications, however, AA6061 parts processed through SLM can be compromised by cracking [81]. This chapter details the tests conducted to improving densities in order to achieve sufficient density, i.e. 99.5% dense. A sequence of tests was attempted until it was not expected that the results could be improved. The results of these tests and the reasoning of the iterations are presented here.

In an attempt to reduce the level of cracking in AA6061, tests were performed using reduced layer thickness and double scanning of each layer. The results from these tests are presented in 4.2 and 4.3. The tests showed that cracking was abundant in all AA6061 samples and no building strategies were deemed to the have the potential for the desired processability.

The proposed solution in this project was to modify the material to improve processability while maintaining the benefits to light weight structural applications. The new material was created from a blended mixture of AA6061 and AlSI10Mg and analysis was done to ensure the homogeneity of the SLM samples. The processability of this material is assessed in this chapter while a comparison of material properties follows in chapter 5.

AlSi10Mg is a readily processable, widely used and much researched alloy in SLM. As a component of the blended material, samples of AlSi10Mg were produced for comparison with the two previously mentioned alloys. The different materials required bespoke parameters to be developed for each and the tests to improve part density are evaluated.

4.1 SLM of AA6061 at 50 µm Layer Thickness

The parameters from a previous study, external and prior to commencing this project [112], were used as a starting point as it was known that built samples would have sufficient density to be measured in the Archimedes method. 50 µm layer thickness was selected as a reasonable layer thickness. Micrographs of cross sectioned samples with highest density (measured using Archimedes method) were produced. These micrographs were used to evaluate the types of defects as well as measuring the cross-sectional density for comparison to Archimedes results.

4.1.1 Test A1: AA6061, 50 µm Layer Thickness CCD DOE

The ranges of values for this first experiment using the DoE were derived from previous tests, with a range of parameters that would possibly encompass the optimum results. The ranges for each variable are listed in Table 7. The aim of these experiments was to understand how densities change with parameters. The ranges for point distance and hatch distance were chosen to be from 30 µm to 170 µm as this is from near minimum value up to the estimated width of the track. The laser power was expected to give optimum results at the maximum value but was tested here to see if this hypothesis was correct. Laser power range was 120 W to 200 W, in five steps of 20 W. From previous work, the exposure times were tested up to 175 µs, with the increasing exposure times improving part density. A broad range was chosen from 100 µs to 500 µs. With regard to the lens position; previous tests have been performed with lens position at 15.00 mm, while the focus was measured to be near 16.20 mm, neither position was assumed to be optimum. The lens positions tested a range of values centred around 15.00 mm. All lens positions in this test focused the beam below the bed, as discussed in section 3.1.1. The number of samples required for CCD with five factors is 54. 64 samples could fit into the build area, so a further 10 blocks were added with values chosen intuitively on the extremes of those presented in Table 7. The order of samples was randomised, and layout was in an eight by eight array.

Table 7 Range of values for Test A1: AA6061, 50 µm layer thickness CCD

	UNIT	MIN	MEAN	MAX
POINT DISTANCE	µm	30	100	170
EXPOSURE	µs	100	300	500
POWER	W	120	160	200
HATCH DISTANCE	mm	0.030	0.100	0.170
LENS POSITION	mm	14.50	15.00	15.50

Sample density was measured using the Archimedes method. Ten samples failed to build due to an unknown hatching fault. The relative density is plotted against energy density (Figure 115). The trend fits the expectations of a logarithmic relationship between energy density and the part density [193]. However, there is a lot of scatter from this trend which obscures where a theoretical sufficient energy density could be. It can be inferred by Figure 115 that the energy density of most samples was below an expected optimum and all measured densities (barring the highlighted outlier) were below the target value of 99.5%. Energy density does not give a complete measure of how the inputs effect the sample but is useful here as it indicates that improved results could be based on increasing the energy input into samples.

One sample, noted on the graph, stands out as an outlier from the general trend. As mentioned in the section 3.8, the choice of methodology of Archimedes was based on the assumption that densities would be sufficiently high that internal pores could not be infiltrated. Based on the parameters of this sample, it would be expected to have one of the lowest densities, so it is likely that the density was too low for this methodology to be effective. This sort of failure from Archimedes is noticed through comparison with the sample micrographs and energy density analysis. This supports the assertion that the highest measured Archimedes densities should be evaluated by micrographic density also, though this sort of error has not been seen in any other sample throughout the rest of the project. The density measured by Archimedes was higher than the expected 100%, which is possible due to overestimating the density of the liquid, as reasoned in section 3.8.

The surface response, calculated through MINITAB, is presented in Figure 116. As explained in section 3.7, the cross sections of the surface response are presented at one parameter set, selected as the interpolated highest density, due to the complexity of the results. The trends of point distance and exposure both suggest the highest density occurs at the extremes of values tested, with the highest energy input. As explained in section 3.10, the extremes within the range of each variable, i.e. the maximum and minimum values, are only tested with the other variables at their mean, or central, values. The calculated improvement in density from applying the extremes of both variables is an extrapolation of the empirical data. Both shortening the point distance and extending the exposure time increase the energy input in each scan track, which was seen as having likely improvement from the interpretation of Figure 115. 385 µs was not the longest exposure time in the build set up but parts with exposure time of 500 µs failed to build. The failure was due to a software error and not from building.

The surface response of power was the steepest, while the ratio of change of highest to lowest value tested was lower than exposure, point distance or hatch distance. This implies that the results have the greatest sensitivity to reducing the power from the maximum output. Accepting that the optimum density is found with the highest power means the number of factors reduces from five to four. This reduces the number of samples in the CCD analysis from 54 to 30.

The trend in hatch distance does not suggest an extreme value as optimum, rather the optimum is near the centre of the CCD values. The trends shown are dependent on the all the variables as they are local cross sections of a six-dimensional surface. The optimum value of hatch distance changes as the other variables change.

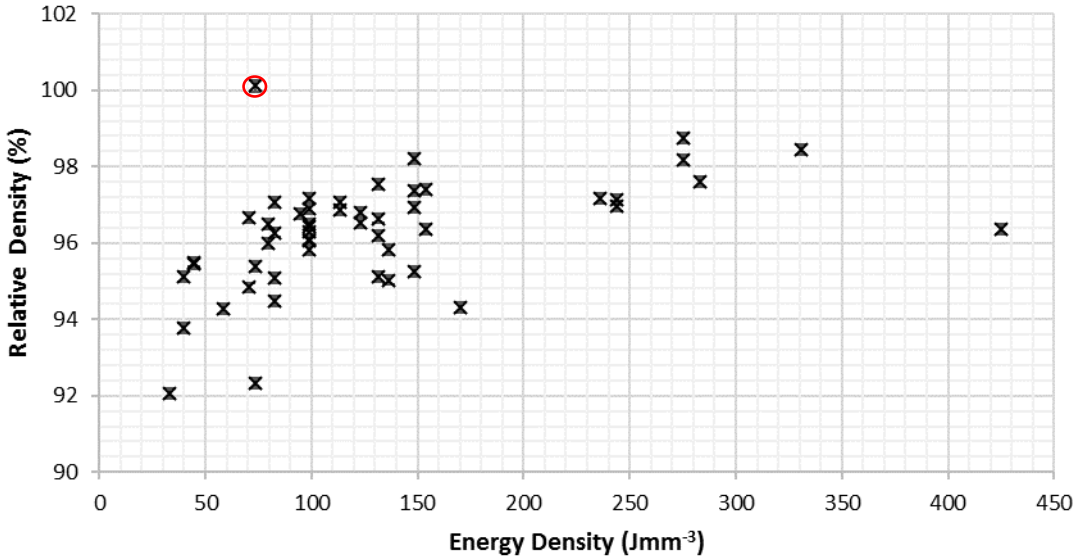

Figure 115 Energy Density vs. Relative Density for test A1: AA6061, 50 µm layer thickness CCD (outlier value is circled)

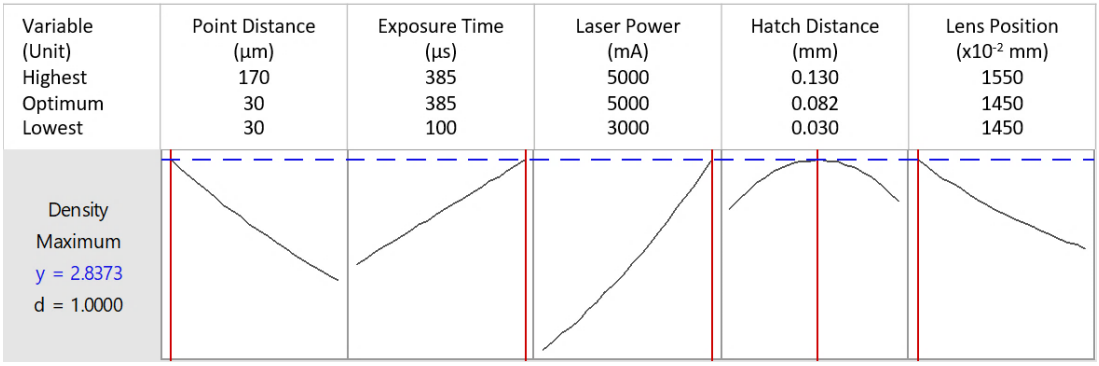

Figure 116 Response surface at the optimum values calculated through MINITAB for test A1: AA6061, 50 µm layer thickness CCD

The five highest densities from test A1 are presented in Table 8, and the cross sections and cross sectional densities are presented in Figure 117. There is often a lack of agreement between densities measured on the different cross sections and with the Archimedes method, as mentioned in 3.8.3.

The highest density recorded with the Archimedes method was sample 21. This sample had unreasonably high density and low volume. From the cross section, Sample 21 has many large pores, which may open the surface to ingress of water. The cross section of sample 10 also shows quite a large amount of porosity, similar to sample 21, and is not in agreement with the Archimedes density. Unlike sample 21, however, the Archimedes density of sample 10 does not appear unusual, the density fits within the trend of energy density and the volume is as expected. Of the other samples, the gravimetric density is in corroboration with the limits of micrographic density. These samples have fewer large pores, and this is especially apparent on the vertical surfaces.

From the results in Table 8, best densities occurred with point distance below mean value, and exposure and power above their mean values and hatch distances near the mean value tested of 0.1 mm. These are all in agreement with the trends seen in the surface response (Figure 116). The lens positions, however, were all at or above the average value which does not agree with the suggested trend from the surface response analysis.

Three types of defect were present: fusion pores, gas pores, and cracking. The presence of fusion pores was most evident in samples 21 and 10 but appear in all samples. These occur as a result of insufficient energy, which supports the reasoning made with regard to the Archimedes densities analysis for test A1, although it should be noted that sample 10 had a relatively high energy input. There is very little evidence of gas porosity in the body of the blocks. It is most noticeably present at the feet of sample 10 and with the raised numbering of sample 22. It is understandable why these would occur here as build is started with an oxygen content between 500 and 100 ppm, which is the limit of what can be achieved through purging the chamber with argon but drops farther below this as the build continues. In this situation, moisture remaining in the chamber is consumed during early processing layers. The case of the raised lettering is the same, as the letters are treated as a new build from the blocks. When the machine stops processing, argon stops flowing, air enters the chamber and oxygen levels rise. The third form of defect is cracking. Cracking appears in all samples. The cause of cracks is discussed in chapter 5. At this stage of the study, it was unclear what the root cause of the cracks is, with accumulated stress, layer of oxides and porosity acting as stress concentrators among the potential causes. One indication of the cause is the different appearance in the samples. The samples with more fusion porosity have wider and more noticeable cracks, but the absence of pores does not lead to the absence of cracks. It is possible the presence of pores promotes the growth of cracks as stress concentration sites or the unbounded material allows for less constraining of material near the cracks, and greater shrinkage.

Table 8 Five highest densities from test A1: AA6061, 50 µm Layer Thickness CCD

#	POINT DISTANCE	EXPO	LASER POWER	HATCH DISTANCE	LENS POSITION	ENERGY DENSITY	$\%\rho_{micro}$	$\%\rho_{arch}$	$\delta\%\rho_{arch}$
	µm	µs	W	mm	mm	J mm^{-3}	%	%	%
21	70	215	164.4	0.130	15.02	73.4	92.08	100.1	0.16
39	70	385	185.6	0.070	15.44	275.4	98.13	98.74	0.13
10	30	300	175.0	0.100	15.23	330.5	92.75	98.44	0.13
25	70	385	185.6	0.130	15.02	148.3	98.43	98.22	0.13
22	70	385	185.6	0.070	15.02	275.4	94.83	98.17	0.13

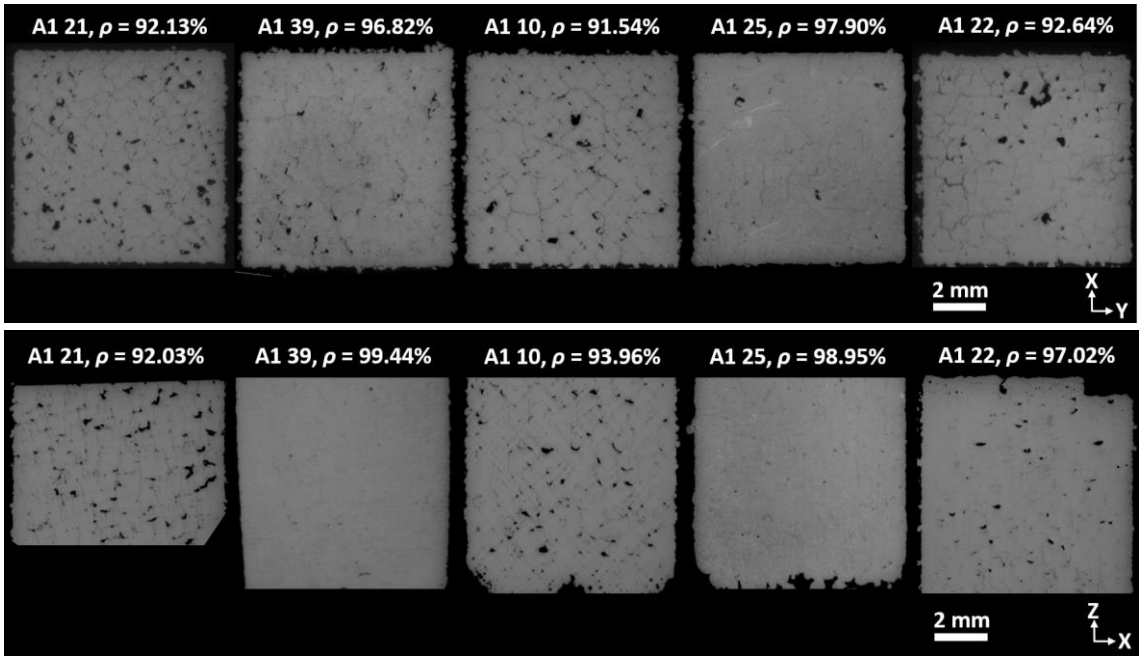

Figure 117 Optical images for sample 21, 39, 10, 25, 22, from test A1, with horizontal cross sections (top) and vertical cross section (bottom), all samples are 8 mm wide

The results from the CCD surface response analysis are supported by the trends in energy density, the values of the highest parameters and the appearance of the defects in the samples. The results indicate that higher density samples will be found with increase in energy input. The concern with this analysis is that ten samples are missing. To give some measure to the built variability and to assess the robustness of the analysis, the build files were remade, and the build was repeated.

4.1.2 Test A2: AA6061, 50 µm Layer Thickness CCD DOE

This build was a repeat of test A1, as some parts had failed due to a hatching error. This error did not reoccur, and all the parts built successfully. The motivation for this build was that it was desirable to get the complete set of results from the first test as well as to test for repeatability. The centre parameters of the CCD are repeated twelve times in each test, but five of these had failed in test A1. The locations of these parts were randomised in both tests. The densities of these centre parameters and their position on the plate are presented in Figure 118. From these data, there is no discernible relationship between part density and location. The density of these parts from test A1 measured 96.30 ± 0.33 % and were higher than the density of the parts in test A2, measured at 95.57 ± 0.42 %. It was noted that sample 21 from A1 measured a density higher than the expected ideal density, and it may be that the measured densities of A1 are higher than reality. This is most likely due to a miscalculation of the water temperature and density, as mentioned as a potential error in section 3.9.

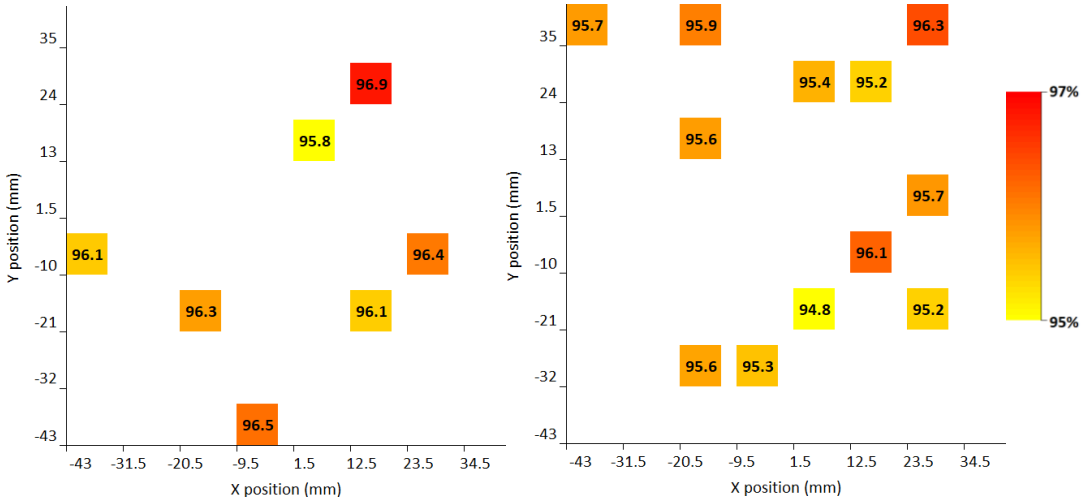

Figure 118 Repeated part in randomised position during test A1 (left) and test A2 (right), the parts are colourised based on their density

When all 43 repeated parts are compared between the two builds, most had a higher density in test 1 (Figure 119). Sample number is used to identify build location, not parameters, and so parts built with the same parameters do not have the same sample number. Two outliers are present, samples 0 and 21 from test A1 had very different densities compared to samples 18 and 57 from test A2, respectively. Regarding test A1, it was discussed how sample 21 had likely been infiltrated by water; sample 0 had a density of 88.42% and maybe its companion piece from test 2 had an opening on the surface allowing infiltration of water. Ignoring these two outliers, comparison showed that samples from test 1 were on average 0.3318 ± 0.5608 % denser than their equivalents from test A2. While evidence suggests that the densities of A1 are recorded as higher than they really are, the difference between the two sets is less than the variation seen with the repeated central parts in Figure 118. Therefore, may not be a result of an inconsistency between builds but rather part variation. It should be noted that part density variation is part dependent, and it can be expected that higher densities will have lower variation, as the variance in the presence become less significant.

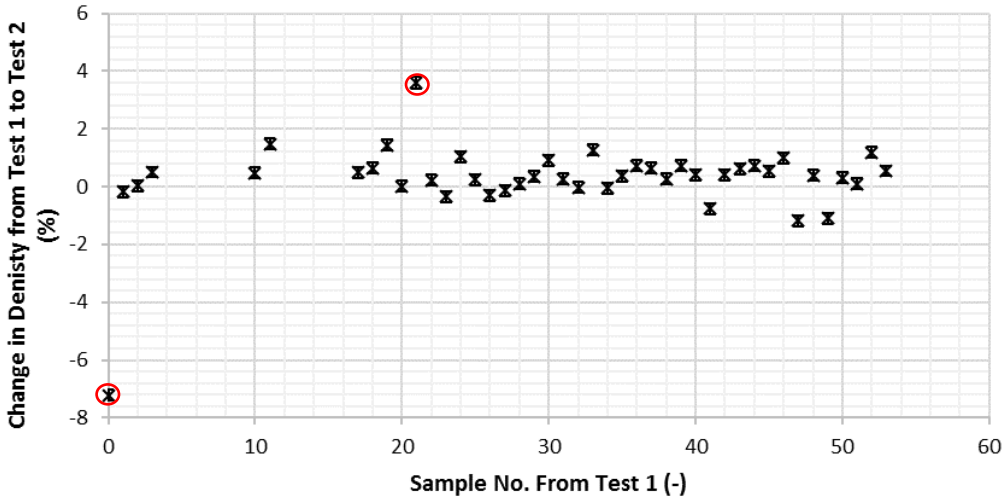

Figure 119 Difference in density of parts with matching parameters compared from A1 to A2 (outlier values are circled)

It would appear that there was an overall shift in densities where test A1 had a higher average density than test A2. This may be from the bias error associated with the Archimedes method, where differences in liquid densities are highly influential. The intention of the use of Archimedes is to understand the trends of densities to improve results and therefore the most significant comparison between the two builds is from the interpretation of the results.

The results in the surface response (Figure 120) and the energy density (Figure 121) are reasonably similar. The conclusions that were drawn from test A1 are the same that can be drawn from these. The only difference was with hatch distance, which instead of predicting an optimum value of 0.082 mm now predicts the extreme minimum value. The interpretation of the results in test A1 suggested that an optimum hatch distance could drop as higher energy per scan line parts are tested, which was the case in this build due to the complete set building successfully. The surface response to lens position suggests that density was not strongly influenced by the parameters tested but furthest defocussed beam gave the best results.

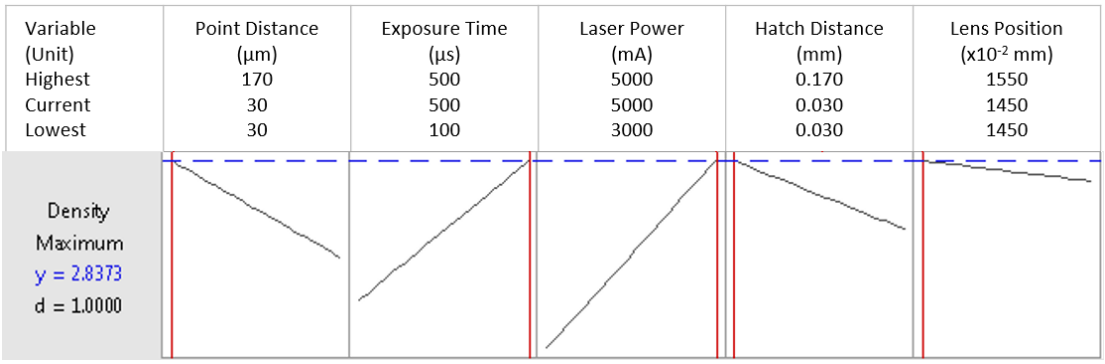

Figure 120 Response surface at the optimum values calculated through MINITAB for test A2: AA6061, 50 µm layer thickness CCD

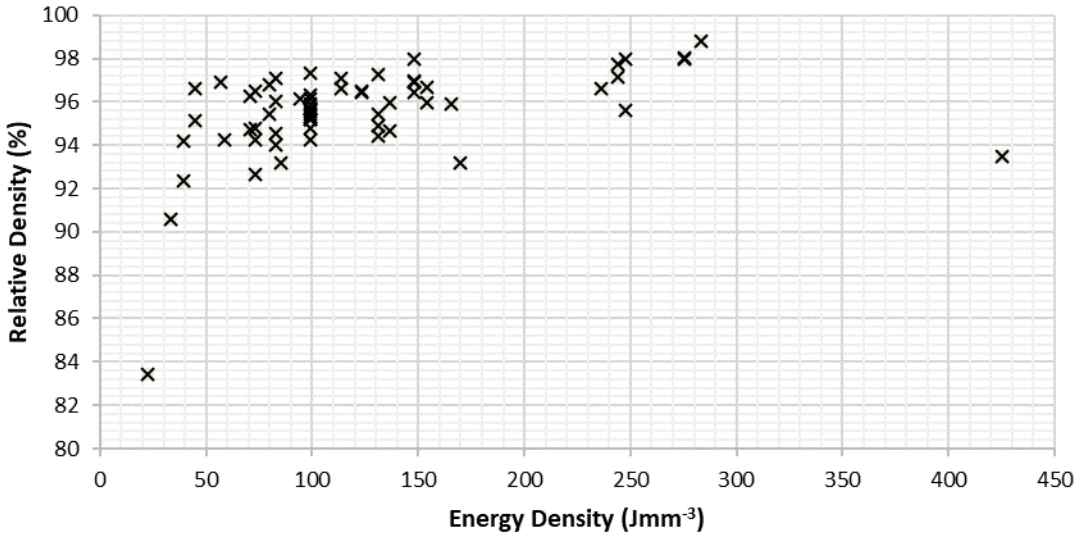

Figure 121 Energy Density vs. Relative Density for test A2: AA6061, 50 µm Layer Thickness CCD

As before, the samples with the highest densities (Table 9) were cross sectioned and analysed. Figure 122 show the cross sections and the calculated micrographic densities. In both test A1 and test A2, the best densities resulted from the same parameters, apart from test 1 sample 21, which had a falsely high reading. Test A1 samples 39, 25, 10, 22 had the same parameters as test A2 samples 43, 45, 16 and 48 respectively. While their gravimetric densities are in accordance with each other, their micrographic densities are not. Sample 22 from test A1 had the same build parameters as sample 48 from test A2; their gravimetric densities differ only by 0.22%, their micrographic densities differ by 3.1%. Fusion pores are clearly evident on all surfaces of both samples 22 and 48, however they are by far most prominent on the vertical surface of 48. This relates to sampling error of the micrographic density. Pores have random occurrence and are not uniformly distributed. The horizontal surfaces in this case were similar but that cannot be said for other paired samples. The cross-sectional density of sample 25 from test A1 had very little porosity, which contrasts with sample 45 from test A2. The reverse of this observation can be seen in sample 10 from test A1 compared to sample 16 in test A2. These are examples of concerns of this method expressed in section 3.8 and the cross-sections are more useful here as a qualitative measure than quantitative.

Table 9 Five highest densities from test A2: AA6061, 50 µm layer thickness CCD

#	POINT DISTANCE	EXPO	LASER POWER	HATCH DISTANCE	LENS POSITIO	ENERGY DENSITY	$\%\rho_{micro}$	$\%\rho_{arch}$	$\delta\%\rho_{arch}$
	µm	µs	W	mm	mm	Jmm^{-3}	%	%	%
43	70	385	185.6	0.070	15.44	275.4	96.68	98.02	0.13
45	70	385	185.6	0.130	15.02	148.3	96.01	97.97	0.13
16	40	300	175.0	0.100	15.23	247.9	97.38	97.96	0.13
48	70	385	185.6	0.070	15.02	275.4	93.21	97.95	0.13
59	70	385	164.4	0.070	15.02	244.0	94.51	97.73	0.13

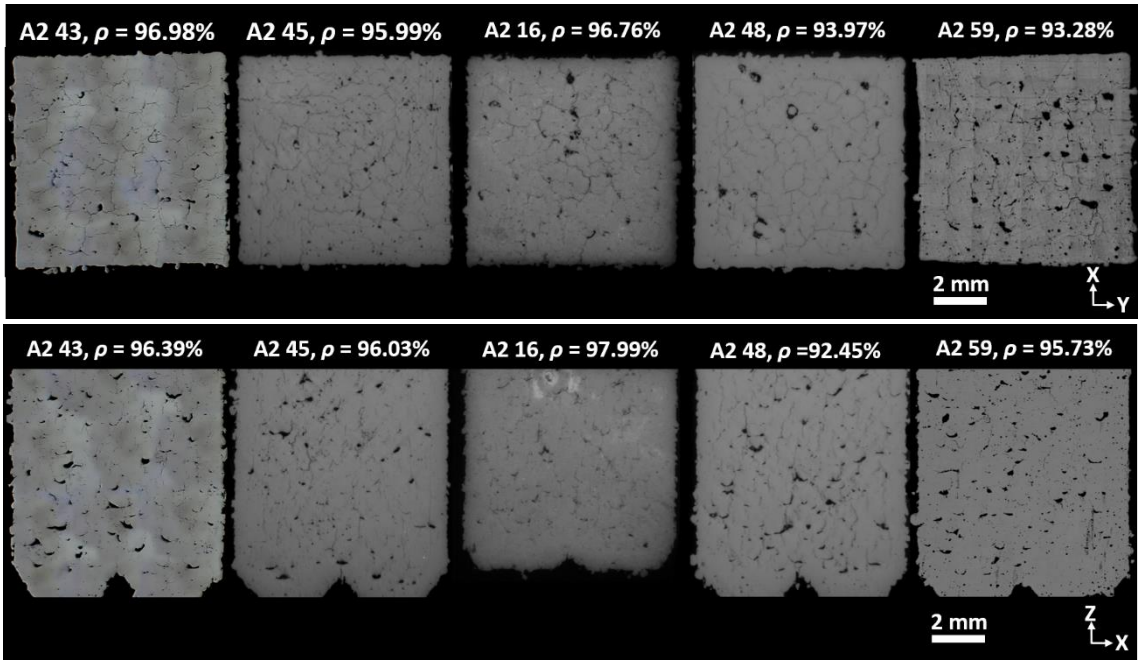

Figure 122 Optical images for samples 43, 45, 16, 48 and 59 from test A2, showing horizontal cross section (top) and vertical cross section (bottom), all samples are 8 mm wide

The comparison of part densities from A2 to A1 gives an assurance that the results are reliable and that neither inter-build nor intra-build repeatability should alter the results nor conclusions significantly. The standard deviation from the parts built with parameters at the centre of the CCD was significantly large but the variance in parts can be expected to decrease as the parameters approach an optimum. Most significantly, both tests identified the same sets of parameters that produced the highest densities and the direction for further improvements.

4.1.3 Test A3: AA6061, 50 µm Layer Thickness CCD DOE

This test was designed from the conclusions drawn from the previous builds. The range of values tested are presented in Table 10. Power was kept to maximum as suggested by the previous results. By reducing the number of factors studied from 5 to 4 reduces the number of parts in the CCD from 54 to 30. In this build, each sample was repeated to test in-build variance and increase the accuracy of results.

The previous results for lens position were ambiguous with the response surface was not in coherent agreement with the best results. Results from A2 suggested that the results were not sensitive to changes across tested range and therefore the range was increased.

The ranges in point distance and hatch distance were decreased, with point distance centred on a lower value, as suggested by parts with highest density in the previous tests. Longer exposure times were tested but there was concern that overheating could cause the build to fail, so only a few high exposure parts were tested along with

very low values. Although no parts failed in the test A2 from overheating, there was evidence of raised corners which are a result of overly melted tracks pushing material to the edge of the parts. These concerns were warranted as this build, test A3, was stopped early as raised parts were damaging the wipers and disrupting the build. The parts did not build the full height but were large enough for analysing densities.

Table 10 Range of values for Test A3: AA6061, 50 µm layer thickness CCD

	UNIT	MIN	MEAN	MAX
POINT DISTANCE	µm	50	90	130
EXPOSURE TIME	µs	60	460	860
HATCH DISTANCE	mm	0.070	0.110	0.150
LENS POSITION	mm	12.25	13.75	15.25

Despite the increase in the energy input into samples and the appearance of samples overheating, the trend suggests that the test was still below the optimum energy density. The trend of increasing density with increasing energy density continues up to the samples with maximum energy input, near 400 Jmm^{-3} (Figure 123). This interpretation is corroborated from the response surface (Figure 124). Point distance and hatch distance are indicating their lowest values and expected maximum is from an exposure time significantly longer than mean tested. As with hatch distance from test A1, this isn't necessarily the absolute optimum exposure but will indicate that the results are closer to ideal, than the previous set of results, test A2. Looking at the best results in Table 11, the trends are somewhat in agreement. The wider range of lens positions tested yields a greater response and the trend in Figure 124, shows that the larger spot size (lower lens position causes a wider spot as in section 3.1.1) helped increase density.

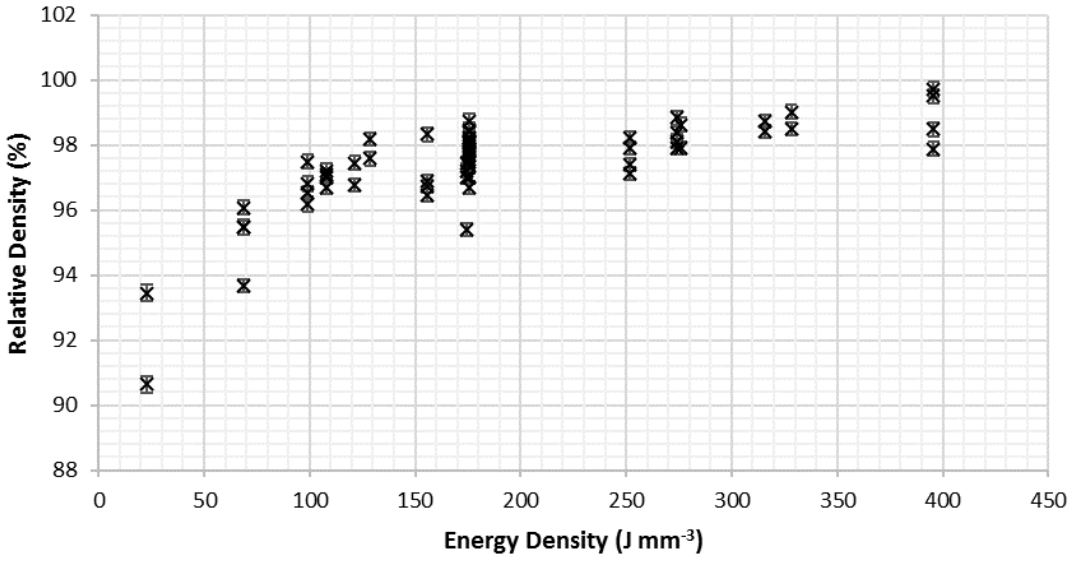

Figure 123 Energy Density vs. Relative Density for test A3: AA6061, 50 µm Layer Thickness CCD

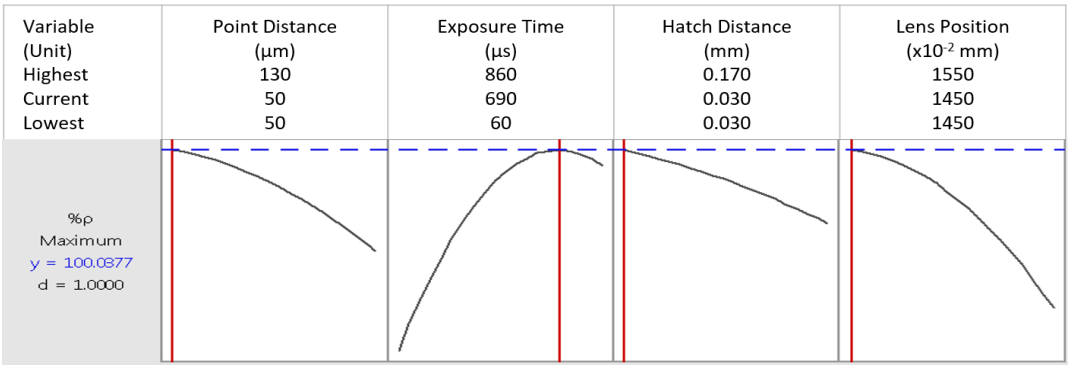

Figure 124 Response surface at the optimum values calculated through MINITAB for test A3: AA6061, 50 µm Layer Thickness CCD

Densities achieved in this build meet the criteria set out at the start of having a density above 99.5% (Table 11). The parameters of the two densest samples, 55 and 38 had the matching parameters, as each part was duplicated in the build. The third highest result, sample 46, had the same parameters apart from the lens position. The duplicate part with matching parameters to sample 46, was sample 51, which had a density of 98.8%. The cross sections of sample 46 showed large irregular shaped pores, unlike cross sections of 55 and 38 (Figure 125 and Figure 126), this evidence suggests pores are caused by fine spot size. They could be fusion pores caused by not heating the surrounding material sufficiently or they could be keyhole pores caused by heating the centre of the tracks too much. This gives some indication of the benefits of defocussing the beam and insight into how this improves build quality. These large irregular shaped pores will be very inconsistent. The large difference in densities from sample 46 to 51 could be as a result of these pores being varied in shape and prevalence.

The cross sections of sample 55 and 38 appear to be largely free of pores, however the samples still had many cracks. Further improvements to this density may be found by fine tuning the test and only considering the parameters over a smaller range centred on those that yielded the best results in this test. These parameters do not avoid cracks, which is important and fine-tuning parameters is unlikely to improve this. At higher densities the observed cracks are finer, although they are just as prevalent. As mentioned in the literature review, the cracks relate to the thermal stresses in the part, which can be altered with parameter selection. Alternative areas within the process window were considered where the thermal stress may be reduced.

Table 11 Five highest densities from test A3: AA6061, 50 µm Layer Thickness CCD

#	POINT DIST.	EXPO	HATCH DIST.	LENS POS.	ENERGY DENSITY	$\%\rho_{micro}$	$\%\rho_{arch}$	$\delta\%\rho_{arch}$
	µm	µs	mm	mm	Jmm^{-3}	%	%	%
55	70	660	0.090	13.00	395.7	99.31	100.0	0.29
38	70	660	0.090	13.00	395.7	98.96	99.77	0.28
46	70	660	0.090	14.50	395.7	96.40	99.76	0.27
20	50	460	0.110	13.75	315.9	98.67	99.50	0.27
14	90	860	0.110	13.75	328.2	99.65	99.48	0.28

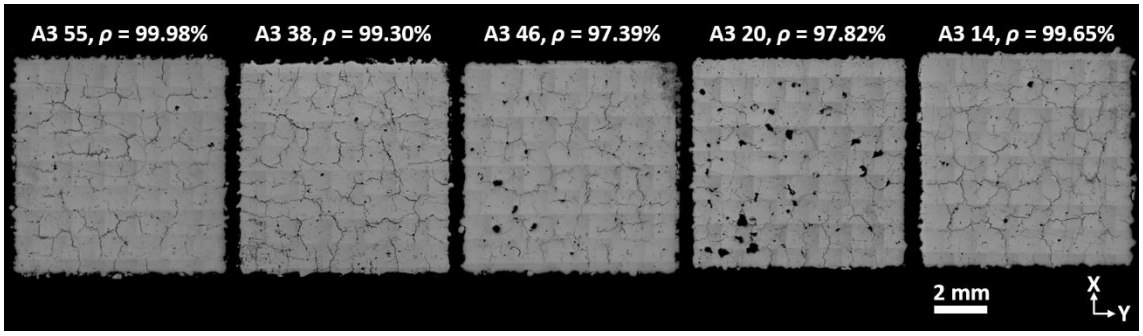

Figure 125 Optical images of horizontal cross sections of samples 55, 38, 46, 20 and 14 from test A3, all samples are 8 mm wide

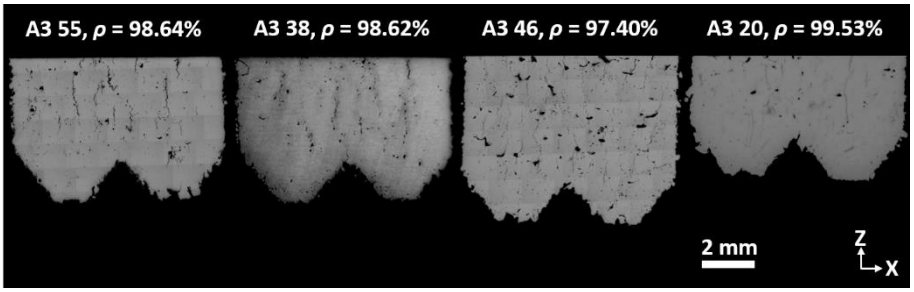

Figure 126 Optical images of vertical cross sections of samples 55, 38, 46, and 14 from test A3, all samples are 8 mm wide

This test found parameters that produced adequately dense parts but could not produce them without the presence of cracks, which are known to compromise the strength of the parts. The trends in the surface response and with energy density suggest that higher densities could be obtained with increased energy input. As the remaining defects are cracks, which are present due to thermal stresses, the increase in energy would not appear a logical solution. An attempt was undertaken in test A4, to examine another area of the parameter window to see if reduced energy input could reduce cracking and maintain sufficient densities.

4.1.4 Test A4: AA6061, 50 µm Layer Thickness CCD DOE

Based on the findings of the previous tests, the CCD DOE was able to direct the process parameter study toward sufficient density samples. However, these samples are compromised by a large number of vertical cracking in each sample. The surface

responses of each test indicated higher density samples could be achieved with high energy input. Higher energy input to samples may lead to higher thermal stresses and therefore are unlikely to alleviate cracking. Test A4 was devised to see if another position within the parameter window could produce sufficient densities without prominent cracks.

Irrespective of the initial cause of the cracks, thermal stresses are necessary to open cracks and allow them to propagate through the samples. This build was an attempt to see if it is possible to achieve the sufficient density results using lower exposure times, either resulting in lower energy density per volume or per scan length, as a way of delivering that energy to explore if this could reduce the amount of cracking in built parts. The intention of lowering exposure time to lower the energy per scan line, and to lower the temperatures of the melt pools and possibly increase overlap between melt pools.

The range of parameters used for this test are presented in Table 12. These included samples with energy densities above 400 Jmm^{-3}, which approach the region where overheating started to be observed in test A3. These parts were also used for a comparison with parts that were double scanned in section 4.3.

Table 12 Range of values for test A4: AA6061, 50 µm layer thickness CCD

	UNIT	MIN	MEAN	MAX
POINT DISTANCE	µm	50	90	130
EXPOSURE TIME	µs	30	230	430
HATCH DISTANCE	mm	0.050	0.100	0.150
LENS POSITION	mm	12.50	14.00	15.50

In Figure 127, there appears to be a logarithmic relationship between energy density and build density that is similar to A1 (Figure 115), with the densities approaching a maximum with energy densities above 340 Jmm^{-3}. High densities were recorded, although none were above the target value of 99.5%.

The surface responses at the estimated optimum density (Figure 128) do not indicate the very extremes of the tested range for exposure time, hatch distance or lens position but from these surface response graphs, it can be concluded that higher energy input could yield higher densities, which is proved true by results of test A3.

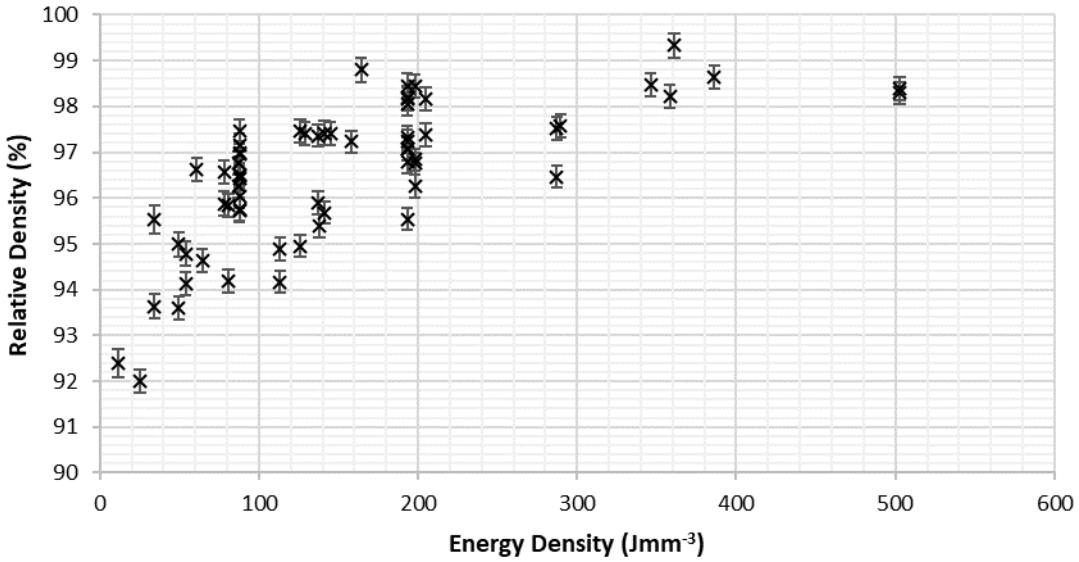

Figure 127 Energy Density vs. Relative Density for test A4: AA6061, 50 µm layer thickness CCD

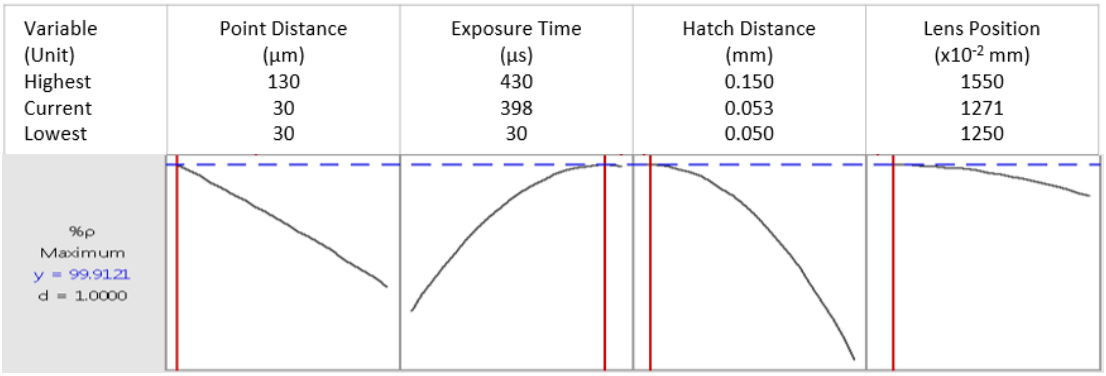

Figure 128 Response surface at the optimum values calculated through MINITAB for test A4: AA6061, 50 µm layer thickness CCD

The purpose of this test was to see if lowering the energy input, or lowering the energy of each scan track, could result in high densities with less cracking. From Table 13, the two best results, samples 1 and 63, suggest that long exposure times are important to get optimum densities. Only two samples were printed with exposure of 430 µs and they recorded the two highest densities from this test, despite sample 63 having a much smaller energy density. It is possible that exposure time plays a more significant role as the higher temperature generated in the tracks may be necessary to facilitate wetting of the tracks to adjacent material. This could also be achieved with a small point distance; the sample with the shortest point distance recorded the third highest density.

The micrographs show that the samples are heavily cracked (Figure 129). With this result, it was decided that there was no evidence that the parts could be printed free from cracks without changing the printing set up beyond adjusting the scanning parameters. In an attempt to have more influence on the stresses generated during processing, the following tests adjust the layer thickness (test A5) and apply double scanning of each layer (tests A6 and A7).

Table 13 Five highest densities from test A4: AA6061, 50 µm layer thickness CCD

#	POINT DIST.	EXPO	HATCH DIST.	LENS POS.	ENERGY DENSITY	$\%\rho_{micro}$	$\%\rho_{arch}$	$\delta\%\rho_{arch}$
	µm	µs	mm	mm	J mm^{-3}	%	%	%
1	60	430	0.075	14.00	361.0	98.38	99.33	0.26
63	90	430	0.110	14.00	164.1	98.95	98.80	0.26
59	30	230	0.075	14.00	386.2	98.20	98.65	0.26
54	60	230	0.075	14.00	193.1	99.05	98.47	0.26
9	40	330	0.090	13.25	318.4	98.44	98.47	0.25

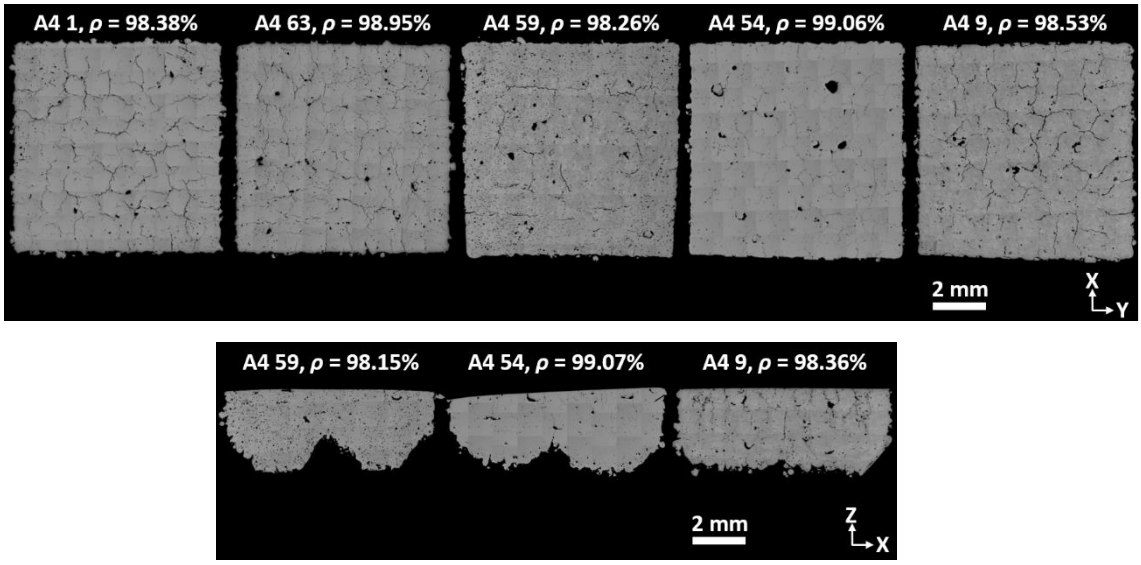

Figure 129 Optical micrographs of horizontal cross sections (top) of samples 1, 63, 59, 54 and 9 and vertical cross sections (bottom) of samples 59, 54 and 9 from test A4: AA6061 50 µm layer thickness CCD, all samples are 8 mm wide

4.2 SLM of AA6061 at 25 µm Layer Thickness

In section 0 all observed parts built with a layer thickness of 50 µm had compromising cracks. It is theorised that reducing thermal stresses in the parts could eliminate crack growth. Shallower layers can have the effect of lessening the amount of material within a weld track and therefore could reduce the amount of local shrinkage and stresses. In this test, the effect of changing layer thickness on cracking in built parts is studied.

The layer thickness was set at 25 µm, which is half the layer thickness used in section 0. The range of variables (Table 14) tested was similar to the test A1 (section 4.1.1), apart from lens position. The range of tested values for lens position was broadened as the range tested in test A1 did not show enough of an effect to evaluate the trend. This build was also used as an opportunity to see the effects scan direction has on crack direction and density. All parts were repeated with and without altering scan direction between layers.

Table 14 Range of values for test A5: AA6061, 25 µm layer thickness CCD

	UNIT	MIN	MEAN	MAX
POINT DISTANCE	µm	30	100	170
EXPOSURE	µs	100	300	500
HATCH DISTANCE	mm	0.030	0.100	0.170
LENS POSITION	mm	12.50	14.50	16.50

Two samples, 6 and 45, which had the same parameters (point distance = 60 µm, exposure = 400 µs, hatch distance = 0.065 mm and lens position = 13.50 mm), failed to build. They were amassing material at the peripheries of the blocks, as pictured in Figure 130. The only difference between the two parts was that one used alternate scanning and the other used unidirectional scanning. These had the highest energy density of all the test parts. Two other parts matched the parameters except the lens position was 15.50 mm, which is nearer focus as identified with focus test in section 3.1.1., built successfully. Other parts with similarly high energy density had built successfully, with lens position of 14.50 mm. Energy density alone is not enough to predict if a part would excessively build up in the corners. It would appear from this build that the spot size is also a key factor. The melt tracks could push material away from the centre of the tracks. If the tracks are wide enough, the successive scans push more material across the scanned surface causing excessive build up at the edges of the part. Energy density will have an impact by either widening the melt tracks or a reduction in hatch distance. The greater spot size from the defocussed beam must increase the weld tracks or cause more material to be pushed to the side.

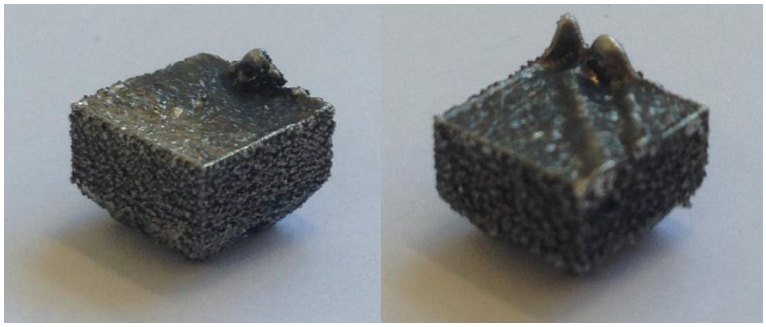

Figure 130 Build defects on sample 45 (left) and sample 6 (right) from test A5: AA6061, 25 µm layer thickness CCD

All the parts produced had high density (but not above the desired density of 99.5%) despite wide ranges selected in all parameters and wide range of energy densities (Figure 131). The reduced layer thickness appears to broaden the processing window. According to the response surface (Figure 132), higher density could be achieved with a higher energy density and further defocussing of the beam. Both trends are reflected in the parts with highest density (Table 15).

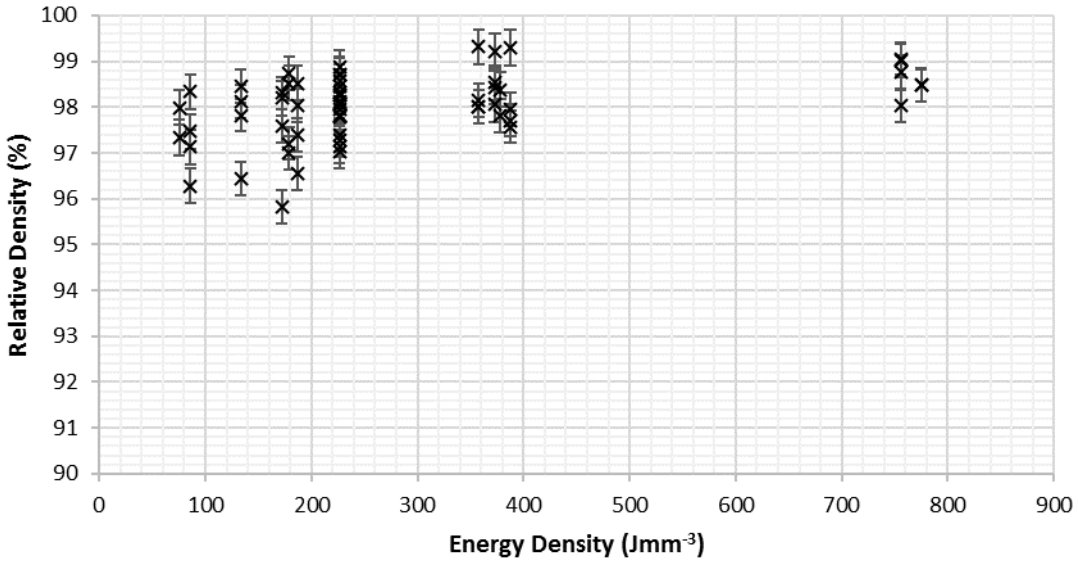

Figure 131 Energy Density vs. Relative Density for test A5: AA6061, 25 µm layer thickness CCD

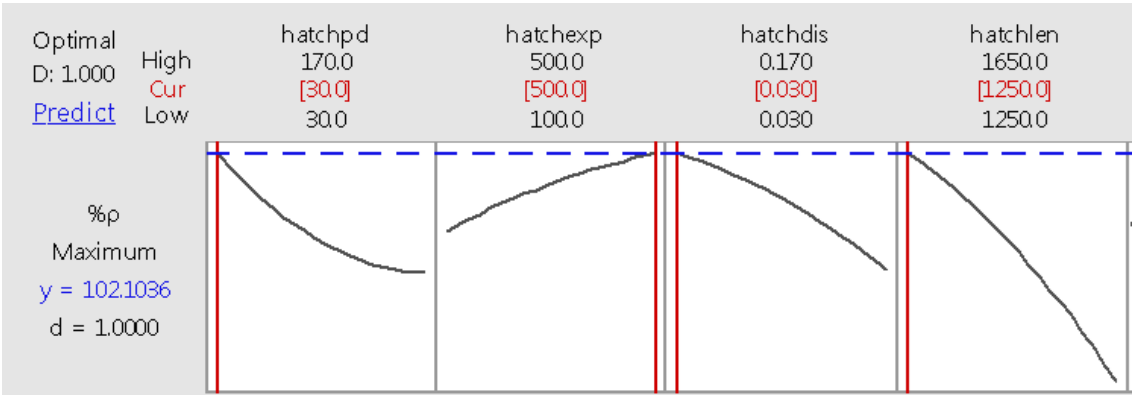

Figure 132 Response surface at the optimum values calculated through MINITAB for test A5: AA6061, 25 µm layer thickness CCD

The five samples with the highest densities are presented in Table 15, and there appears to be two subsets within this data. The first subset comprises of the highest three density samples. These have energy densities between 350 and 400 Jmm^{-3} and the same spot size with lens position at 13.50 mm. In the structure of the CCD, each of these parts were printed with a corresponding sample with a finer spot size (lens position of 15.50 mm) which produced lower densities. This corroborates the response surface of lens position (Figure 132). The other two parts in the top five densities had energy density near twice the value of the top three and focus at 14.50 mm. Other samples with energy density above 700 Jmm^{-3} either had finer spot size (lens position at 15.50 mm) and had lower part density, or wider spot size (lens position of 13.50 mm) and failed to build. The trend identified in the response surface was to increase energy density and spot size. This trend ignores how the parts with the highest energy density and largest spot sizes failed to build as they do not fit within the model, which shows a limit of this method.

The motivation for this build was to see if the reduced layer thickness could influence the cracks. From the cross sections (Figure 133 and Figure 134), it can be seen that the cracks are still present. Parts were built in XY scanning strategy, consistent with builds in section 4.1, and they were repeated with parts with all-X scanning. This demonstrated the orientation of the cracks is in line with the scan lines, and not in the direction of highest stress, as discussed in section 2.6.

Table 15 Five highest densities from test A5: AA6061, 25 µm layer thickness CCD

#	POINT DIST.	EXPO	HATCH DIST.	LENS POS.	ENERGY DENSITY	$\%\rho_{micro}$	$\%\rho_{arch}$	$\delta\%\rho_{arch}$
	µm	µs	mm	Mm	J mm^{-3}	%	%	%
13	130	400	0.065	13.50	357.6	99.11	99.31	0.37
55	60	200	0.065	13.50	387.4	-	99.29	0.38
9	60	400	0.135	13.50	373.1	99.21	99.22	0.37
19	30	300	0.100	14.50	755.5	95.55	99.05	0.36
43	30	300	0.100	14.50	755.5	93.61	99.02	0.37

The horizontal cross sections (Figure 133) show the complete cross-sectional area of sample 19 and the partial cross section of sample 9. Both samples had similar gravimetric densities but micrographic density of sample 19 was much lower than expected. The majority of the porosity is from cracks and while both have a similar concentration of cracking, the cracks in sample 19 are thicker and more prominent. Similar observations can be made with the vertical cross sections of sample 9 and 43, though 43 does appear to have more spherical porosity as well (Figure 134). Samples 19 and 43 were had significantly higher energy densities than sample 9. It is likely that the appearance of cracks is influenced by the relaxing of internal stresses from cross sectioning, as mentioned in 0, and it may be that the stresses are higher with the higher energy input.

Samples 9 and 44 were built with the same parameters but with different scanning strategies and had gravimetric densities of 99.22% and 98.53% respectively. Sample 9 was produced with XY alternating scan strategy and cracks are vertical and align with the scan directions. Sample 44 was produced with all X scan strategy which aligns with the cracks. The vertical cross section of sample 44 shows a plane parallel to the scan direction and no cracks are evident.

Samples 19, 43 and 32 were all produced with energy density of 755.5 Jmm^{-3} and had densities of 99.05%, 99.02% and 98.76% respectively. Samples 19 and 32 were produced with XY alternative scanning, while sample 43 had the same parameters as 19 but was made with all X scanning. Unlike samples 9 and 44, all three of the higher energy samples had a much lower micrographic density than gravimetric density, which may be due to the relaxing of stresses as mentioned above. No significant difference in cracking is observed between the vertical cross sections of the unidirectional scanned sample compared to the alternating scan. These results show

that the cracks align with the scan direction. Further tests are performed in chapter 5 to fully understand the relationship between cracking and accumulations of stresses as influenced by the scan direction as well as scan length and part shape.

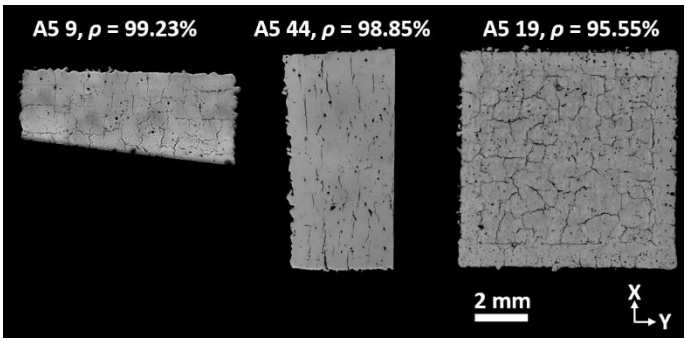

Figure 133 Micrographs of horizontal cross sections of samples 9, 44 and 19 from test A5; AA6061, 25 µm layer thickness

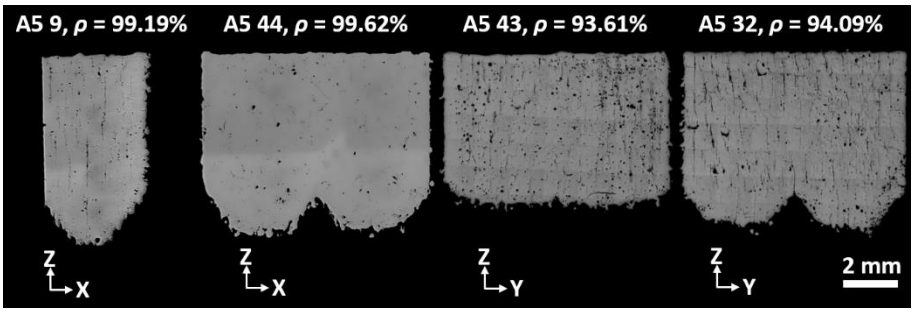

Figure 134 Micrographs of vertical cross sections of samples 9, 44, 43 and 32 from test A5; AA6061, 25 µm layer thickness

4.3 SLM of AA6061 with Double Scanning at 50 µm Layer Thickness

After several attempts at optimising the density of AA6061 using a single scan per layer, the conclusions were that acceptable densities could be achieved but parts were always compromised with fine cracks. In the literature review, double scanning layers was identified as a potential strategy to reducing stresses and avoiding cracks (section 2.6). Work discussed in the literature review demonstrated how horizontal cracks could be avoided through the double scanning method [236], however, no literature has been published with dealing with reducing the vertical cracks observed in SLM of AA6061 through double scanning. As such, several approaches were considered.

The first experiment employed two scans, both with lower energy than was necessary for sufficient melting from a single scan, as observed in previous tests. The thermal stresses of each scan should not accumulate as it does with scans in each layer as a scan should relieve the stresses of the material it melts, which means the thermal history of the first scan is rewritten by the second. It would be expected that the

reduced energy input from the primary scan would leave porosity, which would then be removed by the secondary scan. The scans would have different purposes and the characteristics of the scanned material would be different. The primary scan would scan powder while the secondary would be scanning partially fused material already surrounded by fused material. These differences would affect the laser absorption, heat dissipation and material wetting as well as other factors. There is no necessity for the two scans to share parameters; however, doubling the number of variables would make using testing all of them very time consuming and costly. To reduce this, two strategies were used, adapted from research from Aboulkhair, et al. [166] for processing AlSi10Mg. Their work was based on using a "pre-scan" of either half or the full energy that is applied with a second scan, with results showing a reduction in porosity, both from gas inclusions and failed melting. ALSi10Mg does not crack during SLM processing so the effect on cracking has not been tested, but the observed benefits could still be realised with AA6061.

In this test, adjusting the energy input for the primary and secondary scans were achieved by changing the exposure time. For comparative reasons, the values tested matched parameters used for test A4, and were designed so that the double scanning would result in energy densities near what was seen to be optimised and not to fail from overheating. The range of values are shown in Table 16.

Table 16 Range of values for test A6: AA6061, double scanning with half and full pre-scans

	UNIT	MIN	MEAN	MAX
POINT DISTANCE	µm	50	90	130
EXPOSURE	µs	30	230	430
HATCH DISTANCE	mm	0.070	0.110	0.150
LENS POSITION	mm	12.50	13.75	15.50

The densities from test A6 are presented in Figure 135. The order presented is from the sample with the highest density with a single scan, descending. This order was chosen as it shows how the pre-scans have affected the densities. Where a set of parameters from the single scan produced densities below 98% a pre-scan often increased the density. In most cases the density was highest with the full pre-scan, however where a single scan could achieve densities above 98%, the pre-scans did not improve on this and the highest densities achieved in this set of tested parameters were from the single scanned samples.

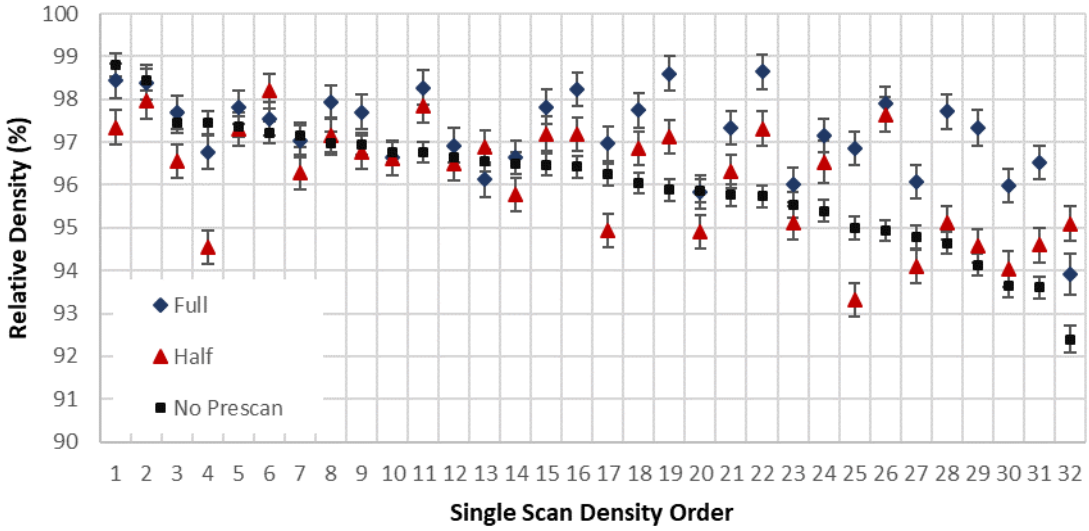

Figure 135 Comparison between relative densities of samples with single scans (no pre-scan) and with a pre-scan of half or full energy. Sample parameters defined by CCD DOE and ordered here from highest to lowest density from the single scan.

Comparing the two pre-scans it is clear that full energy pre-scan consistently outperformed the half energy pre-scan. The full energy pre-scans did improve the density of most of the parts apart from a few of the higher density samples. Figure 136 shows the trend of relative density with the energy density. The trend of full energy pre-scan somewhat aligns with the trend of the single scan. This could be interpreted as a superposition of the energy applied to the parts by the primary and secondary scans, with parts with insufficient energy from a single scan improving with a double scan and overheating at the higher energy inputs, however, it should be noted that all energy densities are at or below that of the optimum values found with samples 55 and 38 from test A3 and therefore there is a decrease in the density achieved with dividing the single scan into two scans. This is more evident with the half energy pre-scans where the trend falls below these others and cannot be regarded as the superposition of energy input. It was mentioned above that the pre-scan changes the characteristics of the scanned material and it cannot be said that the pre-scans improves upon the density of single scanning.

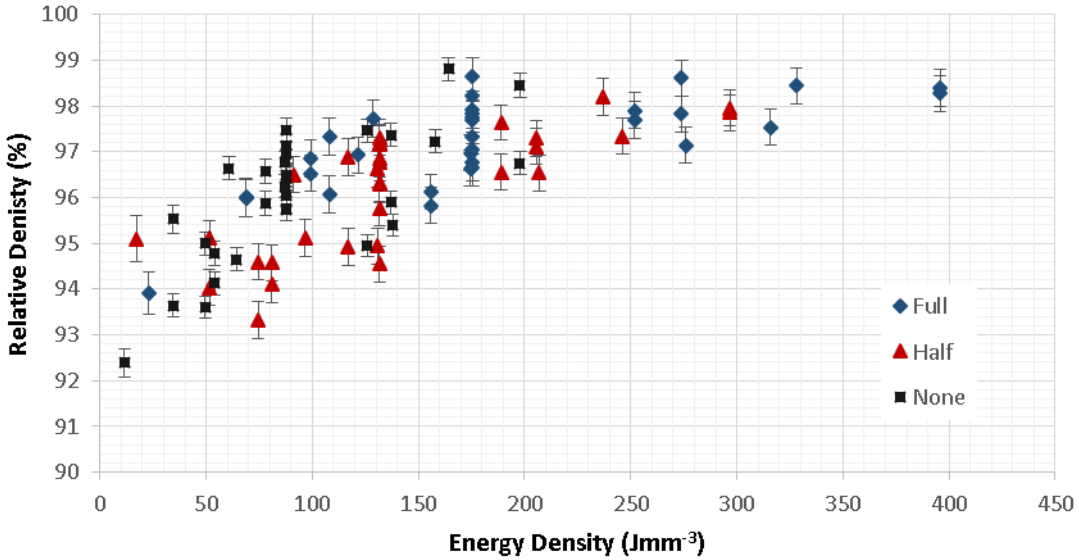

Figure 136 Energy Density vs. Relative Density for test A6: AA6061, double scanning with half and full pre-scans

The highest densities of double scanned samples were all produced from full energy pre-scanning. Figure 137 shows the surface responses from the set of full energy pre-scanned samples. The trends of exposure time and point distance suggests a trend of increasing energy density, reflected in trend of Figure 136. The hatch distance trend is very different with the maximum hatch distance been suggested as favourable.

The hatch distance of 0.150 mm is near what would be expected from the width of the scan tracks. It may be that the this large spacing between tracks leaves large pores, which benefit the coupling of energy from the laser on the second scan. As with CCD parameters tests, the extreme of hatch distance of 0.150 mm was tested with one sample, where all other parameters are at the centre values of the CCD. The part with hatch distance of 0.150 mm had the second highest increase in density when comparing the density from single scan and from double scan, 94.64 ± 0.25% and 97.71 ± 0.40% respectively, and may be due to the type of porosity that was left from the first scan.

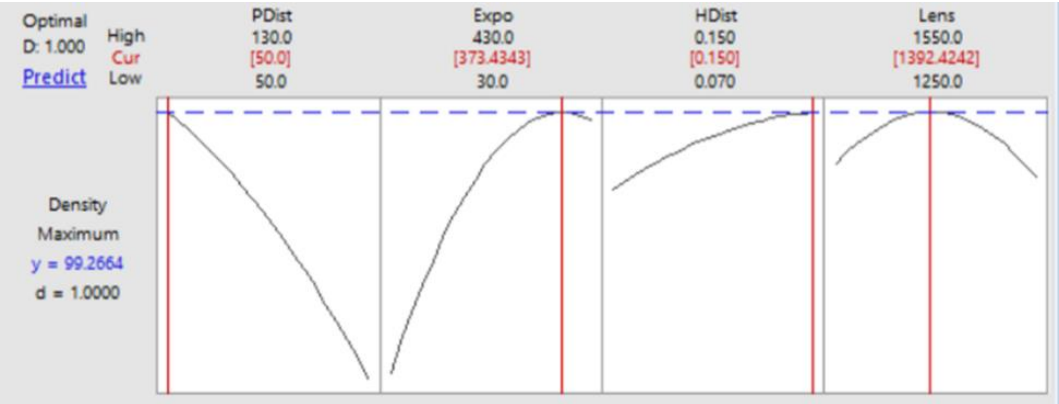

Figure 137 Response surface at the optimum values calculated through MINITAB for test A6: double scanning with half and full pre-scans

The trend of increased density with higher hatch distance is not reflected in the samples with highest densities (Table 17). The highest density found from double scanning was with a part with parameters at the centre of the CCD and it should be noted that the mean density rom the parts at the centre of the CCD was 97.81 ± 0.46 %. The other densities within the five highest densities all had higher exposure times and energy densities.

The parameters of samples 43 and 8 produced the highest densities from the single scanned samples and sample 43 was the sample with the extreme exposure time within the CCD. The parameters of sample 43 match those of sample 63 from test A4 (Figure 129) and had a lower density, 98.44 ±0.4% compared to 98.80 ± 0.26 %. It is not clear from this test if the rescanning of parts can improve upon the densities achievable with single scanning but what is clear from the cross sections is that this approach has not alleviated cracking from the samples (Figure 138).

Table 17 Five highest densities from test A6: AA6061, double scanning with half and full pre-scans

#	POINT DIST.	EXPO	HATCH DIST.	LENS POS.	ENERGY DENSITY	$\%\rho_{micro}$	$\%\rho_{arch}$	$\delta\%\rho_{arch}$
	µm	µs	mm	mm	J mm^{-3}	%	%	%
26	90	230	0.110	14.00	175.5	94.46	98.64	0.40
31	70	330	0.130	13.25	274.0	97.71	98.61	0.40
43	90	430	0.110	14.00	328.2	97.05	98.44	0.40
8	70	330	0.090	13.25	395.7	92.98	98.39	0.40
35	70	330	0.090	14.75	395.7	97.31	98.27	0.40

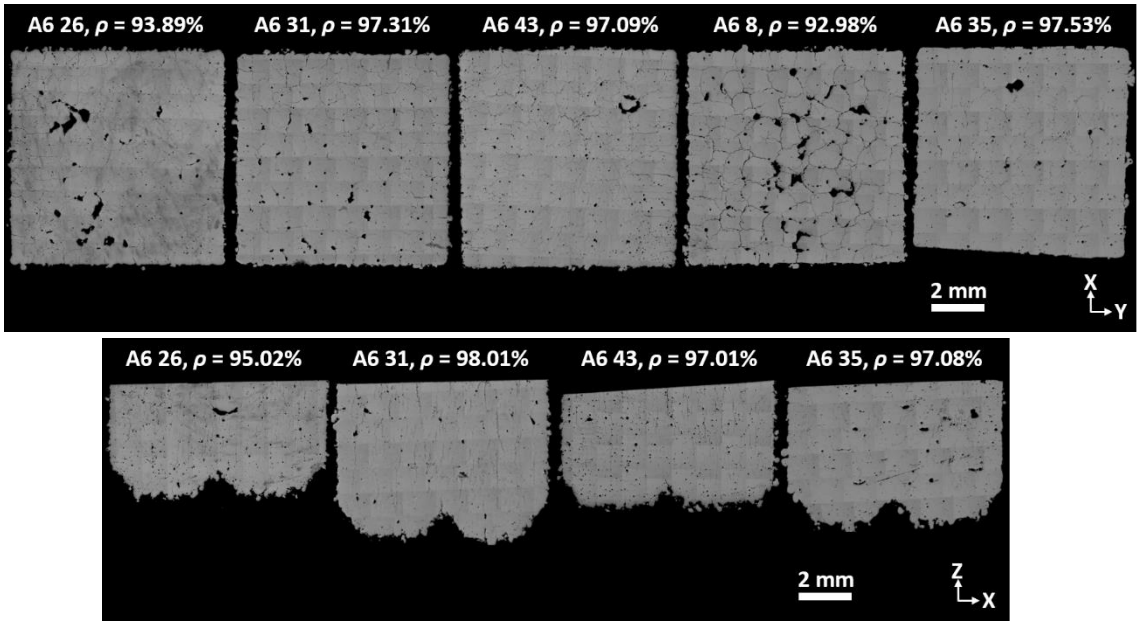

Figure 138 Micrographs of horizontal cross sections (top) of samples 26, 31, 43, 8 and 35 and vertical cross sections (bottom) of samples 26, 31, 43 and 35 from test A6: AA6061 double scanning with half and full pre-scans

The benefits of using a pre-scan that were found by Aboulkhair, et al., [166], were not seen with AA6061 in this experiment. The best results found by Aboulkhair et al., [166] were with a pre-scan of half the energy of the secondary scan. The highest densities with the half energy pre-scan were found with parameters that matched the highest densities of the full energy pre-scan but with lower results (Table 18). The cross sections of the half energy pre-scans reveal a microstructure impaired by fusion pores and cracks similar to the full energy pre-scans and the single scanned samples. As such no benefit has been revealed in this approach for this material.

Table 18 Top three densities achieved with double scanning with half energy pre-scan from test A6, and the full energy pre-scan samples with matching parameters

HALF PRE-SCAN			FULL PRE-SCAN		
#	%ρ	δ%ρ	#	%ρ	δ%ρ
	%	%		%	%
62	97.96	0.40	43	98.44	0.40
58	97.85	0.40	35	98.27	0.40
17	97.34	0.39	8	98.39	0.40

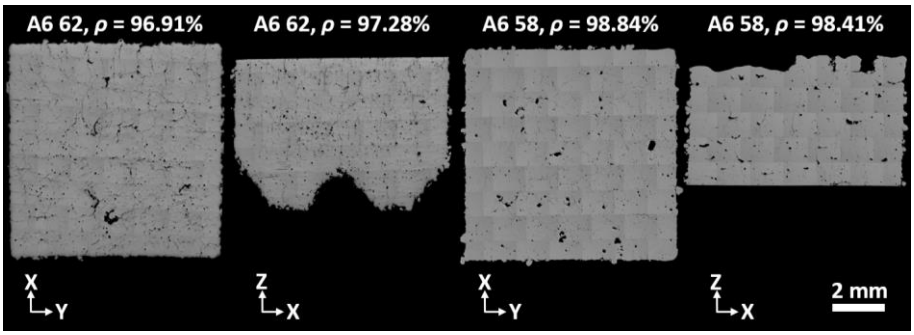

Figure 139 Optical micrographs of horizontal and vertical cross sections of samples 62 and 58 from test A6: AA6061 double scanning with half and full pre-scans

As reasoned earlier, rescanning was examined as it was theorised that it could reduce thermal stresses. Pre-scans of full and half energy of the secondary scan were examined, and no benefit was found with either density or avoidance of cracks. A second experiment was attempted which used the parameters of sample 55 from test A3 to achieve a high density from the primary scan and use a secondary scan to see if the density could be improved. The ambition of the second scan was to provide stress relief and try avoiding the stress to build up enough for cracks to form, or as a scan to try and heal cracks already forming.

The number of variables was reduced to three as lens position was held at 13.00 mm, equal to what was used with the primary scan. The range of parameters is presented in Table 19.

Table 19 Range of values for test A7: AA6061, double scanning with altering secondary scan

	UNIT	MIN	MEAN	MAX
POINT DISTANCE	µm	30	50	70
EXPOSURE	µs	160	410	660
HATCH DISTANCE	mm	0.045	0.067	0.090

All the double scanned parts had a lower density than from the single scan, as seen in Figure 140. The cross sections show that the cracking is still an issue as well as some porosity that wasn't evident in the single scanned samples (Figure 141). These results suggest that this approach does not offer improvement from single scanned and cracking could not be avoided.

An interesting observation from these parts were that the top surface was very visibly more reflective than any of the other parts, including both previously built parts that were double scanned and parts that were scanned only once in the same build. One possible explanation is that there is reduced roughness, but it seems unlikely that all these parts had a reduced roughness while no other double scanned parts did. Another possibility is that there is reduced oxygen in the surface of the formed layers. The second scan on this build may have acted more as a surface treatment than with the previous double scan tests, where the primary scan left greater levels of porosity. Little is understood about the relationship of the appearance of the top surface and level of oxides in the part and this is examined further in chapter 5.

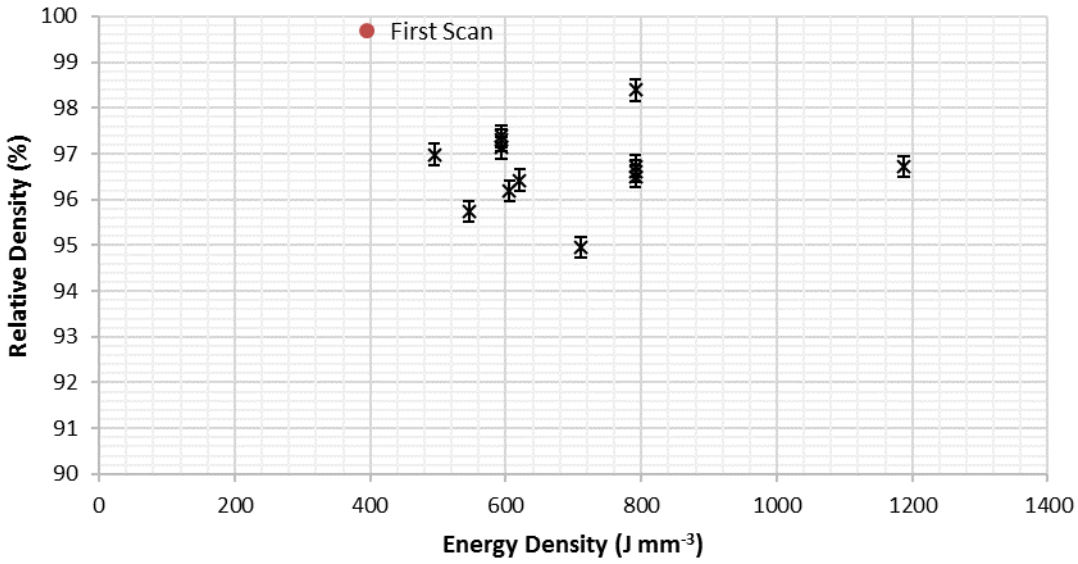

Figure 140 Energy Density vs. Relative Density for test A7: AA6061, 50 µm layer thickness with secondary scan to improve upon primary scan with near optimum density

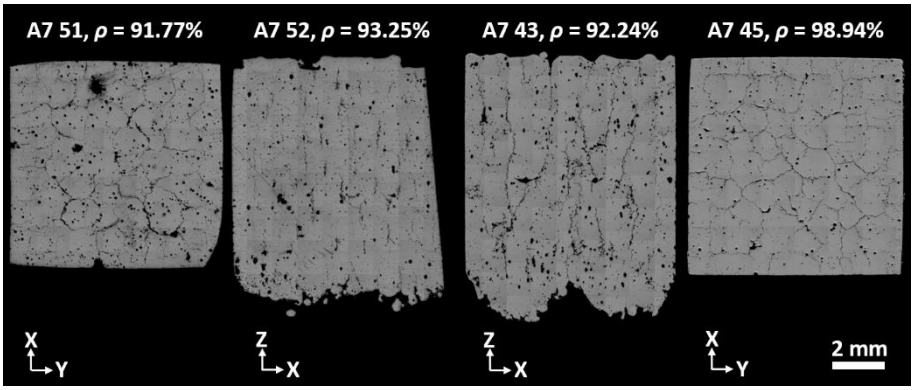

Figure 141 Micrographs of horizontal and vertical cross sections of samples 51, 52, 43 and 45 for test A7: AA6061, 50 µm layer thickness with secondary scan to improve upon primary scan with near optimum density

4.4 SLM of AlSi10Mg

AlSi10Mg is one of the most commonly SLM processed aluminium alloys and is known to process without cracking. In this project AlSi10Mg was used to compare with AA6061 in an attempt to examine the processing and microstructure differences, with a view to potentially explaining the cause of cracks in AA6061.

To examine SLM of AlSi10Mg, samples with sufficiently high density were needed. The initial build with AlSi10Mg used parameters that were found to produce high densities with AA6061. These samples had high levels of fusion porosity. Following this, high density samples were produced with parameters found using a CCD DOE, as was used to find high density AA6061 samples.

4.4.1 Test B1: AlSi10Mg with AA6061 parameters

The first attempt to print AlSi10Mg used parameters that were found to produce the highest densities for AA6061 (Table 20). Parameters were selected from all three conditions that AA6061 samples were printed in, 50 µm layers, 25 µm layers and double scanning. The single scan 50 µm layer parameters were selected from sample 55 from test A3, which produced density of at least 99.77 ± 0.26%. Parameters for 25 µm layer were selected from sample 13 from test A5, which produced density of 99.31 ± 0.37%. Finally, parameters from double scanning are from sample 51 from test A8 (the parameters presented in Table 20 are those of the second scan while the first scan used the single scan parameters). Three samples of each condition were made.

Table 20 Archimedes and micrographic densities of test B1: AlSi10Mg with AA6061 parameters

#	POINT DIST.	EXPO	HATCH DIST.	LENS POS.	ENERGY DENSITY	$\%\rho_{micr}$	$\%\rho_{arch}$
	µm	µs	mm	Mm	J mm^{-3}	%	%
Single Scan (50 µm layer)	70	660	0.090	13.00	395.7	99.11 ± 0.90	98.04 ± 0.35
Single Scan (25 µm layers)	130	400	0.065	13.50	357.6	99.79 ± 0.03	99.50 ± 0.24
Double Scan	70	330	0.045	13.00	791.4	96.41 ± 2.01	97.98 ± 0.29

The parts were printed in a 3x3 array. Archimedes densities are presented in Figure 142. Only parts printed with 25 µm layer thickness had densities above 99%. The density of AA6061 parts were less sensitive to parameter change with the smaller layer thickness and this appears to have been the case with AlSi10Mg. Densities of samples scanned with single and double scanning parameters have similar densities between, with the average value differing only by 0.06%.

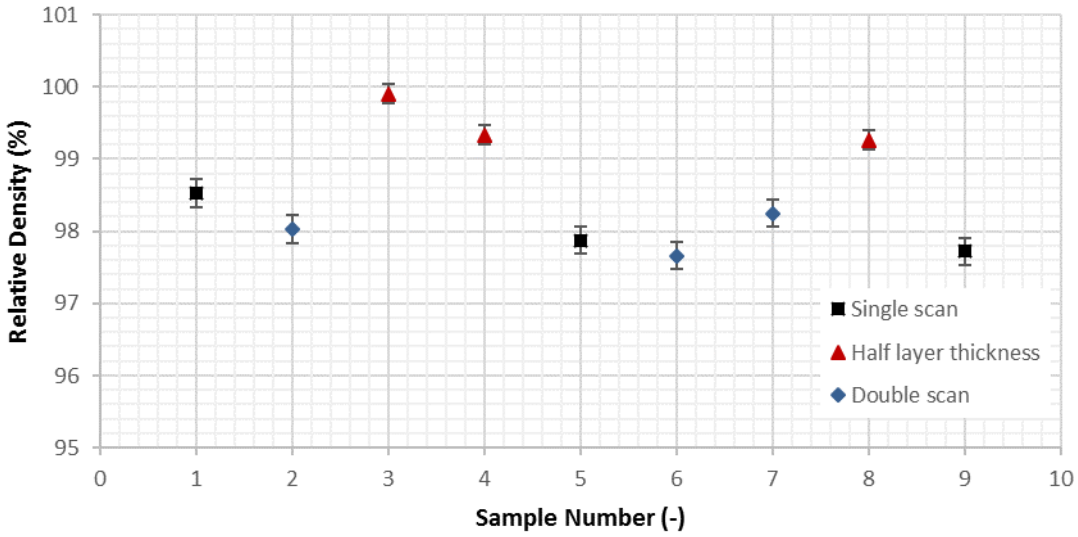

Figure 142 Archimedes densities of test B1: AlSi10Mg with AA6061 parameters

The micrographs show little consistency between cross sections, except for the 25 µm layer samples, which have high densities and few defects (Figure 143, Figure 144 and Figure 145). The main defect appears to be from large irregular shaped pores. The pore shape on the vertical surface, is long, arched and horizontal; this suggested that these flaws are more likely caused by a failure to fuse the weld track to the underlying material and not keyhole pores from overheating. However, the shape is not simply of the melt track failing to fuse to material below, as the height can encompass multiple layers. Oxide surfaces may influence the size and shape of these pores. The length of the pores appears to be longer in the horizontal direction on the double scanned samples compared to the single scanned samples, however the density of

samples is not significantly different. The second scan may have melted less material than the first as more conductive heat paths surround the melt tracks, and it may be that the second scan did not remove porosity but reshaped it. Some similar pores were seen in AA6061 samples but not of the same size. This may be as a result of the short freezing range of AlSi10Mg and the expected faster solidification, with solidification occurring with fusion to adjacent material before gravitational pull reduces the porosity within the powder layers.

The pores appear more at the top of the samples then at then at the feet, as seen in the vertical cross sections, which could be an effect of the changing rates of heat dissipation as the samples change shape.

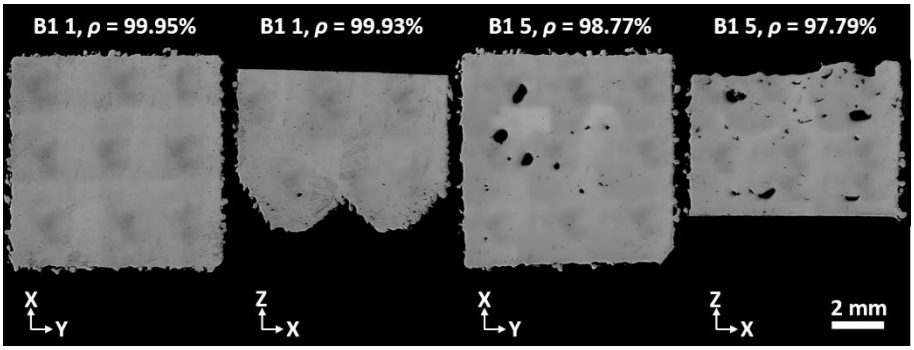

Figure 143 Cross sections showing horizontal and vertical surfaces of single scan samples 1 and 5 from test B1, all samples 8 mm wide

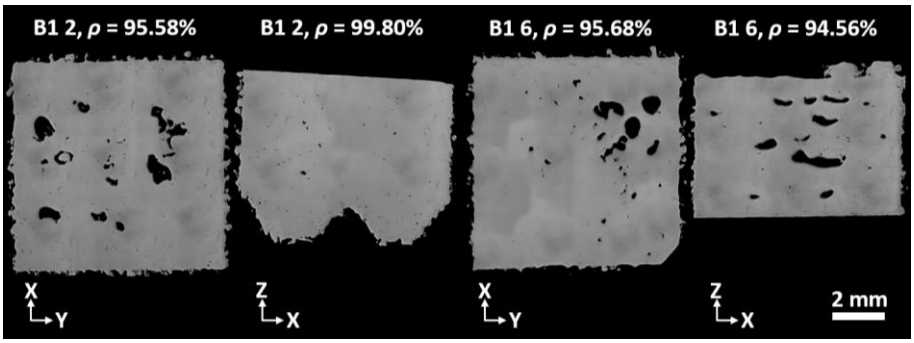

Figure 144 Cross sections showing horizontal and vertical surfaces of double scanned samples 2 and 6 from test B1, all samples 8 mm wide

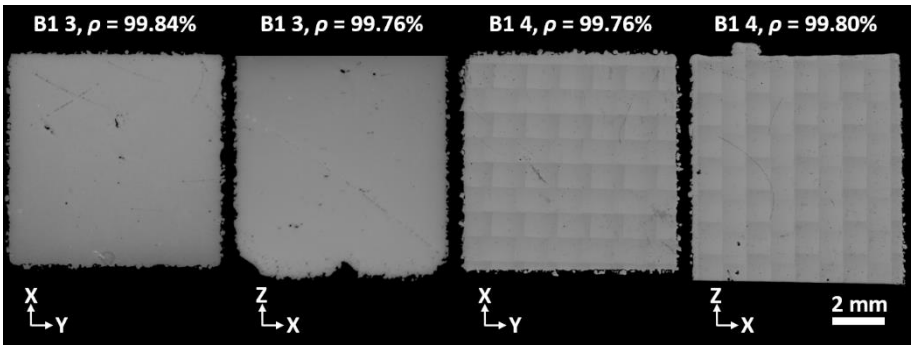

Figure 145 Cross sections of horizontal and vertical surfaces for µm layer samples 3 and 4 from test B1, all samples 8 mm wide

The conclusion from this study was that the parameters were sufficient for 25 µm layer parts, but not so for parts built with 50 µm layers and that there seemed no benefit to double scanning the parts. The challenges with building samples with 25 µm layers was that the powder dosing with the set-up could not be reduced with redesigning the dosing slider. Therefore, the builds were dosed more than the layer required and builds were not as tall due to powder shortages. It was decided better parameters were needed for 50 µm layer single scanned samples. The increased energy needed to entirely fuse the weld track to the previous layer gives the first insight into the material difference between AlSi10Mg and AA6061 as is explored in Chapter 5. The tests that follow are an attempt to improve the density of parts with 50 µm layers.

4.4.2 Test B2: AlSi10Mg, CCD DOE

The first CCD test for AlSi10Mg was centred on the parameters optimised for AA6061 single scanning with 50 µm layer thickness (Table 21). The results from the previous test shown that the main defect was from a lack of fusion, though caution was taken with overheating samples. The range of both point distance and hatch distance were designed to include a minimum value of 30 µm. Exposure was tested 200 µs either side of centre 660 µs value and lens position was tested 1.50 mm either side of 13.00 mm.

Table 21 Range of parameters for test B2: AlSi10Mg, CCD

	UNIT	MIN	MEAN	MAX
POINT DISTANCE	µm	30	70	110
EXPOSURE	µs	460	660	860
HATCH DISTANCE	mm	0.030	0.090	0.150
LENS POSITION	mm	11.50	13.00	14.50

All parts had density exceeding 97%. The relationship between relative density and energy density agrees with the hypothesis that more energy was needed for improved fusion of tracks (Figure 146). Three parts were removed as they suffered build-up of material in their corners. The parameters of these parts are shown in Table 22, these included the sample with the highest energy input (with the central value of lens position), and a part with the largest spot size (with the central value of energy density). The third part had a high energy density and large spot size. Parts with equal energy density and smaller spots as well as parts with equal spot size but lower energy density all built successfully. This suggests that the problem with material being pushed to the corners occurs with a combination of large spot size and high energy input, as was indicated with test A5 (Figure 130). The challenge with this is that the response surfaces suggest that the best results are found in this area (Figure 147). The surface response for hatch distance and lens position both suggest that a trend to

lower their values would improve the density, but the lowest extremities of these parameters were not included in this analysis as the parts failed to build safely.

Table 22 Parameters of failed parts in test B2: AlSi10Mg, CCD

#	POINT DIST.	EXPO	HATCH DIST.	LENS POSITION	ENERGY DENSITY
	µm	µs	mm	mm	J mm^{-3}
24	70	660	0.090	1150	395.7
11	50	760	0.060	1225	957.0
29	70	660	0.030	1300	1187.2

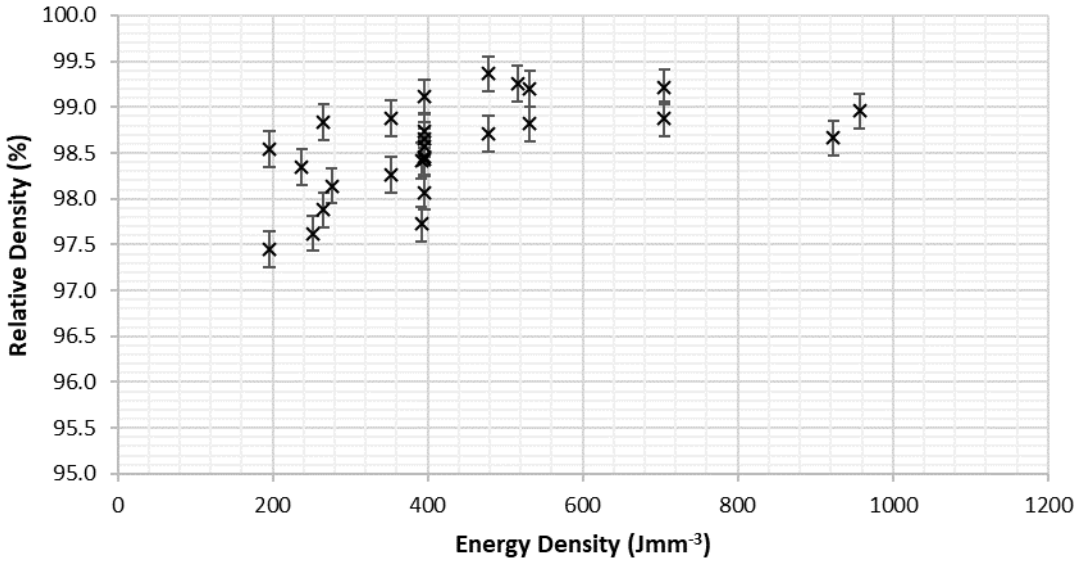

Figure 146 Energy Density vs. Relative Density for test B2: AlSi10Mg, CCD.

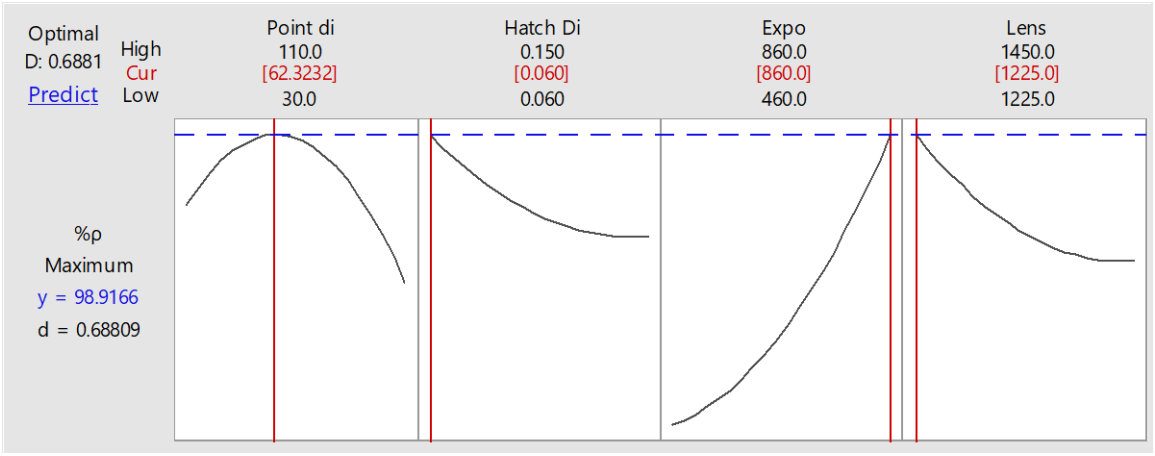

Figure 147 Response surface at the optimum values as calculated through MINITAB for test B2: AlSi10Mg, CCD

The top five densities from this build followed expectations from the surface response, with the energy densities at or above mean and the lens position at or below mean (Table 23). However, the highest density values are very near each other.

Sample 3 was the fifth highest density and was printed with the centre values of the CCD. The average value of these parts was 98.66 ± 0.23 %.

Few defects were found on the micrographs, apart from sample 8, which had similar fusion pores as was event in test B1 (Figure 148). These pores are unevenly distributed which accounts for how they appear in some micrographs more than others, despite samples having similar Archimedes density.

To improve upon these densities the next test had to examine the higher energy densities, as well as the larger spot sizes, while this may risk parts failing as occurred in this build.

Table 23 Top 5 densities recorded from test B2: AlSi10Mg, CCD

#	POINT DISTANCE	EXPOSURE	HATCH DISTANCE	LENS POSITION	ENERGY DENSITY	$\%\rho_{arch}$	$\delta\%\rho_{arch}$
	µm	µs	mm	mm	J mm^{-3}	%	%
6	50	760	0.12	12.25	478.5	99.36	0.19
25	70	860	0.09	13.00	515.7	99.25	0.19
8	50	560	0.06	12.25	705.2	99.22	0.19
1	90	760	0.06	12.25	531.7	99.20	0.19
3	70	660	0.09	13.00	395.7	99.11	0.19

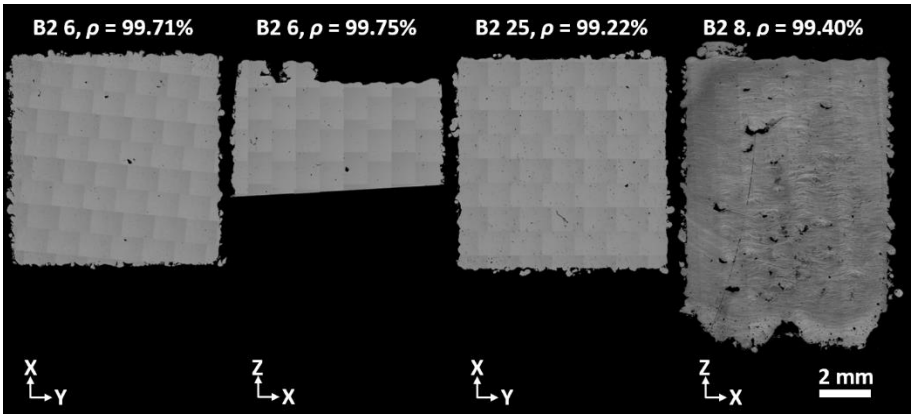

Figure 148 Micrographs of horizontal and vertical cross sections of samples 6, 25 and 8 from test B2: AlSi10Mg, CCD, all samples are 8 mm wide

4.4.3 Test B3: AlSi10Mg, CCD DOE

The results from test B2 suggested that higher energy samples with more diffuse laser beams would yield high density parts but would also move to an area of the process parameter window where part failure was more likely to occur. The caution of part failure is reflected in selection of the range of parameters tested in test B3 (Table 24).

To increase the energy density, longer exposure times were desired, but to lessen the risk of multiple failed parts the minimum value was lowered, and the central value only altered marginally to 700 µs. This ensured, along with hatch and point distances, that a wide range of energy densities were included in the test. The central values of

hatch and point distance was selected as 60 µm, as was suggested by the trend of B2 (Figure 146), though this was to some extent a result of the only sample with a hatch distance of 30 µm failing.

The trend of lens position from B2, strongly indicated that lower values yielded better results, but the lowest value, 11.50 mm, results in a failed part. The range selected included this value as the minimum with the central value reduced from 13.00 mm to 12.50 mm.

Table 24 Range of values for test B3: AlSi10Mg, CCD

	UNIT	MIN	MEAN	MAX
POINT DISTANCE	µm	30	60	90
EXPOSURE	µs	380	700	1020
HATCH DISTANCE	mm	0.030	0.060	0.090
LENS POSITION	mm	11.50	12.50	13.50

As with test B2, three parts failed from material build up in corners. The parameters position within the CCD match those that failed within test B2, with the part with highest energy density, the part with the widest spot and a part with a combination of large spot and high energy density failing (

Table 25). Figure 149 shows how the density of samples from tests B2 and B3 map against their lens position and energy density. The failed samples are on the extreme of spot size and energy density of what has been tested though this does not completely explain the criteria for failure. Of note, is sample 29 from test B2 failed with lens position of 13.00 mm and energy density of 1187.2 Jmm^{-3}, while sample 18 from test B2 built successfully with the same lens position and a similar energy density of 1181.4 Jmm^{-3}.

The difference between the parts for one to build and the other to fail may be due to the hatch distance. It is reasoned in section 4.2 and in chapter 5 that weld tracks are not convex in shape but rather push material away from the centre of the track, with higher energy and large spot size increasing the size of the tracks and the amount of displaced material. If the hatch distance was too narrow, material pushed away from one track gets pushed further with the preceding tracks, appearing to travel perpendicularly to the scan direction. Sample 29 from B2 had a hatch distance of 0.030 mm, half the distance of sample 18 from B3, and this may have been a significant contribution to the part failing.

This may cause material to be swept to the corners of each layer. The alternating scan pattern should start from a different corner with each layer. Starting the scan from the corner should push material away, and avoid the build-up of material, but it was observed in section 3.1.2, that the hatch scans actually start 0.3 mm away from the intended starting point.

Table 25 Parameters of failed parts in test B3: ALSi10Mg, CCD

#	POINT DISTANCE	EXPOSURE	HATCH DISTANCE	LENS POSITION	ENERGY DENSITY
	µm	µs	mm	mm	J mm^{-3}
28	60	700	0.060	11.50	678.0
4	50	860	0.050	12.00	1299.5
21	30	700	0.060	12.50	1356.1

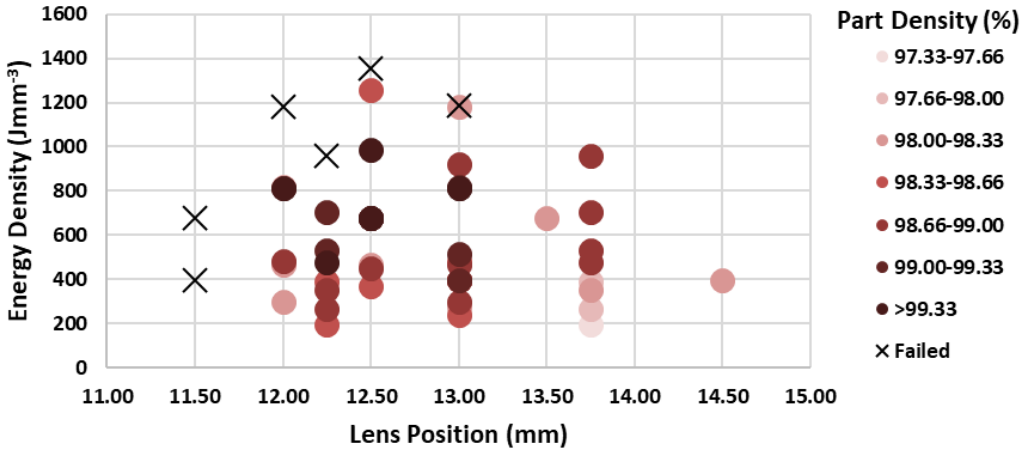

Figure 149 Effect of energy density and lens position on building success of AlSi10Mg, from tests B2 and B3

Many of the samples achieved high densities, near the acceptable level of 99.5% (Figure 150). The surface responses for exposure and hatch distance are similar to trends seen in the previous test but not so for point distance (Figure 151). Though the response surfaces show the extremes in these three cases it can be observed in the results, especially hatch distance and point distance, that extremes did not get the best results. The highest densities suggest that parameters optimised for density are not far from the centre of the CCD. Encouragingly, the lens position surface response suggests that the test was near the optimised value.

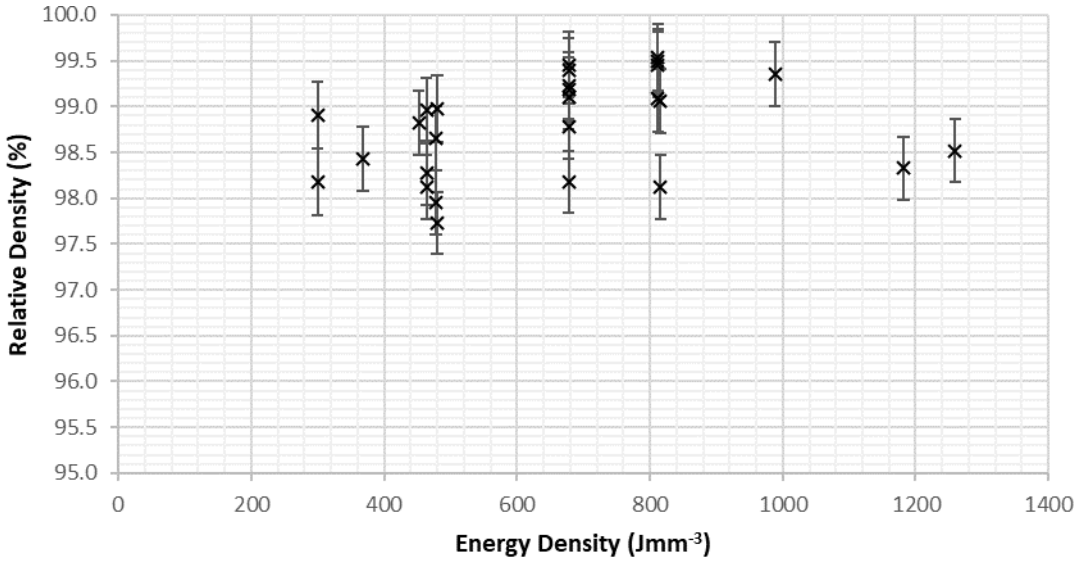

Figure 150 Energy Density vs. Relative Density for test B3: AlSi10Mg, CCD.

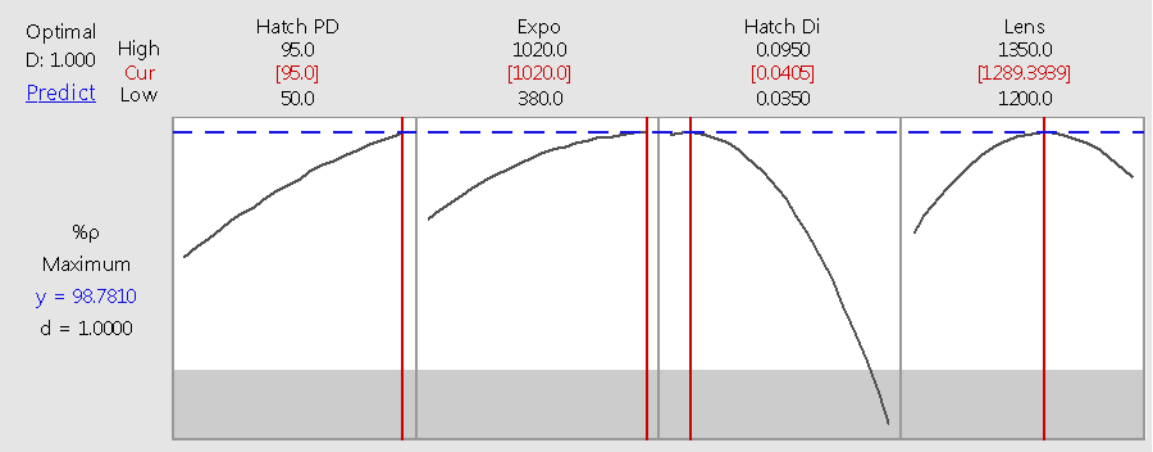

Figure 151 Response surface at the optimum values as calculated through MINITAB for test B3: AlSi10Mg, CCD

The density values did not vary significantly in comparison to their errors (Figure 150), but there was a semblance of an order to the top results. The top three were samples with energy density of 812.2 Jmm^{-3} (Table 26) importantly the top density in this test meets the required density of 99.50%, and the other four values are within 0.11% of this target. One other sample had equal energy density, Sample 5 had the same parameters as sample 15 apart from lens position of 12.00 mm and had a density of 99.09%. Two samples had energy density of 816 Jmm^{-3} with exposures of 540 µs and lower densities which implies that within this region of energy density the exposure time needs to remain high. Five of the six samples below the three highest density samples were all central parameter parts. The average density for these parameters in this build was 99.2 ± 0.22 %.

The cross sections of highest density samples (Figure 152) shown similar features as from test B2 (Figure 148), with fusion porosity more evident in some samples. Equally, it is expected that this can be attributed to issues of sampling and that the parts are expectedly similar.

The highest density from this build was above the acceptable value of 99.5% but not within the margin of error. It was decided to do another build for further improvement. The trends from this build suggests that the optimum value was between the centre of the CCD and higher energy densities near 800 Jmm^{-3}.

Table 26 Top 5 densities recorded from test B3: AlSi10Mg, CCD

#	POINT DISTANCE	EXPOSURE	HATCH DISTANCE	LENS POSITION	ENERGY DENSITY	$\%\rho_{arch}$	$\delta\%\rho_{arch}$
	µm	µs	mm	mm	J mm^{-3}	%	%
8	80	860	0.050	13.00	812.2	99.53	0.36
15	50	860	0.080	13.00	812.2	99.49	0.35
13	80	860	0.050	12.00	812.2	99.46	0.36
23	60	700	0.060	12.50	678.0	99.45	0.36
3	60	700	0.060	12.50	678.0	99.39	0.36

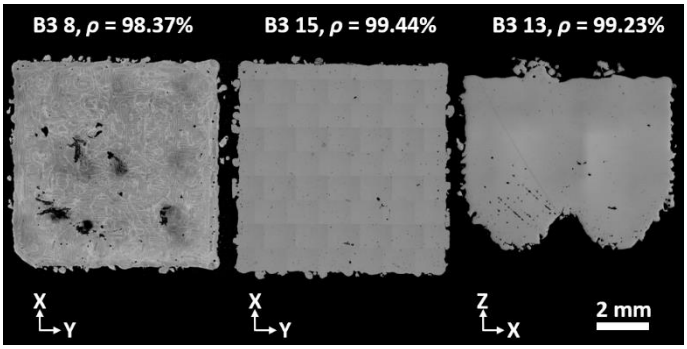

Figure 152 Micrographs of horizontal and vertical cross sections of samples 8,15 and 13 from test B3: AlSi10Mg, CCD, all samples are 8 mm wide

4.4.4 Test B4: AlSi10Mg, CCD DOE

The third CCD DOE test for AlSi10Mg used the same central parameters as used in the previous test but with narrower ranges. The surface responses to hatch distance and point distance were very different (Figure 151), while almost interchangeable when viewing the highest density samples. With the central parameters the same, and the ranges were narrowed. This avoided the hatch distances of 0.030 mm, which caused part failure from pushing material to the corners. The central value of exposure was maintained at 700 µs, with the range shortened. Similarly, the central value of lens position was maintained at 12.50 mm, with a shortened range. Two parts had been built with lens position at 11.00 mm and both failed to build. This was avoided, and the minimum value used in this test was 12.00 mm

Table 27 Range of parameters for test B4: AlSi10Mg, CCD

	UNIT	MIN	MEAN	MAX
POINT DISTANCE	µm	40	60	80
EXPOSURE	µs	500	700	900
HATCH DISTANCE	mm	0.040	0.060	0.080
LENS POSITION	mm	12.00	12.50	13.00

This build completed without any failed parts. All the parts in this build had densities greater than 99% (Figure 153). The central parts of the CCD for test B4 matched those of test B3. These parts were repeated 6 times in both builds with the average densities measuring 99.66 ± 0.19 % from B4 and 99.20 ± 0.22 % from B3. One possible explanation for the increase in results could be that the built samples were taller as the build completed successfully, and the ratio of volume to surface could positively affect results, as could the ratio of sample to feet, where gas porosity is most likely

observed. Another possible contributing factor could have been from the failed parts in test B3, which disrupted the deposition of the powder layer.

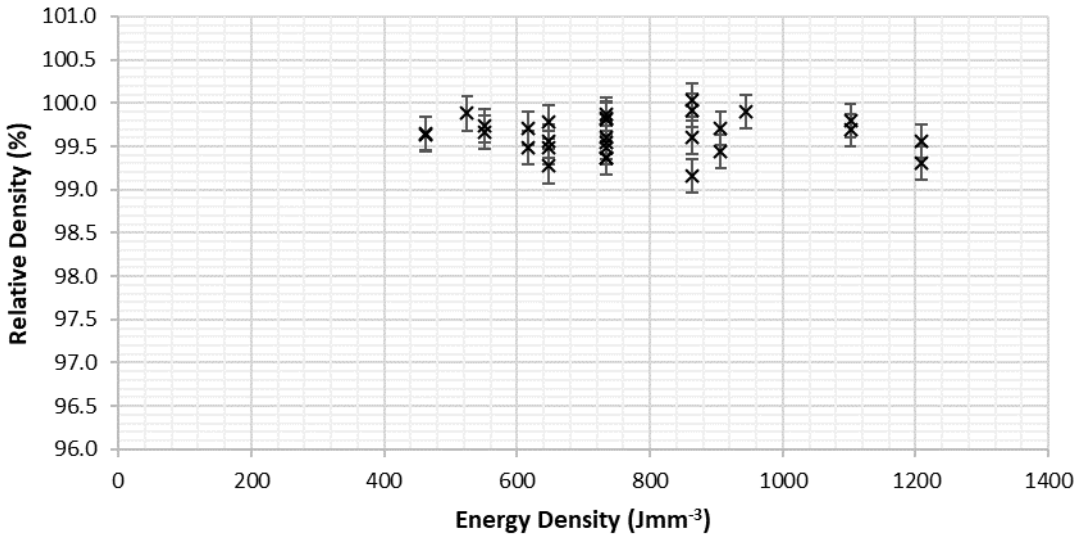

Figure 153 Energy Density vs. Relative Density for test B4: AlSi10Mg, CCD

The surface responses of the parameters (Figure 154) are very different to test B3 (Figure 151). Hatch distance, point distance and exposure are all directed to the opposite extreme, showing a decrease of density with increasing values of these parameters, and lens position no longer appears near central. The fit of these trends to the data causes acceptable residual errors but does not agree with trends visible in the data. The fault in this could arise from the clustered density values. As the densities are all within 99 % – 100 %, there is logically little to differentiate the effect of parameters. This would mark a rational junction to stop using the CCD surface response.

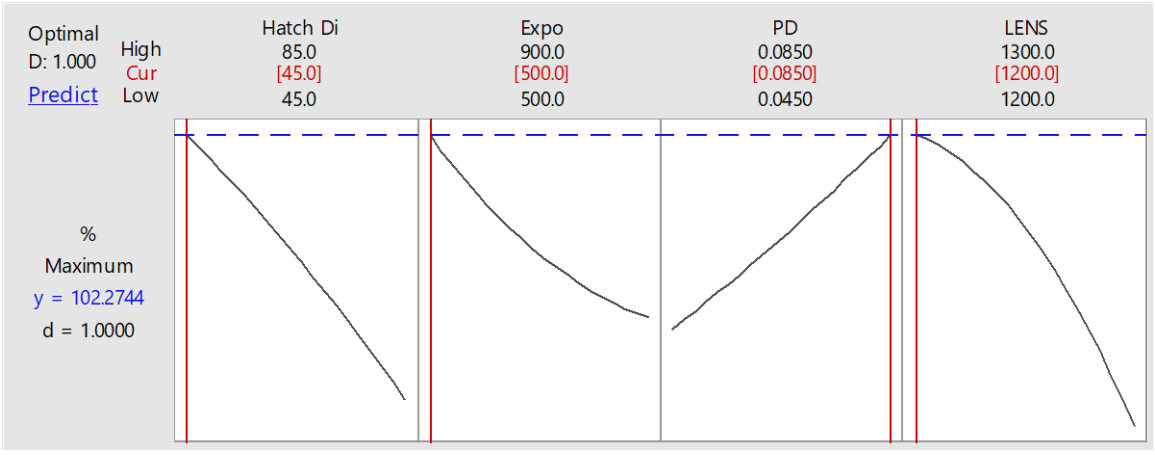

Figure 154 Response surface at the optimum values as calculated through MINITAB for AlSi10Mg single scan test 4

As with test B3, the densities are not differentiated much compared to the errors, but an order does appear: the two highest density samples have similar parameters to that those in the test B3, but all densities are satisfactorily high. This is supported by

the cross sections, which have few defects. There are a few fusion defects still visible but the most porosity is seen at the feet of sample 25. The samples are taller than from test B3, reducing the influence of the porosity in the feet on sample density. As with test B3, the centre parameters produced parts with densities close to the highest densities of the build, sample 23 (Table 28). Samples 19, 20 and 23 have the same parameters apart from exposure. Their near equal densities were unexpected but may just be coincidence with error of the readings.

It may be that the parameters could be improved upon by furthering investigating the region of the samples 7 and 25 from this test and sample 8, 15 and 13 from test B3 but evidence suggests that these parameters are satisfactory.

Table 28 Top 5 densities recorded from test B4: AlSi10Mg, CCD

#	POINT DISTANCE	EXPOSURE	HATCH DISTANCE	LENS POSITION	ENERGY DENSITY	$\%\rho_{arch}$	$\delta\%\rho_{arch}$
	µm	µs	mm	mm	J mm^{-3}	%	%
7	70	800	0.05	12.75	863.5	100.0	0.19
25	50	800	0.07	12.25	863.5	99.92	0.20
19	60	900	0.06	12.50	944.4	99.91	0.19
20	60	500	0.06	12.50	524.7	99.88	0.20
23	60	700	0.06	12.50	734.5	99.88	0.19

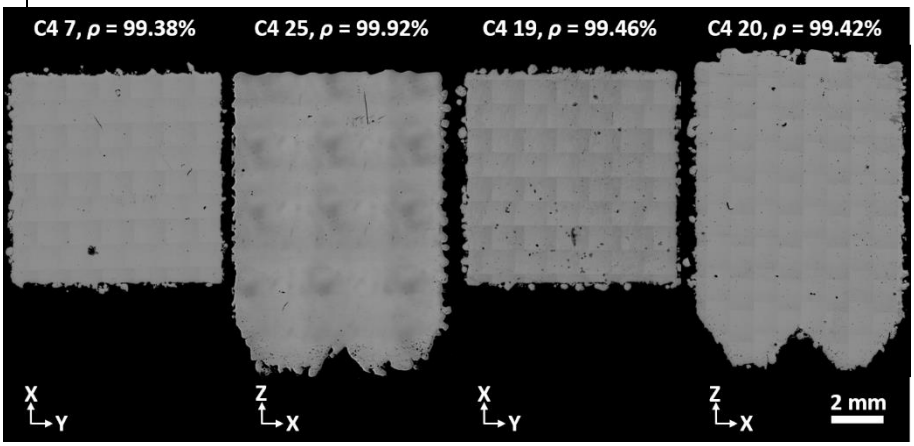

Figure 155 Micrographs of horizontal and vertical cross sections of samples 7, 25, 19 and 20 from test B4: AlSi10Mg, CCD, all samples are 8 mm wide

4.5 SLM of AA6061 - AlSi10Mg Blended Powder

In the previous sections it was shown that cracking was an unavoidable feature when processing AA6061. In the literature review, it was discussed that autogenously welded AA6061 suffers from solidification cracking. There are many similarities between SLM and autogenously welding though the differences do result in a different microstructure and the smaller tracks are expected to reduce the probability of cracking. As such it is unclear how closely the two processes relate. A regularly used solution for solidification cracking in welding AA6061 is to incorporate a filler material

to adjust the composition, typically by increasing silicon content. AlSi10Mg is an appropriate filler material and it was decided that its inclusion could be performed by blending the powders. A blend of powder was prepared with 90% AA6061 and 10% AlSi10Mg, which would increase the silicon content of the AA6061 by 1%. The combined chemical composition is presented in chapter 3.

As with AlSi10Mg the first attempt to the build samples were made using the parameters found for AA6061, and also included were samples built with parameters found for AlSi10Mg. These parts did not have sufficient density and therefore a CCD DOE was employed to find appropriate parameters. The intention of this material was to test if cracking could be reduced and no cracking was evidenced in any of the samples built during this work.

4.5.1 Test C1: Blended Material with AA6061 parameters

As with AlSi10Mg, the first attempt to print blended material used parameters that were found for AA6061 (Table 20) and were printed in the same 3x3 array. The densities are presented in Table 29. Following the parameter development study of AlSi10Mg, samples of the blended material were also printed with the best parameters for AlSi10Mg, from sample 7 from test B4. These results have been included in Table 29.

Table 29 Archimedes and micrographic densities of test C1: blended material printed with AA6061 and AlSi10Mg parameters

	POINT DIST	EXPO	HATCH DIST	LENS	ENERGY DENSITY	$\%\rho_{micr}$	$\%\rho_{arch}$
	Mm	µs	mm	mm	J mm^{-3}	%	%
AA6061 Parameter							
Single Scan (50 µm layer)	70	660	0.090	13.00	395.7	99.05 ± 0.57	99.17 ± 0.76
Single Scan (25 µm layers)	130	400	0.065	13.50	357.6	99.73 ± 0.11	99.55 ± 0.06
Double Scan	70	330	0.045	13.00	791.4	99.76 ± 0.08	99.09 ± 0.70
AlSi10Mg Parameter	70	800	0.050	12.75	863.5	99.22 ± 0.13	100.02 ± 0.31

The densities were all similar for the AA6061 parameters, but slightly higher for the AlSi10Mg parameters (Figure 156). The actual ideal density of this material is not known, and a weighted average was used to calculate the expected value. Two of the three samples printed with the AlSi10Mg parameters recorded densities higher than this theoretical value. It is most likely that ideal density is wrong and more work would be needed to measure this correctly.

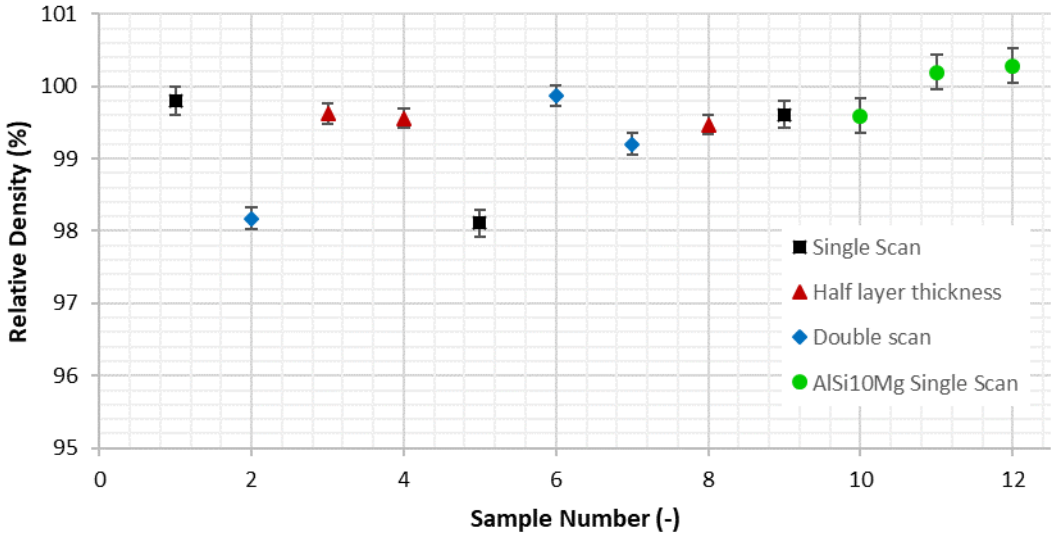

Figure 156 Archimedes densities of test C1: blended material printed with AA6061 and AlSi10Mg parameters

The first notable feature from the cross sections is that there are no cracks present despite only a small change in silicon content, which supports the hypothesis that this material could be an improvement on AA6061 (Figure 157, Figure 158, Figure 159 and Figure 160). There is a small amount of evidence of fusion pores in the blended material samples, which was the main defect in AlSi10Mg samples. The horizontal surface of single scanned sample 5 has large irregular shaped pores which are likely to be fusion pores but neither vertical surface of sample 1 nor 5 show evidence of the pores seen in AlSi10Mg. The double scanned samples show more evidence of fusion porosity. The arced shape of these pores on both the horizontal and vertical surfaces could be fusion pores, or could be examples of surface oxides preventing fusion. The presence of oxides within the samples is discussed in chapter 5, but from that analysis it is improbable that the oxides would be incorporated during the second scan, therefore in either case the flaw is unlikely to have originated in the second scan unless caused by keyhole porosity.

Much of the porosity present is gas porosity. Both the 50 µm and 25 µm layer thickness single scanned parts show large amounts of gas porosity. In samples 3 and 4, there are very fine pores evenly distributed. The porosity in the 50 µm layer thickness samples is less uniform. The vertical surface of sample 5 shows rows of very fine pores a layer thickness apart, while the vertical surface of sample 1 shows larger and randomly distributed pores. The difference in the appearance in porosity could be based on location and how far from the edge the cross section is. No gas porosity is seen in the double scanned parts. Gas porosity can be removed if the solidification is slow enough to allow the gas to escape, or rescanning can allow this to happen. Samples 10, 11 and 12 had less gas porosity and were scanned with longer exposure times. The issue with gas porosity could be caused by moisture being carried into the chamber by the gas or from the powder. It is most likely that the moisture was carried

in to the chamber from the powder, which can deteriorate with age, as discussed in the literature (section 2.3). The study of the oxides, in chapter 5, shown evidence of the AA6061 powder aging, with greater presence of oxides in later produced samples. The conclusion from this is that this material requires more energy than was needed for AA6061 and may need longer melting times to allow for the removal of gas porosity.

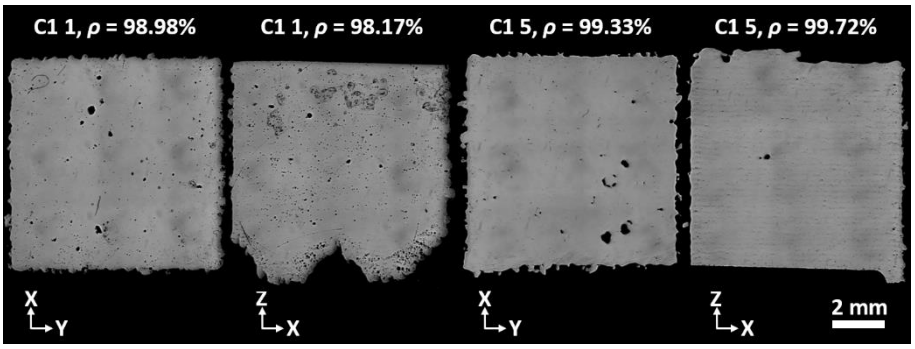

Figure 157 Micrographs of horizontal and vertical cross sections of single scanned samples 1 and 5 from test C1

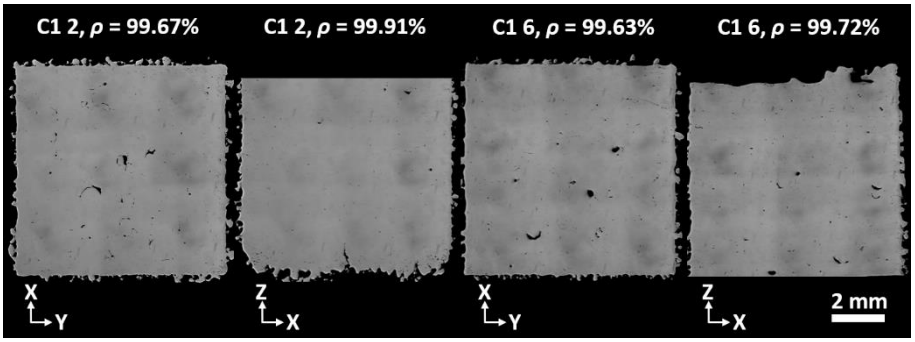

Figure 158 Micrographs of horizontal and vertical cross sections of double scanned samples 2 and 6 from test C1

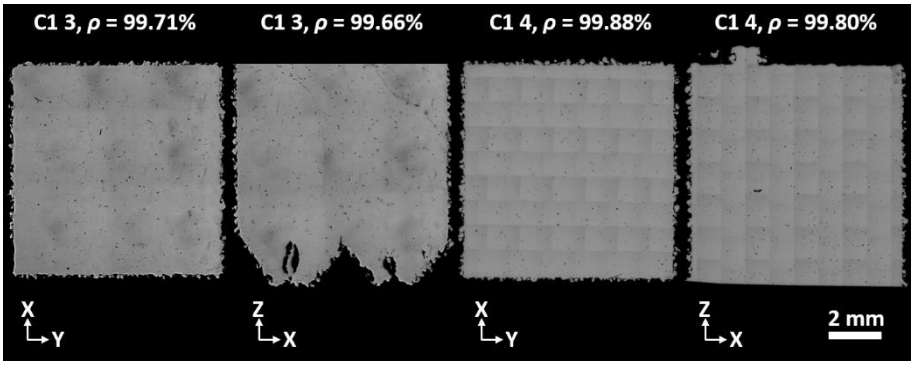

Figure 159 Micrographs of horizontal and vertical cross sections of single scanned, 25µm layer samples 3 and 4 from test C1

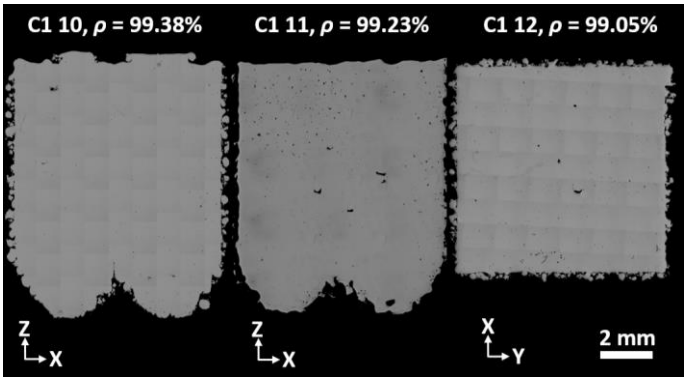

Figure 160 Micrographs of horizontal and vertical cross sections of single scanned samples printed with AlSi10Mg parameters from test C1

4.5.2 Homogeneity of blended parts

As the blocks were made with using a blend of powders it is important that the powder mixed sufficiently. EDX elemental maps were used to examine the homogeneity of the built parts. As can be seen in Figure 161, there are no obvious areas of differing composition, as was seen in the EDX of the powder (Figure 103). There is a preferential element count towards the bottom right corner of each image, which is a result of the position of the EDX detector. This is a good indication that the powders mixed successfully.

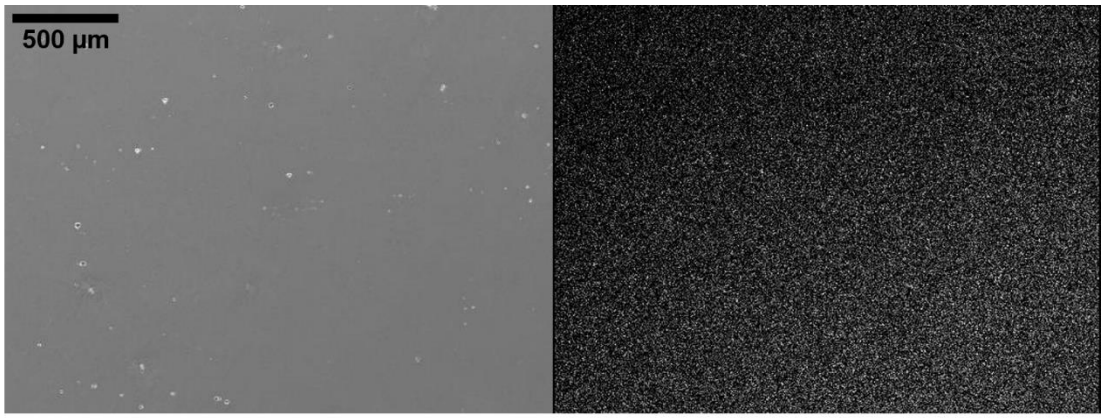

Figure 161 SEM and EDX silicon map of the vertical cross section of blended power sample 1 from test C1

The overall composition and the composition near the pores were examined. In Figure 162 spectrums 3 and 4 are spot measurements placed directly on pores, while spectrum 5 is a spot measurement of the bulk material. Spectrum 2 is a measurement of the entire area.

Spectrum 2 shows acceptable presence for the three main elements, aluminium, silicon and magnesium, though the oxygen content is a little higher than would be desirable. The pores have a higher oxygen content and fractionally higher silicon

content and the impression from these results is that the pores are drawing the silicon from the solid material to the pores. It was observed that in previous work (Louvis, 2011) that the oxides from AlSi10Mg were decorated with silicon. The relationship of oxygen interaction with the alloying elements is studied further in the following chapter. For this section, this result is enough to show that the two powders mix sufficiently to create a homogenous material.

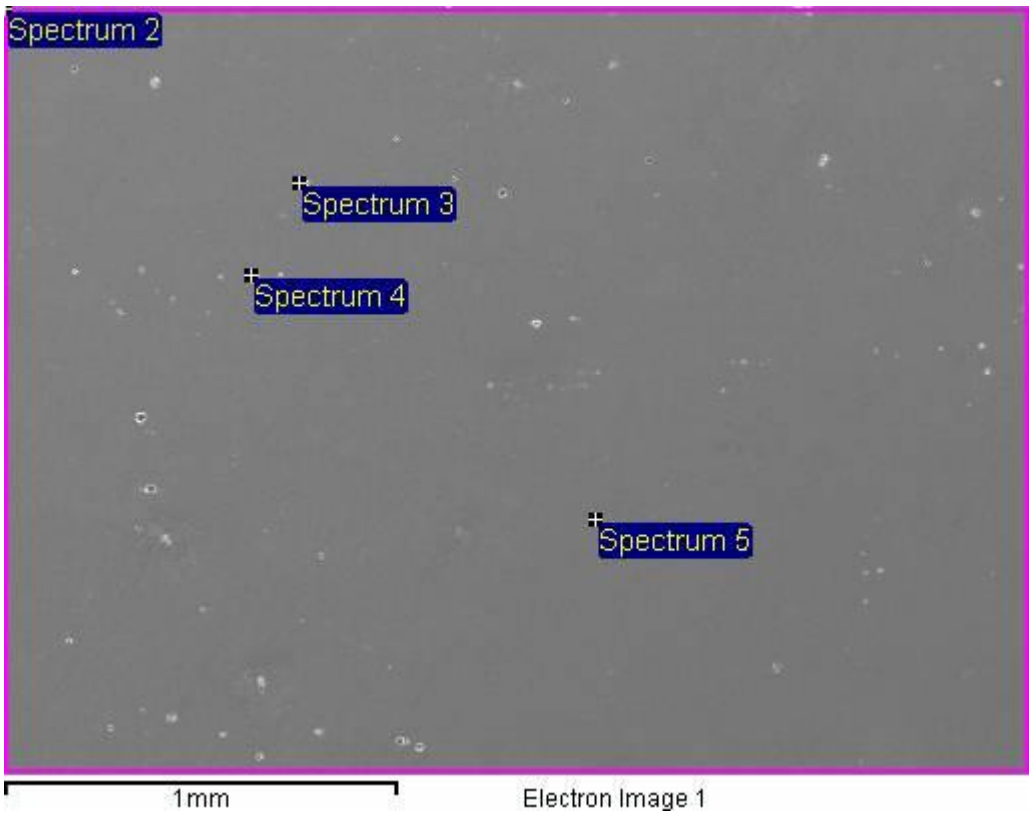

Spectrum	Al	O	Mg	Si
2	97.23	0.80	0.45	1.52
3	86.34	11.40	0.02	2.24
4	67.53	24.43	0.67	7.37
5	97.14	1.41	0.59	0.86

Figure 162 EDX of the vertical cross section of blended power sample 1 from test C1.

4.5.3 Test C2: Blended Powder, CCD

The blended material samples did not process satisfactorily with either the AA6061 or AlSi10Mg parameters. The cross sections of the blended material samples showed a large amount of gas porosity, especially with those processed with the AA6061 parameters for single scanned 50 µm layers. The expected solution to removing gas pores, as suggested in literature, is to increase the time of heating and therefore slow the solidification rate to allow more time for the expelled gas to float through the molten metal. Without decreasing the power, this will increase the energy density of

the parts. Encouragingly, parts processed with AlSi10Mg parameters had higher energy density and lower porosity.

With these deductions, it was decided to test a parameter window between that of the AA6061 and AlSi10Mg parameters as well as extending to high energy density samples. The parameters that were selected for the CCD DOE are presented in Table 30. Ranges of exposure time and lens position tested between the best values found for AlSi10Mg and AA6061, while wider ranges for hatch distance and point distance were tested, which would extend the energy density of samples beyond that of the AlSi10Mg samples.

Table 30 Range of parameters for test C2: blended material, CCD

	UNIT	MIN	MEAN	MAX
POINT DISTANCE	µm	30	70	110
HATCH DISTANCE	mm	0.030	0.070	0.110
EXPOSURE	µs	660	730	800
LENS POSITION	mm	12.00	12.50	13.00

Most of the samples recorded higher densities than the expected ideal density (for consistency the relative density is still reported despite this) (Figure 163). There is no clear trend in the density compared with energy density. The densities of each sample are not differentiated by much and, as with AlSi10Mg CCD DOE test 3, this make observed trends less trustworthy. The six samples printed with central parameters had an average density of 100.27 ± 0.39 % and as such 23 of the 30 samples recorded densities within one deviation of the central parameters.

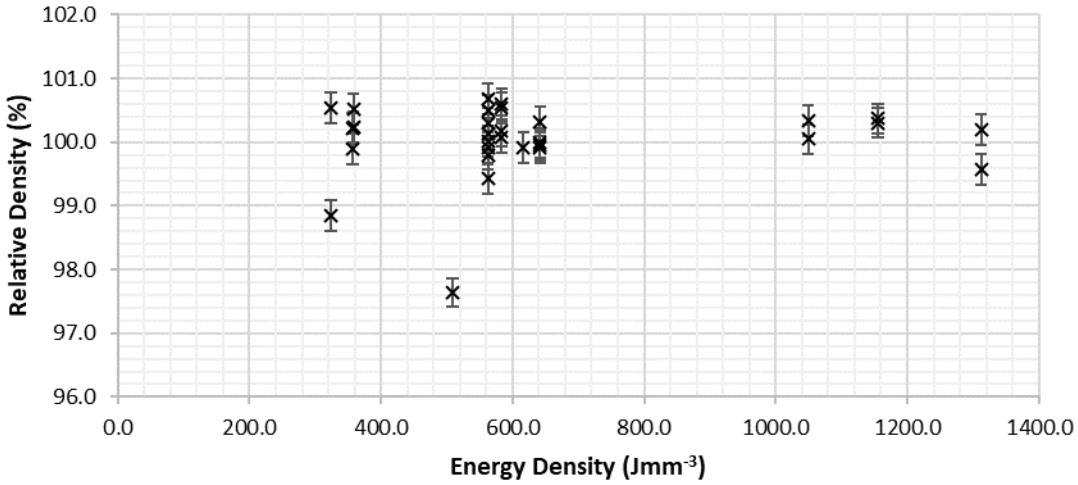

Figure 163 Energy Density vs. Relative Density for test C2: blended material, CCD

With only a small change in the density across the samples there is a higher risk of the surface response showing incorrect trends, as was evident with test B4. The surface responses suggest a lower energy input per scan line compared to the two previous

materials, with low exposure time and above average point distance (Figure 164). The trends of hatch distance and lower lens position could relate to greater overlap of scan tracks, which may enable reduced gas porosity, comparable to the double scanned parts.

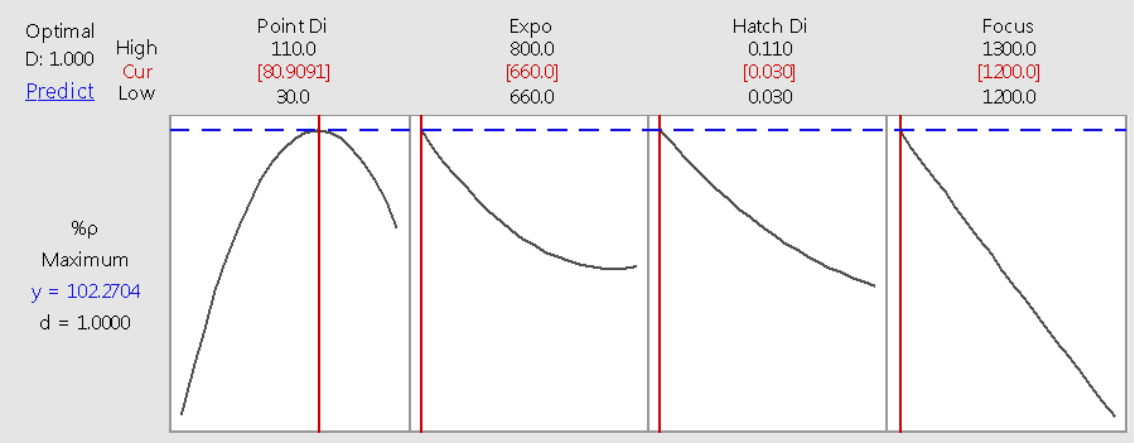

Figure 164 Response surface at the optimum values calculated through MINITAB for test C2: blended material, CCD

The five highest densities (Table 31) did not follow the all trends of the response surfaces. The highest density sample was found with the sample with the finest spot size, in contradiction to the surface response. This sample had a value of point distance, hatch distance and exposure from the centre of the CCD. These parameters were also printed the lens position at the mean value of 12.50 mm, with an average density of 100.27 ± 0.39 %, and with lens position at 12.00 mm, with density of 100.30 ± 0.24%.

No samples within the five highest densities had very high energy densities. Only one sample had a point distance below the mean and none had exposure time above the mean values, which is in agreement with the surface response, but all samples had a hatch distance at or above the mean tested.

The cross sections (Figure 165) all had micrographic densities that are reasonably high. Samples 14 and 13 have some irregular shaped pores, likely to be fusion pores. The other three samples only reveal very fine spherical pores, likely to be gas porosity (Figure 166).

Table 31 Five highest densities from test C2: blended material, CCD

#	POINT DIST.	EXPO	HATCH DIST.	LENS POS.	ENERGY DENSITY	$\%\rho_{micro}$	$\%\rho_{arch}$	$\delta\%\rho_{arch}$
	µm	µs	mm	mm	J mm^{-3}	%	%	%
22	70	730	0.07	13.00	562.5	99.87	100.7	0.24
15	50	695	0.09	12.75	583.2	99.79	100.6	0.24
14	90	695	0.09	12.25	324.0	99.58	100.5	0.24
24	110	730	0.07	12.50	358.0	99.80	100.5	0.24
13	70	730	0.07	12.50	562.5	99.46	100.5	0.24

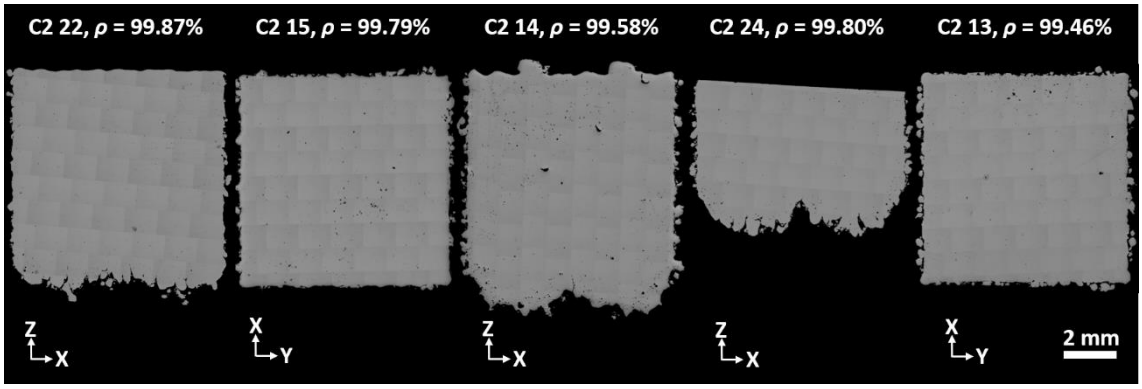

Figure 165 Optical images of horizontal and vertical cross sections of samples 22, 15, 14, 24, 13 from test C2, all samples are 8 mm wide

As no ideal density is known for this material, and efforts to calculate the density have evidently underestimated the real value, the Archimedes density can not be used to measure the correct relative density. The highest density recorded with this material was 2.7139 ± 0.065 %. In this instance, micrographic density is more appropriate to gauge the relative density. The micrographic density of sample 22 is sufficient despite the gas porosity (Figure 166). It was decided to accept these parameters and progress to evaluating the microstructure of the materials in the succeeding chapter.

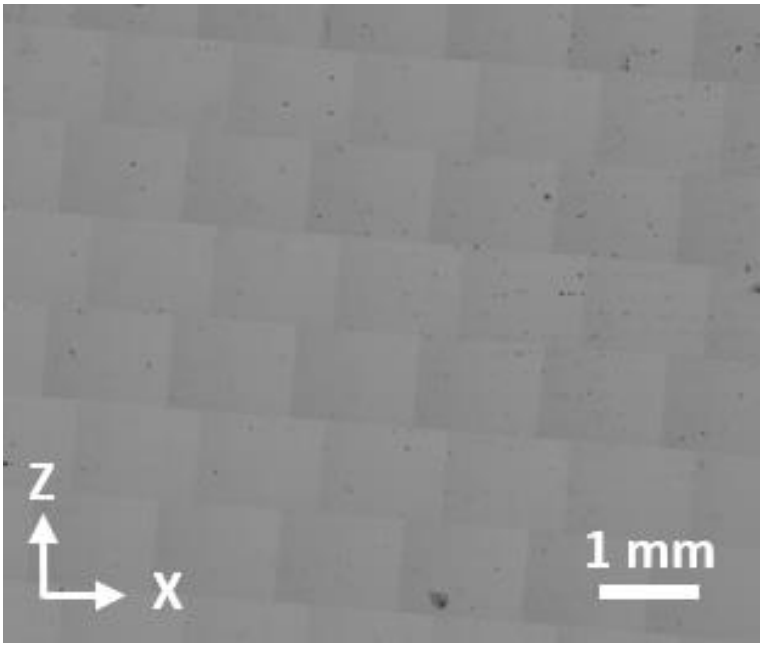

Figure 166 Optical microscopy of the vertical surface of sample 22 from test C2

4.6 Summary

In this work it was observed how AA6061 processed through SLM. It was found that high densities could be achieved but all parts were compromised by cracking. Different processing parameters and conditions were tested to influence the cracking

behaviour in AA6061 with no success. The solution of modifying the material was very successful and no cracking was observed in any samples.

In chapter 5, the differences of the materials are evaluated to understand the cause of the cracking in AA6061, and the effect of the material change. In order to perform this analysis, it is important to have high density samples. Parameters to achieve the high densities were achieved by following the CCD DOE described in section 3.8. The number of tests to achieve the selected parameters was different with each material. The parameters to achieve the highest density samples for AA6061 was found after two iterations of the CCD, with following experiments testing if cracking could be reduced. AlSi10Mg required three iterations, and the blended material requiring only one CCD test. Challenges with this method were created with failed parts, which weren't registered with results. The surface responses of the final test did not predict optimum parameters that were internal to results, but rather extrapolated results to predict higher density beyond the tested processing window. Critical judgement was needed to assess the reasons for the trends shown in the response surface and conclude parameter optimisation. As an example, the surface responses of the final result of AlSi10Mg (test B4) predicted lower energy density than was in the test but this did not agree with the trend of the highest densities and as sufficient density was achieved, it was decided to stop. Improvements to this method could be from developing better fitting models to the results, as the relationship is limited to being interpreted as a quadrilateral equation and not as a logarithmic relationship observed in the energy density vs. part density graphs. The DOE used proved successful in directing the tested parameters toward higher densities. Should this approach be used where quality and reliability are more critical, as in industrial applications, fine tuning parameters may be necessary. Defining the optimum process parameters was challenging with surface response not agreeing with visual results. It may be more advantageous to use this DOE to define a reduced process window, within which a full factor parameter study can be performed. For the purpose of this research the desired densities for all materials was achieved.

Challenges with measuring the sample densities were also observed. Errors in the Archimedes density measurements were evident in test A1, with water infiltrating a part with low density. In this instance, a different methodology should be used. This form of error was not observed in following tests but could cast some doubt on the reliability of these results. Another error with this method found with test A1, was from miscalculating the density, likely from miscalculating the density of the liquid. More accurate results could be found by using a thermometer submerged in the liquid.

Measuring the relative density of the blended material proved difficult as the attempt to calculate the ideal density proved incorrect. One suggestion is calculating the ideal

density by producing a sample from the powder by HIP (Hot Isostatic Pressing) process to create a highly dense sample to compare to.

Without knowing the ideal density, the test relied on the micrographic density to determine the suitability of the process parameters. The reliability of these results could be questioned as tests throughout this chapter have displayed the challenges of sampling error associated with this method.

It was decided that the process parameters were appropriate to continue to the analysis of these materials. In this, the design of experiments approach proved successful, though the method could be refined, with the suggestions above. In the subsequent chapter, the material microstructure is analysed alongside crack analysis and presence of oxides. The intention of this is to determine the cause of cracking with AA6061 and potential suitability of the blended material for AM processed lightweight structural applications.

5 Investigation into Cracking in AA6061

In chapter 4 it was shown that cracking could not be avoided when processing AA6061 through SLM, irrespective of process parameters. An alternative material with a higher silicon content was devised which processed readily without any cracks appearing. This material was the product of blending AA6061 and AlSi10Mg powders and will be referred to in this chapter simply as blended material. The intention of this chapter is to investigate the cause of cracks within AA6061 and explain why cracks do not appear in either AlSi10Mg or the blended material.

It was discussed in the literature review that the suspected cause of cracks within AA6061 was from solidification cracking. The identification of this problem is not obvious from the literature and different theories exist of the mechanisms involved in causing the cracks. In order to identify that this was the cause, it is necessary to discount other potential causes, and so other potential causes that were identified in the literature are also assessed in this chapter.

The main potential causes of cracking that were considered were; residual thermal stresses, solidification cracking, and detrimental inclusions, such as oxides. These were assessed by examining the sample microstructure, the composition of cracks and the location of cracks within the built samples and within the grain structure, as well as deep etching samples to reveal the oxides present.

The conclusion from this analysis was that cracks were cause by solidification cracking, which initiate as pores present within grain boundaries, with all other potential causes considered disproved. This proposed explained is added to by the solution of increasing the silicon in the alloy, which fills gaps between the grain boundaries and prevents the cracks initiating.

5.1 Effect of Part Shape and Scan Direction on Cracks within AA6061 Parts

One of the potential causes of cracking is from thermal stresses, as this is known to cause cracking in SLM processed alloys [236]. Furthermore, irrespective of the initial cause of the cracks, thermal stresses, created from the unevenly shrinking material, will open cracks surfaces and propagate the cracks through the material, as discussed in the literature review. The geometry of the weld tracks effects the magnitude and direction of the stresses and the addition of weld tracks effect the accumulation of stresses.

Considerable literature has been published on the accumulation of residual thermal stresses with SLM parts and it has been shown that the highest stresses occur vertically causing horizontally oriented cracks (Figure 60), though due to the anisotropy, residual stresses can alternatively cause cracks from horizontal stresses (Figure 61). It was shown in test A5 how cracks oriented with the scan tracks (Figure 133). This is not the direction of principle stress and therefore implies a weakness from which the cracks initiate but does not explain how the cracks are affected by the accumulation of stresses.

A test was devised to examine the relationship that cracking has with the accumulation of stresses by assessing the location of cracks within parts of different shape and track orientation (Table 32). Three scanning strategies and four shapes were used to examine how the cracks are influenced by scanning direction and accumulation of stresses. The part shapes were designed with height and width (in Y direction) of 8 mm but varying in lengths (in X direction) of 4 mm, 8 mm, 16 mm, and 32 mm. The scanning strategies that were tested were XY alternating, all-X, and all-Y. The omission of the top surface images of the 4 mm long samples was an error as the samples were not photographed before mounting and polishing. A corner was removed from the 8 mm long samples to identify orientation. The 32 mm long samples were sectioned to show the side view of the cracks. The all-Y 32 mm sample broke when removing from the build plate, revealing a crack surface that was examined below (5.1.1).

The results show that the cracks, though not perfectly straight occur in the direction of the scans and part shape has no influence. The cracks do not occur under the accumulation of stresses which would alter with the different shapes but rather they occur under stresses local to the cracks. It can further be inferred that cracks occur during processing and the most likely scenario is that the cracks permeate the layer as it solidifies, evidence of this appears in the vertical cross sections, where cracks propagate through the top layer.

The cracks are evenly spaced and appear 0.9 mm apart in all unidirectional parts. This equals ten times the hatch distance. It is plausible it takes multiple scans for the stresses to accumulate in this area before the cracks appear and the shape of the part had no effect as it is on a larger scale with cracks providing stress relief. In this, the part doesn't have to suffer specific weakening at ten hatch spacings, but rather the continuous weakening in the scan direction will cause the cracks to be spaced evenly. This may change with different laser parameters.

Table 32 Images of top surfaces and corresponding cross sections of AA6061 samples printed with varying scanning strategies and sample length

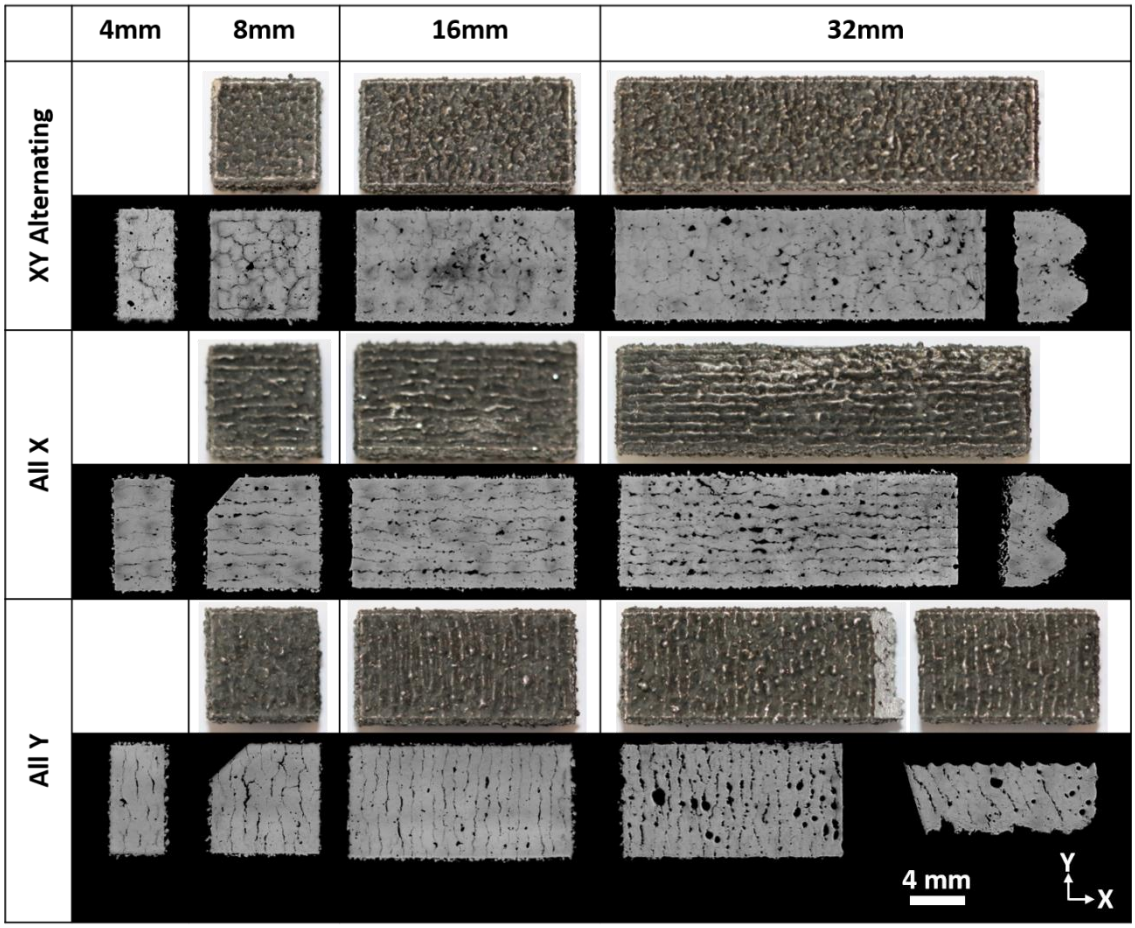

Parts scanned with all-x strategy show no cracking across the track irrespective of the track length. The longer the track length the greater the stresses, which is a strong sign that the thermal stresses generated would not cause cracking apart from a weakness parallel to the track direction.

It has been observed in titanium samples, processed in SLM, that stresses are greatest parallel to the scan direction [186], which is the direction that the tracks undergo the greatest shrinkage. The cracks do not appear in the direction of greatest stress but in the direction of the weld track. This resembles the solidification cracks that appear in welded samples (Figure 72) but could also be caused by weakness such as oxides forming between tracks.

It is a great challenge to understand when and where oxides form in SLM of aluminium. Oxides could be forming on the sides of weld tracks during processing and it has been suggested in the literature that oxides can be pushed through samples with subsequent scan tracks, as occurs in cast aluminium [176]. The wavy top surface may be a result of surface tension that is worsened by the presence of oxides and occasionally gets incorporated into the sample body. Alternatively, the oxides could be partially broken but remain, weakening the bond between tracks. This would pose a better explanation to the consistency of the cracks.

Another consideration that must be made, is that the cracks may not be from the same source as in the density samples but from imperfectly fusing adjacent tracks, as the parameters that were used were found for alternating scanning and not unidirectional scanning. The higher levels of porosity may be evidence that the parameters could introduce other sources of weakness that could lead to samples cracking. The presence of pores could act as stress concentrator and be the initiation point for cracks to propagate. Alternatively, the pores could act as stress reducers by relieving shrinkage, so it is difficult to estimate what affect they have had on the results. To ensure that the conclusions drawn from this experiment with unidirectional scanned parts can be used in analysis of the XY alternative scanned parts, the surfaces of the cracks in both are analysed through SEM and EDX, in sections 5.1.1 and 5.1.2. This analysis further informs how the cracks form.

5.1.1 Fractography of All-Y Scanned Sample Crack Surface

The all-Y 32 mm long sample fractured while removing from the build plate, revealing the crack surface. The sample was placed in an SEM and examined using EDX. In Figure 167, the part was aligned to try and measure both the top surface and the cracked surface for comparison.

Spectrum 1 recorded the chemistry of the top surface, while the spectrum 2 recorded the chemistry of the crack surface. The top surface had very high levels of oxygen as well as magnesium and zinc. The presence of these two metals has been observed in SLM aluminium oxides in literature with the argument that their comparatively low evaporation temperatures lends them to vaporise and react with oxygen and condense onto the surface of the samples [212]. The zinc reading is still unreasonably high as AA6061 only contains trace levels of zinc up to 0.25 %. It was observed that the EDX overcounts oxygen (section 3.3.4) but the level of oxygen is still excessive giving strong indication of its presence on both surfaces. Spectrum 6 is a point reading on the top surface. The reading has lower oxygen level but is largely in agreement with the area spectrum.

Spectrum 2 shows a lower but still high level of oxygen. The magnesium level is very high while zinc was not observed. The cracked surface showed trails of a material that distinguishes itself from the bulk as it has a different intensity, possibly from charging due to poor conductivity of oxides. These trails appear darker to the fracture surface in optical microscopy, and similar in tone to the top surfaces. On this trail were unmelted powder particles, which implies they hindered melting and fusion of tracks. Spectrum 3 shows the point measurement for the bulk material. The magnesium count is very high but the rest of the elemental count is not unreasonable. Spectrum 4 shows the composition of the trail of charging material. The material is closer to what was seen on the top surface, though maybe in less concentration with more bulk material being included in the measurement. Spectrum 5 was another attempt to

measure this composition but was not in agreement with spectrum 4. The angle of the sample may have caused an error in where the point measurement was registering counts. The surface roughness and the angles at which the detectors operate can cause misalignment of the recorded locations. To improve this and to view the surface at a more direct angle, the sample was sectioned and remeasured.

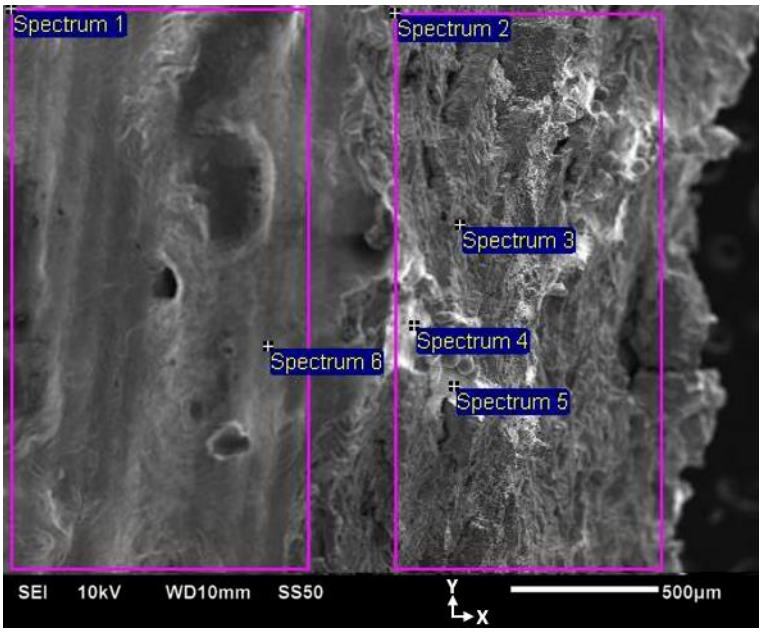

Spectrum	Al	O	Mg	Si	Zn
1	46.54	27.95	10.07	0.22	15.22
2	76.40	10.11	11.85	0.16	-
3	91.63	0.01	7.50	0.87	-
4	72.56	16.02	6.07	0.24	5.11
5	87.68	0.04	12.28	-	-
6	55.88	15.48	13.29	0.23	15.12

Figure 167 Top surface of all-Y scanned part and fracture surface along the face of a crack that occurred during the build, and EDX composition analysis (wt%)

Figure 168 shows an SE image of the fractured surface from the 32 mm all-Y sample, with EDX composition measurement. The magnesium content is much lower than was measured in Figure 167. A thin layer of magnesium may be on the surface and therefore the depth of the measurement, which is influenced by angle of incidence, will proportion the magnesium differently. A small increase in magnesium can be expected to be found within the grain boundaries, alongside silicon, and failure could have occurred along could account for the higher values compared to material's bulk composition. Alternatively, magnesium has a very high affinity for oxygen and the fracture surface show magnesium oxides.

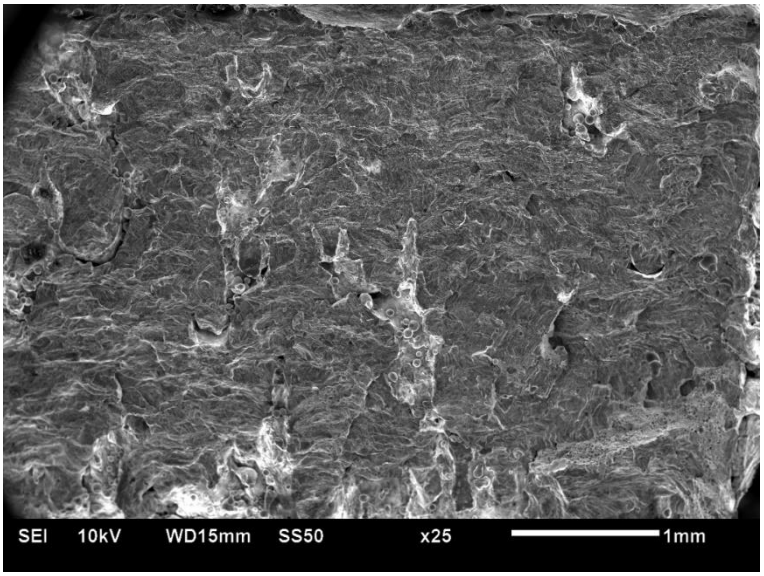

Spectrum	Al	O	Mg	Si	Zn
1	81.14	14.27	1.80	1.73	0.45

Figure 168 Fracture surface of all-Y scanned part, revealing the face of the crack that occurred during the build, and EDX composition (wt%)

The fracture surface is very jagged with many differing features, including apparent fusion pores. The lighter toned areas do not exhibit structures associated with brittle or ductile fractured surfaces and have unmelted or partially melted powder particles attached (Figure 169). It was seen in Figure 167, that they are comparable in composition to the oxides on the top surface. This could support the hypothesis that the oxides that are forming on top of the samples are infiltrating the parts causing weak fusion of aluminium, alternatively, analysis of oxides forming between cracks in section 5.4.4, suggests that strong oxides form on exposed crack surfaces during the build, similar to oxides seen on the top surface (Figure 214).

The appearance of the oxide surface suggests it has not fractured, but rather that solidified molten metal. It is possible that molten material could have infiltrated an existing crack, without filling the gap with oxide forming on the open surface. If the gap was large enough for this to be the case, then it may have been large enough for power particles to fall within the crevasse. This is supported by the location of the oxide and unmelted powders at the site of crescent shaped fusion pores.

The closer view of the fusion pores (Figure 169) revealed that some microcrack defects connected to the pores, but these are below the pores and are not continued above. From considering the results from Table 32, it was perceived that the cracks were likely to propagate through a layer during scanning and so the fusion pore is unlikely to cause cracking below. Reversely, fusion of the melt track could be hindered by the defect below. It may be worth considering that the fractured surface is parallel with the scan tracks, despite the fusion defect taking the crescent shape of a weld track and the microcracks run perpendicular to the primary crack. The shape of the fusion pore is likely explained as part of molten scan tracks that drop between

crevasses formed from the formed cracks and therefore are a feature formed due to cracking and not a source of it.

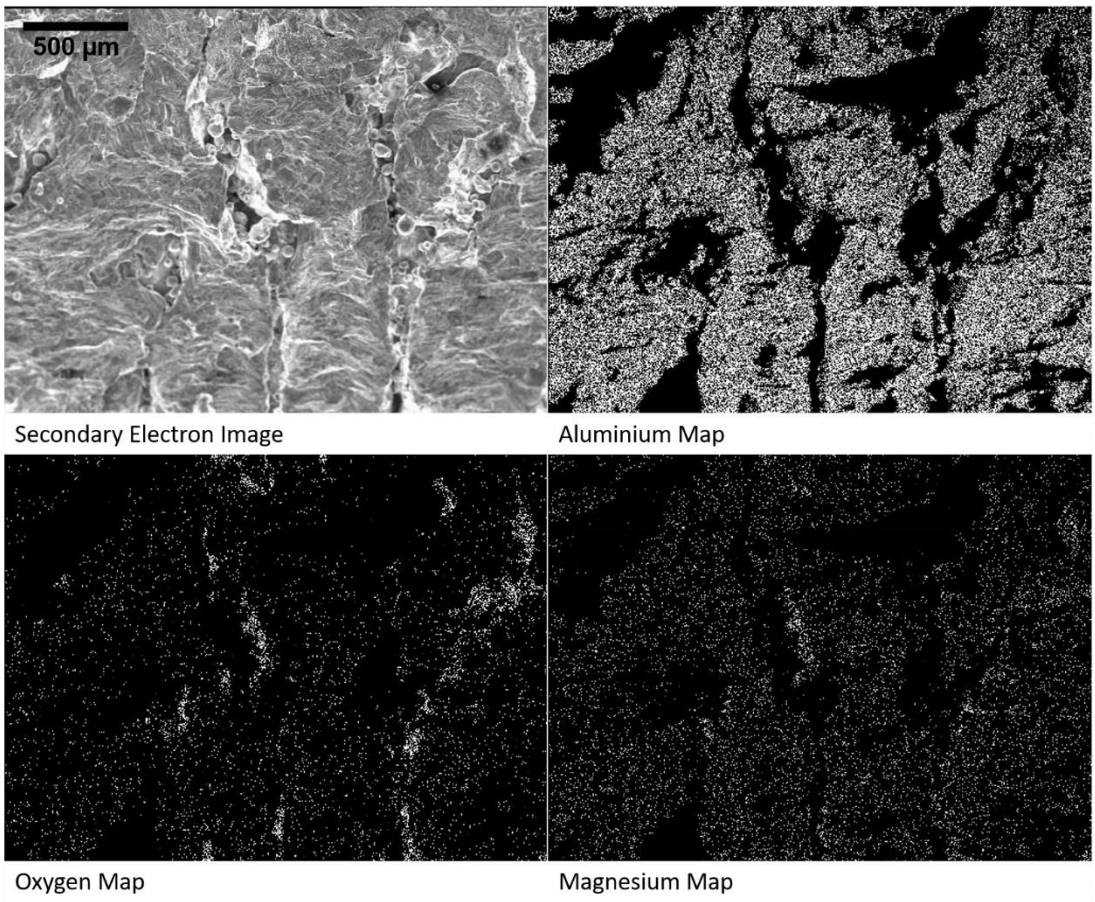

Spectrum	Al	O	Mg	Si	Zn
20 kV	92.43	4.93	1.4	0.75	0.48

Figure 169 SE image of fracture surface from all-Y scanned sample and EDX elemental maps and composition of the most prominent elements (wt%)

The elemental maps (Figure 169) from these cracks show areas of high oxygen and low aluminium content. The areas of high oxygen map closely to the areas of charging in the SEM image, as well as having higher magnesium concentrations. The maps are lacking in detail and many areas in the map are blank as the detector did not have a direct line of sight due to the rough surface. To improve the detail of areas with oxides another EDX analysis was performed with a higher magnification.

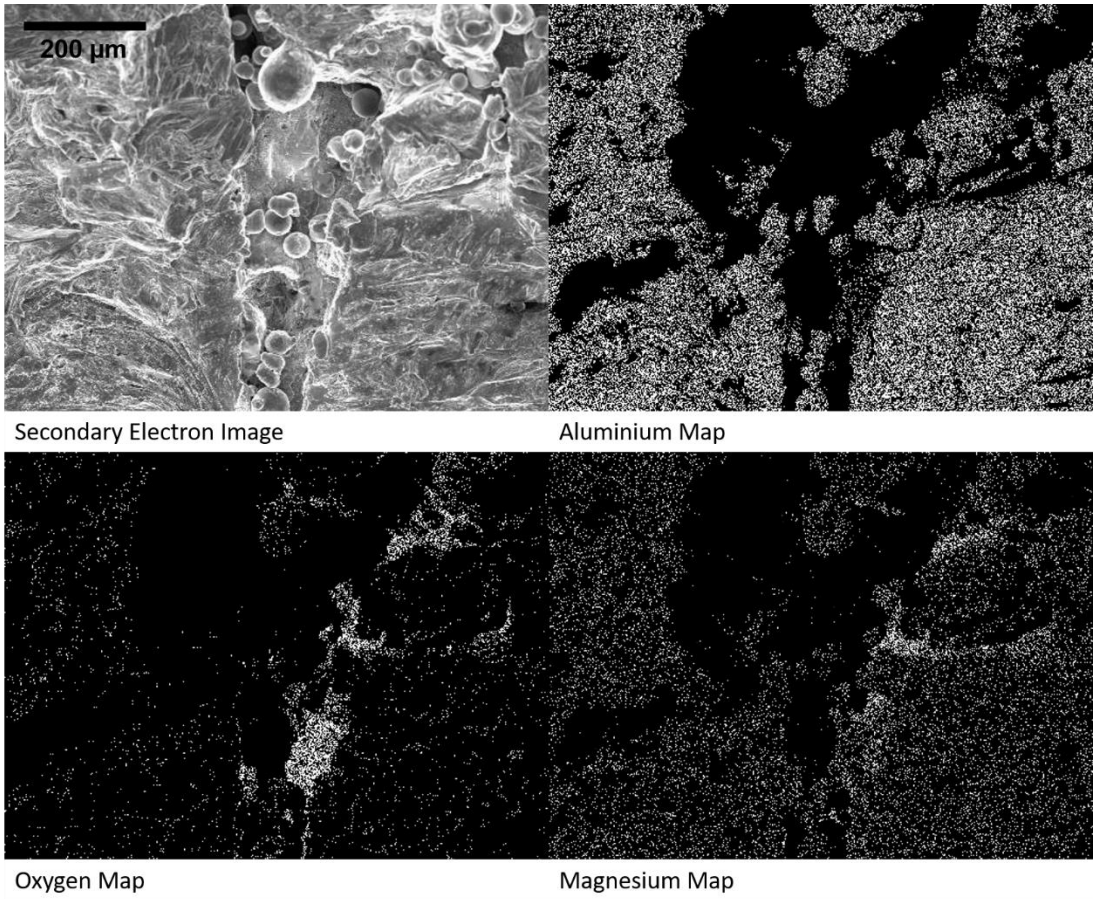

Spectrum	Al	O	Mg	Si	Zn
	91.12	5.89	1.59	0.67	0.73

Figure 170 High magnification SE image of fracture surface of all-Y scanned sample and EDX elemental maps and composition (wt%)

Figure 170 shows clear areas with high oxygen content and lower aluminium. These areas also shown higher concentrations of magnesium (as well as zinc, not pictured). Much inside and on the left side of the pore registered no counts, as the detector did not have clear line of sight. The only area of the pore which registered was the right side, and it is left to assumption that the rest of the pore surface is the same.

The evidence from this crack surface shows evidence of oxides similar in composition to the oxides found on the top surface of the samples, though these oxides are not likely to have caused the cracking but rather formed when molten materials entered pre-existing cracks. No other evidence of chemical or physical crack initiation points were observed on the surface. This does not disqualify thin oxides or inclusions that weaken grain boundaries as they would be undetectable with EDX, as this method does not directly measure surface composition but rather composition of a volume of material near the surface. The next tests look at the crack surfaces of XY scanned parts to examine evidence of oxides on the crack surfaces, to compare with the all Y scanned crack surface.

5.1.2 Fractography of XY Alternating Scanned Crack Surface

Fracturing the XY-alternating scanned parts along the crack is more difficult than with unidirectionally scanned parts, as the cracks are not uniformly aligned. The challenge of identifying crack surface and fracture surface is greater than with the unidirectional samples. The cracks appearance and chemical composition was considered before analysing a fractured surface.

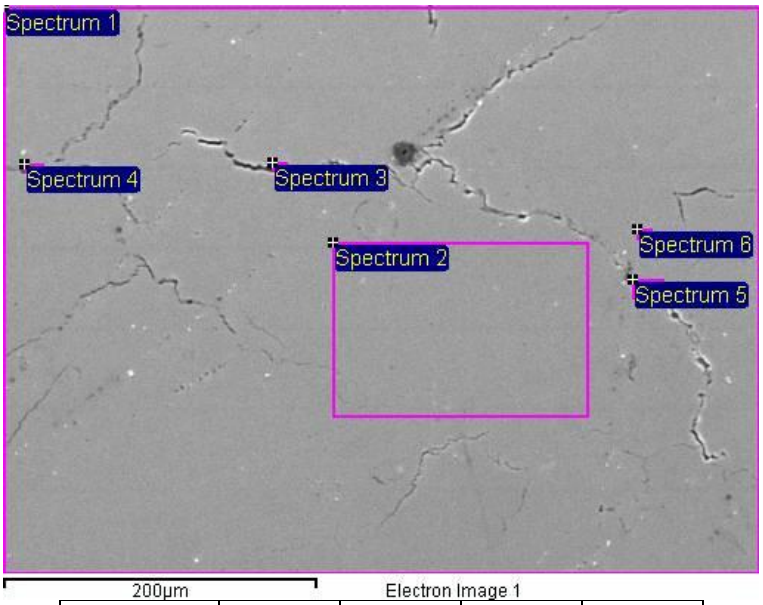

Spectrum	Al	O	Mg	Si
1	95.91	2.46	0.60	1.03
2	96.95	1.59	0.58	0.88
3	58.32	14.45	0.33	26.91
4	81.27	17.28	0.52	0.93
5	79.50	18.81	0.55	1.14
6	84.19	12.40	0.60	2.81

Figure 171 Horizontal cross section of AA6061 sample with EDX composition measurements of bulk material and of cracks (wt%)

Figure 171 shows a horizontal cross section of a high density AA6061 sample. Some cracks have charging around the crack edge and may be an indication of oxides. The composition of spectrum 2 is reasonable for bulk material, except for an excess of oxygen, which will be over counted. Four measurements were taken along the cracks. Spectrums 4 and 6 measured areas along the cracks that were absent of charging. The cracks showed an excess of oxygen and very different levels of silicon. Spectrums 3 and 5 measured areas along the cracks where charging was evident. Both showed similar concentrations of oxygen as the other sections of the cracks. Spectrum 3 counted a very high proportion of silicon, but this was not seen in spectrum 5. As such it not obvious if the different appearance along the cracks is from different chemical compositions or if the difference is physical. The areas along the cracks where charging occurs appear on the thicker sections of the cracks. The SEM image may be

detecting larger amount of surface oxides inside the thicker crack sections, as more of the crack surface is revealed. The EDX detector is dependent on the angle of the measurement and the alignment of the crack. It could be that spectrum 3 had the best alignment and the cracks area characterised by an excess of silicon, but that is speculation.

All cracks showed a prominent level of oxygen. Oxides could be present on the crack surface, either by being present before the crack and weakening the fusion of material or forming on the crack surface at an elevated temperature.

To view the cracks surfaces directly, an attempt was made to fracture the samples along the crack. The samples would break along the crack as they are a source of weakness in the samples. The crack surface of the unidirectionally scanned samples was easily revealed as cracks existed almost across an entire plane and severely weakened the parts to stress perpendicular to that plane. Fracturing the XY alternating scanned sample to reveal the crack surface was more complicated as the cracks are less continuous in direction or length. The cracks are likely to change direction with scanning direction and so an attempt to view the crack surface may not show potential initiation points, which could occur on a different plane.

To view the crack surface within XY alternating scanned parts, samples were thinned to less than 5 mm thick, ground to reveal cracks in the samples and broken by bending the sample using hand held pliers. Figure 172 shows the fractured surfaces of the AA6061 samples printed with 50 µm and 25 µm layer thicknesses. The sample ductility was less than expected for aluminium and appeared to suffer brittle failure. The fractures were uneven and it was attempted to examine the flattest surfaces in SEM and EDX.

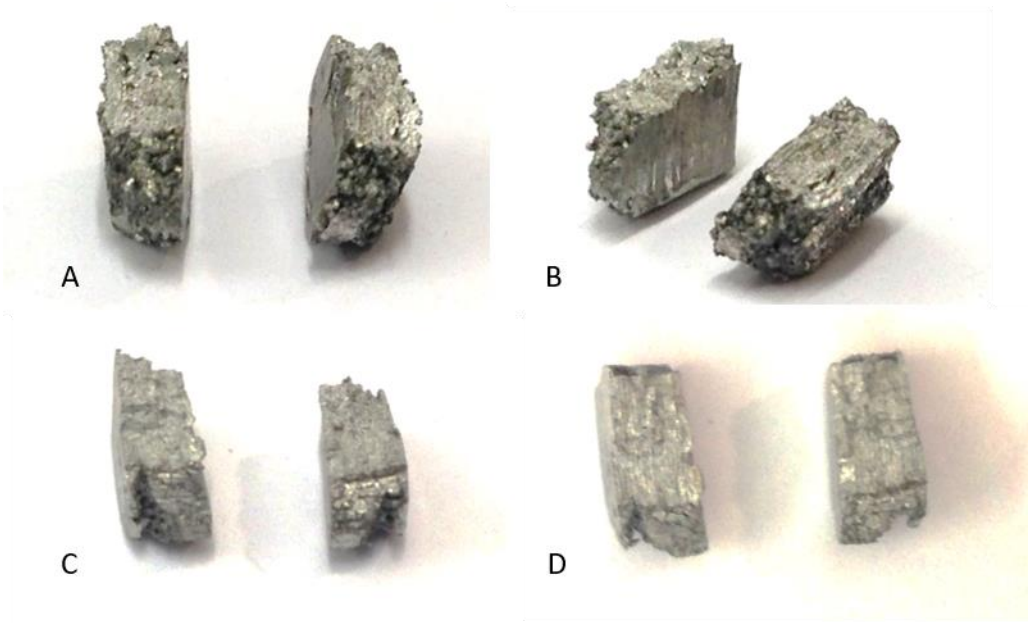

Figure 172 Fractured samples of AA6061 for examining the crack surface, A and B show sample 14 from density test A3 and C and D show sample 19 from density test A5.

Sample 14 from test A3 was used to create the fractured surface representing samples produced with 50µm layer. This was chosen as the density was relatively high, at 99.02%, to try to capture the cracks and not porosity. The fractured surface (Figure 173) shows many cracks running through the sample, as well as many pock marks, which could be from porosity or from local ductile failures. The oxide surfaces revealed in the unidirectional scanned parts were not evident in this part.

The area around the cracks running into the sample are the most likely to reveal crack surfaces on the fracture surface as cracks often intersect perpendicularly. Two distinct textures are seen near the cracks (Figure 174); one texture with the appearance of contouring (as located at spectrum 4) and the other appears mottled (spectrum 6). Both could be the fractured surface with the mottled surface showing brittle failure and the contours showing fatigue. Otherwise, they could just be a result of the inhomogeneous microstructure of the part. The structure inside the crack is hard to view but appears closer to the contoured surface. This contoured surface appears to cover most of the fractured surface, while the mottled surface seems to be nearer the cracks.

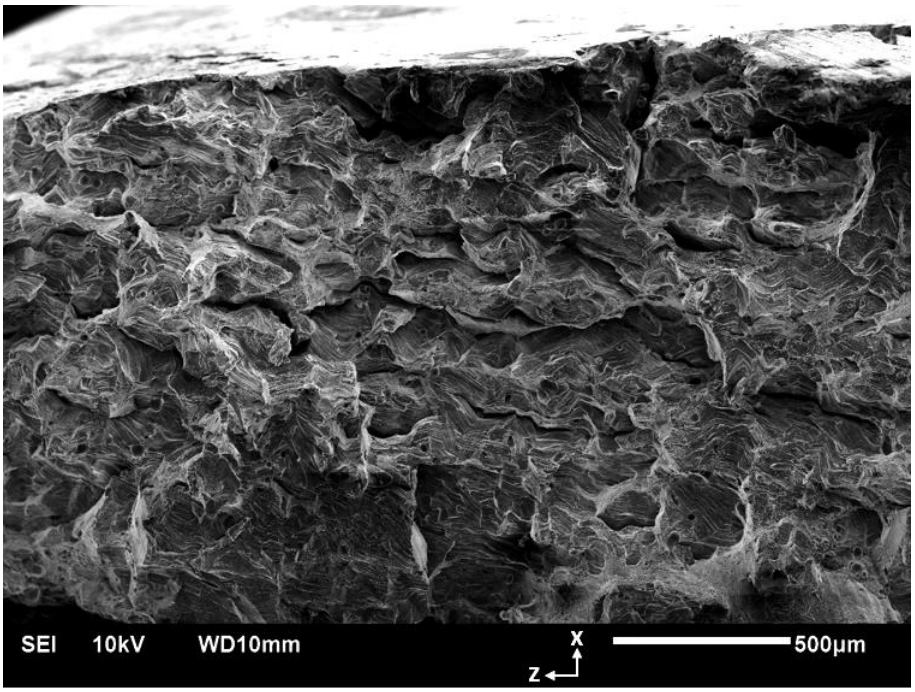

Figure 173 Fracture surface of AA6061 sample 14 from test A3 produced with 50 µm layer thickness.

The EDX analysis does not demonstrate obvious distinctions between the two surfaces. No inordinate chemical imbalance is seen except for the high levels of oxygen. The spectrums of areas 2 and 3 both have a very high amount of oxygen, though the point analysis did not back this up. Spectrum 6 was taken in a mottled area and found very low oxygen content. Spectrum 4 had a considerable amount of oxygen but less than suggested by area spectrum 2. Spectrum 5 also measures an area of contours and measures much lower oxygen. It may be that the oxides are on the surface and may be thinner than the penetrative depth of the electron beam, so the

angle of the surface could affect the measurement. Alternatively, the two areas could be effectively the same with different modes of failure and local inhomogeneity causes the difference in point measurements, while the area measures capture are closer to the true bulk material. This leads the conclusion from this sample to be uncertain. Another attempt was made with a sample produced with 25 µm layer thickness as these showed a more rigid structure in crack growth and therefore the surfaces may be less uneven.

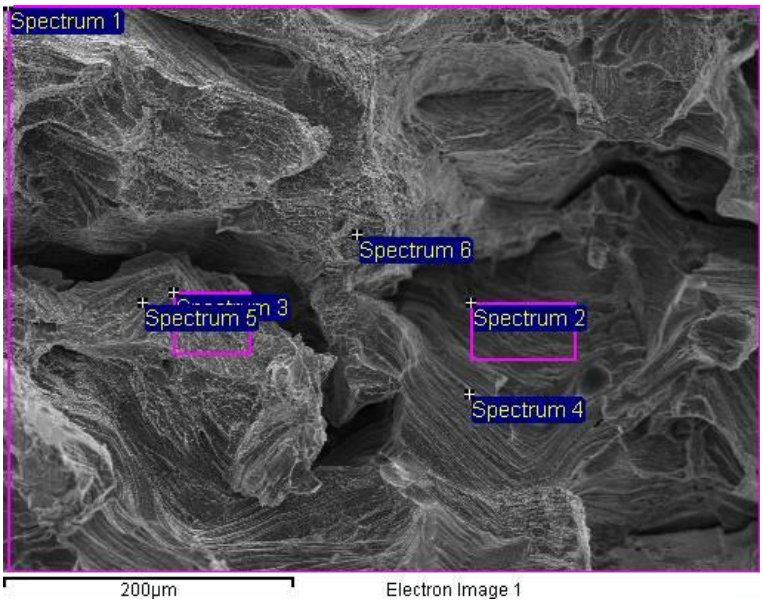

Spectrum	Al	O	Mg	Si
1	92.28	5.52	0.90	1.29
2	89.50	8.78	1.41	0.31
3	87.34	10.58	0.90	1.18
4	91.12	6.77	0.96	1.15
5	98.98	0.66	0.36	-
6	98.40	0.48	0.70	0.43

Figure 174 EDX measurements (wt%) of fracture surface of SLM AA6061 sample 14 from test A3.

Sample 19, with density of 99.05%, was selected from test A5 to view the crack surfaces within SLM AA6061 samples produced with 25 µm layer thickness. The surfaces appear similar to that of the previous fractured sample though faces appear straighter and more orderly (Figure 175). The same observation was made of the cracks on the cross-sectional images (section 4.2), which is a favourable observation for the confidence that crack surfaces are present, even if they are not obvious. Fusion pores and the thick oxide surface that were seen in the unidirectional scanned parts are absent.

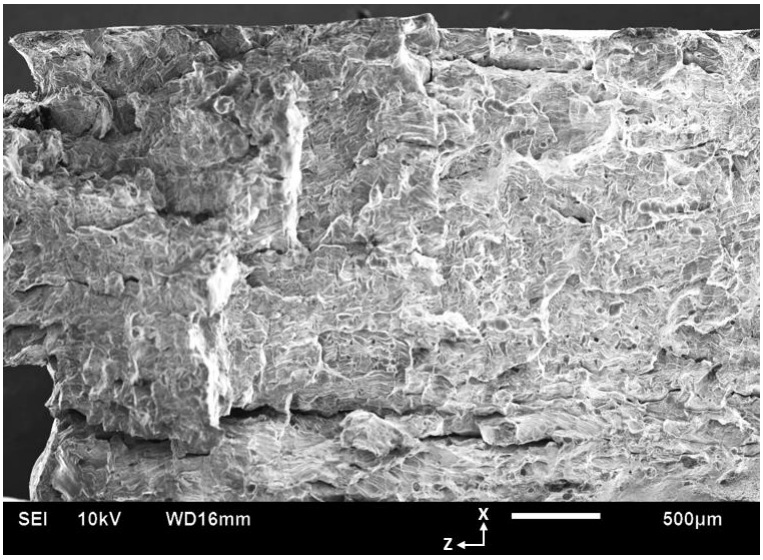

Figure 175 Fracture surface of AA6061 sample 19 from test A5, produced with 25 µm layer thickness.

As with the previous sample, chemical composition was measured to assess potential weaknesses that could promote cracking (Figure 176). To this end, no unwanted elements were found except oxygen. Three areas were analysed; spectrum 2 measured a flat surface, spectrum 3 measured the rough surface and spectrum 4 measured the areas around a perpendicular crack. The flat surface at spectrum 2 may suggest a crack surface pre-existing to fracturing the sample and a distinction between spectrum 3 could differentiate a crack from fractured surface.

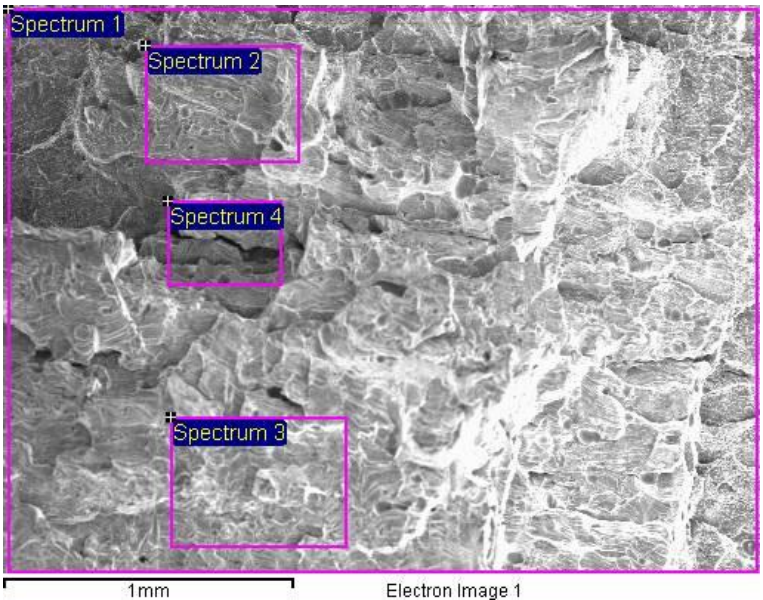

Spectrum	Al	O	Mg	Si
1	92.41	5.35	1.04	1.20
2	94.61	3.33	1.04	1.03
3	92.44	5.02	0.98	1.56
4	94.70	3.98	0.78	0.54

Figure 176 EDX compositional measurements (wt%) of fracture surface of SLM AA6061 sample 19 from test A5

The oxide content of the different surface textures does not differ greatly. The measured oxygen content near the crack and on the flat surface (spectrums 4 and 2) are lower than the bulk value and on the rough surface (samples 1 and 3). Oxygen appears plentiful in the sample, but it is unclear if its presence relates to crack growth or if the rough surface causes overestimation of its presence, due to the higher surface to volume ratio in the measurement.

To view the location of oxygen in the samples an elemental map was produced (Figure 177). A small area was selected for the elemental map, compared to the composition scans (Figure 176), for better readability of the maps and to account for the greater time required to generate. An area near the crack was chosen, which exhibits the flat and rough surfaces similar to what was measured above.

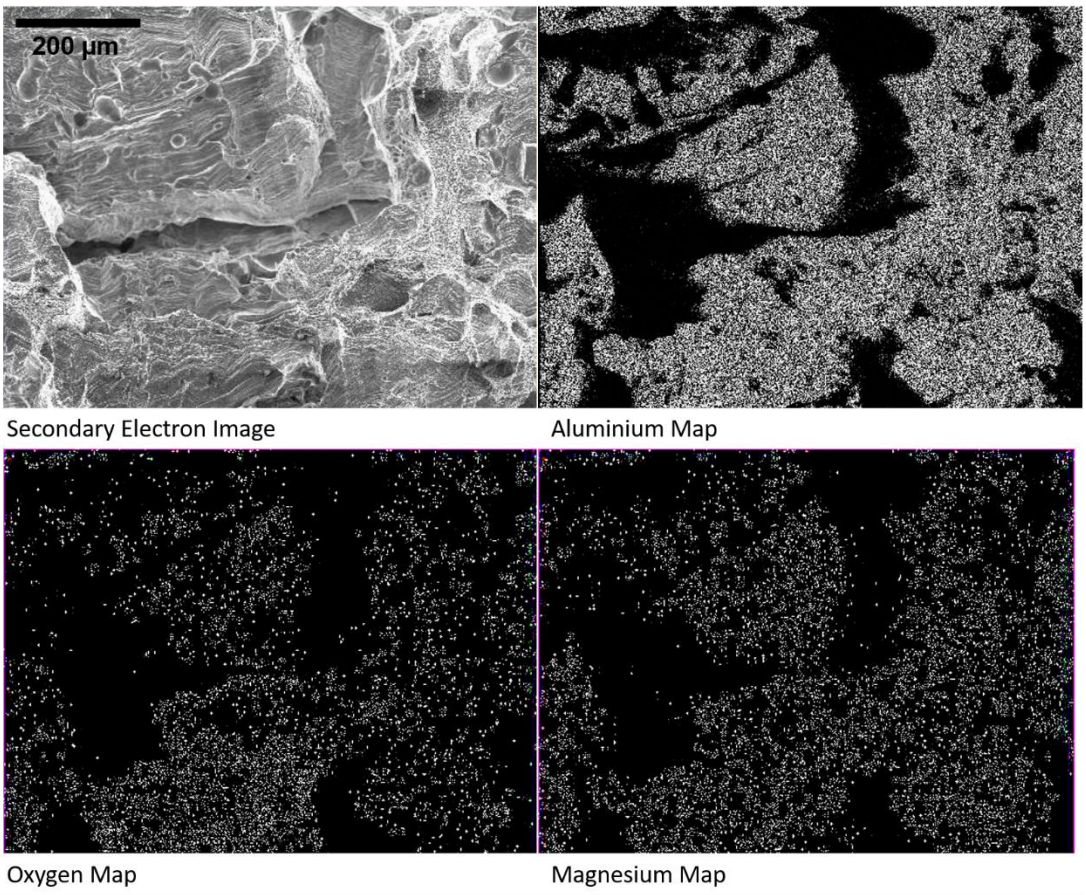

Spectrum	Al	O	Mg	Si
	93.79	5.00	0.76	0.45

Figure 177 SE image of fracture surface of sample 19 from test A5 and EDX elemental maps of the most prominent elements and calculated composition (%wt)

An area near a crack was chosen to generate an elemental map. The map shows that there are areas where no elements are found. This is a result of the rough surface blocking the line of sight of the EDX detector and creating shadows on the image. Ignoring these areas, there is little to note. The elements are relatively evenly dispersed. This does not support the hypothesis that the cracks are caused by oxides but does not complete disprove it either. It may be that the surface of the cracks do

not differ from the induced fracture as the cracks could be propagation of failure that started in a different area of the part. However, it can be expected that the cracks form while the part is heated and therefore if open to the surrounding environment the surface would develop a thicker oxide than on the fracture surface, which occurs at room temperature. This is not seen.

5.1.3 Microstructure of Unidirectional Scanned Parts

The chemical analysis of the cracks surface did not provide a conclusive cause of the cracks. To give some context to the cracks within AA6061, 16 mm long samples of AlSi10Mg and blended material were printed using all three scanning strategies (Table 33). It was decided that only one length was needed as the cracks did not appear to be influenced by part shape.

Table 33 Images of top surface and corresponding cross sections of AlSi10Mg and blended material samples printed with different scanning strategies

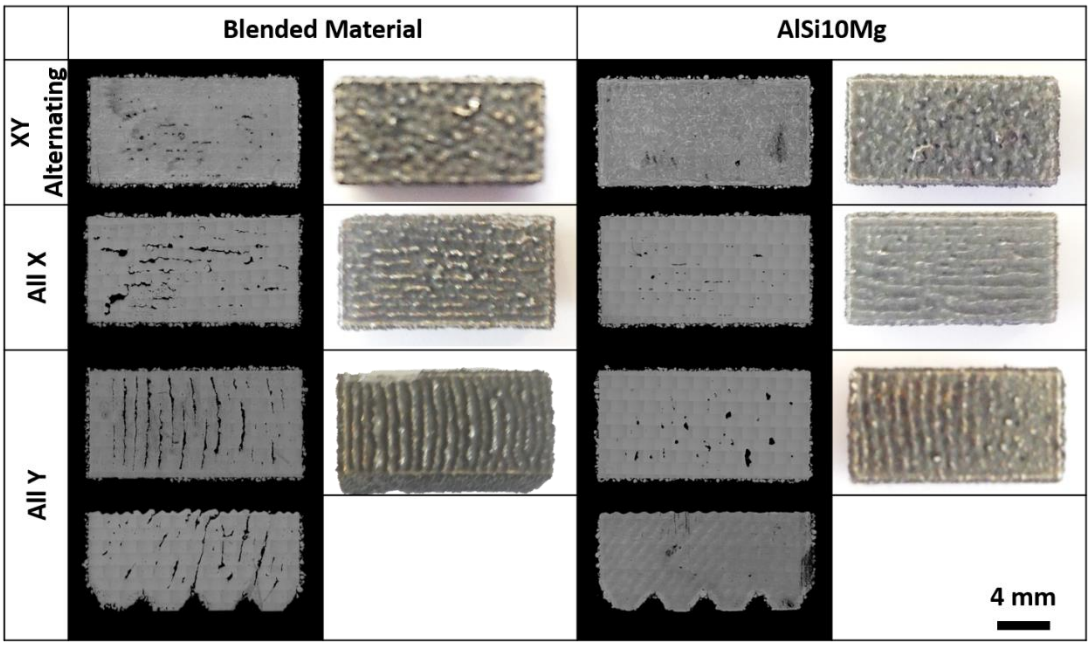

The AlSi10Mg samples produced with XY alternating and all X processed reasonably well, with a few pores, with higher levels of porosity in the all Y samples. The pores in the all X and all Y show clear alignment with the scanning direction and will be due to insufficient wetting to adjacent tracks, possibly exacerbated by the wavy top surface these scan strategies have induced. The blended material samples had a substantial number of pores on the XY alternating surface but no cracks. The unidirectionally scanned samples had a large number of cracks, but not as many as in AA6061, nor were they as consistent in size or location. The silicon content of the blended material was predicted to reduce the susceptibility to solidification cracking but not to completely remove the risk, as is the case with AlSi10Mg, and the appear and abundance of cracks within these samples is in agreement with this hypothesis.

The cracks on the horizontal surface of the all Y scanned blended samples seem to evolve from thin straight cracks on the left into thicker, arced cracks that are shorter in length, before returning to thin, straight crack though not as consistent in presence. The arced crack is likely to relate to the curved ridges on top of the sample, which was the result of the sample raising in the middle and protruding above the level of the powder bed during the build. It is not known why the parts built this way. The cracks seem to alternate sides in this area. The vertical cross section of this sample shows the cracks are a lot less consistent than in the AA6061 sample. Perhaps most relevant to difference in the materials is that the cracks on the vertical cross section show that they are not continuous and may be able to heal. The cracks will provide a point of weakness to allow them to propagate but will also provide stress relief to the surrounding material. While the cracks in AA6061 are evenly dispersed and stable, the cracks in the blended material may be competing and resolved to the pattern seen on the horizontal cross section. The pattern may relieve stress unevenly and cause the part to distort and this could be the reason for the raised middle section.

The vertical cross sections of the unidirectional scans show the cracks do not propagate directly upwards as was seen in the XY alternating scans. The cracks grow at an angle and are located at the trough of the undulating top surface. The all Y scanned AlSi10Mg samples showed the wavy top surface without the presence of cracks, which proves that they are not a product of the cracks' presence. The waves on the top surface of the AlSi10Mg sample seem to build gently and then dampen to a smoother surface as the scans progress from left to right. The temperature of the part will rise as the scan progresses, which will alter the melt pool temperatures and reduce the solidification rate and thermal stresses. It is not known what the difference in temperature will be from the start of the scan to the end or what affect that it would have, so this is an untested hypothesis, but the implication would be that the wavy surface is a result of the metal solidifying before settling on a more stable level surface. This is distinct from balling which is caused by the contraction by surface tension into stable spherical shapes. The unidirectional scanning may be repeatedly pushing molten material across the part, in this case from left to right, and building unstable crashing waves. The cracks appear at the trough of the waves, as it is the weakest locations in the parts and as the cracks move from left to right, the waves move equally.

AlSi10Mg shows that the wavy surface develops without the cracks, but it appears that they exacerbate the problem, especially seen in the blended material. To understand the propagation of the cracks within these samples electron channel contrast imaging (ECCI) was used to view the grain structure where the cracks appear near the top surface (Figure 178).

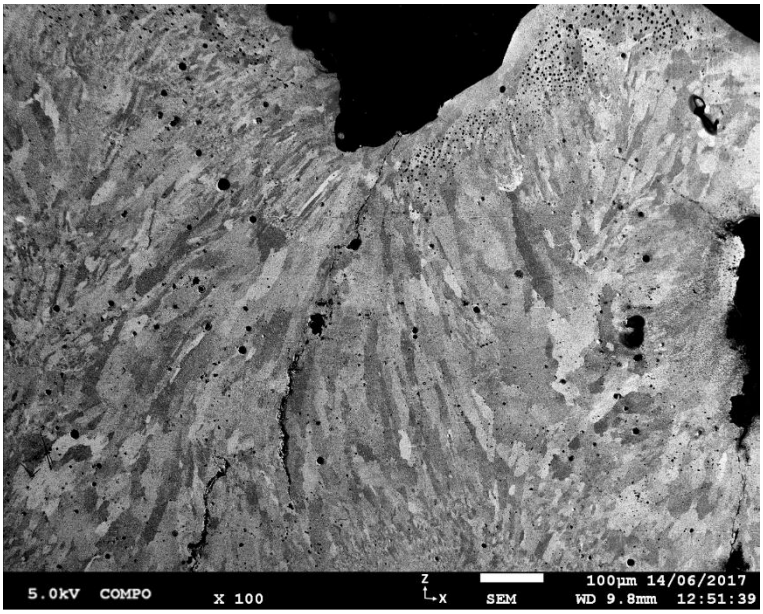

Figure 178 Electron channelling contrast imaging of the vertical cross section surface of AA6061 sample scanned in all-Y direction.

The grain structure shows that the grains left of the crack are elongated largely in the same direction as the crack growth while the grains on the right of the crack are not. This may be the location of greatest misalignment of the grains and the greatest point of weakness. Grain growth can be expected to be epitaxial from the grains below but will also be affect by the thermal gradients in a weld tracks, which are from the periphery inwards, as such the grains on the right of the weld track can be expected to grow to the left and vice versa. The scanning tracks proceed from left to right and as such re-melts a larger portion of grains that have grown right to left. This is clear in the AlSi10Mg samples where the weld tracks are most apparent and almost all of the right side of scan tracks are rescanned by the subsequent track (Figure 179). The result of this may be that not only is material being pushed from left to right but that predominant grain orientation is from left to right. This preferential grain orientation may contribute to the unstable top surface, with molten metal being drawn unsustainably in this direction.

The propagation of the uneven surface can be seen throughout the AlSi10Mg sample (Figure 179). The propagation of the crests of the wave are seen from the lighter colour caused by the increase in silicon at the boundaries of the weld pools. The crests of the waves are also the location of the least overlap, with weld tracks showing larger areas not remelted with adjacent tracks. It may be expected that powder dosing would leave large volume of powder at the troughs and that this would lead to larger melt tracks, but this is evidently not the case. The shape of the weld tracks follows from the previous layers, due to preferential heat paths.

It is seen in Figure 178, that grains appear to grow perpendicular to the top surface, which is a sign that this surface could be an initiation point for grain growth. The gas porosity in the sample is another indication that this is the case. The gas porosity

seems to build in frequency and size up to a distance of 50 µm from the boundary. The gas pores generated during freezing will be pulled upward through the liquid metal due to buoyancy forces. This may have occurred with the metal freezing from the base of the weld pool. The pores would travel up and conglomerate to appear larger, until confronted with solid material that was cooling from the top of the weld pool. The absence of pores in this solid material may have been that the gas could escape during solidification as the material was partially liquid and any trapped gas remains as very small/imperceptible pores. It is likely that, for most layers this texture is removed by remelting, leaving the appearance of only growth from the base of the weld track. The appearance of grain structure and the absences of dispersion of fine gas pores throughout the sample indicate that this is the case, though larger distances between weld track boundaries are seen at the crest of the waves, and therefore these locations may allow for epitaxial growth from grains perpendicular to the surface and not from left to right as reasoned above.

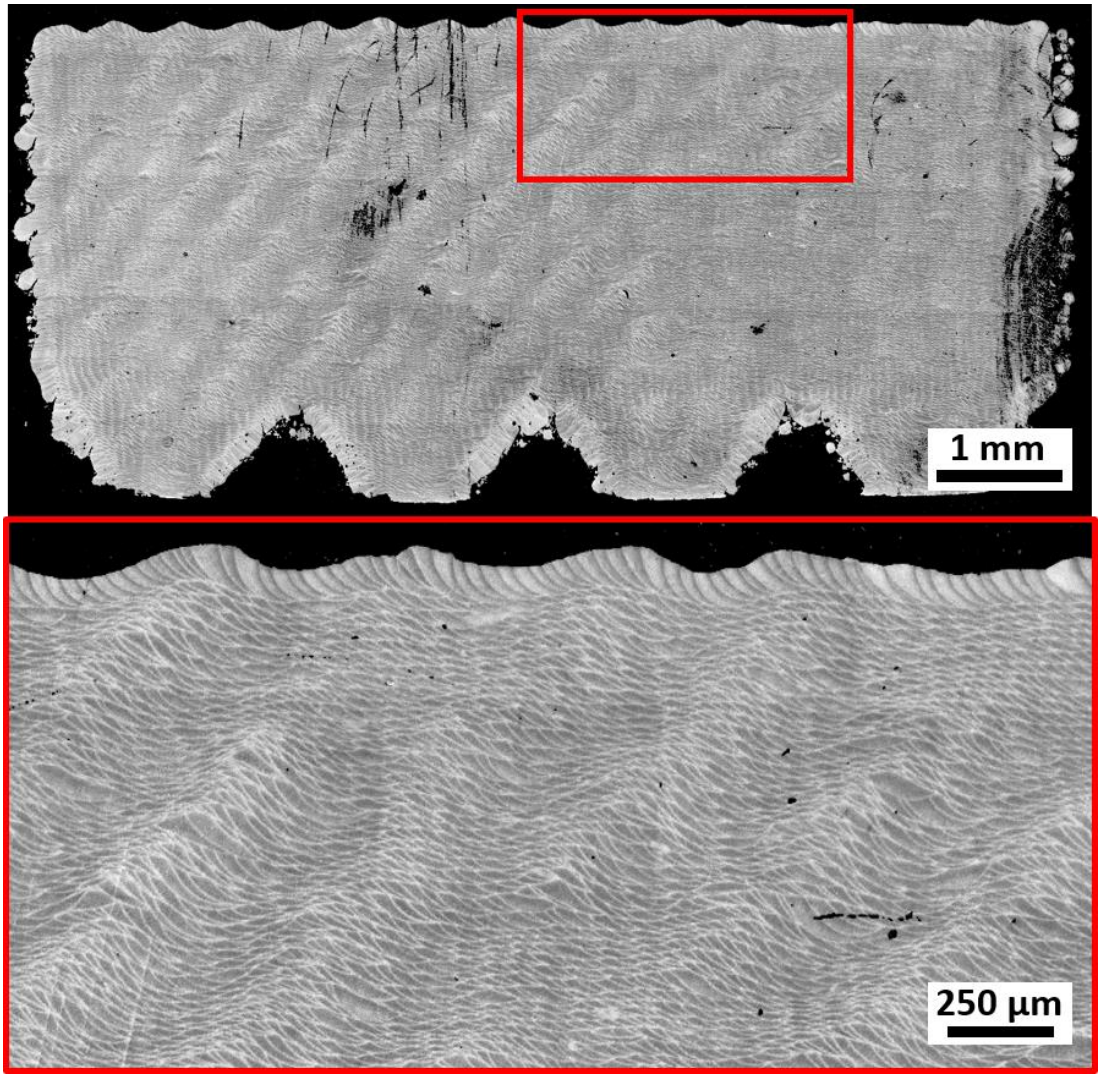

Figure 179 Optical image of a vertical cross-section of SLM AlSi10Mg scanned with all-Y unidirectional scanning strategy, with a higher magnification image showing the detail of the weld track boundaries at the top of the sample.

Crack initiation and growth occurs at the trough of these waves in the AA6061 samples. The view of the weld tracks in AlSi10Mg show imbalances within the first few layers start the wavy surfaces and how these propagate through. In this, it is suggested that the reason for crack location is due to the greatest misalignment of grains caused by the grain growth inward from the bowl-shaped trough, as is similar to solidification cracking in the centre-line of AA6061 weld tracks (Figure 72).

5.2 Location of Cracks within Weld Tracks

Cross sections of AA6061 single scanned samples were etched with sodium hydroxide to reveal the weld track boundaries and their relation to the location of the cracks. Figure 180 shows the etched surfaces of sample 1 from test A3. The etched horizontal cross-sections show how weld pools have been sectioned at different heights and it is difficult to interpret how this relates to the cracks. The vertical surface revealed how the cracks pass though weld tracks. More cracks are revealed than was expected, with most appearing finer than any seen from the sample micrographs in chapter 4. The etchant will have penetrated cracks, eroding the edges and this may have exaggerated very fine cracks that existed but were not visible on the polished surface.

The weld tracks appear to have a limited influence on the cracks as they pass through weld track boundaries, at the centre of some and the side of others. It is likely that the cracks direction is in line with grain growth, consistent with the epitaxial grain growth. As such, the position of the cracks within the weld pool is dependent on an underlying defect. In some instances, weld track boundaries are a location where cracks start or end. This could relate to impeding grains stopping the cracks or fine-grained regions at the boundaries preventing crack growth, as is argued in 5.3. From the view of the weld tracks alone, it is not obvious why these cracks are arrested while surrounding cracks continue.

The 25 µm layer specimens had cracks which appeared more orderly than those created in the 50 µm layer specimens. Sample 9 from A5 was etched to show crack growth through the weld tracks (Figure 181). As with the above sample the number of cracks was higher than expected. The cracks are aligned closer to the vertical than with 50 µm layer sample and cracks that do change direction have shallower deflections. This is likely to be a result of a higher alignment of grains in the 25 µm samples.

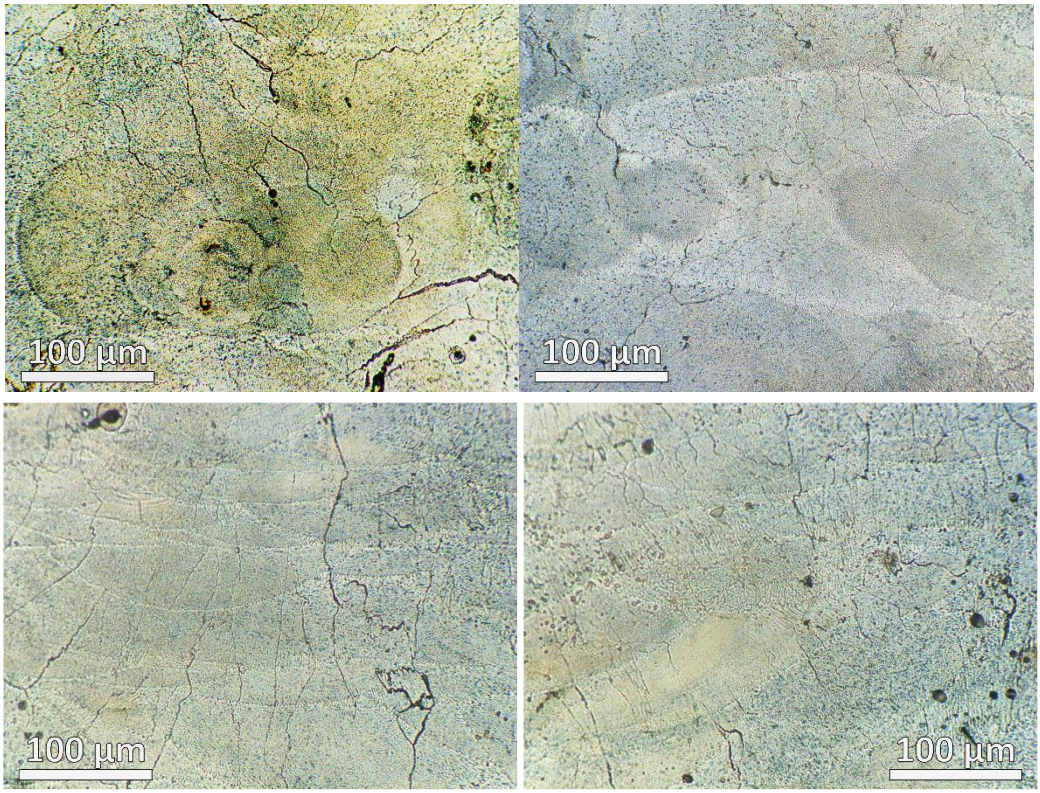

Figure 180 AA6061 sample produced with 50 µm layers, etched with sodium hydroxide showing weld track boundaries and cracks on the horizontal cross section (top) and vertical cross section (bottom)

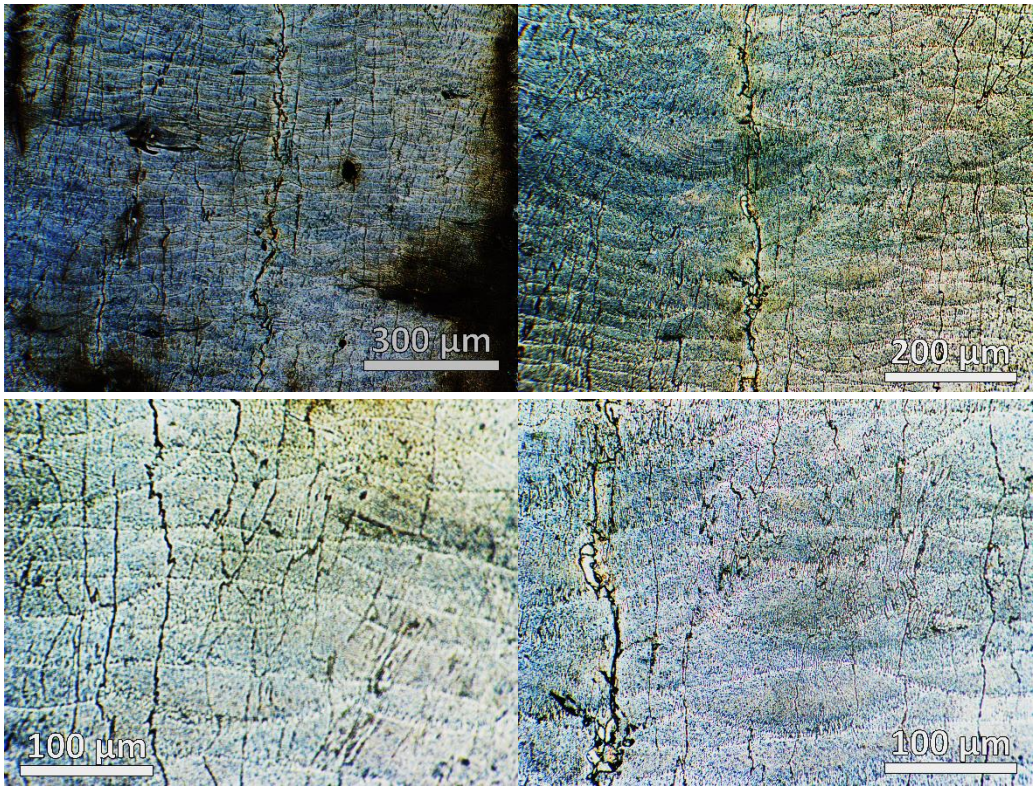

Figure 181 AA6061 sample produced with 25 µm layers, etched with sodium hydroxide showing weld track boundaries and cracks on the horizontal cross section (top) and vertical cross section (bottom)

5.3 Location of Cracks within Microstructure

Electron channelling contrast imaging (ECCI) was used to view the grain structure of aluminium samples. ECCI does not give any indication of direction but for most grains this can be inferred by grain shape and build orientation. As implied by the literature (section 2.5.2), solidification can be assumed to occur solely at the solid-liquid interface of the weld tracks. Electron backscatter diffraction (EBSD) was used to test if the grain orientation had insights into the structure of the material.

The grain structure of AA6061 is compared to AlSi10Mg and blended material to explain how the microstructure affects the presence and location of cracks. AA6061 microstructure of samples produced with 50 µm layers are compared with samples produced with 25 µm to explain the different appearance of cracks in the two different set-ups as this is linked to the microstructure.

High contrast images are used to differentiate grains, but this also causes issues with the imbalance in sample radiation intensity as seen in Figure 182. This issue is reduced by looking at smaller areas, and digitally enhancing the contrast across the image. Multiple images are required to capture the trends in grains structure across the samples and specific areas capture the grains.

5.3.1 Grain Structure of AA6061 at 50 µm layer thickness

Figure 182 shows the horizontal cross section of sample 38 from test A3. The cracks are jagged and most grow in the general direction of the scan tracks but not all as seen in image A. The microstructure on the horizontal surface has areas of fine grains and coarse grains (image B). The etched horizontal surface (Figure 180) showed how a cross section captures welds of different depths. It is likely that the different grain size relates to location within the weld with fine grains appearing near the periphery of the weld tracks.

Image C shows the grain structure around the large crack running in the y direction. The crack has appeared between many comparably large grains, though it appears that there are finer grains near where the crack fragments. The matching profiles of the cracks show that the crack split along the grain boundary of fully formed grains and the displacement shows the direction of the applied force was almost entirely in the x-axis, perpendicularly to the general direction of the crack. The crack will fracture in the path of least resistance. The jagged path may simply relate to the irregular shape of grains before the stress separates them or could be prompted by varying weaknesses in the grain boundaries, i.e. solidification cracking.

Image D shows the crack running in the x-direction. The crack appears to have concurrent surfaces, implying that it appeared from a rupture of solid material. The surfaces imply the stress is mainly in the y-direction, with some displacement in the

x-direction. If the scans dictate the direction of stress, then compound stresses can be expected throughout the samples. Unlike in image C, the distinction of grains does not show the crack always running through the grain boundaries.

In B, C and D, micro cracks, as well as unconnected pores appear along grain boundaries. These defects are a source of weakness as the material in the grain boundaries may be insufficient to bind the grains.

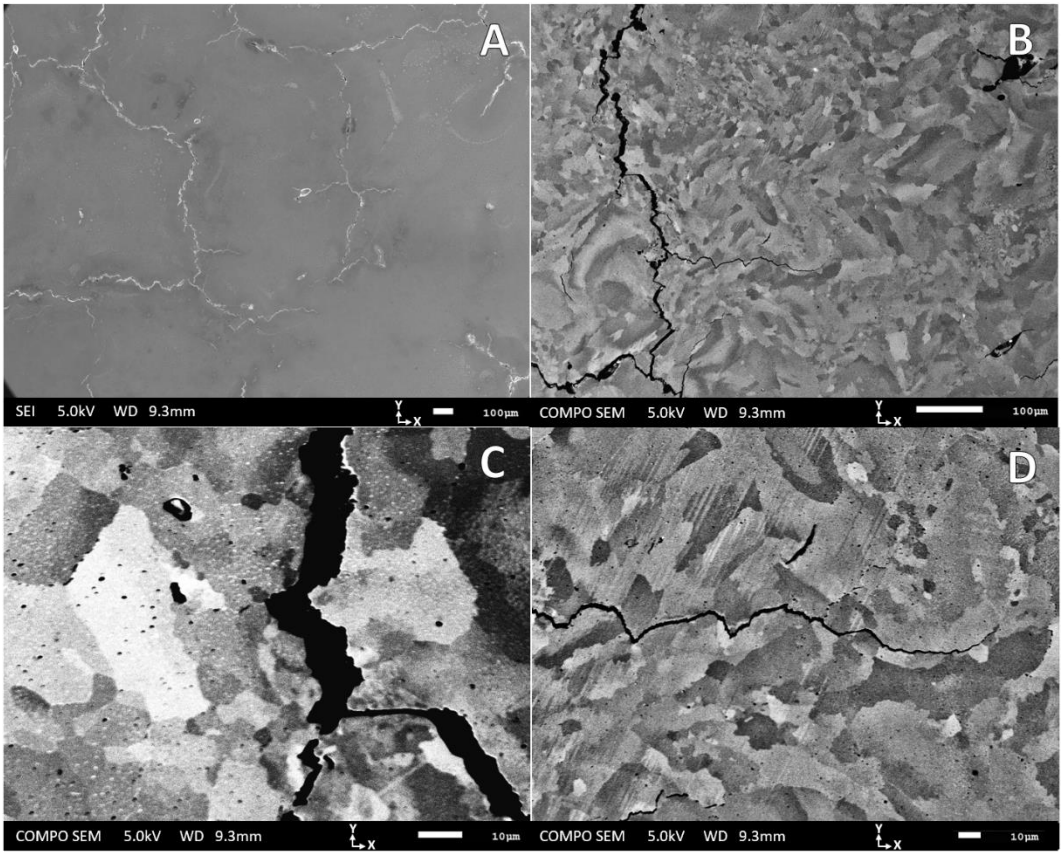

Figure 182 ECCI of horizontal cross section of sample 38 from test A3

Figure 183 shows another horizontal cross section of sample 38 from test A3. The grain structure is visually similar to Figure 182, with pockets of fine grains within a coarser grain structure. This area examines the grain structure near where cracks intersect.

The intersection of cracks in image B shows the change in stresses, as the left arm of crack along the x-direction is under stress applied in the y-direction, while the bottom crack running in the y-direction is under stress applied in the x-direction. The applied force on the right arm is not obvious but the direction of the crack is likely influenced by the pores. The intersection shows a combination of both stresses and will be a result of the alternating direction of primary stresses with alternate scanning.

The presence of existing cracks will provide a weakness from further crack growth. The cracking running in the y-direction, in image B, is likely to be an off shoot from the larger crack with the “V” shape kink acting as a stress concentrator. The kink

themselves may be caused by scans that ran perpendicular to the crack. It was argued that cracks shown in Figure 182 displayed stress perpendicular to scan direction and the general direction of crack, and not local crack direction as is influenced by grain boundaries.

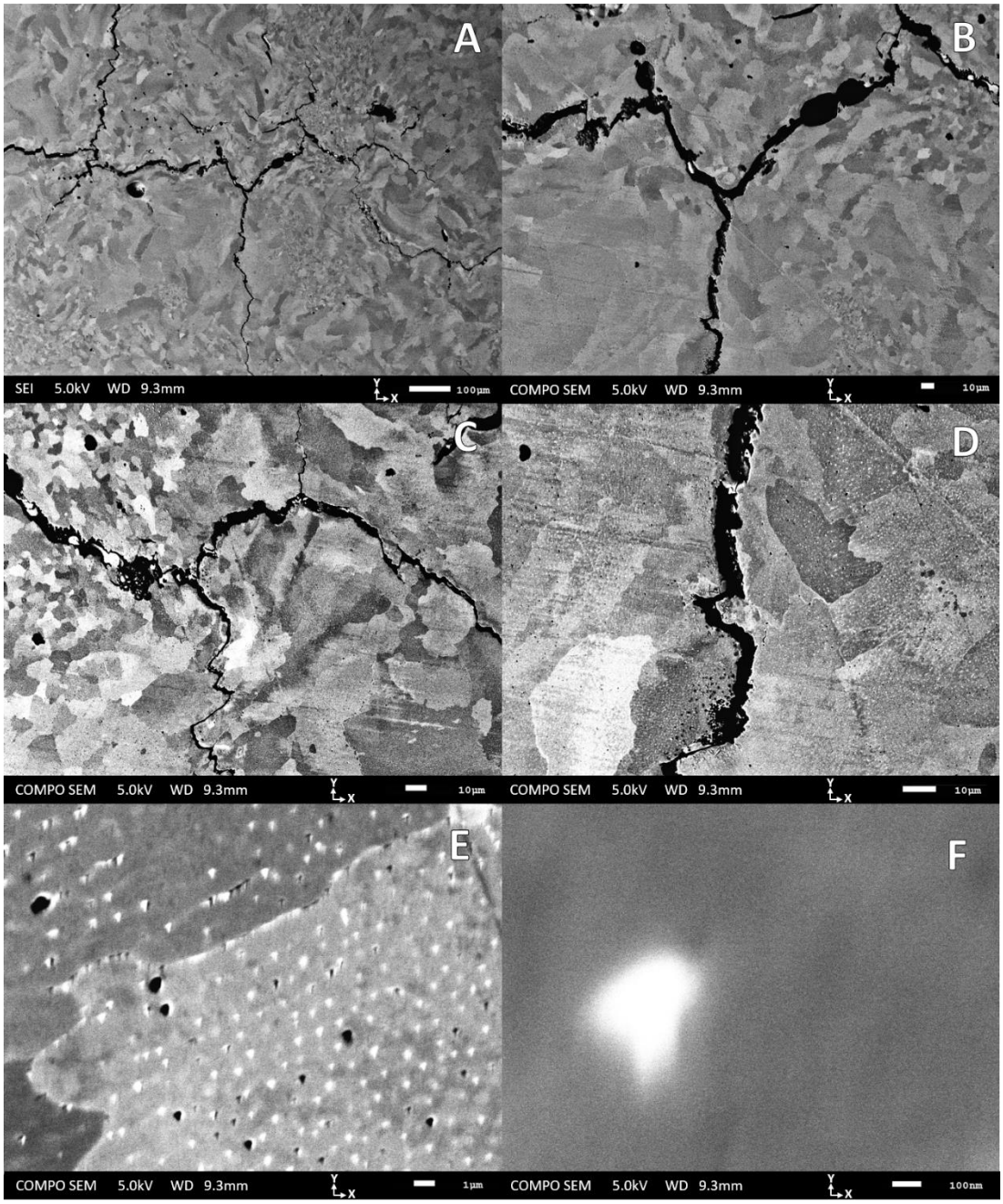

Figure 183 ECCI of horizontal cross section of sample 38 from test A3

The crack intersection in image C (Figure 183) shows the change in the appearance around fine grain and large grains. The crack is very disjointed as it passes through the fine grains. The appearance of material between parallel surfaces, may indicate material infiltrating the crack, similar to how molten material infiltrate the crack in the unidirectional part (Figure 168).

Image D shows a high magnification on a crack also seen in image B. The cracks surfaces show that the applied stress was in the x-direction, however, the surface profiles do not match. The crack appears between grains, but the fractured surface appears to have had ductile failure. The grains may not have finished solidifying before the crack separated them. The malleable solidifying material would not have separated as neatly as the fully formed grains and the final solidified grains would take a slightly different shape. It is not clear what stages of solidification and cooling that the cracks appear, but this shows that, at least, some form before the solidification has been complete.

Image E shows grains that are right of the crack from image D, in an area where, it can be assumed, experienced similar stress before the stress relief provided by the crack. The grains show white flecks of silicon, and black flecks, which are pores, possibly gas. The silicon does not completely fill the grain boundary but leaves black marks which are likely pores. A white fleck is imaged in F, which confirmed that it's composition as silicon. Silicon precipitates out the alloy as pure silicon as was seen in the phase diagram (Figure 4).

The cross section of sample 45 from test A2, appears to show an orderly grain structure of a single scanned layer without disruption from preceding or succeeding layers (Figure 184). The grain structure bears a resemblance to single welding tracks as the grains grow toward the centre of the moving weld pool. The alternating track direction is disguised as the grains grow at 45° to the scan direction. The tracks appear with constant width and the grain structure does not alter in accordance to the 130 µm point distance but appears to have formed from a weld pool travelling at constant speed.

The primary cracks grow along where the misalignment of grains is greatest. This region could be the centre of weld tracks or the edge. The apparent track width is created by the hatch distance of 130 µm. If the weld track was larger than the hatch distance, then every scan would remelt the centre of the previous scan and the misalignment of grains would occur at the edge of the weld tracks. However, the hatch distance is larger than the expected weld track. Thus, the change in grain direction occurs at the centre of the weld tracks. Epitaxial growth can be expected for grains at the edge of the weld pools, masking the change in scan direction.

Secondary cracks branch off from the primary crack. These cracks arise between the large grains. The unrelieved stresses parallel to the scan and potentially underlying cracks from the previous scan may cause these cracks to appear. The alignment of grains prevents these cracks from growing in this direction beyond one hatch distance but promote the cracks to propagate along the centre. Image B shows an area where more cracks appear within the long grain boundaries then within along the centre lines. Despite this the cracks will remain comparatively short unless they continue along the centre of the tracks.

The weakness in the material occurs within grain boundaries and this dictates the direction of the crack growth. Cracks grow in the direction of the scan tracks because of the alignment of grains, and not the direction of the greatest stress. The implication of assuming that the cracks grow along the centre of the weld track is that the weak grain boundaries may be the only mechanism responsible for the defects, while preferred cracking in the edge of weld tracks could be blamed on fusion defects or oxides on the weld track surface.

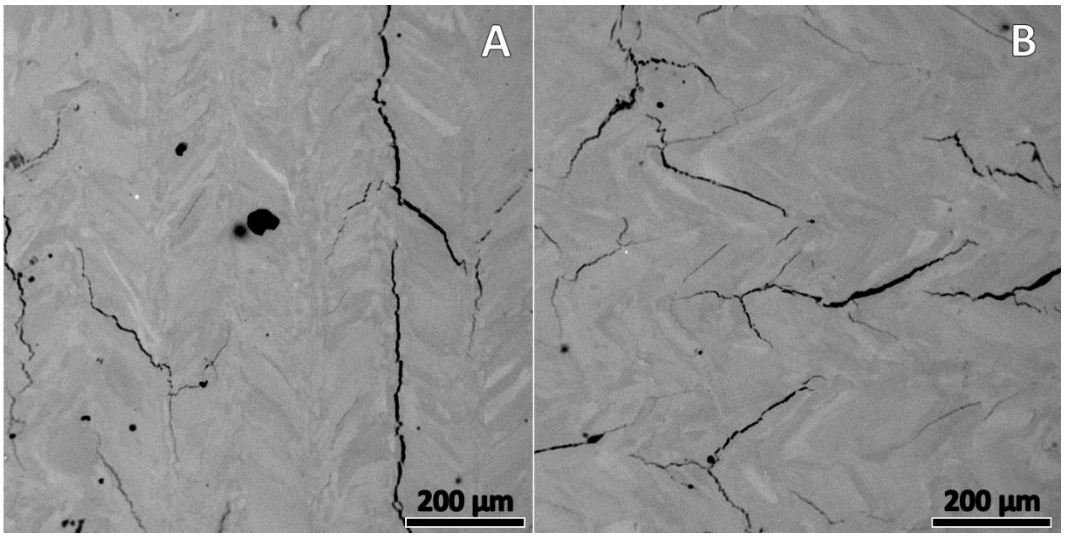

Figure 184 ECCI of horizontal cross section of sample 45 from test A2

Most of the horizontal cross sections did not show distinct weld tracks. The horizontal cross sections can include tracks from multiple layers, as seen in the etched surface of Figure 180, which will obfuscate the grain structure of the weld tracks. Areas on sample 45 from A2 were found where this did not happen. The weld tracks were more identifiable as their centre of the tracks were recognisable. The tracks of this sample may have less overlap than other analysed samples as the weld tracks were comparatively low energy with a wide hatch distance. Track overlap can remelt large portions of the centre of the previous tracks and disrupt the cracks path. This could explain why the tracks were not as clearly defined and why the cracks do not appear to run through the centre of weld tracks seen in the etched surfaces of Figure 180 and Figure 181.

The grain structure of vertical cross sections was analysed using ECCI to assess the evolution of grains within the weld tracks and relationship to the location of cracks. The vertical cross section of sample 38 from test A3 was imaged (Figure 185). ECCI images are very sensitive to dirt and oils on the surface and some small black features on the surface appear due to surface cleanliness.

The grain structure shows areas of fine grains and coarse grains, as was seen on the horizontal surface (Figure 182 and Figure 183). The fine grains are likely to appear at the weld track boundaries, before larger grains develop due to favourable growth.

The shapes of the fine grain regions resemble the arced boundaries of the scan tracks, though not all weld track boundaries are represented by fine grains.

The length of coarse grains show that they extend over multiple layers. The scan direction rotates by 90° each layer, changing the preferred direction of grain growth. The grains will appear different in size and shape depending on the direction of growth relative to the cross section. The regions of fine grains are distinct from these grains as the difference in size is too vast. Nucleation of new grains must occur.

The nucleation could be triggered by disruption to the underlying grains, either by a potential inclusion, such as oxides, or by cracks. The inclusion of oxides was not observed in chemical analysis of the samples, in section 5.1.1, but that analysis would not be able to detect oxide layers that could be a few nanometres in thickness. It was suggested in SLM of aluminium scandium alloys, by Spierings et al, [224], that fine grain areas are a result of oxides. The oxide hypothesis would have to explain the sporadic nature of where the fine grains appear.

Cracks grow between grains but could disrupt the epitaxial grain growth if they decouple the heat flow in the sample. Nucleation would occur if the liquid metal solidifies against the crack face rather than the typical mushy zone of the weld track. Evidence against this hypothesis exists in the unidirectional scanned parts where fine grains regions appear separate to the crack location (Figure 178). Furthermore, the fine grain regions appear in the blended material microstructure without any cracks present (Figure 189)

The thermal gradients and underlying grain orientation effect the probability of nucleation, which are inconsistent throughout the build. At certain locations where the thermal gradients are sufficient for nucleation to occur it may be that the orientation of the underlying grain hinders the competitive growth of that grain. Larger grains increase the likelihood of this happening. The sporadic manifestation of these regions relates the growth and size of the underlying grains.

Images A and B (Figure 185) show multiple cracks with differing characteristics. Thick, disjointed cracks are prominent in both images. The profiles of the crack surfaces do not match as neatly as was observed on the horizontal cross sections, highlighting that horizontal stresses change along the crack.

The direction of the cracks is dependent on grain orientation and change with the grains as the tracks change direction. This could cause the cracks to appear disjointed in the vertical cross sections as the direction of growth weaves in and out of the vertical plane. The apparent gaps in the cracks would have a prominent vertical component, which is not present in the disjointed appearance of the large cracks.

The disjointed appearance of the cracks is more likely caused by the crack having more than one initiation point. The stress is predominantly horizontal. The tip of an existing crack will present a point of weakness within the material from which the crack will

propagate through the tracks, as was evidenced in the etched cross sections (Figure 180 and Figure 181). The presence of another crack would relieve the stress of the shrinking material and prevent the cracks progress. The crack tips align in the direction where stress would have been greatest as the cracks advance until affected by the stress relief.

In the presence of another crack, the stress concentration around the crack tips would cause the cracks to want to grow toward each other and appear as one crack. The direction and size of grains inhibits this, but it could explain some dramatic changes in the crack direction.

Pores seem to form in line with the thick cracks. The stress concentration area around pores may be expected to attract cracks but it may also be the case that the cracks introduce porosity by hindering fusion.

The large thick cracks do appear to develop from thinner cracks, and cracks will only grow in the positive z direction, as dictated by the development of horizontal stresses (section 2.6.2). The thin cracks, as seen in images C to F, appear in the boundaries of coarse grains. The cracks can extend across multiple grain boundaries and, alongside grains, can extend across weld tracks. The fine grains appear to be an area where the thin cracks are arrested. The lack of epitaxial growth and the increased strength from the grain size will hinder the growth of the cracks. Larger cracks do not stop at these fine grain regions. The thickness of the crack may be a symptom of the horizontal stresses, with the cracks providing stress relief. Thinner cracks may not be in areas of higher stress, with surrounding cracks providing relief, and therefore maybe the stresses are not high enough for the cracks to propagate through the fine grains.

The thin cracks do not always reach a fine grain region before they stop, as seen in images E and F. In image F, the crack on the left stops at a horizontal level aligned with the start of the crack on the right. This can be explained as the cracks providing horizontal stress relief. It could be expected that the crack on the left would provide a location for the crack to propagate and provide stress relief. For the crack on the right an initiation point must be created that provides a preferential location for the crack to grow. The boundaries of the weld tracks are characterised by a faint increase in the amount of silicon. The location of the boundaries is subject to interpretation in these images, but it appears that a faint increase in silicon is seen between the crack tips. The position of where the cracks begin and end may be at a scan track boundary.

In both images E and F, very fine cracks and/or pores align within the grain boundaries. It is suspected that these are the inception of the cracks, with the weakest location or the highest stress results in larger cracks growing. The cracks can provide a point of weakness within the weld boundaries and propagate upward, in the build direction, as well as along the scan directions as seen in the horizontal cross sections. The crack thickness could grow as the cracks weaken the material.

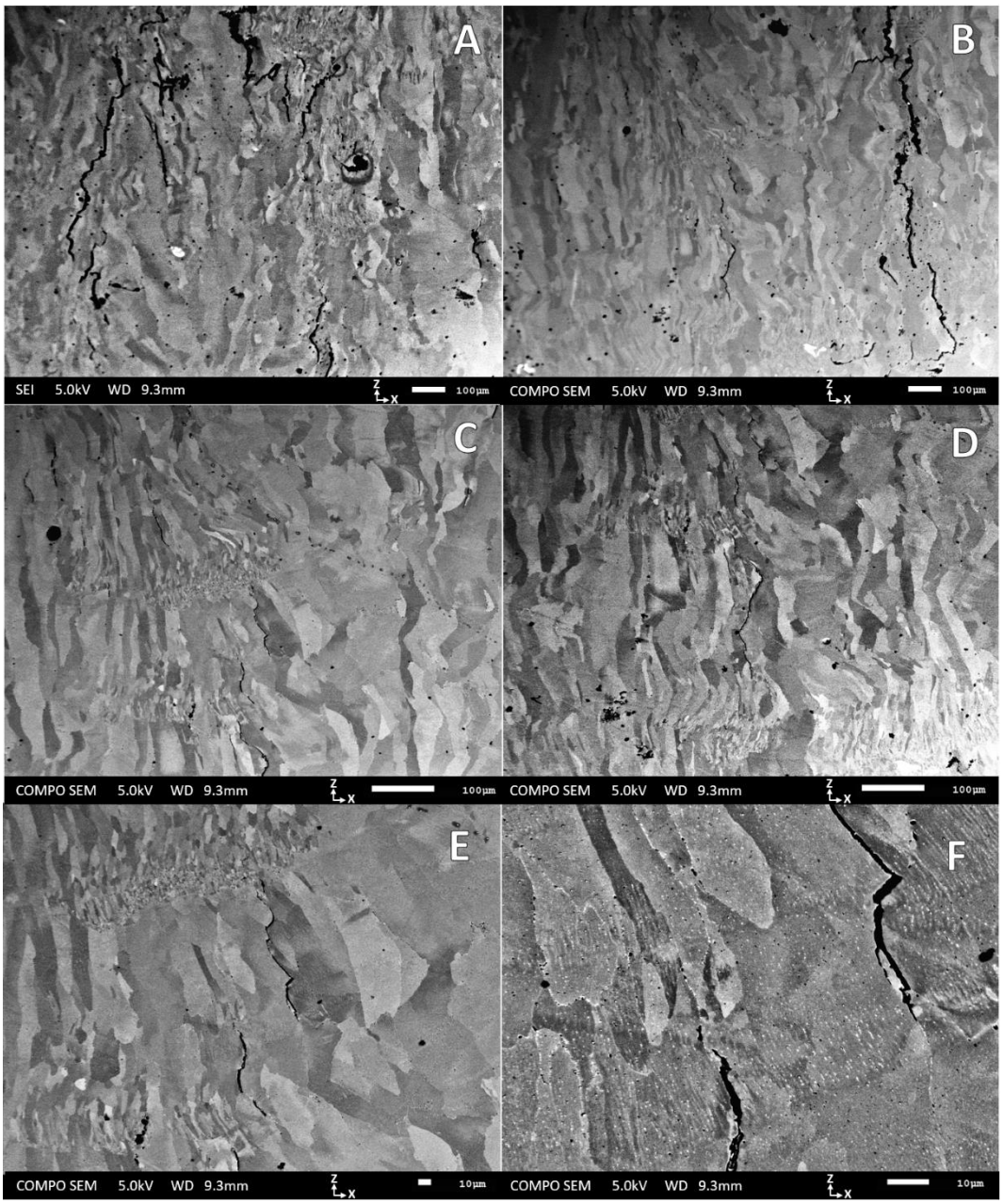

Figure 185 ECCI of vertical cross section of sample 38 from test A3

5.3.2 Grain Structure of AA6061 at 25 µm layer thickness

The thickness of the layers had an effect on the direction of grain growth, as was implied with the direction of the cracks. The direction of grain growth within samples produced with 25 µm layers was closer to the vertical (Figure 187) than for samples produced with 50 µm layers. The cracks on the horizontal surface seem to align to the scan direction more closely than was the case with the 50 µm layer parts (Figure 186). The grain structure and the cracks in image A, bare a strong resemblance to that of Figure 184. It may also be the case the both parts had scan strategies with little overlapping of tracks, maintaining a more identifiable grain structure, as both used hatch distance of 130 µm.

It was judged that Figure 184 happened to capture a horizontal cross section where a single layer was visible, while Figure 182 & Figure 183, showed areas of weld tracks from different layers and different scan directions. The cross-section of Figure 186 may capture different layer but there is just lest distinction between layers as the microstructure appears more highly ordered as it is inherent with the reduced layer thickness. The cross section has areas of fine grains as well as coarse grains, which supports the hypothesis that this cross section intersects welds at different heights of the grain development and different direction.

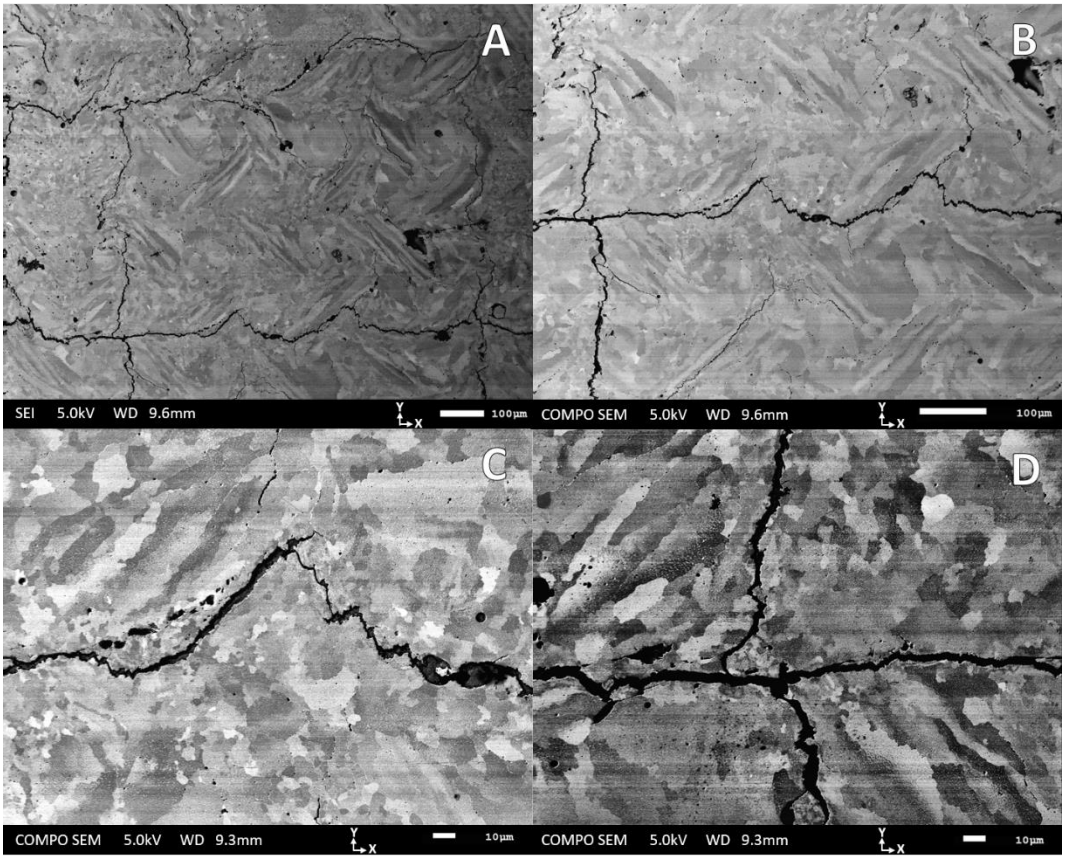

Figure 186 ECCI of horizontal cross section of AA6061 sample 9 from test A5

Image B shows cracks, running in the x direction and y direction. The crack running in the x direction has two prominent "V" kinks, which are a regular feature within cracks. The location and length of the cracks within the grain boundary show how the kinks relate to the secondary cracks from Figure 184, and to the compound stresses that arise with alternating scan pattern, that cause the cracks to change direction, as in Figure 183.

The kinks are a development from the cracks due to alternating scan direction and stresses, that were described from Figure 184. The kink will increase the stress in surrounding material and could form a crack running in the y direction. Fine cracks nearby (image C) could be an indication of this arising. The distance between the kinks, and between the cracks is roughly 260 µm, which is twice the hatch distance of this sample. The scanning strategy means that kinks arise within the same scan

direction, while the scan tracks that travelled in the opposite have not had an equal effect. The reason for this bias is not known but the direction of underlying grain will have an influence.

Many fine cracks that appear within the grain boundaries unconnected to the thicker cracks. These are most prominent in long grain boundaries, which may be especially weak. Epitaxial growth has occurred across adjacent weld tracks, producing grains wider than a hatch distance. If these is a weakness between long grains, they could cause cracks that do not appear in the scan direction, which is a rarer occurrence. It is therefore considered that direction of stresses is more important than grain size and orientation in determining prominence of cracks.

The intersection of cracks on image F appears to have a kink in the y-direction crack, which the x-direction crack does not bisect evenly. The fine grains near the intersection may influence this direction, but equally, the crack intersection may disrupt the growth of grains, causing the fine-grained region.

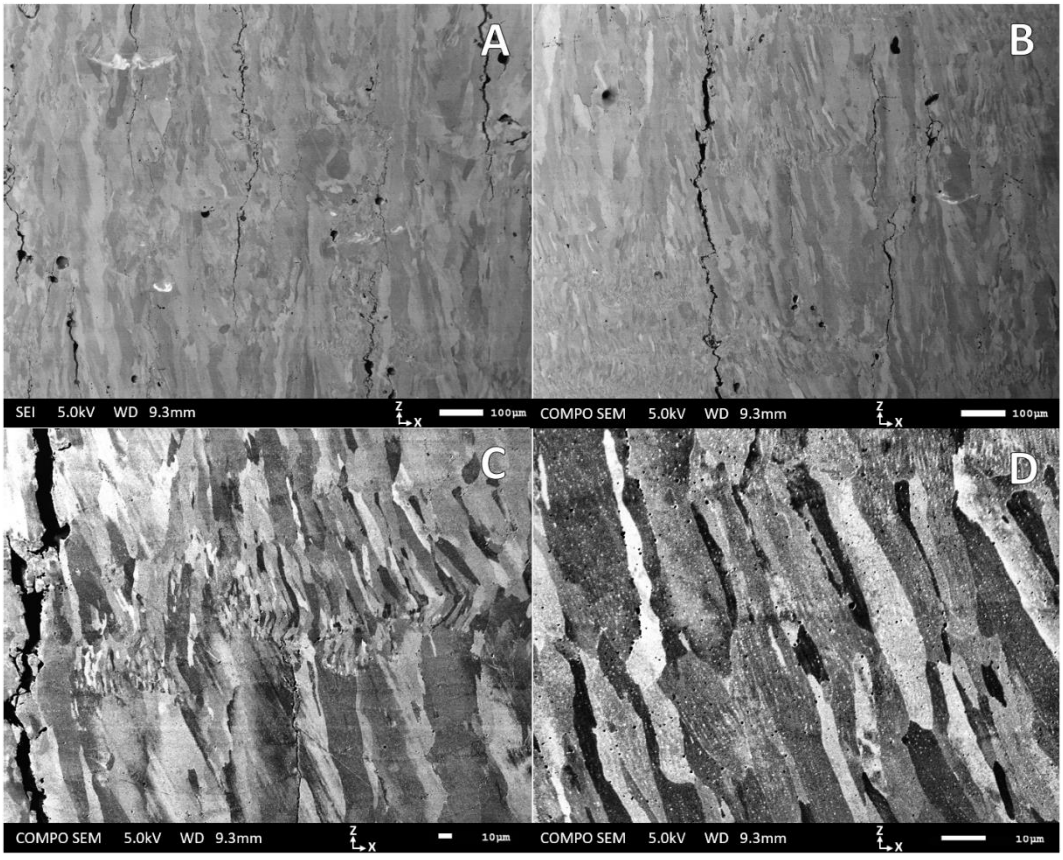

Figure 187 ECCI of vertical cross section of AA6061 sample 9 from test A5

Figure 187 shows the grain structure produced with 25 µm layers. The grain structure, as was indicated by the cracks, are closer aligned to the vertical than was the case with the 50 µm samples. The grain structure is similar and includes areas with fine grains. It can be seen that competitive growth occurs from the fine grains into larger vertical grains (image B). The causes for these regions under consideration were oxides disrupting the grain growth or from changes in growth direction where the

underlying grain proved uncompetitive. Should the latter be accurate then frequency of the regions could be influenced by the size of the weld tracks and thermal gradients generated. More evidence is present that the fine grain restricts crack growth (image C). Image D shows the region where the favourable grains have prospered and pores start to emerge along the grain boundaries, where misalignment is higher (as characterised by high contrast between grains).

5.3.3 Grain Structure of AlSi10Mg

The grain structure of AlSi10Mg was examined to compare to AA6061, to understand the reason why one cracks, and the other doesn't. Samples 20 and 13 from tests B4 and B3 respectively, were examined as both samples had high densities (Figure 188). Only the vertical surfaces were examined as they expose information on how the material solidifies and where cracks start.

The thermal properties, such as freezing temperature range, of AA6061 and AlSi10Mg are different, as discussed in the literature review (section 2.5.2), which shows in the microstructure. AlSi10Mg is a near eutectic alloy, with a short freezing range, while AA6061 has a freezing range more than three times in magnitude. The solidifying front for AlSi10Mg will advance within a smaller band of material, as seen in (Figure 31). Greater competition between grains exists as a result, and grain boundaries are jagged and more interconnected then seen with AA6061 (image A).

The weld boundaries are very faintly visible from the bands of increased silicon and grains changing direction. Elongated grains with epitaxial growth are evident while the areas of very fine grains, that was seen in AA6061, are not present. One hypothesis for these areas was from the inclusions of oxide. This theory would have to account for the lack of fine grains in the AlSi10Mg samples. The high amount of silicon in AlSi10Mg may alter the oxide from alumina to silica, which would be easier to break up. Another hypothesis was that the areas of fine grains nucleated where the underlying grain could not provide competitive epitaxial growth in the direction of cooling. Considerable undercooling would be need for nucleation to occur compared to epitaxial growth and the shorter freezing range may suppress this. This is supported by the view of grains with greater changes in direction appearing in AlSi10Mg than was seen in AA6061 (image D).

Images E and F shows the eutectic structure of Al-Si and Si, which is very different to AA6061.

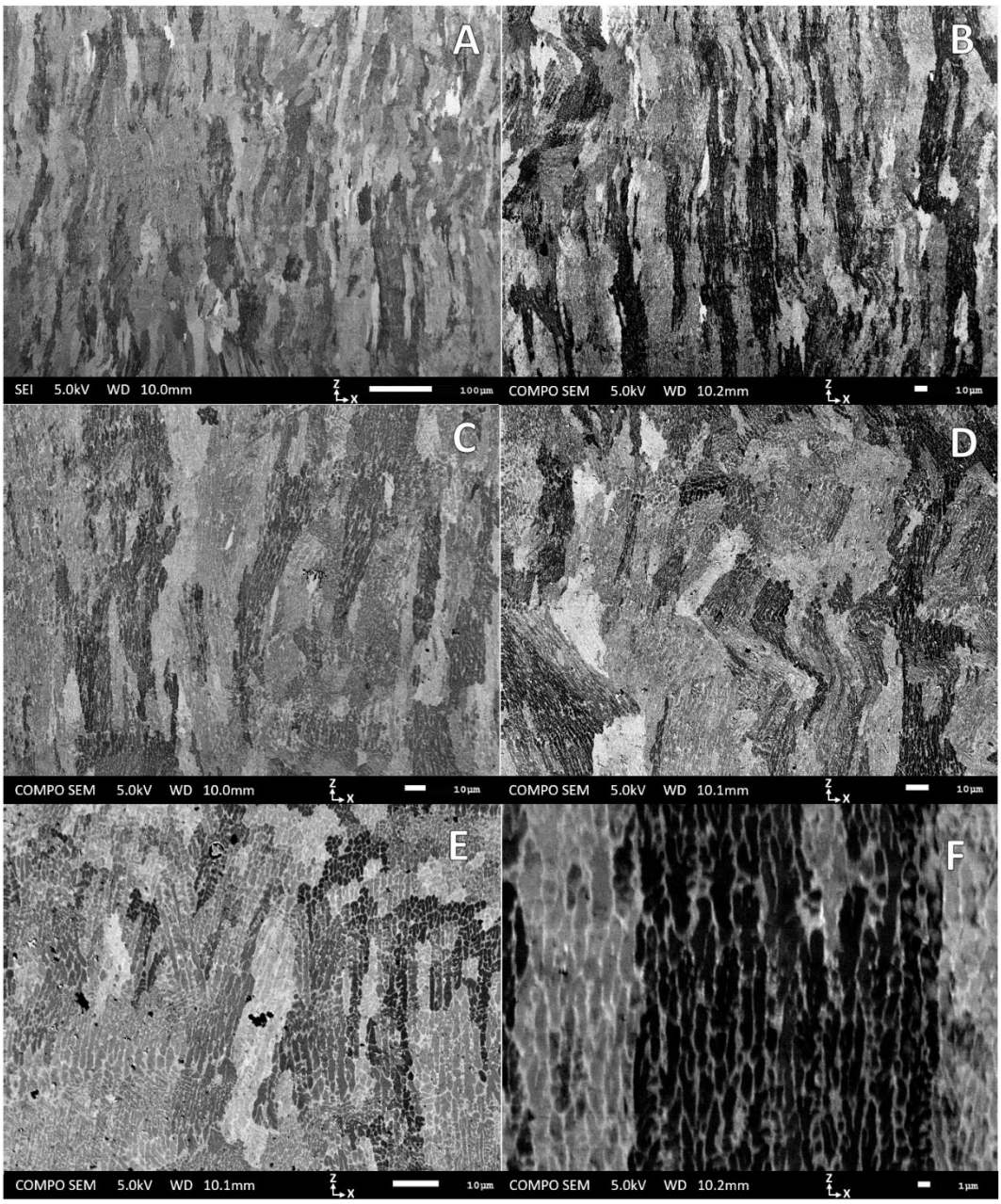

Figure 188 ECCI of vertical cross sections of AlSi10Mg samples 20 and 13 from tests B4 and B3 respectively

5.3.4 Grain Structure of Blended Material

The grain structure of the blended material (Figure 189) is visually similar to AA6061, with many regions of fine grains interrupting elongated coarse grains, and not like the jagged grains within AlSi10Mg. The increase in silicon does not exceed the solid solubility and the freezing range is extended. The effect is the solidification appears the same as AA6061 but more silicon precipitates out during cooling.

The direction of grain growth seems to be less vertical and more affected by the scan direction. It can be expected that scan parameters bare influence on the grain structure [201]. The difference between the parameters of the AA6061 sample 38 from test A3 (as imaged in section 5.3.1) and the blended material sample 14 from

test C2 (Figure 189) was that the blended material sample was printed with faster scan speed (695 µs exposure with 90 µm point distance, compared to 660 µs and 70 µm) and a wider spot. The laser spot size for the blended material sample will only be 13% larger (as calculated from Figure 82 Focus test for SLM 100, lens position vs. spot size), but the differences in weld pool sizes, may be different. It is unlikely that the parameters alone have caused the difference in orientation.

It was predicted in 5.1.3 that the cracks are located at the greatest grain misalignment. It may be the that presence of cracks hinder areas of misalignment from propagating and due to horizontal stresses, promote grains growing closer to the vertical.

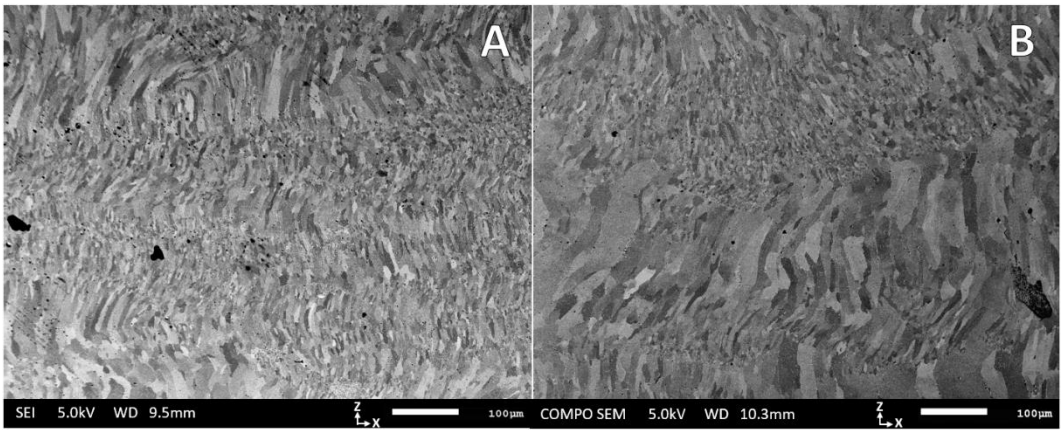

Figure 189 ECCI of vertical cross sections of blended material sample 14 from test C2, showing grain orientation

The coarse grains of the blended material match those of the AA6061 (Figure 190). The grains direction is influenced by the tracks. It was observed in the AA6061 samples that the cracks were likely to have formed in the grain boundaries of the long grains. The grain boundaries of the blended material do not feature pores or cracks, rather they are more prominent with silicon (image B).

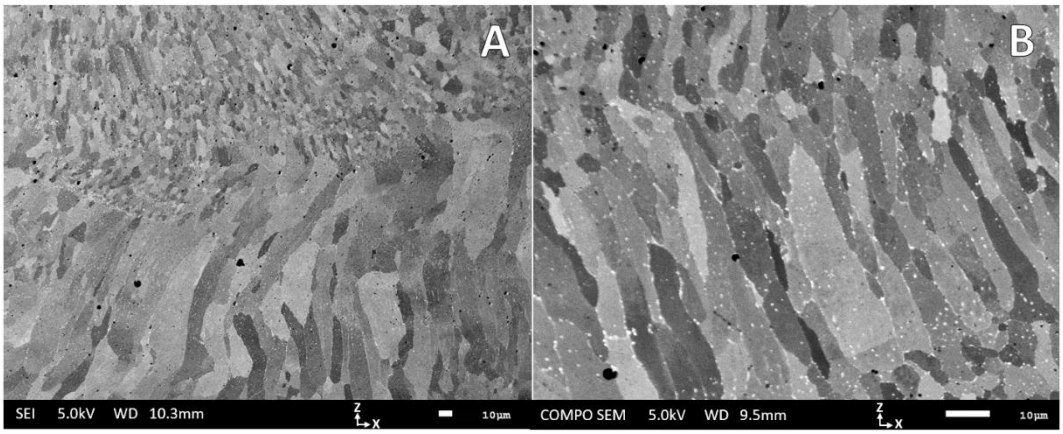

Figure 190 ECCI of vertical cross sections of blended material sample 14 from test C2, showing coarse grains and grain boundaries

Regions of fine grains appear as in AA6061 and not in AlSi10Mg (Figure 191) The size of the grains show that nucleation must take place. The shape of the nucleation of the fine grains describes the base of weld pools. Two hypothesised causes were

presented. The first hypothesis was that the presence of oxides disrupts the grain growth, with the lack of fine grains in AlSi10Mg explained by the oxides changing from alumina to silica due to the increased presence of silicon. The oxides in the blended material will be similar to what is in AA6061. Hydrogen pores were a defect that was more regular in the blended material than AA6061. The heightened presence of hydrogen suggests an accompanying presence of oxygen [159]. This could be the reason for the higher frequency of the nucleation events in the blended material samples (Figure 189) than is seen in the AA6061 sample (Figure 185).

The other hypothesised cause for the nucleation at the weld track boundaries was that epitaxial growth may not have been as favourable. It was reasoned that the changes in direction of grains in AlSi10Mg were an indication that these events were less likely, and this was why fine-grained regions may not appear. The grains in the blended material show steep changes in direction, not as steep as is seen in AlSi10Mg samples, and with a higher frequency of fine grain regions compared to AA6061. Therefore, this reasoning reaches an impasse and can be disregarded.

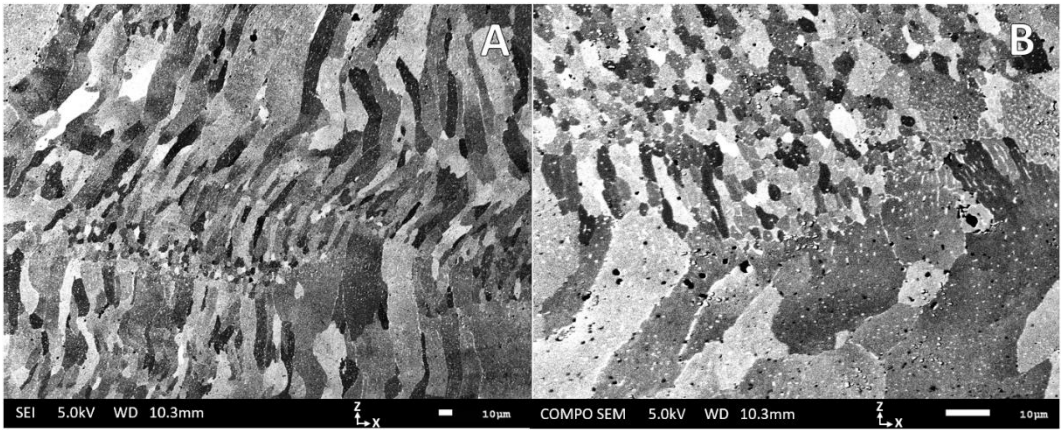

Figure 191 ECCI of vertical cross sections of blended material showing the interface between coarse grains and fine grains.

The coarse grains are not equilateral and therefore the apparent size is dependent on the cross section. Some areas of coarse grains can appear as finer equilateral grains, as seen in Figure 192. The width of the grains remains similar and do not seem to compete to develop into the larger grains. It is important to draw a distinction between these and the fine-grained regions, as evidence that nucleation occurs, within the samples.

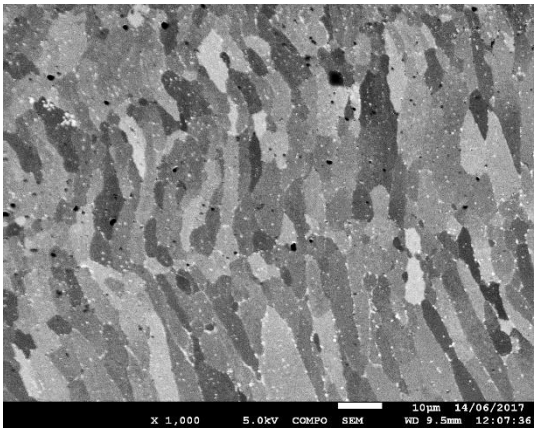

Figure 192 ECCI of vertical cross sections of blended material showing anisotropy of cross sectioned coarse grains

The effect of cross sectioning grains to appear more equilateral than they can also affect the appearance of the fine grain regions. In some regions, the fine grains develop into coarse grains quickly (Figure 193 image A). In other regions the grains exist for larger regions (Figure 193 image B). The larger regions of fine grains may be from nearby nucleation growing toward the vertical cross section, competing and growing elongated perpendicular to the cross section.

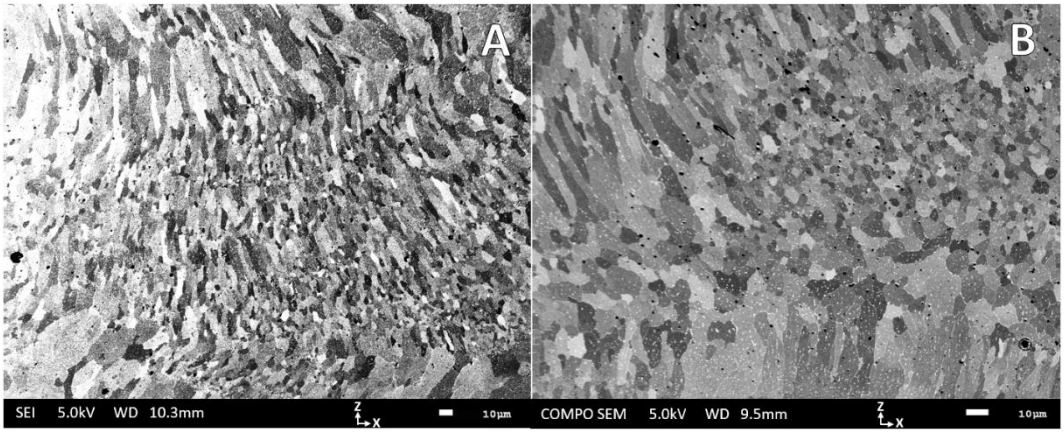

Figure 193 ECCI of vertical cross sections of blended material showing regions of fine grains that do not resolve into coarse grains across a layer thickness

5.3.5 EBSD of AA6061, AlSi10Mg and Blended Material

EBSD data was gathered to have more information on the grain sizes and orientation. The first attempted sample was the horizontal surface of sample 55 from test A3 (Figure 194). This sample was selected as this was the highest density recorded from the AA6061 tests and so it would have the least interference from porosity. However, a pore did appear on the surface and there was interference from scratches on the surface. AA6061 samples proved more difficult to produce a sufficiently scratch free surface finish, than either AlSi10Mg samples or blended material samples. This is likely due to the presence of cracks, which harbour abrasive material.

The scratches on the surfaces cloud the information from the grain boundaries, but it can still be seen that there are areas of fine and coarse grains, and that the coarse grains are elongated 45° to the scan direction, as was indicated by the ECCI analysis (Figure 184). No further insight can be made about the location or appearance of the grain structure and the relationship to cracking.

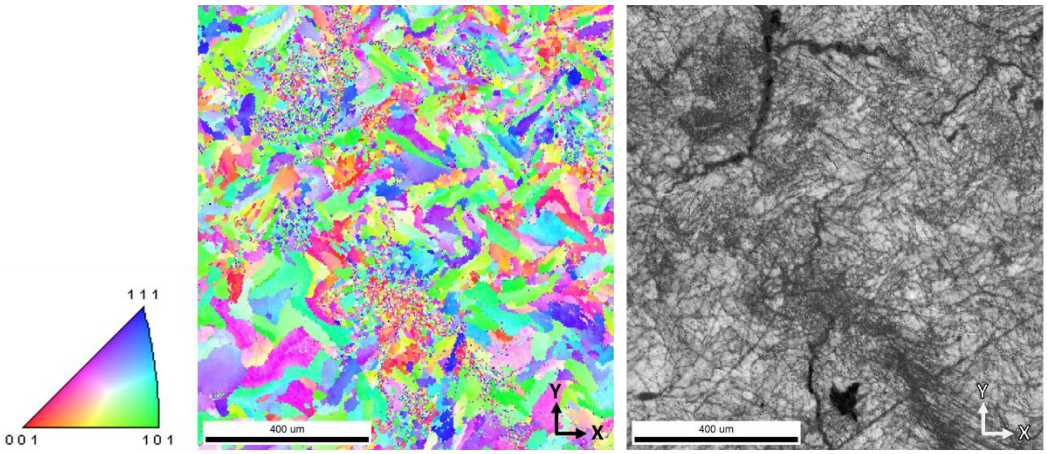

Figure 194 EBSD of a horizontal cross section of AA6061 sample 55 from test A3, showing orientation map (middle) and grain boundaries (right), orientation map coloured according to invert pole figure (left)

A vertical cross section from sample 38 from test A3 was also analysed by EBSD (Figure 195). As with the horizontal image, scratch free images proved too difficult to obtain. The image of grain boundaries shows a clearer view of the presence and location of fine-grained regions than was possible with ECCI images. It is clear from this image that the fine-grained regions are located at the base of the pool tracks based on their shape. The location of the fine grain regions appears to be random and independent from the location of cracks.

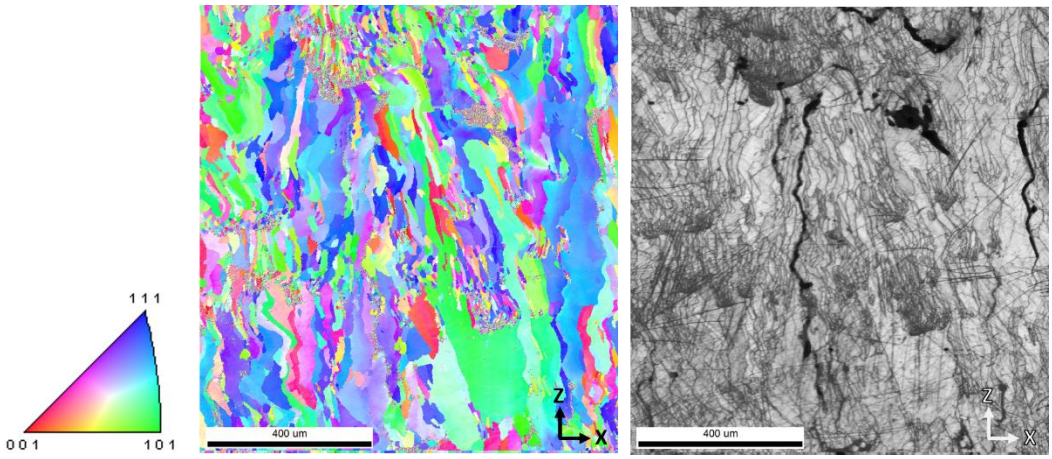

Figure 195 EBSD of a vertical cross section of AA6061 sample 38 from test A3, showing orientation map (middle) and grain boundaries (right), orientation map coloured according to invert pole figure (left)

The EBSD of the blended material shows a very similar microstructure and similar grain orientation (Figure 196). Unlike AA6061 samples, scratch free samples were produced, and a clearer image obtained. A clear image of the nucleation sites can be

seen and how, from competitive growth, they develop into the course microstructure. It is difficult to see any trend in the location of the fine grain nucleation sites. They are not evenly distributed and there does not appear to be any preceding trend from the underlying material, with nucleation occurring on both course and fine grain regions.

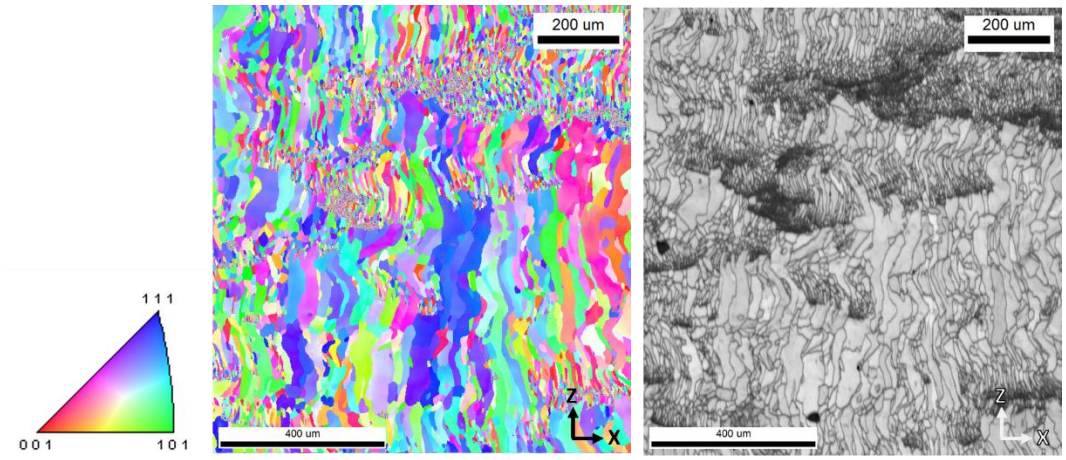

Figure 196 EBSD of vertical cross section of blended material sample 25 from test B2, showing orientation map (middle) and grain boundaries (right), orientation map coloured according to invert pole figure (left)

Figure 197 shows a nucleation site within the blended material at a higher magnification. There is no obvious indication what causes the nucleation to occur. If the oxide films are present, they would not be detected through this method, nor from the SEM analysis. The size of the fine grains at the periphery with the course, are between 1 and 10 µm in diameter.

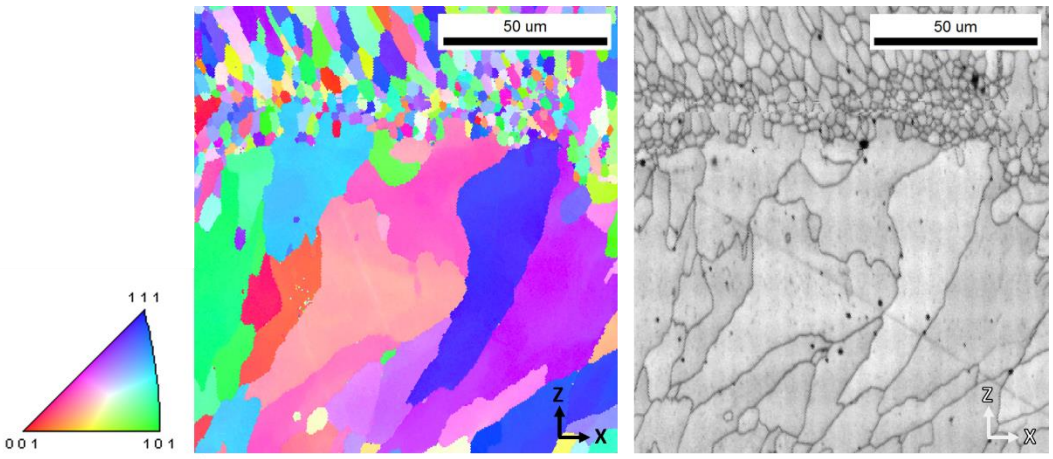

Figure 197 EBSD of blended material nucleation site showing orientation map (middle) and grain boundaries (right), orientation map coloured according to invert pole figure (left)

EBSD of AlSi10Mg was also performed on sample 7 from test B4 (Figure 198). The grain structure is very different to AA6061 and the blended material, with no regions of fine grains. Grain orientation is different for AlSi10Mg than for the other two materials. Both AA6061 and the blended material have a strong presence of grains orientated in 111 direction, and this is absent from the AlSi10Mg sample. The presence of this grain orientation in AA6061 is consistent with the grain elongating at

45° to the scan tracks (Figure 184), which is not present in AlSi10Mg (Figure 24). The difference in these microstructures relates to how these materials solidify (as explained in section 2.5). The blended material solidifies in a manner similar to AA6061, which nullifies claims that cracking is inherent with the microstructure or with the freezing temperature range.

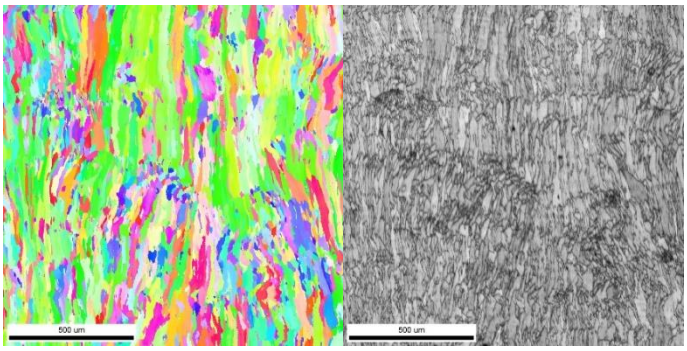

Figure 198 EBSD of vertical cross section of AlSi10Mg sample 7 from test B4 showing orientation map (middle) and grain boundaries (right), orientation map coloured according to invert pole figure (left)

The size distributions of grain in AA6061 and AlSi10Mg appear to be bimodal unlike the blended material (Figure 199). This is not as was expected from the grain boundary maps above. The bimodal measurement likely relates to the alternating scan directions, with grains growing parallel to the cross section showing a larger size than those growing in and out of the plane.

The lower and more uniformly distributed grain sizes of the blended material is likely a result of the nucleation sites that occur in the material. It was expected the grain sizes of AA6061 would be similar in size to the blended material. One source of error is from that cracks on the surface are included as grain boundaries and this will corrupt the grain size calculations. This will skew the data toward smaller grain sizes, however, the grain sizes of AA6061 are larger than the blended material. One possible explanation would be that the process parameter was different for the different materials and this could have an influence on this. Another possible explanation could be that more fine-grained regions exist in the blended material. This could relate to sampling error from the small areas measured, but ECCI images from section 5.3 suggest do support this belief.

AA6061 may appear to have a bimodal size distribution as enough coarse grains are included in the measurement for the differences from orientation to be apparent, while the fine-grained regions in the blended material may cause enough disruption to obscure it.

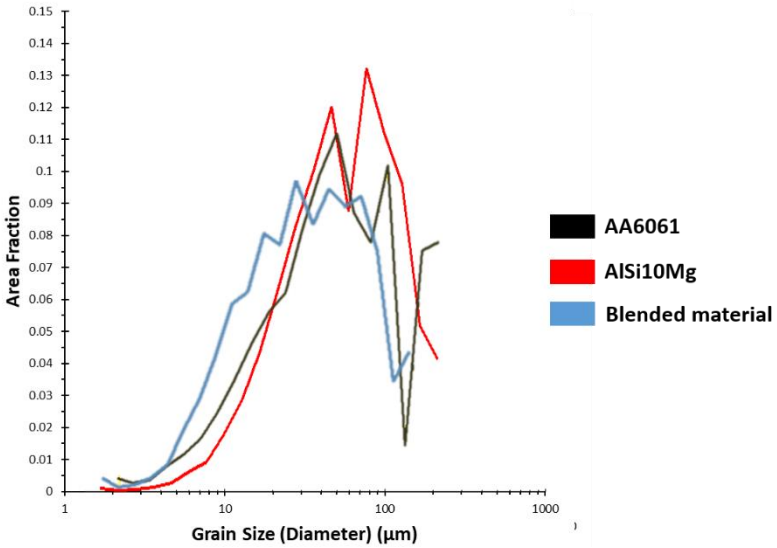

Figure 199 Distribution of grain sizes for AA6061, AlSi10Mg, and blend material samples, measured along vertical cross sections

5.4 Presence of Oxides with AA6061 samples and on Top Surface

The analysis of the fracture surfaces and microstructures does not indicate that inclusions, such as oxides are the cause of the cracks forming. Oxides may still be present. Some oxides on the crack surfaces were found, but this is likely to form post crack and not before. Thin films oxides are also suggested as the most plausible reason for nucleation sites within AA6061 and blended material samples. As such, the presence of oxides within the material remains a concern as it creates a potential weakness in specimen. Another concern exists from the discolouration of the top surface of parts, which is likely produced by oxidation, as seen in welding of aluminium [90]. Discolouration occurs after each layer and the concern is that these oxides get included into the body of the material. The presence and effect of oxygen within aluminium alloys produced by SLM has not been fully established, partly due to the challenges in detecting oxides.

During this project it was observed how rescanning the aluminium samples could remove the dark discoloured appearance and produce a reflective surface (Figure 200). The implication of this is that parts can be cleansed of oxygen through remelting, though it must be considered if the oxides get incorporated into the material. It does show that the oxides are introduced from the powder, as the only scan that will produce enough free oxygen to react with the molten tracks occurs when powder is added. The effects are local, as oxides are cleansed from the part and not from the environment. Two samples, that were produced within the same build, and therefore within the same environment, were evaluated with EDX. The aim of the analysis is to

understand how the second scan effects the oxides and give insight into how the oxides form and are removed (Figure 200).

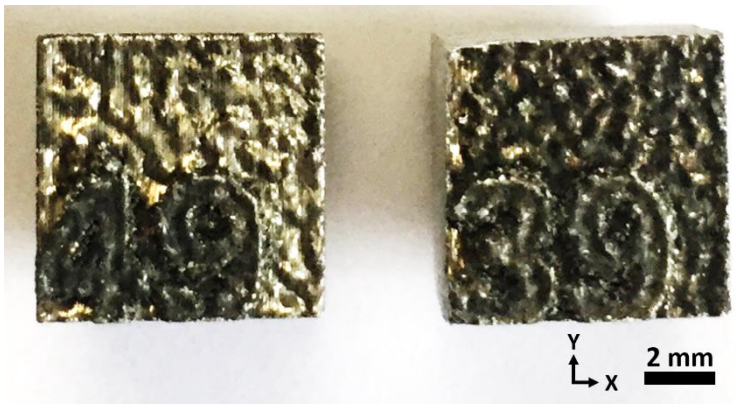

Figure 200 Images of the top surface of double scanned (left) and single scanned (right) parts showing the effect of repeated scanning on surface reflectivity. Numbers are scanned with single scanning.

After establishing how surface reflectivity relates to the presence of oxides, the effect of beam size was considered. The results from the Renishaw AM 125 showed how a finer beam could increase the surface reflectivity of parts without rescanning (section 3.2.1). The oxygen content of these samples were analysed to establish if the effect of the finer beam lowered the oxygen content within the body of the samples, as well as on the top surface.

5.4.1 Effect of Rescanning on Oxides on Top Surface

Samples of AA6061 produced with the Realizer SLM 100 had dark coloured top surfaces, which is expected to be a result of oxidation. The reflectivity of the top surface, and of each layer, is increased with rescanning. The top surfaces of a single scanned and double scanned parts were examined through EDX to confirm that the appearance relates to oxidisation.

EDX is not a surface measurement technique but measures x-rays emitted from a volume of material beneath the surface (Figure 98). To detect the presence of oxides within the top surface of the parts, two measurements, with different penetrative depths, from accelerating voltages of 5 kV and 20 kV, were taken. Assuming the material is mostly aluminium, the depth from which the X-rays can be sourced is estimated as 2.08 µm from a 20 kV beam and 0.206 µm from a 5 kV beam (as calculated from Kanaya and Okayama [275]). The intention of the two measurements was for both to measure a different ratio of surface oxide to bulk material and therefore the presence of the surface oxides can be detected and differentiated from oxides within the bulk of the material.

Both the single scanned and the double scanned samples had high level of oxygen, from both measurements (Figure 201 and Figure 202). The increase portion of oxygen seen with reduced penetrative depth indicates that both samples had oxide on the surface. The oxide layer on the double scanned part is reduced but not completely

removed, suggesting a certain amount of cleansing occurs. The surface reflectivity visibly improves with repeated scans and this result suggest that the removal of oxides may be achieved with repeated scans, practical concerns notwithstanding.

The elemental maps show that the location of oxides can be seen to relate to the scan tracks of the top layer. The scan tracks are revealed in the SEM images of the surfaces as the striations are spaced a hatch distance apart (90 µm for Figure 201 and 100 µm for Figure 202). The centre of scan tracks has a stronger presence of aluminium, while the sides of weld tracks have stronger presence of oxygen. This is similar to results found by Thijs, et al [173] with SLM of maraging steel, who reasoned that the oxides prefer to form at the edge of tracks and are also forced to the edges by the Marangoni effect. Another possible explanation could be that oxides form around the weld tracks and remain after rescanning. The alignment of oxides perpendicular to the surface will increase their observed presence.

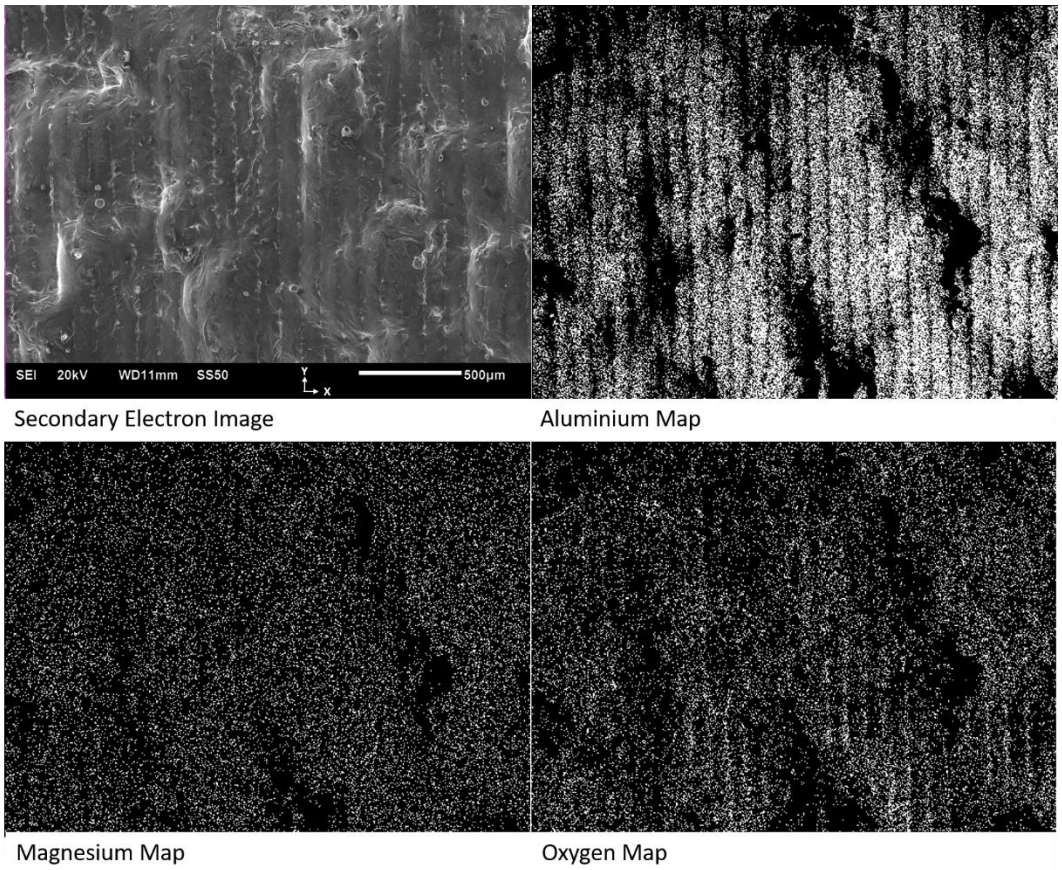

Spectrum	Al	O	Mg	Si	Zn
20 kV	68.54	27.22	2.41	0.64	1.19
5 kV	21.32	63.31	5.19	0	7.98

Figure 201 SEM, EDX elemental maps and the composition of prominent elements of the top surface of single scanned AA6061, sample 22 from test A4

With the detection of oxides, magnesium and zinc are also concentrated at the top surface. This result matches the measurement of the unidirectional scan surface in Figure 167. It has been proposed that the presence of these elements suggest that the oxides form with materials that evaporate and condense on the surface [212]. The

rescanning of the surface could reduce the amount of oxides as these elements evaporate and condense in other locations in the machine. The elemental map of magnesium in single scanned sample, shows that it has strongest presences coincident with oxygen (Figure 201).

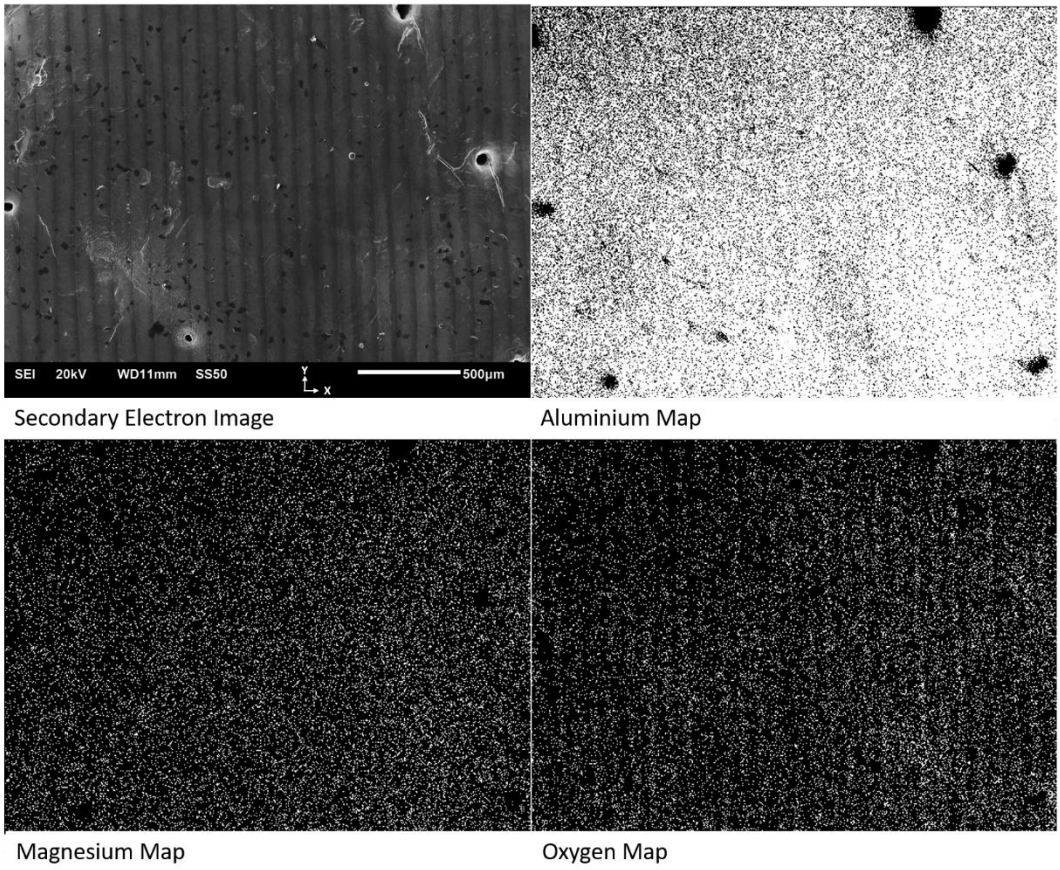

	Al	O	Mg	Si	Zn
20 kV	84.08	14.48	0.62	0.40	0.42
5 kV	53.12	39.06	3.43	0.95	1.07

Figure 202 EDX elemental maps and of the most prominent elements and the composition of the top surface of double scanned AA6061, sample 46 from A7

The top surface of the single scanned part was not flat which has a distortion on results as the proportion of surface oxides would increase. The presence of oxides, confirmed to be present at the side of tracks, are seen as bright marks in the SEM. The operation of the SEM requires that the measured sample is conductive. Oxides have a low conductivity and therefore thick oxides cause charging. The result is that EDX data is lost. The uneven surface of the sample could contribute to charging oxides, where a steep angle could be causing the beam to be interacting with a higher quantity of oxides. The step angle could also create shadows in the EDX map, where the EDX does not have line of sight with the X-ray source.

To further examine the presence of oxides within weld boundaries a higher magnification region was analysed for both samples (Figure 203 and Figure 204). Only 20 kV beam was used for this analysis and the chemical compositions of these areas

were in good agreement with the measurements of larger areas (Figure 201 and Figure 202).

Figure 203 shows the top surface of a sample produced through single scanning. The EDX element maps unequivocally show the concentration of oxides corresponds to the light ridges. The ridges are 90 µm apart which equals the hatch distance of this part. Cracks on the surface show that the underlying grains run at around 45° to the track direction. This could be the result of oxides forming at the centre of tracks but, as with Figure 184, it is likely that the centre gets remelted with adjacent tracks and therefor the ridges are at the edge of scan tracks. Part of the tracks show loss of data, which could be due to surface charging or shadowing on the EDX detector, as above.

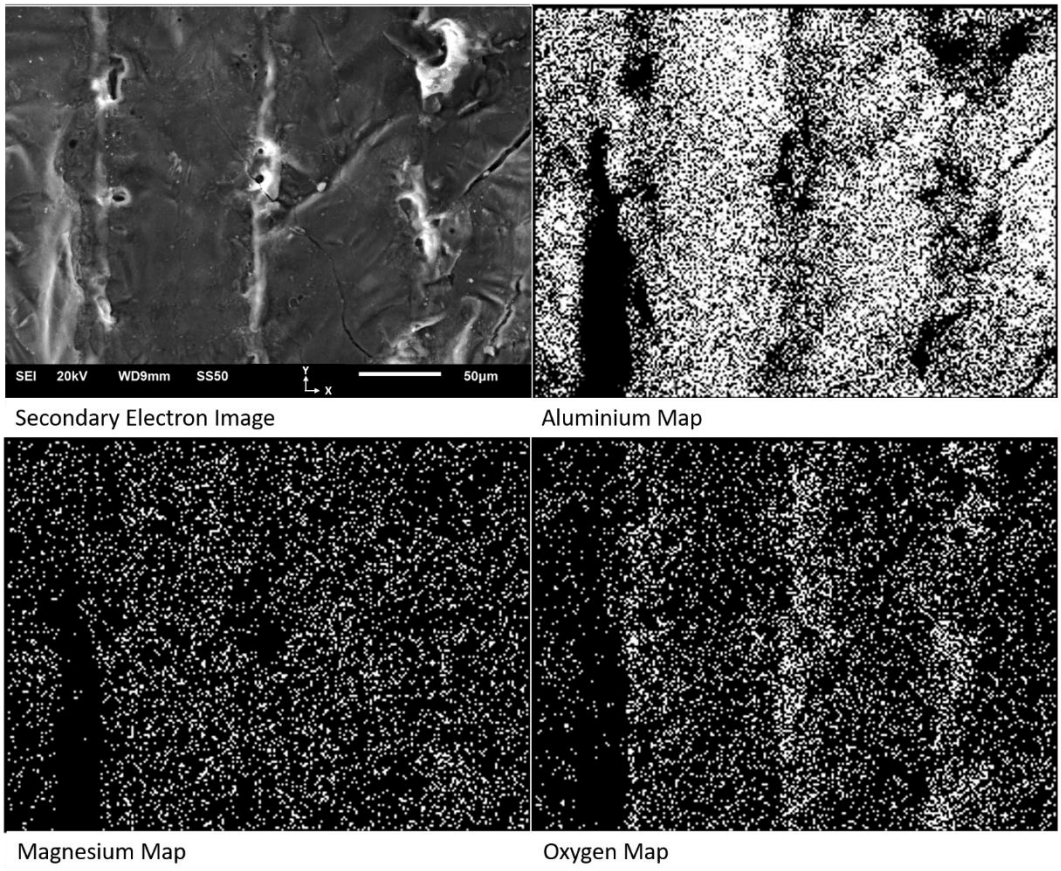

Spectrum	Al	O	Mg	Si	Zn
20 kV	72.51	23.71	1.74	0.60	1.44

Figure 203 EDX elemental maps and of the most prominent elements and the composition of the top surface of single scanned AA6061, sample 22 from A4

These images do not eliminate the possible explanation that the oxide peaks actually protrude from the surface. The weld tracks can push material away from the centre of the tracks and could cause the raised ridges near the edge of the weld tracks. Their lighter appearance would be from the increase intensity of electron radiating the surface. This is consistent with other topographical features on this and other SEM images. Oxygen is a light element and emitted x-rays do not travel far through solid material. The increased counts of oxygen would be explained by the increased surface

area as well as the increased probability of the emission escaping without interaction with surrounding material.

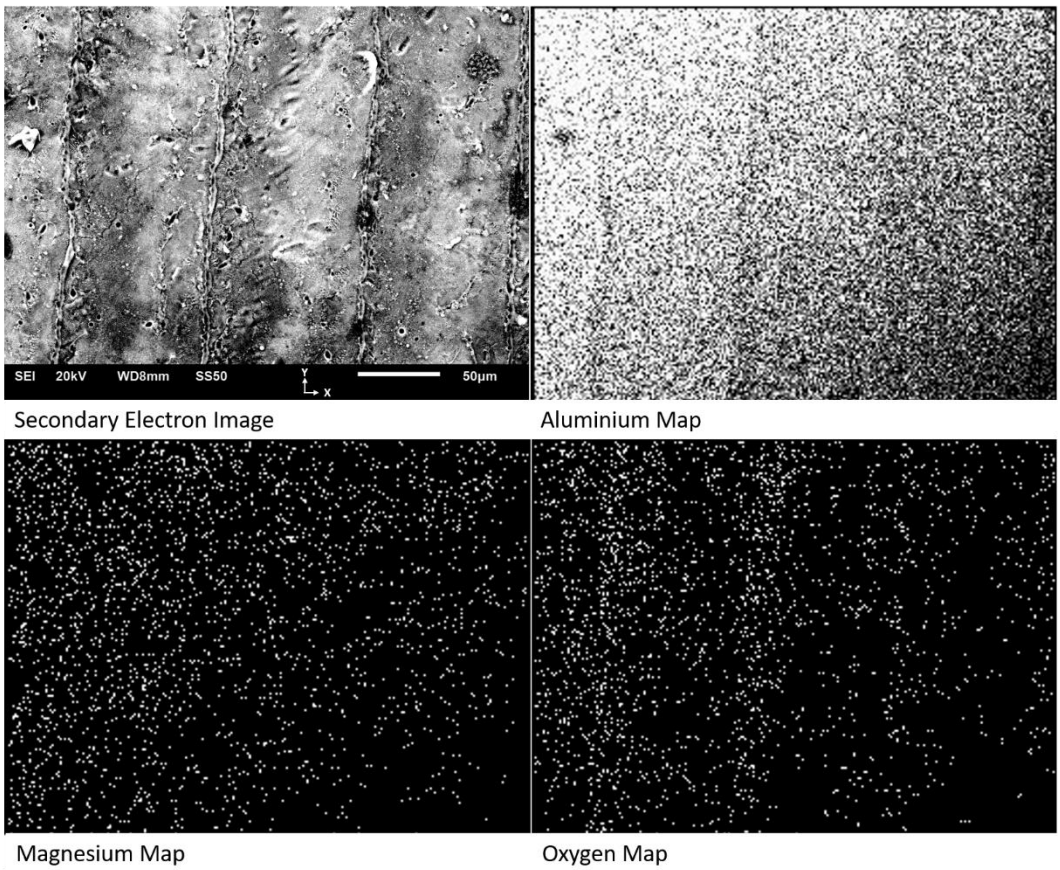

Spectrum	Al	O	Mg	Si	Zn
20 kV	84.12	14.27	0.61	0.61	0.40

Figure 204 SEM x400 and EDX elemental maps of the most prominent elements and the composition of the top surface of double scanned AA6061, sample 46 from test A7

The tracks in double scanned samples appear quite different to the single scanned tracks. The striations of the tracks in the SEM image show a darker appearance on the left-hand side of the tracks and a brighter right-hand side. The darker side corresponds to the location of observed oxygen, which is unlike what was observed with the single scanned samples (Figure 203). The explanation of the oxides corresponding to the brighter regions in the single scanned part was that the oxides were causing charging due to poor conductivity. Charging only occurs with oxides of sufficient thickness [171] and it was observed above, that the surface oxides are reduced with double scanning. In the absence of charging, the change in colour could relate to a chemical change, or from surface topography. Oxides are the most plausible explanation of the change in intensity, as their presence could reduce the number of electrons emitted from the sample.

The effect of rescanning the samples is that it reduces the oxide on the top layer, though questions remain as to how the oxides form and how the rescanning physically affects these oxides. The presence of oxides coincides with the side of the scan tracks,

though the analysis of the top surface can not determine if the oxides are only on the surface or if the higher presence is due to the observation of oxides forming on the side of weld tracks. If oxides are forming on the side of weld tracks, then these will also be visible on the vertical surface perpendicular to the scan track orientation. This is performed in the next section.

It can be seen that thick oxides form on the single scanned sample, which are removed by double scanning, with thinner oxides forming on this surface. One possibility is that the rescanning stirs the oxides into the part. To determine if double scanning reduces the overall amount of oxides within an SLM AA6061 sample, EDX of the vertical surface was performed.

5.4.2 Effect of Rescanning on Oxides within the Bulk Material

EDX analysis of the top surface showed oxide layers coating both the single scanned and double scanned samples, with a concentration of oxides at the side of the scan tracks. Vertical cross sections of the samples, perpendicular to the scan direction displayed on the top surface, were analysed to view the profile of the scan tracks and measure the presence of oxides near the top surface. The cross sections showed the unevenness of the top surface (Figure 205 and Figure 206). Surface topography was a possible explanation for the appearance of oxides along the scan directions, but the cross sections show that the top surface does not have a consistent undulating pattern necessary to create the oxide patterns.

Areas near the top surface of the vertical cross section were analysed to try to detect the pattern of oxides seen from the top surface. The area viewed was such that at least two scan tracks should be present. The elemental maps do not show any trend in oxygen or aluminium that could imply that the oxides within the material are located specific to sides of weld tracks. If the oxide patterns seen from the top surface are a result of oxides aligning perpendicular to the surface, they would be equally perpendicular to the cross section of the vertical plane, though the depth of these oxides is not known.

Line scans were used to collect the trends of aluminium and oxygen within 10 µm from the top surface. Two dips in aluminium content were present along the line scan of the single scanned sample. The distance between the dips is greater than 220 µm, while the distance between dips in aluminium was observed to be 90 µm on the top surface, matching the hatch distance. The dips in aluminium and the peaks in oxygen, which are not coincident, are more likely to be due to defects on the cross section and are not consistent with the view of oxides on the top surface. The oxide peak on the right seems to link to some tarnishing of the surface, possibly a contamination for the grinding disk. This shows that the surface oxides are very shallow. This disproves the hypothesis that the alignment of oxides with hatch spacings in due to the oxides forming on the side of each weld track as they are formed and remaining as adjacent

tracks are added. Oxides form on the top surface either form preferentially away from the centre of the melt tracks or are forced to the sides by buoyancy and Marangoni forces.

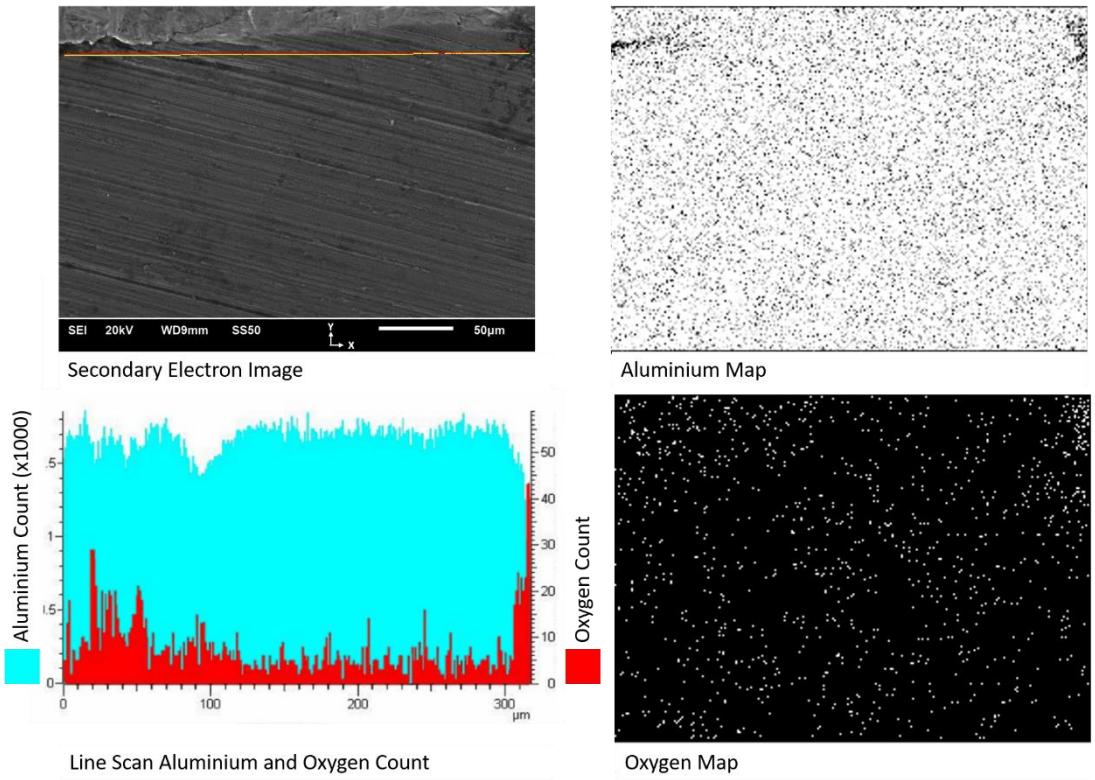

	Al	O	Mg	Si	Zn
Map	95.15	3.15	0.46	0.76	0.48
Line scan	95.48	2.80	0.51	0.84	0.37

Figure 205 SE image, EDX elemental maps of aluminium and oxygen with line scan near the top of the sample, and composition calculations of single scanned AA6061, sample 22 from A4

The same approach was taken with the double scanned sample (Figure 206). The elemental maps found several areas of concentrated oxygen that are just on the top surface rather than on the vertical cross section. The line scan had a rather low count and did not pick up any trends involving the hatch distance.

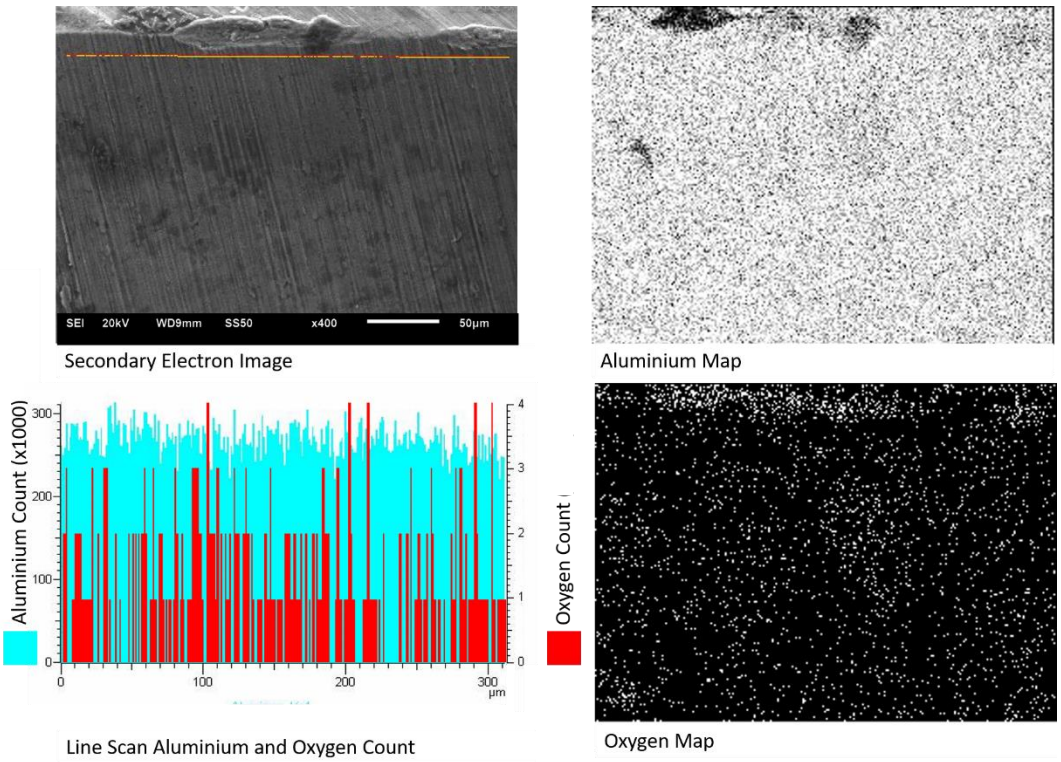

	Al	O	Mg	Si	Zn
Map	95.37	3.28	0.37	0.74	0.23
Line scan	94.46	4.15	0.32	0.78	0.29

Figure 206 SE image, EDX elemental maps of aluminium and oxygen with line scan near the top of the sample, and composition calculations of single scanned AA6061, sample 46 from test A7

Oxygen content measured from the collection of the map data detected a higher oxygen content within the double scanned sample than was measured within the single scanned sample, though the difference was minimal. It was seen from the top surfaces how rescanning reduced the oxide film on the top layer. As no reduction in oxides are seen within the body of the samples it may be the same mechanisms are occurring in both samples. Each layer of the single scanned samples undergoes remelting with subsequent layers and it may be that this has the same effect on the surface oxides as occurs with rescanning in the double scanned samples. The oxygen content of both is above the threshold value of 2.17%, as measured against a conventionally manufactured AA6061 sample, confidently implying oxides are present within the parts. Melting the material with each layer may cause the oxides to break-up and stir into the melt pools. Aluminium oxides float upon molten aluminium and it may be expected that the oxides are carried to the top of the parts, through buoyancy forces, but the solidification of metal within SLM is in inequilibrium. The difference between oxides found on the top surface of single scanned samples versus double scanned indicates that the oxides are not simply on the top surface due to buoyancy, but that fresh oxides are created during the first scan, likely from oxygen contained within the powder. The second scan disrupts these oxides with a visibly more reflective surface produced and lower oxygen content detected. A high quantity

of oxides are measured near the surface of the double scanned samples. If these are due to the disrupted oxides floating to the top surface, then a trend would be visible on the vertical cross sections. Alternatively, the surface oxides on the double scanned samples could be freshly formed as well but with less available oxygen for the reaction. If the oxides formed on the first layer are disintegrated and removed with spatter and condensation within the chamber, then then overall level of oxygen within the part would reduce. Alternatively, if the oxides formed on the first layer are stirred into the parts, then oxides formed on the second scan would increase the overall quantity of oxygen measured within the samples. The quantity of oxygen with the double scanned sample does increase, but only by a small amount and therefore the assessment is inconclusive.

Samples with different surface reflectivity were produced within the Renishaw AM125 with equal processing parameters apart from a changing spot size. The change in surface reflectivity implies that the surface oxidisation is not inherent in all single scanned samples but can be influenced with machine parameters. Furthermore, as the second scan is not used, where the oxides may be stirred into the parts, the surface reflectivity may imply a reduction in the overall oxygen content of the part.

5.4.3 Effect of Spot Size on Oxides

During tests with the Renishaw AM125, the top surfaces of the parts had different levels of reflectivity depending on location. Spot size tests found a strong correlation between the reflective surfaces and finer spot size. It was shown in the analysis above that the discolouration corresponded to oxides on the top surface. To test the effect of the inconsistent spot size on part density an array of 6 x 6 repeated blocks was built. These blocks are used here to measure the different levels of oxygen left on the top surface from the different spot sizes. Not all the blocks were needed so only one row of blocks was assessed (blocks numbered from 13 to 18).

Readings using the 20 kV accelerating voltage beam were recorded for all samples on the top surface and on a vertical cross section, to measure the internal oxygen content (Table 34). There is no discernible trend between spot size and oxygen content, measured either at the top of samples or within the body. Samples 13, 14 and 17 measured similar values of oxygen on the top surface and on the side of the samples. This subset includes the samples with the largest and smallest average spot size. The change in spot size is noticeable, not only with the surface reflectivity, but with sample densities, but a significant change in oxygen content was not measured.

Samples 16 and 18 stand out as having a very different oxygen content compared to the other four samples. Sample 18 measured the highest amount of surface oxides but the lowest bulk oxides. The reverse is true of sample 16, with the lowest surface oxides and highest bulk oxides. This relationship of the oxides found on the top surface, with less in bulk material could be caused by the melt pool allowing more

time for oxides to float to the surface, and therefore removing them from the body of the sample. However, there is no obvious reason why samples 18 and 16 would be affected in this way while surrounding samples are not.

During the build, the scanning order of the samples was from left to right (i.e. starting at 13 and ending at 18) and the gas flow was directed from right to left. Both factors could influence part quality. The highly focussed beam in the Renishaw AM125 created a lot of spatter, which blew on previously scanned samples to the left of the spatter origin. It can be seen in the elemental maps that the spatter is extremely high in oxygen and contributes significantly to the overall oxide reading on the top surfaces and may get incorporated into the bulk of the samples with subsequent layers.

In the SE images it can be seen that the spatter is charging. This is caused by the lack of a conductive path for the electrons, caused by the oxide. For some of these spatter particles, with very high levels of charging, no x-rays are detected and therefore the extra oxygen content from the spatter does not contribute to the calculated composition.

It is also worth noting that sample 18 was the only sample which had no spatter, as it was in the rightmost position, and this contained the highest oxygen content on the top surface.

Table 34 Location influence on density and the presence of oxides within AlSi10Mg samples

Block number	**13**	**14**	**15**	**16**	**17**	**18**
Average Spot Size (pixel)	70.31 ± 3.33	62.29 ± 3.15	70.75 ± 5.08	69.16 ± 5.58	58.78 ± 3.28	66.45 ± 3.23
Relative Density (%)	96.04	95.71	97.3	98.24	94.88	96.13
Oxygen Content						
Top Surface, 20 kV	15.27	15.14	12.27	11.38	15.88	17.42
Vertical Cross section, 20 kV	4. 18	3.82	2.79	5.57	3.08	1.41

The location of the oxides on the top surface of the Renishaw AM125 samples was on the side of weld tracks, as was the case with the Realiser SLM100 samples (Figure 207, Figure 208, and Figure 209). The SE images reveal globules seen on the side of weld tracks, which weren't seen in the Realiser parts (Figure 210 and Figure 211). It appears that balling is occurring on the top surface and being pushed to the edge of the tracks. Oxides covering the aluminium material would be expected to reduce the surface tension and therefore be less likely to cause balling. One consideration is that these samples are made with AlSi10Mg, while the samples examined in rescanning were built with AA6061 and therefore the material and the oxide may be affected by the compositional change.

It is noticeable that there are no globules on Sample 18 (Figure 212). This sample was the last sample scanned and spatter generated from this sample was blown toward the other samples. This suggests that the globules are in fact spatter generated on adjacent samples. This then raises the question of why the globules align with the edge of scan tracks. Spatter evident on the top layer does not have to be freshly placed on the layer, but may be placed earlier and then moved to the side of the weld track, either partially submerged or floating but maintaining the solid oxide shell. If the spatter particle is not disintegrated, but maintained within the SLM sample, evidence would appear as either concentrations of oxides or microstructure inconsistent with the rest of the sample. The former of these was tested during EDX compositional calculations of the vertical cross sections of samples and no inconsistent areas were observed. The latter was not tested due to limits of time.

The disparity between the surface oxides and the reflective appearance may relate to the topography of the samples. Sample 13 had a very rough surface. This may have impacted the ability to measure an accurate EDX measurement and large shadows are observed in the elemental maps (Figure 207). A shallower reading, made with 5 kV accelerating voltage, had an oxygen reading of 4.07%, similar to the bulk reading of 4.18%, was much lower than deeper 20 kV measurement. The implication of this is there is a higher concentration of oxides within the sample than on the surface, which is not a believable result.

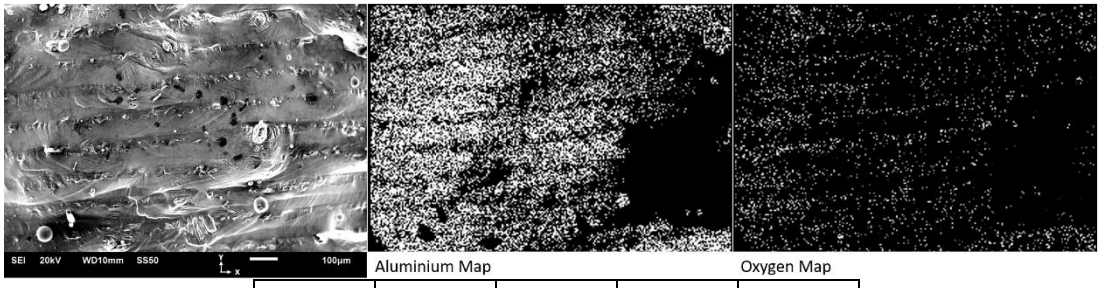

	Al	O	Mg	Si
5 kV	91.27	4.07	4.35	0.48
20 kV	76.71	15.27	1.01	7.01

Figure 207 Sample 13 from ALSi10Mg Renishaw AM125 repeatability test, SEM, EDX elemental maps and composition calculated with two accelerating voltages

Sample 14 was produced with a much finer beam, and produced a much brighter top surface. The SE image revealed a much flatter surface though it was covered in globules, which may have been spatter. The EDX maps, which did not find elements across the complete measured area, measured a similar composition to sample 15, when measured with the 20 kV beam. The measurement with a 5 kV beam found a similar oxygen content, but higher silicon content.

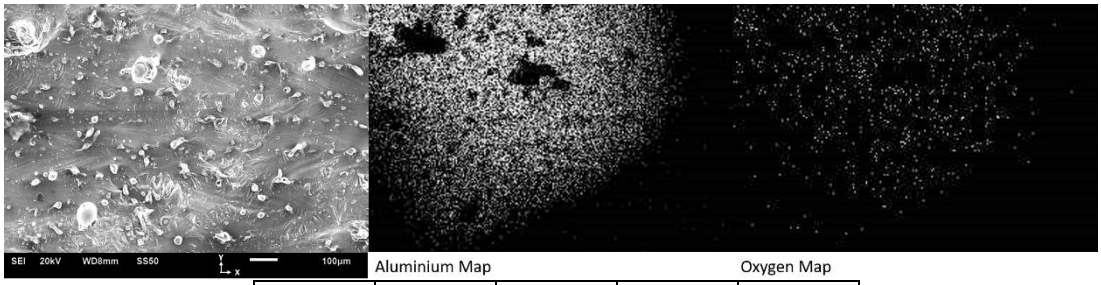

	Al	O	Mg	Si
5 kV	71.49	16.77	0.62	11.26
20 kV	77.57	15.14	0.45	6.54

Figure 208 Sample 14 from AlSi10Mg Renishaw AM125 repeatability test, SEM, EDX elemental maps and composition calculated with two accelerating voltages

Sample 15 was a high density block, with spot size larger than that of samples 14 or 13, and produced a dark top surface. The surface had the clearest bands of oxide and aluminium with the clearest alignment of globules with the side of scan tracks. The surface bore a similar flat surface as sample 14, proving the surface reflectively is not solely dependent on surface roughness.

This was the only Renishaw sample which measured a higher oxygen content with the shallower penetrative depth, as indicates a surface oxide.

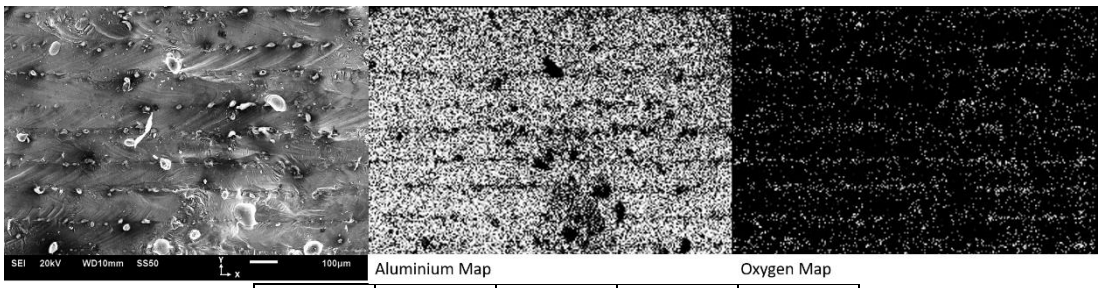

	Al	O	Mg	Si
5 kV	65.97	22.49	2.23	9.03
20 kV	79.08	12.27	0.32	8.22

Figure 209 Sample 15 from Renishaw AM125 repeatability test, SEM, EDX elemental maps and composition calculated with two accelerating voltages

As the change in the spot size was elliptical, the reverse trend of spot sizes from sample 13, 14 and 15 should be seen in samples 16, 17 and 18, though the measured average spot sizes are smaller than their mirror counterparts. As the parts are to the right of the samples previous set, it could be expected that the surfaces contained less spatter and changes in part oxide surfaces and topography would be more apparent. However, this is not evident in the results.

The oxygen content measured on the top surfaces of samples 16 and 17 was similar to corresponding samples 15 and 14, with similar spot size. Samples 16 (Figure 210) had a much wider spot size and darker surface than sample 17 (Figure 211). The expectation that the more reflective surface would show lower oxygen content was confounded, as with sample 14. An observation with the oxides within sample 16 is

that the oxides do not only show a higher concentration at the spatter locations but a faint underlying trend within the grain boundary. Sample 17 shows much higher prominence of oxides on globules, believed likely to be spatter. This is similar to samples 15 and 14, where a strong trend of oxides at the side of scan tracks was observed with the sample produced with the larger beam size, while oxygen is only evident on globules of the sample produced with the finer spot. The concentration and appearance of the spatter may be hiding any measured change that the spot size has on the surface oxides of the parts.

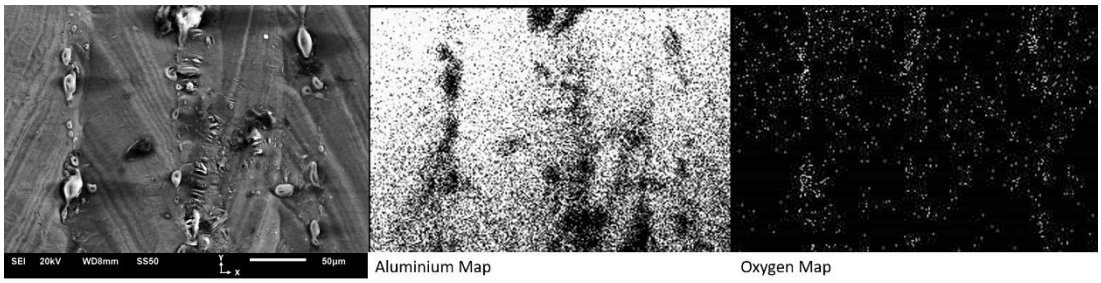

	Al	O	Mg	Si
20 kV	79.81	11.38	0.16	8.75

Figure 210 Sample 16 from AlSi10Mg Renishaw AM125 repeatability test, SEM, EDX elemental maps and composition

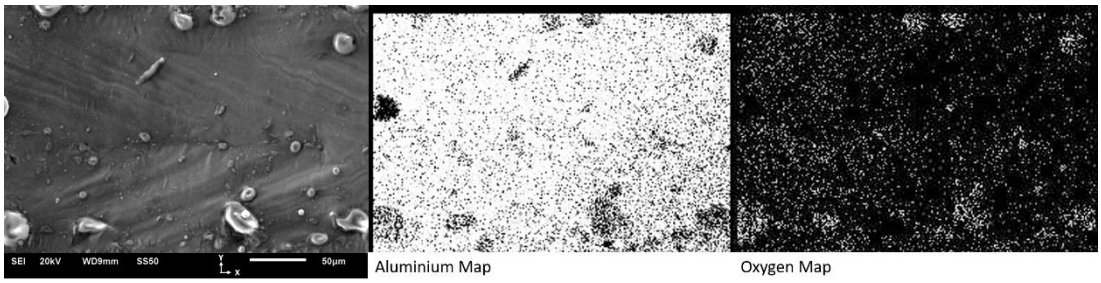

	Al	O	Mg	Si
20 kV	75.23	15.88	0.61	8.84

Figure 211Sample 17 from AlSi10Mg Renishaw AM125 repeatability test, SEM, EDX elemental maps and composition

No globules were evident on the top surface of sample 18. As this sample was nearest the gas inlet, this shows that the globules are not generated on the parts themselves but from spatter of adjacent parts. Interestingly the top surface, free from interference from spatter particles, measured a high concentration of oxides than other samples.

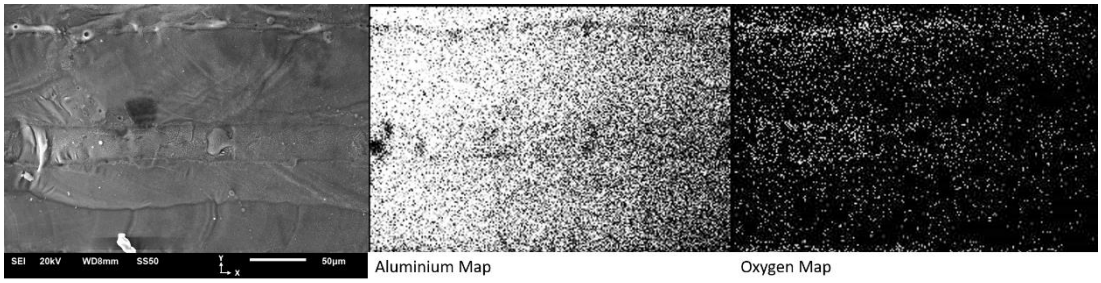

	Al	O	Mg	Si
20 kV	74.96	17.42	1.2	6.44

Figure 212 Sample 18 from AlSi10Mg Renishaw AM125 repeatability test, SEM, EDX elemental maps and composition

5.4.4 **Deep Etched Samples**

The EDX analysis revealed that the top surface of aluminium samples had a coating of thick oxides and that the internal body of the samples had oxygen levels higher than the accepted benchmark. No trend was revealed as to the location of oxides within the body of the samples or of the composition of the oxides. The challenge with this is due to the very fine nature of the oxides requiring greater resolution than EDX offered. It was decided that samples were to be deep etched to remove the aluminium and to assess what material remained, which should be oxides. To do this, 2 mm slices of samples were mounted and deep etched with 25% sodium hydroxide solution for 6 hours.

A horizontal section of each material was made with the top surface mounted in resin, as it was known that the top surface contained thick oxides, and these would remain after etching. A vertical cross section, 2 mm thick, of each material was made to include the centre of the sample feet up to the top of the sample to capture any oxides within the body of the samples.

Two sets were created from the SLM AA6061 samples. The first set was created with samples from an early build (test A1), produced when the powder was young (Figure 213). Only a small amount of oxide remained etching, including on the top surface. The second set was produced from samples that were produced later (test A4) (Figure 214). The level of oxides that remained with the second set of samples stands in stark contrast to first. The structure of the oxides left in Figure 214 appears to have been created from oxides coating the walls of the cracks. The parameters of the samples were selected to be as similar as possible so that their effect would be minimised and what remains is arguably signs of the powder aging and taking more oxides into the samples. There is no significant difference between the levels of cracking observed in samples produced from test A1 and test A4, and cracks were evident in the samples of Figure 213 before etching. Oxides may have existed on the crack surfaces of test A1 samples but may not have survived the etching process if they were discontinuous or if they were not as thick or robust as the oxides seen from test A4. This is a reasonable assessment as the deep etched samples are not completely free from oxides.

However, the disparity in levels of oxides, in contrast to the similar levels of cracking, points to the lack of relationship between the two phenomena and is further evidence that oxides within the SLM samples do not cause the formation of cracks.

During the unidirectional scanned test (section 5.1) it was reasoned that the cracks are formed during processing and propagate through each layer as they are scanned. This creates crack surfaces open to the chamber environment and available for the formation of oxides, just as is evident with oxides forming on the top surface of each scanned layer. The thickness of the remaining oxides in Figure 214 is a testament to the oxides forming at elevated temperatures and the increased moisture content of the aged powder.

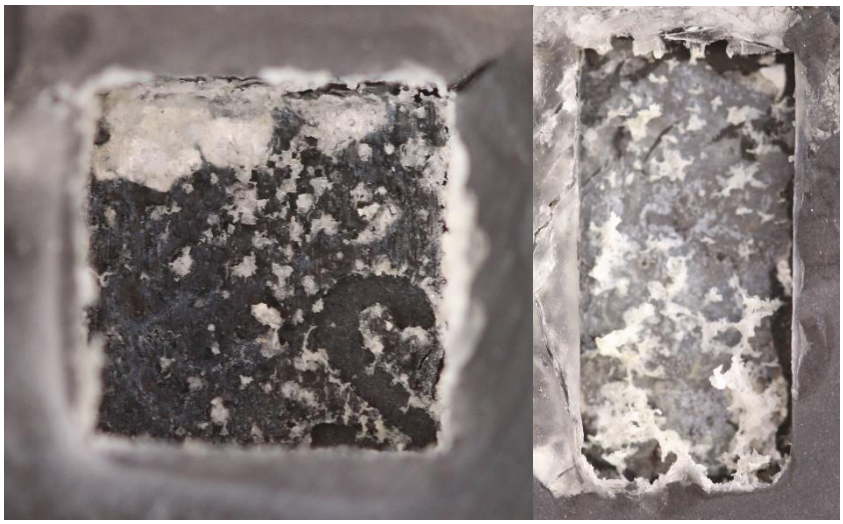

Figure 213 Residual oxides from deep etching of AA6061 single scanned samples, horizontal cross section of sample 2 (left) and vertical cross section of sample 14 (right) from test A1

Figure 214 Residual oxides from deep etched AA6061 single scanned samples, horizontal cross section of sample 22 (left) and vertical cross section of sample 23 (right) from test A4

The effects of rescanning are seen in Figure 215. The horizontal cross section appears as a honeycomb structure with hexagonal cells. The second scan was expected to provide some stress relief, which may have permitted the samples, unrestrained where cracks appear, to reshape. The extra time to form into a desired shape may have permitted the oxide and the metals within to take a sturdier structure. A low amount of oxides are observed at the base of the horizontal sample, which corresponds to the top layer of the build, compared to the single scanned sample in Figure 214. The samples in Figure 214 and Figure 215 were built concurrently and therefore differences in powder characteristics can be dismissed. It was observed how rescanning reduced the level of oxides seen on the top surface, and this effect can be seen here also. The vertical cross section of the deep etched samples shows the oxides as planes with a robust network of oxides running from the feet of the sample all the way to the top surface. The shape of the oxides in the vertical cross section of the double scanned and single scanned samples are very similar. A higher content of oxides has survived the etching process from the double scanned samples. This could relate to the reshaping of the network of cracks and oxide. It might be suspected that the thick oxides on the crack surfaces of the single scanned samples may inhibit any reparation of the cracks that was hoped for with the rescanning, but the horizontal cross sections show that breaking up the thick oxides to allow the fusion of aluminium occurs during the SLM process.

Rescanning the sample reduced the amount of oxide on the top layer of the samples, but it is unclear if it has had any positive effects on the oxides with the samples and the levels of oxides are not as low as seen with the samples produced with fresh powder.

Figure 215 Residual oxides from deep etched AA6061 double scanned, horizontal cross section of sample 44 (left) and vertical cross section of sample 46 (right) from test A7

The composition of the oxides was measured with EDX (Figure 216) which revealed that the oxides are largely aluminium and magnesium oxides. High levels of

magnesium were also observed with the surface oxides (Figure 167). The intention of magnesium within this alloy is to form Mg_2Si precipitates, which give the alloy strength. The reaction of the magnesium to oxygen will reduce the amount the magnesium within the body of the alloy that is available to create these precipitates. It is not known what proportion of magnesium reacts with the oxygen, but the effective compositional change is a concern with moving forward with these alloys systems. Even, with the best case scenario, where the oxides only form on the outer surfaces of the SLM parts, the aging of the powder had a significant influence on the quantity of oxides that formed, and this creates an instability in controlling the alloy composition.

A caveat of these results is that only oxides that appear to decorate the crack surfaces, which are already a critical problem, and the top surfaces were found but this does not mean these are the only oxides existing in the parts. Oxides not connected to the surfaces of the etched samples would be washed away with the solution. It is therefore unclear what all oxides exist and what detrimental effects the oxygen content may have. Future work may consider attempting to collect remnants of solid within the etching solution for further analysis.

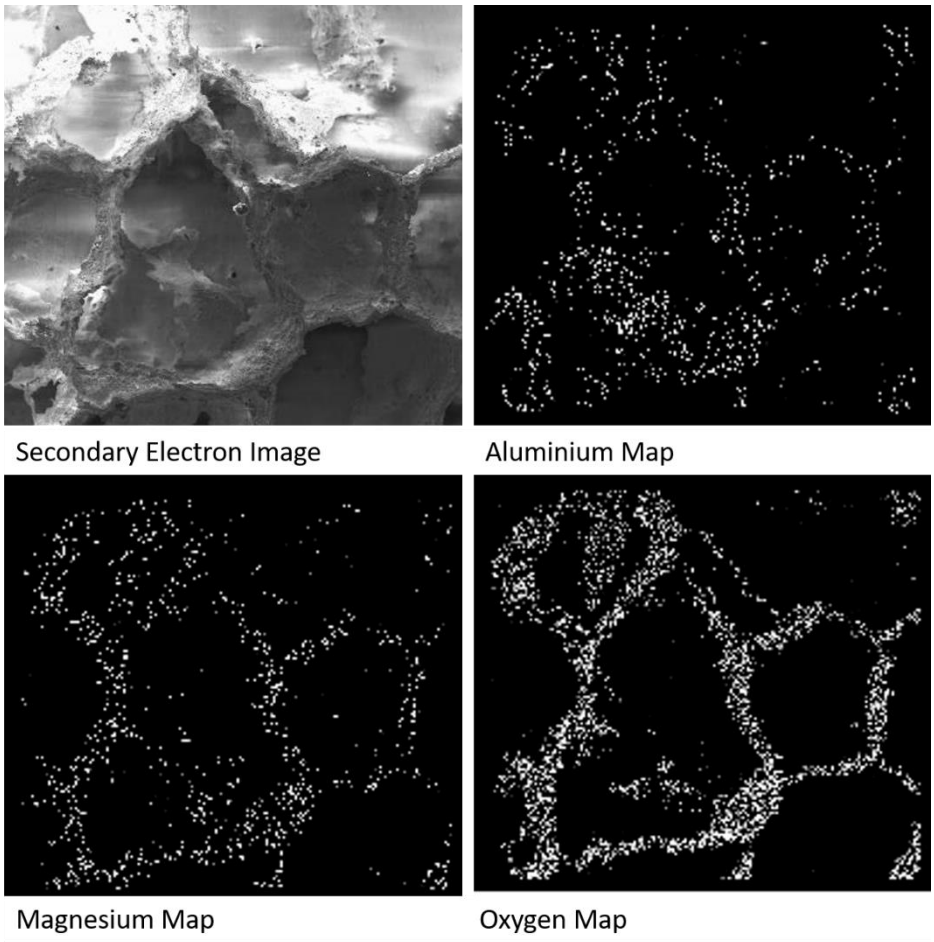

	O	Mg	Si	Al
20 kV	72.24	13.19	0.67	13.90

Figure 216 EDX composition analysis of AA6061 oxides

Horizontal and vertical sections of AlSi10Mg samples were deep etched in the same way as the AA6061samples (Figure 217). The appearance of the remaining material is very different. EDX analysis revealed that the remaining material was mostly made up of silicon (Figure 218), which has a higher concentration at the weld pool boundaries. Horizontal sheets of silicon prevent the penetration of the etchant into the horizontal cross section sample, while the almost all the material has been corroded from the vertical samples.

Figure 217 Residual oxides from deep etched AlSi10Mg, horizontal cross section of sample 5 (left) and vertical cross section of sample 12 (right) from test B4

The etchant did appear to be most effective at corners of the samples and SE imaging revealed the extent of the layered structure through the sample (Figure 218). The high magnification image of the material shows the same structure of silicon that was observed in the microstructural analysis of the samples (Figure 188). The layers are likely silicon concentrated at the base of the weld pools and connected across each scanned layer. Silicon is a brittle material and therefore the layer provides the location of failure with the as-built samples (Figure 34).

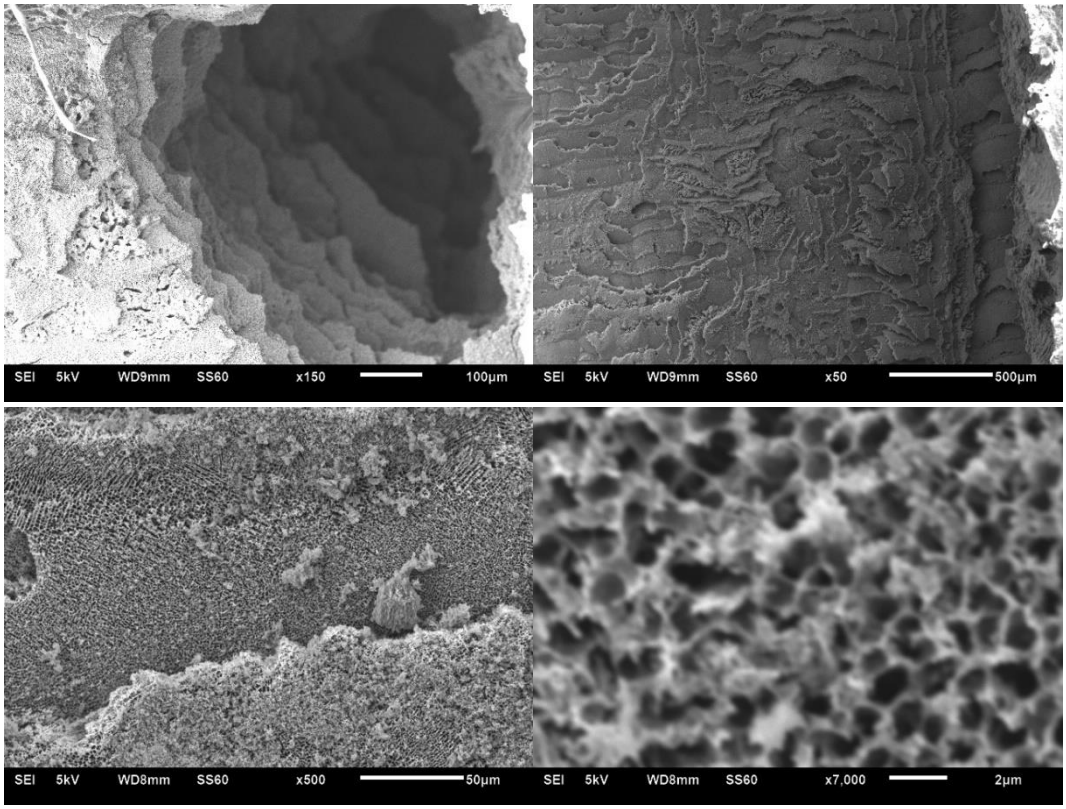

	O	Mg	Si	Al
20 kV	13.52	3.43	76.00	7.05

Figure 218 SEM and EDX composition analysis of AlSi10Mg deep etched horizontal sample

Deep etching of the blended material samples revealed a structure more similar in appearance to the silicon observed in AlSi10Mg, than the oxides observed from AA6061 (Figure 219). This is interesting as the deep etched AlSi10Mg samples revealed the silicon structure that closely associated with the microstructure of the alloy, while the microstructure the blended material was similar to AA6061.

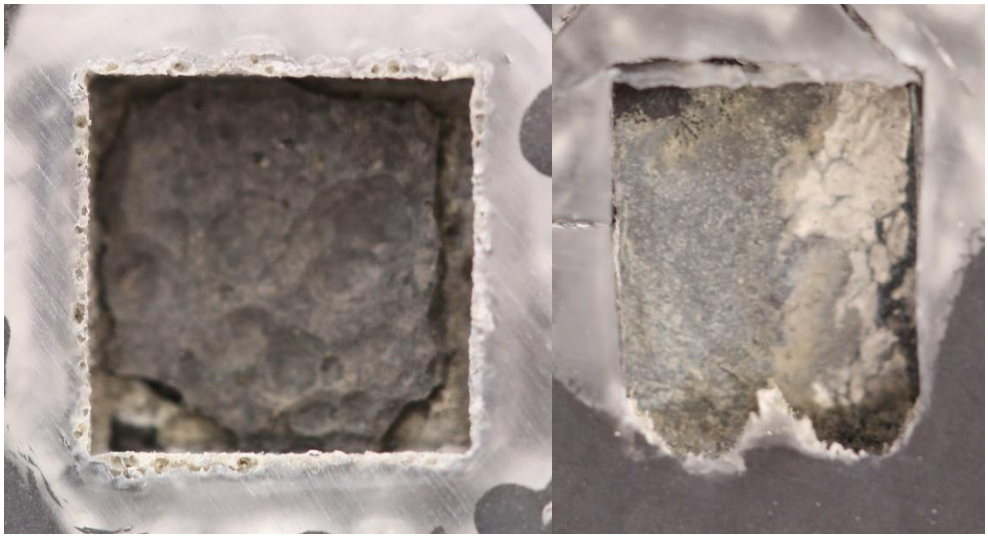

Figure 219 Residual oxides from deep etched blended material, samples 5 (left) and 12 (right) from test F4

What remained from the deep etched AlSI10Mg samples was shielded by layers of silicon which was concentrated at the weld boundaries. The same layered structure is not apparent with the deep etched blended material samples (Figure 220), which is not surprising as there were not observed changed in the composition at weld boundaries of this material. The remaining material from the deep etched blended material appears to be a more amorphous interconnected material. The observations into the difference between AA6061 and the blended material concluded that cracking was prevented due to higher silicon content being available to fill grain boundaries. The remaining material may be the interconnected grain boundaries, preventing the penetration of the etchant.

EDX was used to calculate the content of these grain boundaries and found a high oxygen content. Oxides could be located within the grain boundaries of the material which would be a concern for embrittling the as-built material and potentially preventing severely altering the reaction to heat treatment. It is possible that AA6061 may have a similar material but would not remain after the etching process as pores and discontinuities in the grain boundaries would cause the structure to crumble.

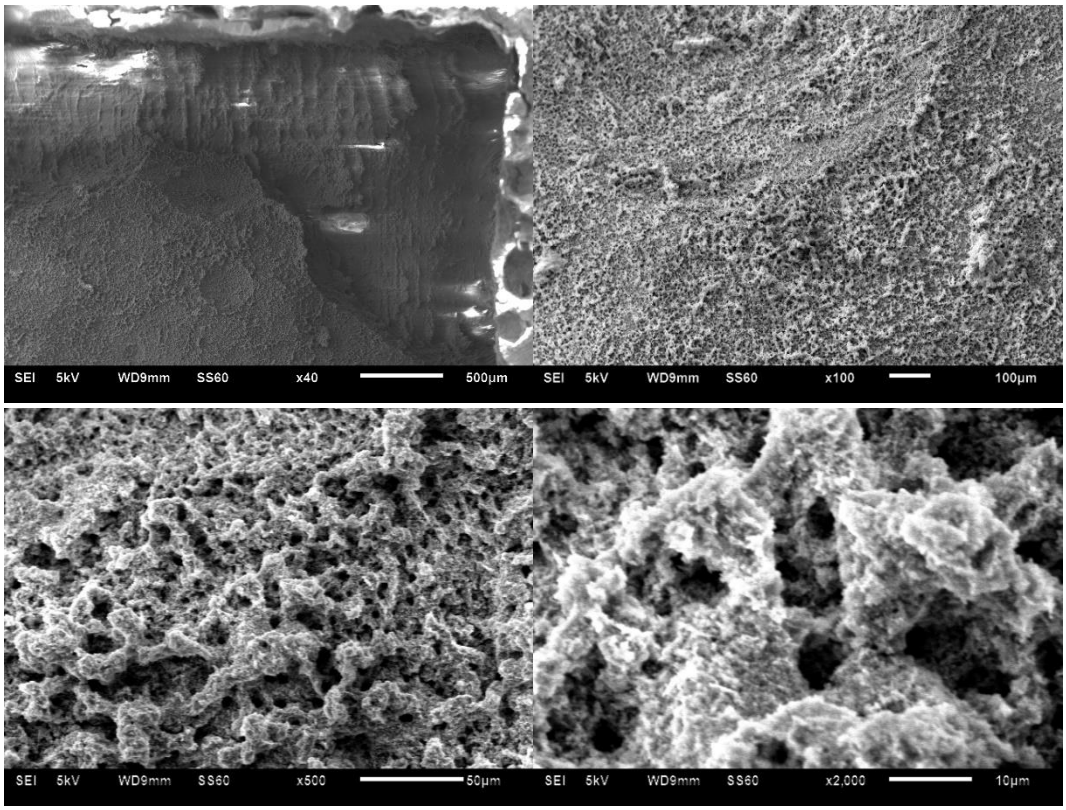

	O	Mg	Si	Al
20 kV	53.27	12.15	16.01	18.57

Figure 220 SEM and EDX composition analysis of blended material oxides

5.5 Summary

The location of the crack within a part and the influence of part shape and scanning strategy were used to determine how stresses affect cracking. The findings showed that failure occurred under local stresses and was not influenced by the accumulation of stresses over the entire part. The location of the cracks within the weld track and the microstructure show how the cracks propagate through the material and are indicators that solidification cracking was the cause. Finally, the potential inclusion of destructive elements was examined using EDX on the crack surfaces as well as investigating the presence and effect of the oxides within the samples. The conclusion from this was that oxides are present and could weaken the material but that they are not a cause of the cracking. This leaves solidification cracking as the only viable reason for the cracking.

6 Conclusion

The aim of this research was to increase understanding of the behaviour of aluminium alloys during SLM processing, so as to improve the quality of components produced. This new knowledge will increase understanding of the problems associated with processing aluminium and its alloys using SLM and this will hopefully help lead in the future to the design and manufacture of environmentally friendly ultra-lightweight parts for application in the aerospace and automotive sectors.

This project came from the desire for aerospace and automotive industries to utilise metal additive manufacturing for the production of light weight structural components and the need for alloys that improve upon the specific strength of currently available systems. A review of the current literature identified cracking susceptibility as an important problem with the light alloys in SLM, while the literature on welding hinted at a possible solution to the problem and involved modifications to the alloy compositions away from those used conventionally. The alloy AA6061 was selected for investigation as it is used in many applications and a compositional change was possible by blending it with AlSi10Mg, another alloy widely available in powdered form.

A parameter study of AA6061 showed the build characteristics and confirmed the extensive cracking of this alloy with SLM processing, the cracks mainly developing due to horizontal stresses, with the cracks being along the scan directions. Initially techniques were developed and tested that were thought to reduce these stresses. The first was to use lower energy density to reduce thermal gradients around the solidifying melt pool. The second was to reduce the layer thickness, as reducing the track depth has been found to reduce stress and cracking in weld tracks. The third method was to scan each layer twice, which had been shown by others to reduce residual stresses by up to 55%. The results from these tests unfortunately showed that they had no significant effect on cracking with this alloy and that a different approach was required.

In contrast when the blended powder mix of AA6061 and AlSi10Mg was processed by SLM no cracking was observed when using conventional build strategies but some were with unidirectional builds, even though the powder had aged significantly by this stage in the project. The ageing had led to the pickup of moisture on the powder and led to the formation of small gas pores in the alloy on freezing during SLM processing. This idea of an ageing effect was supported by the detection of thicker oxides on open surfaces than when the powder was new. The ageing of the powder could be slowed by designing powder handling so as to limit the availability of moisture but given the reactivity of aluminium and its affinity for moisture it is likely that aluminium powders will have limited life. The SLM system and sieving set-up used often requires the

powder bottles to be opened in an uncontrolled environment and some improvement could be achieved by keeping the powders under a controlled atmosphere at all time.

Another challenge to producing homogeneous parts with mixed powders is avoiding powder segregation and it was easier to get a more even distribution by mixing two alloys than adding raw materials. When AlSi10Mg was mixed at a ratio of 9:1 with AA6061, the silicon content reached the range where reduced cracking was seen, whereas if pure silicon had been used a ratio of 99:1 was required and this would rich significant segregation effects. The parts produced showed that the powders mixed within the melt pool to produce a homogeneous microstructure and this was a valid methodology for producing novel alloys with low cost.

The research showed that cracking in AA6061 built parts was significant compared to AlSi10Mg and the blended material samples and the only significant difference was the microstructure changes due to the change in the silicon level. It was hypothesised that the cracking mechanism was the same as in welded aluminium, and that the same alloy mixing used in welding was applicable here. Electron channelling contrast imaging of the microstructure of the alloys revealed pores and fine cracks within the grain boundaries of only the AA6061 samples. These probably act as the nucleation points for the more extensive cracking that develops as the part builds. Cracks are most prominent within the grain boundaries of larger grains and this is similar to that seen in welding and may be due to either voids occurring on shrinkage or incomplete liquid inflow during final freezing. Thermal stresses then cause these cracks to propagate along the grain boundary. With the blended material no defects were found within the grain boundaries, the difference in behaviour possibly being due to the final material freezing over a narrow temperature range as a near eutectic material is the last liquid to freeze, although it cannot be discounted that the presence of silicon may alter segregation to the boundary.

The grain structures of the blended alloy and AA6061 were very similar after SLM processing while the silicon rich AlSi10Mg was noticeably different. The similarity of the blended material and the AA6061 was encouraging as the compositions are similar and both compositions are within the solid solubility limits of Al-Mg_2Si, with comparatively large freezing ranges. This contrasts with the microstructure observed with AlSi10Mg which has a near eutectic composition and a narrow freezing range. Both AA6061 and the blended samples had regions of very fine microstructures at the base of some of the scan tracks, pointing to new grains being nucleated rather than the pre-existing grain growing, indicating changes in the interface at the base of the melt pool. This is similar to the observations of Spierings et al., [224] with aluminium-scandium alloys and Montero-Sistiaga (2016) with AA7075+Si, who both also reported the nucleation of fine grained material. In each of these cases for new grains to nucleate, the growth of the underlying pre-existing solid must be suppressed either

by segregation to the interface or possibly the presence of an oxide. A complicating factor in understanding what is occurring is the high levels of hydrogen porosity in the blended alloy due to the age of the powder, an effect that could be investigated due to a lack of time and money. The presence of hydrogen porosity alludes to the presence of oxides, as both are created when water molecules breakdown. The oxide may stop the underlying grain growing while also providing nucleation sites for the new grains.

The microstructure of AlSi10Mg is considerably different from AA6061 and the blended material samples. Thijis et al. [198] argued that AlSi10Mg was crack free due to the narrow freezing range and subsequent microstructure. The behaviour of the blended material in not cracking even though it has a wider melting range than AA6061 points to a different mechanism operating in these experiments.

Tests with changing scan direction and part shape indicated that the cracks are uniformly spread throughout the part and this will lead to local changes in stress. The cracks appear parallel to the build direction rather than across the weld where the greatest stress would be expected. This points to a weakness in the structure parallel to the build direction. It was observed that the location of the cracks occurs with the greatest misalignment of grains and this could be a location of high grain boundary defects as well as higher stresses due to shrinkage. The separation of the cracks within the AA6061 samples was on a larger scale than the weld pools. This could imply that accumulation of stresses has an effect. The spacing of the cracks may not relate to the magnitude of thermal stresses, as the grain structure also has an influence. Altering the stresses may simply change how wide the crack is opened, rather than altering the spacing or number of cracks.

On the horizontal surfaces, grain orientation dictated the direction of crack growth. It was observed with ECCI that cracks growing parallel to the scan track travel through the grain boundaries at the centre of the scan tracks, while cracks growing perpendicular to the scan direction are more restricted, due to the orientation of grains as they grow toward the centre of the scan tracks.

Unidirectionally scanned samples produced with the blended material did crack, although the cracks were characteristically different from those within AA6061. Cracks within both materials are likely to be produced from the same cracking mechanisms, though unlike AA6061, the cracks within the blended material samples did not crack in a consistent pattern. Cracks within the AA6061 samples were spaced consistently 900 µm apart and ran from the bottom to the top layer, directed by epitaxial grain growth. Cracks within the blended samples appeared to originate at different locations before interacting and competing. It was observed that cracks did not propagate through all the layers but could be arrested, as healing of the crack could take place.

Oxides and other inclusions were considered as a potential source of cracking. Oxides are an issue with casting aluminium due to the metal's high affinity for oxygen and the toughness of the formed oxide. Oxides are known to induce cracks and failures of castings, and in the SLM of aluminium they create an oxide film on each layer of metal. It was observed that aluminium samples produced using the Realizer 100 were discoloured after each layer was scanned. EDX analysis attests to the significant presence of oxides on the top surface of all samples, the quantity of which means the oxides formed within the chamber while the samples are heated. Rescanning layers reduced the surface oxides significantly but did little change to the oxide content within the bulk of the sample. The implications of this are that rescanning has the same effect on the oxides as the remelting had, that occurs with fusion of subsequent layers. Thus, rescanning may not cause removal of oxides, but could stir them into the part.

Oxides were observed on the crack surfaces, but the shape of the cracks indicated that the cracks were not due to the failure of bonding due to oxide films. Deep etching samples indicated that the oxides formed after the crack face formed, but while the surface was hot. Deep etching of AA6061 samples revealed the network of cracks within samples. The quantity of oxides is likely to relate to the presence of moisture, brought into the build chamber with the powder. Samples produced with older power exhibited more oxides. Deep etched AlSi10Mg samples revealed the network of silicon that exists within the eutectic microstructure. Deep etching of the blended material revealed a similar structure to AlSi10Mg, though with much higher oxygen content. Oxides within the material may be being pushed to grain boundaries, as can occur in cast aluminium [176]. The better-connected grain boundaries within the blended samples may enable the structure to withstand the deep etching process, while the grain boundaries of AA6061 are less likely to remain intact. Further research is needed to explain the potential inclusions of oxides with SLM aluminium samples and how they affect the material properties.

6.1 Future Work

This work was carried out to better understand the challenges of processing aluminium alloys using SLM, with a view to developing high strength alloys. The design of alloys factors in the end use of the material and the processing of that alloy. Therefore, bespoke alloys designed for processing through SLM may be necessary to maximise the utilisation of the technology. Work in this thesis has demonstrated how cracking within a conventional high-medium strength aluminium alloys occurs and that this can be remedied through adjusting the alloy composition. It is recommended that the full implications of this change in composition be considered, such as mechanical performance and the development of heat treatments. The novel alloy

proposed in this thesis was developed by blending two powders based on the crack sensitivity data of Al-Mg_2Si. As no optimisation of either the blending or the composition was performed this needs to be fully investigated to identify the role of using blended powders, the optimum process temperatures and the effects of composition.

The understanding of the cracking mechanism developed in this work could be tested with other alloys and the principles of the alloy development can be utilised for alternative alloy systems. The design of the alloy should have a target end use and further alloy development may require an industrial oversight for commercial exploitation.

As yet, comprehensive understanding of SLM aluminium is not yet realised. The presence of oxides within SLM parts remains a concern. It was shown in this work that strong oxides are created on the top surfaces of parts within the Realiser SLM 100. Rescanning appeared to break up the oxides, but the oxygen content remained as high within the body of samples as was seen with single scanning and the difference in melting point between the alloy and the oxide remains a serious challenge in the processing of aluminium alloys in SLM.

The challenge with identifying oxide films within aluminium samples is that they can be very thin and not visible with SEM until decorated by other phases such as silicon. A full understanding of where the oxides end up in the microstructure will come from a full study of the materials using high resolution techniques such as transmission electron microscopy.

7 References

[1] G. M. Shashi, M. A. R. Laskar, H. Biswas and A. K. Saha, “A Brief Review of Additive Manufacturing with Applications,” *Proceedings of 14th Global Engineering and Technology Conference,* 2017.

[2] C. Y. Yap, C. K. Chua, Z. L. Dong, Z. H. Liu, D. Q. Zhang, L. E. Loh and S. L. Sing, “Review of Selective Laser Melting: Materials and Applications,” *Applied Physics Reviews,* vol. 2, no. 4, p. 041101, 2015.

[3] M. Attaran, “The Rise of 3-D Printing: The Advantages of Additive Manufacturing Over Traditional Manufacturing,” *Business Horizons,* vol. 60, pp. 677-388, 2017.

[4] TCT Magazine, “Autodesk Teams with Airbus on 3D Printed Bionic Aeroplane Component,” 2 December 2015. [Online]. Available: https://www.tctmagazine.com/3d-printing-news/autodesk-teams-with-airbus-on-3d-printed-bionic-parition/. [Accessed 20 January 2018].

[5] C. W. Hull.US Patent US 4575330 A, 1986.

[6] C. Kurzmann, K. Janjić, H. Shokoohi-Tabrizi, M. Edelmayer, M. Pensch, A. Moritz and H. Agis, “Evaluation of Resins for Stereolithographic 3D-Printed Surgical Guides: The Response of L929 Cells and Human Gingival Fibroblasts,” *BioMed Research International,* pp. 1-11, 2017.

[7] C. Deckard.US Patent 4683538, 1989.

[8] L. L. Kimble, “The Materials Advantage of the SLS(TM) Selective Laser Sintering Process,” *Proceedings from the Solid Freefrom Fabrication Symposium,* pp. 212-219, 1992.

[9] C. Scuria-Fontana, “Wax Prototyping for Auto Parts,” *Mechanical Engineering,* vol. 115, no. 10, 1993.

[10] P. Forderhase, K. McAlea, M. Michalewicz, M. Ganninger and K. Firestone, “SLS(TM) Prototypes from Nylon,” *Proceedings from Solid Freeform Fabrication Symposium,* pp. 102-109, 1994.

[11] M. Berzins, T. Childs and G. Ryder, “The Selective Laser Sintering of Polycarbonate,” *CIRP Annals,* vol. 45, no. 1, pp. 187-190, 1996.

[12] L. Yang and H. Miyanaji, “Ceramic Additive Manufacturing: A Review Of Current Status and Challenges,” *Solid Freeform Fabrication Symposium,* pp. 652-679, 2017.

[13] M. M. A. Dewidar, “Direct and Indirect Laser Sintering of Metals,” *Thesis,* 2002.

[14] W. T. Carter and M. G. Jones, “Direct Laser Sintering of Metals,” *SFF Symposium,* pp. 51-59, 1993.

[15] D. Bourell, J. P. Kruth, M. Leu, G. Levy, D. Rosen, A. M. Beese and A. Clare, “Materials for Additive Manufacturing,” *CIRP Annals - Manufacturing Technology,* vol. 66, pp. 659-681, 2017.

[16] I. Palcic, M. Balazic, M. Milfelner and B. Buchmeister, “Potential of Laser Engineered Net Shaping (LENS) Technology,” *Materials and Manufacturing,* vol. 24, no. 7/8, pp. 750-753, 2009.

[17] J. Yellup, “Laser cladding using the powder blowing technique,” *Surface and Coatings Technology,* vol. 71, no. 2, pp. 121-128, 1995.

[18] K. V. Wong and A. Hernandez, “A Review of Additive Manufacturing,” *ISRN Mechancial Engineering,* 2012.

[19] C. Korner, “Additive Manufacturing of Metallic Components by Selective Electron Beam Melting - a Review,” *International Materials Reviews,* vol. 61, no. 5, pp. 361-377, 2016.

[20] R. Larson, “Method and Device for Producing Three-Dimensional Bodies”. US Patent 5786562, 1998.

[21] Royal Academy of Engineers, “Additive Manufacturing: OPportunities and Constraints,” 23 May 2013. [Online]. Available: http://www.raeng.org.uk/publications/reports/additive-manufacturing. [Accessed 29 September 2017].

[22] E. Winick, “Additive Manufacturing in the Aerospace Industry,” 31 January 2017. [Online]. Available: https://www.engineering.com/AdvancedManufacturing/ArticleID/14218/Additive-Manufacturing-in-the-Aerospace-Industry.aspx. [Accessed 20 February 2018].

[23] J. Flaig, “Batteries and Additive Manufacturing Among £54m Aerospace Investments,” 30 November 2017. [Online]. Available: https://www.imeche.org/news/news-article/batteries-and-additive-manufacturing-among-54m-aerospace-investments. [Accessed 20 February 2018].

[24] TCT Magazine, “GE to acquire additive manufacturing firms SLM Solutions and Arcam AB for $1.4 billion,” 6 September 2016. [Online]. Available: https://www.tctmagazine.com/3d-printing-news/ge-acquires-slm-solutions-and-arcam/. [Accessed 29 September 2017].

[25] Reuters, “GE buys Germany's Concept Laser after SLM bid fails,” 2016. [Online]. Available: http://uk.reuters.com/article/us-ge-3dprinting-germany/ge-buys-germanys-concept-laser-after-slm-bid-fails-idUKKCN12R0JT. [Accessed 29 September 2017].

[26] Optics.org, “Metal Additive Manufacturing Sector in 'Pivotal' year - Report,” 2017. [Online]. Available: http://optics.org/news/8/4/1. [Accessed 29 September 2017].

[27] Plastics Engineering, “Wohlers report documents slowdown in 3d printing growth,” *Plastics Engineering,* vol. 73, no. 5, p. 54, May 2017.

[28] IATA, “IATA Carbon Offset Program,” 24 August 2015. [Online]. Available: https://www.iata.org/whatwedo/environment/Documents/carbon-offset-program-faq-airline-participants.pdf. [Accessed 25 February 2018].

[29] L. Wang, Q. Wei, P. Xue and Y. Shi, “Fabricate Mould Insert With Conformal Cooling Channel Using Selective Laser Melting,” *Progress in New Materials and Mechanics Research,* vol. 502, pp. 67-71, 2012.

[30] M. Petch, “3D Printed Jet Engine Certified for Use, GE Concept Laser Deal Update,” 23 December 2016. [Online]. Available: https://3dprintingindustry.com/news/3d-printed-jet-engine-certified-use-ge-concept-laser-deal-update-101792/. [Accessed 29 September 2017].

[31] T. Kellner, “The FAA Cleared the First 3D Printed Part to Fly in a Commercial Jet Engine from GE,” 2015. [Online]. Available: https://www.ge.com/reports/post/116402870270/the-faa-cleared-the-first-3d-printed-part-to-fly-2/. [Accessed 29 September 2017].

[32] S. Davies, “GE Aviation tests 35% additive manufactured Advanced Turboprop engine,” 2 November 2016. [Online]. Available: https://www.tctmagazine.com/3d-printing-news/ge-aviation-tests-additive-manufactured-turboprop-engine/. [Accessed 29 September 2017].

[33] GE Additive, “GE’s new aviation plant in the heart of Europe will build engines with 3D printed parts for next-gen Cessna Denali,” 17 September 2017. [Online]. Available: https://www.ge.com/additive/case-study/ges-new-aviation-plant-heart-europe-will-build-engines-3d-printed-parts-next-gen-cessna. [Accessed 15 February 2018].

[34] M. Molitch-Hou, “Rolls-Royce To Fly Largest 3D Printed Part Ever Flown,” 19 February 2015. [Online]. Available: https://3dprintingindustry.com/news/rolls-royce-to-fly-largest-3d-printed-part-ever-flown-42795/. [Accessed 19 February 2018].

[35] J. Pomichter, “Pratt & Whitney to Deliver First Entry Into Service Engine Parts Using Additive Manufacturing,” 1 April 2015. [Online]. Available: http://additivemanufacturing.com/2015/04/06/pratt-whitney-to-deliver-first-entry-into-service-engine-parts-using-additive-manufacturing/. [Accessed 26 February 2018].

[36] M. Baumers, C. Tuck, R. Wildman, I. Ashcroft and R. Hague, “Energy Inputs to Additive Manufacturing: Does Capacity Utilization Matter?,” University of Loughborough, 2011.

[37] M. Brown, “Methane-Fueled Rocket Aims for Mars,” 2 November 2015. [Online]. Available: https://www.engineering.com/DesignerEdge/DesignerEdgeArticles/ArticleID/10910/Methane-Fueled-Rocket-Aims-for-Mars.aspx. [Accessed 19 February 2018].

[38] M. Molitch-Hou, “GKN Launches into Aerospace 3D Printing,” 12 July 2017. [Online]. Available: https://www.engineering.com/3DPrinting/3DPrintingArticles/ArticleID/152

18/GKN-Launches-into-Aerospace-3D-Printing.aspx. [Accessed 20 February 2018].

[39] SpaceX, “SpaceX Launches 3D-Printed Part To Spacem Creates Printed Engine Chamber,” 31 July 2014. [Online]. Available: http://www.spacex.com/news/2014/07/31/spacex-launches-3d-printed-part-space-creates-printed-engine-chamber-crewed. [Accessed 20 February 2018].

[40] I. Wright, “The Airbus Roadmap to Additive Manufacturing,” 24 October 2017. [Online]. Available: https://www.engineering.com/AdvancedManufacturing/ArticleID/15886/The-Airbus-Roadmap-to-Additive-Manufacturing.aspx. [Accessed 20 February 2018].

[41] Boeing, “Boeing Records and Important First in Additive Manufacturing Technology,” 15 June 2015. [Online]. Available: http://www.boeing.com/features/2015/06/corp-printed-parts-06-15.page. [Accessed 7 February 2018].

[42] C. Clarke, “SatRevolution Building New Satellite Plant In Poland with Partners APWorks,” 16 February 2017. [Online]. Available: https://3dprintingindustry.com/news/satrevolution-building-new-satellite-plant-poland-partners-apworks-105853/. [Accessed 7 February 2018].

[43] W. Lewis, “SSL Demonstrates Innovative Use of Advanced Technologies,” 7 March 2017. [Online]. Available: https://sslmda.com/html/pressreleases/pr20170307.html. [Accessed 29 September 2017].

[44] C. Scott, “Space Systems Loral Launches a New Satellite and a New Era of Manufacturing With Partially 3D Printed JCSAT-110A,” 9 March 2017. [Online]. Available: https://3dprint.com/167418/jcsat-110-a-space-systems-loral/. [Accessed 29 September 2017].

[45] M. Molith-Hou, “Boeing Talks 3D Printing for Aerospace,” 16 August 2017. [Online]. Available: https://www.engineering.com/3DPrinting/3DPrintingArticles/ArticleID/15475/Boeing-Talks-3D-Printing-for-Aerospace.aspx. [Accessed 16 February 2018].

[46] Norsk Titanium AS, “Technology,” 2018. [Online]. Available: http://www.norsktitanium.com/technology. [Accessed 26 February 2018].

[47] A. Scott, “Printed Titanium Parts Expected to Save Millions in Boeing Dreamliner Costs,” 10 April 2017. [Online]. Available: https://www.reuters.com/article/us-norsk-boeing/printed-titanium-parts-expected-to-save-millions-in-boeing-dreamliner-costs-idUSKBN17C264. [Accessed 10 April 2018].

[48] Boeing, “Orders and Deliveries,” 30th June 2018. [Online]. Available: http://www.boeing.com/commercial/#/orders-deliveries. [Accessed 24 July 2018].

[49] Metal AM, “Boeing and Norsk Titanium Recognised for Metal Additively Manufactured Structural Components,” 25 January 2018. [Online]. Available: http://www.metal-am.com/boeing-norsk-titanium-recognised-metal-additively-manufactured-structural-components/. [Accessed 15 February 2018].

[50] L. Griffiths, “Stratasys Reveals Over 1,000 3D Printed Parts On Board Airbus A350 XWB Aircraft,” 6 May 2015. [Online]. Available: https://www.tctmagazine.com/3d-printing-news/over-1000-3d-printed-parts-on-airbus-a350-xwb-aircraft/. [Accessed 20 February 2018].

[51] TCT Magazine, “TCT Show Exhibitors Concept Laser with a World First for Aerospace,” 1 October 2014. [Online]. Available: https://www.tctmagazine.com/tct-events/formnext-powered-by-tct/tct-show-exhibitors-concept-laser/. [Accessed 20 February 2018].

[52] Safran, “Safran Landing Systems and Airbus Team Up on Additive Manufacturing,” 22 June 2017. [Online]. Available: https://www.safran-landing-systems.com/media/safran-landing-systems-and-airbus-team-additive-manufacturing-20170622. [Accessed 26 February 2018].

[53] M. Tomlin and J. Meyer, “Topology Optimization of an Additive Layer Manufactured (ALM) Aerospace Part,” The 7th Altair CAE Technology Conference, 2011.

[54] AP Works, “Scalmalloy,” 2018. [Online]. Available: http://www.apworks.de/en/scalmalloy/. [Accessed 20 February 2018].

[55] A. B. Spierings, K. Dawson, T. Heeling, P. J. Uggowitzer, R. Schaublin, F. Palm and K. Wegener, “Microstructural Features of Sc- and Zr- Modified Al-Mg Alloys Processed by Selective Laser Melting,” *Materials and Design,* vol. 115, pp. 52-63, 2017.

[56] N. Hall, “Top 10 3D Printed Automotive Industry Innovations Available Right Now,” 20 June 2016. [Online]. Available: https://3dprintingindustry.com/news/3d-printing-automotive-industry-2-82838/. [Accessed 20 February 2018].

[57] BMW Group, “Press Release: BMW Group plans Additive Manufacturing Campus: Technological Expertise in Industrial-scale 3D Printing to be Consolidated at New Location,” 16 April 2018. [Online]. Available: https://www.press.bmwgroup.com/global/article/detail/T0280159EN/bmw-group-plans-additive-manufacturing-campus:-technological-expertise-in-industrial-scale-3d-printing-to-be-consolidated-at-new-location?language=en. [Accessed 30 July 2018].

[58] J. M. Gitlin, “Porsche and Bugatti Turn to 3D Printing for Complex or Rare Parts,” 15 March 2018. [Online]. Available: https://arstechnica.com/cars/2018/03/lightweight-calipers-and-rare-old-parts-3d-printing-at-bugatti-and-porsche/. [Accessed 10 April 2018].

[59] BMW Group, “Additive Manufacturing: 3D Printing to Perfection,” 2018. [Online]. Available: https://www.bmw.com/en/innovation/3d-print.html. [Accessed 30 July 2018].

[60] Porsche, “Porsche Classic Supplies Classic Parts from a 3D Printer,” 12 February 2018. [Online]. Available: https://newsroom.porsche.com/en/company/porsche-classic-3d-printer-spare-parts-sls-printer-production-cars-innovative-14816.html. [Accessed 30 July 2018].

[61] M. Petch, “Audi Gives Update on Use of SLM Metal 3D Printing for the Automotive Industry,” 22 February 2018. [Online]. Available: https://3dprintingindustry.com/news/audi-gives-update-use-slm-metal-3d-printing-automotive-industry-129376/. [Accessed 30 July 2018].

[62] S. Hoeges, “GKN and Porsche Engineering: Growing Metal AM for New E-Drive Powertrain Applications,” 24 March 2018. [Online]. Available: https://sintermedia.gkn.com/blog/growing-metal-am-with-new-e-drive-powertrain-applications. [Accessed 30 July 2018].

[63] SPI Lasers, “Recent Advances at Audi in the Use of Additive Manufacturing,” 2018. [Online]. Available: https://www.spilasers.com/news/recent-advances-audi-use-additive-manufacturing/. [Accessed 30th July 2018].

[64] 3T RPD, “Formula 1 and AM,” 28 NOvember 2016. [Online]. Available: https://www.3trpd.co.uk/formula-1-and-am/. [Accessed 10 April 2018].

[65] D. E. Cooper, M. Stanford, K. A. Kibble and G. J. Gibbons, “Additive Manufacturing for Product Improvement at Red Bull Technology,” *Materials and DEsign,* vol. 41, pp. 226-230, 2012.

[66] SmarTech, Additive Manufacturing Opportunities In The Automotive Industry: A Ten-Year Forecast, USA: SmartTechMarkets Publishing, 2018.

[67] M. Santorinaios, W. Brooks, R. A. W. Mines and C. J. Suttcliffe, “Crush Behaviour of Open Cellular Lattice Structures Manufactured Using Selective Laser Melting,” in *High Performance Structures and Materials III*, vol. 85, WIT Press, 2006, pp. 481-490.

[68] ATKINS, “ATKINS: Manufacturing a Low Carbon Footprint,” 2007.

[69] W. S. Gora, Y. Tian, A. P. Cabo, M. Ardron, R. R. Maier, P. Prangnell, N. J. Weston and D. P. Hand, “Enhancing Surface Finish of Additivelly Manufactured Titanium and Cobalt Chrome Elements Using Laser Based Finishing,” *Physics Procedia,* vol. 83, pp. 258-263, 2016.

[70] W. T. Carter and M. G. Jones, “Direct Laser Sintering of Metals,” *Solid Freeform Fabrication Symposium,* 1993.

[71] T. LPW, Interviewee, *Discussion on cost of materials.* [Interview]. 19 May 2014.

[72] I. Polmear, Light alloys from traditional alloys to nanocrystals, 4th ed., Oxford: Butterworth-Heinemann, 2006.

[73] C. C. Ng, M. M. Savalani, H. C. Man and I. Gibson, “Layer Manufacturing of Magnesium and its Alloy Structures for Future Applications,” *Virtual and Physical Prototyping,* vol. 5, no. 1, pp. 13 - 19, 2010.

[74] B. Zhang, H. Liao and C. Coddet, “Effects of Processing Parameters on Properties of Selective Laser Melting Mg–9%Al Powder Mixture,” *Materials and Design,* vol. 34, p. 753 – 758, 2012.

[75] K. Wei, M. Gao, Z. Wang and X. Zeng, “Effect of Energy Input on Formability, Microstructure and Mechanical Properties of Selective Laser Melted AZ91D Magnesium Alloy,” *Materials Science and Engineering: A,* vol. 611, pp. 212-222, 2014.

[76] M. Gieseke, C. Noelke, S. Kaierle, V. Wesling and H. Haferkamp, “Selective Laser Melting of Magnesium and Magnesium Alloys,” *Magnesium Technology 2013,* pp. 65 - 68, 2013.

[77] V. Manakari, G. Parande and M. Gupta, “Selective Laser Melting of Magnesium and Magnesium Alloy Powders: A Review,” *Metals,* vol. 7, no. 1, 2017.

[78] A. B. Spierings, K. Dawson, K. Kern, F. Palm and K. Wegener, “SLM-procesed Sc- and Zr- modified Al-Mg alloy: Mechanical properties and microstructural effects of heat treatment,” *Materials Science & Engineering A,* vol. 701, pp. 264-273, 2017.

[79] N. T. Aboulkhair, N. M. Everitt, I. Maskery, I. Ashcroft and C. Tuck, “Selective Laser Melting of Aluminium Alloys,” *MRS Bulletin,* vol. 42, no. 4, pp. 311-319, 2017.

[80] D. Buchbinder, H. Schleifenbaum, S. Heidrich, W. Meiners and J. Bultmann, “High Power Selective Laser Melting (HP SLM) of Aluminium Parts,” *Physics Procedia,* vol. 12, pp. 271 - 278, 2011.

[81] B. A. Fulcher, D. K. Leigh and T. J. Watt, “Comparison of AlSi10Mg and Al 6061 Processed Through DMLS,” *SFF Symposium ,* 2014.

[82] D. Koutny, D. Palousek, O. Koukal, T. Zikmund, L. Pantelejev and F. Dokoupil, “Processing of High Strength Al-Cu Alloy Using 400W Selective Laser Melting - Initial Study,” *Proceedings of the Lasers in Manufacturing Conference,* 2015.

[83] T. Qi, H. Zhu, J. Yin, B. Chen, Z. Hu and X. Zeng, “Porosity Development and Cracking Behaviour of Al-Zn-Mg-Cu Alloys Fabricated by Selective Laser Melting,” *Proceedings of the 28th Annual International Solid Freeform Fabrication Symposium,* vol. 28, 2017.

[84] GKN, “Additive Manufacturing in Automotive - Enabled by New Steel Alloy Development,” 2017. [Online]. Available: https://www.gkn.com/en/our-divisions/gkn-additive/additive-manufacturing-in-automotive--enabled-by-new-steel-alloy-development/. [Accessed 20 January 2018].

[85] GKN, “GKN Additive Launches Titanium Beta 21S Powder for Additive Manufacturing,” 2017. [Online]. Available: https://www.gkn.com/en/newsroom/news-releases/additive-

manufacturing/2017/gkn-additive-launches-titanium-beta-21s-powder-for-additive-manufacturing/. [Accessed 20 February 2018].

[86] N. J. Harrison, I. Todd and K. Mumtaz, "Reduction of Micro-Cracking in Nickel Superalloys Processed by Selective Laser Melting: A Fundamental Alloy Design Approach," *Acta Materialia,* vol. 94, pp. 59-68, 2015.

[87] E. O. Olakanmi, R. F. Cochrane and K. W. Dalgarno, "A Review of Selective Laser Sintering/Melting (SLS/SLM) of Aluminium Alloy Powders: Processing, MIcrostructure, and Properties," *Progress in Materials Science,* vol. 74, pp. 401-477, 2015.

[88] M. Wong, S. Tsopanos, C. Sutcliffe and I. Owen, "Selective Laser Melting of heat transfer devices," *Rapid Prototyping Journal,* vol. 13, no. 5, pp. 291-297, 2007.

[89] P. Jerrard, L. Hao, S. Dadbakhsh and K. Evans, "Consolidation behaviour and microstructure characteristics of pure aluminium and alloy powders following SLM processing," *Proceedings of the 36th International MATADOR Conference,* pp. 487-490, 2010.

[90] G. Mathers, The Welding of Aluminium and Its Alloys, Cambridge: Woodhead Publishing, 2002.

[91] W. Kurz and D. J. Fisher, Fundamentals of Solidification, 3rd ed., Aedermannsdorf: Trans Tech Publications Ltd, 1986.

[92] BS EN 573-1, "Aluminium and Aluminium Alloys - Chemical composition and orm of wrought products," British Standards Online, London, 2004.

[93] BS EN 1706, "Aluminium and Aluminium Alloys - Castings - Chemical Composition adn Mechanical Properties," British Standards Online, London, 2010.

[94] E. O. Olakanmi, Direct Selective Laser Sintering of Aluminium Alloy Powders, Thesis ed., University of Leeds, 2008.

[95] M. Warmuzek, "Introduction to Aluminium-Silicon Casting Alloys," in *Aluminum-silicon Casting Alloys: An Atlas of Microfractographs*, Ohio, USA, ASM International, 2004.

[96] E. O. Olakanmia, "Selective laser sintering/melting (SLS/SLM) of pure Al, Al–Mg, and Al–Si powders: Effect of processing conditions and powder properties," *Journal of Materials Processing Technology ,* vol. 213, p. 1387–1405, 2013.

[97] S. H. Park, B. H. Hur, S. Y. Kim, D. K. Ahn and D. I. Ha, "A Study on teh Viscosity and Surface Tension for Al Foaming and the Effects of Addition Elements," *Proceedings of the 65th World Foundry Congress,* pp. 515-524, 2002.

[98] P. Ma, K. G. Pranshanth, S. Scudino, Y. Jia, H. Wang, C. Zou, Z. Wei and J. Eckert, "Influence of annealing on mechanical properties of Al-20Si processed by Selective Laser Melting," *Metals,* vol. 4, pp. 28-36, 2014.

[99] T. Ullsperger, G. Matthaus, L. Kaden, H. Engelhardt, M. Rettenmayr, S. Risse, A. Tunnermann and S. Nolte, "Selective Laser Melting of Hypereutectic Al-

Si40 Powder Using Ultra-Short Laser Pulses," *Applied Physics A,* vol. 123, p. 798, 2017.

[100] T. Kimura and T. Nakamoto, "Microstructures and mechanical properties of A356 (AlSi7Mg0.3) aluminum alloy fabricated by selective laser melting," *Materials and Design,* vol. 89, pp. 1294-1301, 2016.

[101] A. Aversa, M. Moshiri, E. Librera, M. Hadi, G. Marchese, D. Manfredi, M. Lorusso, F. Calignano, S. Biamino, M. Lombardi and M. Pavese, "Single Scan Track Analyses on Aluminium based Powders," *Journal of Materials Processing Technology,* 2017.

[102] R. Cook, "Grain Refinement of Aluminium-Silicon Foundry Alloys," 1998. [Online]. Available: www.metallurgal.com. [Accessed 04 11 2013].

[103] X. Li, G. Ji, Z. Chen, A. Addad, Y. Wu, H. Wang, J. Vleugels, J. Van Humbeeck and J. Kruth, "Selective Laser Melting of Nano-TiB2 decorated AlSi10Mg alloy with High Fracture Strength and Ductility," *Acta Materialia,* vol. 129, pp. 183-193, 2017.

[104] CES, Granta Design, *Cambridge Engineering Selector,* 2014.

[105] J. Li, X. Cheng, S.-Q. Zhang, Z. Li, B. He and H.-M. Wang, "Phase Evolution of a Heat-Treatable Aluminium Alloy During Laser Additive Manufacturing," *Materials Letters,* vol. 214, pp. 56-59, 2018.

[106] K. Bartkowiak, S. Ullrich, T. Frick and M. Schmidt, "New Developments of Laser Processing Aluminium Alloys via Additive Manufacturing Technique," *Physics Procedia,* vol. 12, pp. 393-401, 2011.

[107] P. Jerrard, L. Hao, S. Dadbakhsh and K. Evans, "Consolidation Behaviour and Microstructural Characteristics of Al and a Mixture of Al-Cu Alloy Powders Following Selective Laser Melting Process," *Lasers in Engineering,* vol. 22, pp. 371 - 381, 2011.

[108] H. Zhang, H. Zhu, T. Qi, Z. Hu and X. Zeng, "Selective laser melting of high strength Al–Cu–Mg alloys: Processing, microstructure and mechanical properties," *Materials Science & Engineering A,* vol. 656, pp. 47-54, 2016.

[109] S. Kou, "Solidification and Liquation Cracking Issues in Welding," *Journal of Metallurgy,* vol. June, pp. 37-42, 2003.

[110] M. Karg, B. Ahuja, S. Kuryntsev, A. Gorunov and M. Schmidt, "Processability of High Strength Aluminium Copper Alloys AW-2022 and 2024 by Laser Beam Melting in Powder Bed," *Proceedings from the 25th Annual International Solid Freeform Fabrication Symposium,* 2014.

[111] S. Kou, Welding Metallurgy, 2nd ed., Hoboken, New Jersey: John Wiley & Sons, 2003.

[112] M. Ameli, B. Agnew, P. Leung, C. Slutciffe, J. Singh and R. McGlen, "A Novel Method for Manufacturing Sintered Aluminium Heat Pipes (SAHP)," *Applied Thermal Engineering,* vol. 52, pp. 498-504, 2013.

[113] J. Weston, J. W. Yoon and E. R. Wallace, “Laser Welding of Aluminium Alloys Using Different Laser Sources,” *CISFFEL6, 6 th International Conference on Welding and Melting by Electron and Laser Beams,* 1998.

[114] British Standard Institute, *BS 2901-4: Filler rods and wires for gas-shielded arc welding - Part 4: Specification for aluminium and aluminium alloys and magnesium alloys,* London: British Standards Institute, 1990.

[115] R. Braun, “Nd:YAG Laser Butt Welding of AA6013 Using Silicon and Magnesium Containing Filler Powders,” *Materials Science and Engineering,* vol. 426, pp. 250-262, 2006.

[116] T. Wang, Z.-m. Yin, K. Shen, J. Li and J.-W. Huang, “Singel-Aging Characteristics of 7055 Aluminium Alloy,” *Transactions of Nonferrous Metals Society of China,* vol. 17, pp. 548-552, 2007.

[117] L. W. Crane, Melting and Solidification of Zinc-Aluminium Alloys, Birmingham: The University of Aston, 1997.

[118] M. L. Montero Sistiaga, R. Mertens, B. Vrancken, X. Wang, B. van Hooreweder, J.-P. Kruth and J. van Humbeeck, “Changing the Alloy Composition of Al7075 for Better Processibilty by Selective Laser Melting,” *Journal of Materials Processing Technology,* vol. 238, pp. 437-445, 2016.

[119] P. Wang, H. C. Li, K. G. Prashanth, J. Eckert and S. Scudino, “Selective Laser Melting of Al-Zn-Mg-Cu: Heat Treatment, Microstructure and Mechanical Properties,” *Journals of Alloys and Compounds,* vol. 707, pp. 287-290, 2017.

[120] S. Dadbakhsh, L. Hao, P. Jerrard and D. Zhang, “Experimental Investigation on Selective Laser Melting Behaviour and Processing Windows of In Situ reacted Al/Fe2O3 Powder Mixture,” *Powder Technology,* vol. 231, pp. 112 - 121, 2012.

[121] K. Prashanth, H. Shakur Shahabi, H. Attar, V. Srivastava, N. Ellendt, V. Uhlenwinkel, J. Eckert and S. Scudino, “Production of high strength Al85Nd8Ni5Co2 alloy by selective laser melting,” *Additive Manufacturing,* vol. 6, pp. 1-5, 2015.

[122] A. Plotkowski, O. Rios, N. Sridharan, Z. Sims, K. Unocic, R. Ott, R. Dehoff and S. Babu, “Evaluation of an Al-Ce Alloy for Laser Additive Manufacturing,” *Acta Materialia,* vol. 126, pp. 507-519, 2017.

[123] K. Schmidtke, F. Palm, A. Hawkins and C. Emmelmann, “Process and Mechanical Properties: Applicability of a Scandium modified Al-alloy for Laser Additive Manufacturing,” *Physics Procedia,* vol. 12, pp. 369-374, 2011.

[124] M. Awd, J. Tenkamp, M. Hirtler, S. Siddique, M. Bambach and F. Walther, “Comparison of Microstructure and Mechanical Properties of Scalmalloy(R) Produced by Selective Laser Melting and Laser Metal Deposition,” *Materials,* vol. 11, p. 17, 2018.

[125] K. V. Yang, Y. Shi, F. Palm, X. Wu and P. Rometsch, “Columnar to Equiaxed Transition in Al-Mg(-Sc)-Zr Alloys Produced by Selective Laser Melting,” *Scripta Materialia,* vol. 145, pp. 113-117, 2018.

[126] R. Li, M. Wang, T. Yuan, B. Song, C. Chen, K. Zhou and P. Cao, “Selective Laser Melting of a Novel Sc and Zr Modified Al-6.2 Mg Alloy: Processing, Microstructure, and Properties,” *Powder Technology,* Vols. 117-128, p. 319, 2017.

[127] A. B. Spierings, K. Dawson, M. Voegtlin, F. Palm and P. J. Uggowitzer, “Microstructure and mechanical properties of as-processed scandium-modified aluminium using selective laser melting,” *CIRP Annals - Manufacturing Technology,* vol. 65, pp. 213-216, 2016.

[128] Q. Jia, P. Rometsch, S. Cao, K. Zhang, A. Huang and Z. Wu, “Characterisation of AlScZr and AlErZr Alloys Processed by Rapid Laser Melting,” *Scripta Materialia,* vol. 151, pp. 42-46, 2018.

[129] H. Zhang, H. Zhu, X. Nie, J. Yin, Z. Hu and X. Zeng, “Effect of Zirconium Addition on Crack, Microstructure and Mechanical Behavior of Selective Laser Melted Al-Cu-Mg Alloy,” *Scripta Materialia,* vol. 134, pp. 6-10, 2017.

[130] R. M. Clayton, “The Use of Elemental Powder Mixes in Laser-Based Additive Manufacturing,” Master Theses, 7194, MIssouri University of Science and Technology, 2013.

[131] S. Dietrich, M. Wunderer, A. Huissel and M. Zaeh, “A New Approach For A Flexible Powder Production For Additive Manufacturing,” *Procedia Manufacturing,* vol. 6, pp. 88-95, 2016.

[132] J. Dawes, R. Bowerman and R. Trepleton, “Introduction to the Additive Manufacturing Powder Metallurgy Supply Chain,” *Johnson Matthey Technology Review,* vol. 59, no. 3, pp. 243-256, 2015.

[133] C. Si, X. Tang, X. Zhang, J. Wang and W. Wu, “Characteristics of 7055Al Alloy Powders Manufactured by Gas-Solid Two-Phase Atomization: A Comparison With Gas Atomization Process,” *Materials and Design,* vol. 118, pp. 66-74, 2017.

[134] LPW Technology, “Standard Powders - Laser Metal Deposition & Additive manufacture,” February 2012. [Online]. Available: https://s2g.eshop-systems.net/s2g/lpwtech/LPW%20Standard%20Compositions_Feb%202012.pdf. [Accessed 8 May 2012].

[135] A. J. Pinkerton and L. Li, “Direct additive laser manufacturing using gas- and water-atomised H13 tool steel,” *International Journal of Advanced Manufacturing Technology,* p. Vol. 25: 471–479, 2005.

[136] LPW Technology UK), “Powder Production,” 2018. [Online]. Available: https://www.lpwtechnology.com/technical-library/powder-production/. [Accessed 22 March 2018].

[137] K. Abd-Elghany and D. Bourell, “Property Evaluation of 304L Stainless Steel Fabricated by Selective Laser Melting,” *Rapid Prototyping Journal,* vol. 18, no. 5, pp. 420-428, 2012.

[138] T. F. Murphy, “Metallographic Testing of Powders Intended For Use in Additive Manufacturing,” *International Journal of Powder Metallurgy,* vol. 52, no. 1, pp. 25-35, 2016.

[139] S. Berretta, O. Ghita, K. Evans, A. Anderson and C. Newman, “Size, Shape and Flow of Powders for use in Selective Laser Sintering (SLS),” *Proceedings of VRAP 2013, 6th International Conference on Advanced Research in Virtual and Rapid Prototyping,* pp. 49-54, 2013.

[140] B. Thomas , “When Powders Flow Like Water: Addressing Two-Phase Flow Effects in Tablet Feed Systems,” *Tablets & Capsules,* vol. March, 2009.

[141] J. C. M. Lobato, A. L. A. Mesquita and A. L. A. Mesquita, “Conical Hopper Design for Mass Flow - Case Study for Red Mud Powder,” *15th Brazilian Congress of Thermal Sciences and Engineering,* 2014.

[142] N. P. Karapatis, G. Egger, P. E. Gygax and G. Glardon, “Optimization of Powder Layer Density in Selective Laser Sintering,” *Proceding of the 9th Solid Freeform Fabrication Symposium,* 1999.

[143] N. T. Aboulkhair, I. Maskery, I. Ashcroft, C. Tuck and N. M. Everitt, “The Role of Powder Properties on the Processability of Aluminium Alloys in Selective Laser Melting,” *Lasers in Manufacturing Conference,* 2015.

[144] B. Liu, R. Wildman, C. Tuck, I. Ashcroft and R. Hague, “Investigation The Effect of Particle Size Distribution on Processing Parameters Optimisation in Selective Laser Melting Process,” *Additive Manufacturing Research Group; Loughborough University,* 2011.

[145] K. Boivie, “Limits of Loose Metal Powder Density in the Sinterstation,” *Proceedings of the SFF Symposium,* pp. 264-275, 2001.

[146] Q. Li, V. Rudolph, B. Weigl and A. Earl, “Interparticle van der Waals Force in Powder Flowability and Compactibility,” *Internationa Journal of Pharmaceutics,* vol. 280, no. 1-2, pp. 77-93, 2004.

[147] LPW Technology UK, “Powder Range,” November 2016. [Online]. Available: https://www.lpwtechnology.com/wp-content/uploads/2016/11/LPW_PowderRange_Brochure_web_pdf.pdf. [Accessed 4 May 2018].

[148] Endecotts, “Precision Test Sieves | Sieve Shakers,” [Online]. Available: https://www.endecotts.com/dltmp/www/56607c62-8044-4b33-ba08-2482bc282b86-400f14323e75/brochure_endecotts_general_en.pdf. [Accessed 4 May 2018].

[149] G. Strano, L. Hao, R. M. Everson and K. E. Evans, “Surface Roughness Analysis, Modelling and Prediction in Selective Laser Melting,” *Journal of Materials Processing Technology,* vol. 213, pp. 589-597, 2013.

[150] A. B. Spierings, N. Herres and G. Levy, “Influence of the particle size distribution on surface quality and mechanical properties in AM steel parts,” *Rapid Prototyping Journal,* vol. 17, no. 3, pp. 195-202, 2011.

[151] A. B. Spierings and G. Levy, “Comparison of Density of Stainless Steel 316L Parts Produced With Selective Laser Melting Using Different Powder Grades,” *SFF Symposium,* 2009.

[152] Q. B. Nguyen, M. L. S. Nai, Z. Zhu, C.-N. Sun, J. Wei and W. Zhou, “Characteristics of Inconel Powders for Powder-Bed Additive Manufacturing,” *Engineering,* vol. 3, pp. 695-700, 2017.

[153] L. C. Ardila, F. Garciandia, J. B. Gonzalez-Diaz, P. Alvarez, A. Echeverria, M. M. Petite, R. Deffley and J. Ochao, “Effect of IN718 Recycled Powder Reuse on Properties of Parts Manufactured by Means of Selective Laser Mmelting,” *Physics Procedia,* vol. 56, pp. 99-107, 2014.

[154] J. W. Carson, T. A. Royal and D. Goodwill, “Understanding and Eliminating Particle Segregation Problems,” *Bulk Solids Handling,* vol. 6, no. Feb, pp. 139-144, 1986.

[155] V. Seyda, N. Kaufmann and C. Emmelmann, “Investigation of Aging Processes of Ti-6Al-4V Powder Materila in Laer Melting,” *Physics Procedia,* vol. 39, pp. 425-431, 2012.

[156] R. O'Leary, R. Setchi, P. Prickett, G. Hankins and N. Jones, “An Investigation into the Recycling of Ti-6Al-4V Powder Used Within SLM to Improve Sustainability,” *The Journal of Innovation Impact,* vol. 15, pp. 377-388, 2015.

[157] F. Del Re, V. Contaldi, A. Astarita, B. Palumbo, A. Squillace, P. Corrado and P. Di Petta, “Statistical Approach for Assessing the Effect of Powder Reuse on the Final Quality of AlSi10Mg Parts Produced by Laser Powder Bed Fusion Additive Manufacturing,” *The International Journal of Advanced Manufacturing Technology,* vol. 97, pp. 2231-2240, 2018.

[158] U. Tradowsky, J. White, R. Ward, N. Read, W. Reimers and M. Attallah, “Selective Laser Melting of AlSi10Mg: Influence of Post-Processing on the Microstructural and Tensile Properties Development,” *Materials and Design,* vol. 105, pp. 212-222, 2016.

[159] C. Weingarten, D. Buchbinder, N. Pirch, W. Meiners, K. Wissenbach and R. Poprawe, “Formation and Reduction of Hydrogen Porosity During Selective Laser Melting of AlSi10Mg,” *Journal of Materials Processing Technology,* vol. 221, pp. 112-120, 2015.

[160] B. Zhang, H. Liao and C. Coddet, “Selective laser Melting Commercially Pure Ti Under Vacuum,” *Vacuum,* vol. 95, pp. 25-29, 2013.

[161] E. Louvis, P. Fox and C. Sutcliffe, “Selective Laser Melting of Aluminium Components,” *Journal of Materials Processing Technology,* vol. 211, p. 275 – 284, 2011.

[162] X. J. Wang, L. C. Zhang, M. H. Fang and T. B. Sercombe, “The Effect of Atmosphere on the Structure and Properties of a Selective Laser Melted Al-12Si Alloy,” *Materials Science and Engineering A,* vol. 597, pp. 370-375, 2014.

[163] H. Asgharzadeh and A. Simchi, “Effect of Sintering Atmosphere and Carbon Content on the Densification and MIcrostrucure of Laser-Sintered M2 High-

Speed Steel Powder," *Materials Science and Engineering A,* vol. 403, pp. 290-298, 2005.

[164] A. Simchi and H. Pohl, "Effects of Laser Sintering Processing Parameters on the Microstructure and Densification of Iron Powder," *Materials and Engineering A,* vol. 359, pp. 119-128, 2003.

[165] E. Louvis, *Techniques for Producing High Relative Density Aluminium Alloy Components with Selective Laser Melting,* Univeristy of Liverpool, 2012.

[166] N. T. Aboulkhair, N. M. Everitt, I. Ashcroft and C. Tuck, "Reducing porosity in AlSi10Mg parts processed by selective laser melting," *Additive Manufacturing,* 2014.

[167] X. Li, K. O'Donnell and T. Sercombe, "Selective Laser Melting of Al-12Si Alloy: Enhanced Densification via Powder Drying," *Additive Manufacturing,* vol. 10, pp. 10-14, 2016.

[168] R. Xiao and X. Zhang, "Problems and Issues in Laser Beam Welding of Aluminium-Lithium," *Journal of Manufacturing Processes,* vol. 16, no. 2, pp. 166-175, 2014.

[169] Q. G. Wang, P. Crepeau, C. J. Davidson and J. R. Griffiths, "Oxide films, Pores and the Fatigue Lives of Cast Aluminum Alloys," *Metallurgical and Materials Transactions B,* vol. 37, no. 6, pp. 887-895, 2006.

[170] C. Hauser, T. Childs, K. Dalgano and R. Eane, "Atmospheric Control during Direct Selective Laser Sintering of Stainless Steel 314S Powder," *Proceedings of the 10th Solid Freeform Fabrication Symposium,* vol. 10, pp. 265-272, 1999.

[171] X. Cao and J. Campbell, "Effect of Sr on Primary a-Fe phase in liquid Al-11.5Si-0.4Mg cast alloy," *Materials Science and Technology,* vol. 20, no. April, pp. 514-520, 2004.

[172] J.-P. Kruth, L. Froyen, J. van Vaerenberg, P. Mercelis, M. Rombouts and B. Lauwers, "Selective Laser Melting of Iron-Based Powder," *Journal of Materials Proessing Technology,* vol. 149, pp. 616 - 622, 2004.

[173] L. Thijs, J. Van Humbeeck, K. Kempen, E. Yasas, J. P. Kruth and M. Rombouts, "Investigation on the Inclusions in Maraging Steel Produced by Selective LAser Melting," *Virtual and Physical Prototyping: Proceedings of the 5th International Conference on Advanced Research in Virtual and Rapid Prototyping,* pp. 297-304, 2011.

[174] S. Dadbakhsh and L. Hao, "Effect of Layer Thickness in Selective Laser Melting on Microstructure of Al/5wt.%Fe2O3 Powder Consolidated Parts," *The Scientific World Journal,* vol. 2014, 2014.

[175] M. Tang and C. P. Pistorius, "Oxides, porosity and fatigue performance of AlSi10Mg parts produced by selective laser melting," *International Journal of Fatigue,* vol. 94, no. 2, pp. 192-201, 2017.

[176] C. Nyahumwa, N. Green and J. Campbell, "The Concept of the Fatigue Potential of Cast Alloys," *Journal of the Mechanical Behavior of Materials,* vol. 9, no. 4, pp. 227-236, 1998.

[177] Y.-J. Chen, H.-Y. Teng and Y.-T. Tsai, “Diagnosis of Oxide Films in Cast Aluminium Alloys,” *Journal of Materials Engineering and Performance,* vol. 13, no. 1, pp. 69-77, 2004.

[178] S. Bremen, W. Meiners and A. Diatlov, “Selective Laser Melting: A Manufacturing Technology for the Future,” WILEY-VCH Verlag GmbH, Weinheim, 2012.

[179] R. Deffley, Development of Processing Strategies for the Additive Layer Manufacturing of Aerospace Components in Inconel 718, PhD Thesis ed., University of Sheffield, 2012.

[180] J. Trapp, A. M. Rubenchik, G. Guss and M. J. Matthews, “ In Situ Absorptvity Measurements of Metallic Powders During Laser Powder-Bed Fusion Additive Manufacturing,” *Applied Materials Today,* vol. 9, pp. 341-349, 2017.

[181] W. E. King, H. D. Barth, V. M. Castillo, G. F. Gallegos, J. W. Gibbs, D. E. Hahn, C. Kamath and A. M. Rubenchik, “Observation of Keyhole-Mode Laser Melting in Laser Powder-Bed Fusion Additive Manufacturing,” *Journal of Materials Processing Technology,* vol. 214, pp. 2915-2925, 2014.

[182] N. T. Aboulkhair, I. Maskery, C. Tuck, I. Ashcroft and N. M. Everitt, “On the Formation of AlSi10Mg Single Tracks and Layers in Selective laser Melting: Microstructure and Nano-Mechanical Properties,” *Journal of Materials Processing Technology,* vol. 230, pp. 88-98, 2016.

[183] M. Krishnan, E. Atzeni, R. Canali, F. Calignano, D. Manfredi, E. P. Ambrosio and L. Iuliano, “On the Effect of Process Parameters on Properties of AlSi10Mg Parts Produced by DMLS,” *Rapid Prototyping,* vol. 20, no. 6, pp. 449-458, 2013.

[184] A. B. Spierings, K. Dawson, T. Heeling, P. J. Uggowitzer, R. Schaublin, F. Palm and K. Wegener, “Microstructural Features of Sc- and Zr- Modified Al-Mg Alloys Processed by Selective Laser Melting,” *Materials and Design,* vol. 115, pp. 52-63, 2017.

[185] F. Abe, K. Osakada, M. Shiomi, K. Uematsu and M. Matsumoto, “The Manufacturing of Hard Tools from Metallic Powders by Selective Laser Melting,” *Journal of Materials Processing Technology,* vol. 111, pp. 210-213, 2001.

[186] J. Robinson, Optimisation of Selective Laser Melting of Process for the Production of Hybrid Orthopaedic Devices, University of Liverpool, 2014.

[187] D. Gu and Y. Shen, “Balling Phenomena in Direct Laser Sintering of Stainless Steel Powder Metallurgical Mechanisms and Control Methods,” *Materials and Design,* vol. 30, pp. 2903 - 2910, 2009.

[188] M. Rombouts, J.-P. Kruth, L. Froyen and P. Mercelis, “Fundamentals of Selective Laser Melting of Alloyed Steel Powders,” *CIRPO Annals - Manufacturing Technology,* vol. 55, no. 1, pp. 187 - 192, 2006.

[189] Z. Shi, S. Ma, C. Liu, C. Chen, Q. Wu, X. Chen and J. Lu, “Performance of High Layer Thickness in Selective Laser Melting of Ti6Al4V,” *Materials,* vol. 9, p. 975, 2016.

[190] R. Li, J. Liu, Y. Shi, L. Wang and W. Jiang, “Balling Behavior of Stainless Steel and Nickel Powder during Selective Laser Melting Process,” *International Journal of Advanced Manufacturing Technology,* vol. 59, pp. 1025-1035, 2012.

[191] N. Takata, H. Kodaira, A. Suzuki and M. Kobashi, “Size Dependence of Microstructure of AlSi10Mg alloy fabricated by Selective Laser Melting,” *Materials Characterization,* 2017.

[192] R. Morgan, A. Papworth, C. Sutcliffe, P. Fox and B. O'Neill, “Direct Metal Laser Re-Melting of 316L Stainless Steel Powder Part 2: Analysis of Cubic Primitives,” *Proceedings of the SFF Symposium,* pp. 283-295, 2001.

[193] J. Sanz-Guerrero and J. Ramos-Grez, “Effect of Total Applied Energy Denisty on the Densification of Copper-Titanium Slabs Produced by the DMLF Process,” *Journal of Materials Processing Technology,* vol. 202, pp. 339-346, 2008.

[194] N. T. Aboulkhair, I. Maskery, C. Tuck, I. Ashcroft and N. M. Everitt, “Improving the Fatigue Behaviour of a Selectively Laser Melted Aluminium Alloy: Influence of Heat Treatment and Surface Finish,” *Materials & Design,* vol. 104, no. August, pp. 174-182, 2016.

[195] K. G. Prashanth, S. Scudino, T. Maity, J. Das and J. Eckert, “Is th Energy Density a Reliable Parameter for Materials Synthesis by Selective Laser Melting?,” *Materials Research Letters,* vol. 5, no. 6, pp. 386-390, 2017.

[196] K. Kempen, L. Thijs, E. Yasa, M. Badrossamay, W. Verheecke and J.-P. Kruth, “Process Optimization and Microstructural Analysis for Selective LAser Melting of AlSi10Mg,” *Solid Freeform Fabrication Proceedings,* pp. 484 - 495, 2011.

[197] E. Yasa and J.-P. Kruth, “Applications of Laser Re-Melting on Selective Laser Melting Parts,” *Advances in Production Engineering & Management,* vol. 6, no. 4, pp. 259 - 270, 2011.

[198] L. Thijs, K. Kempen, J.-P. Kruth and J. van Humbeeck, “Fine-Structured Aluminium Products with Controlable Texture by Selective Laser Melting of Pre-Alloyed AlSiMg Powder,” *Acta Materialia,* vol. 61, pp. 1809 - 1819, 2013.

[199] D. Srivastava, I. Chang and M. Loretto, “The Effect of Process Parameters and Heat Treatment on the Microstructure of Direct Laser Fabricated TiAl Alloy Samples,” *Intermetallics,* vol. 9, pp. 1003-1013, 2001.

[200] T. Mukherjee, H. Wei, A. De and T. DebRoy, “Heat and fluid flow in additive manufacturing – Part II: Powder bed fusion of stainless steel, and titanium, nickel and aluminum base alloys,” *Computational Materials Science,* vol. 150, no. July, pp. 369-380, 2018.

[201] F. Geiger, K. Kunze and T. Etter, “Tailoring the Texture of IN738LC Processed by Selective Laser Melting (SLM) by Specific Scanning Strategies,” *Materials Science and Engineering: A,* vol. 661, pp. 240-246, 2016.

[202] P. Rangaswamy, M. L. Griffith, M. B. Prime, T. M. Holden, R. B. Rogge, J. M. Edwards and R. J. Sebring, “Residual Stresses in LENS (R) Components using Neutron Diffraction and Contour Method,” *Materials Science and Engineering A,* vol. 399, pp. 72-83, 2005.

[203] E. Brandl, U. Heckenberg, V. Holzinger and D. Buchbinder, “Additive manufactured AlSi10Mg samples using Selective Laser Melting (SLM): Microstructure, high cycle fatigue, and fracture behavior,” *Materials and Design,* vol. 34, pp. 159 -169, 2012.

[204] V. S. Sufiiarov, A. A. Popovich, E. V. Borisov, I. A. Polozov, D. V. Masaylo and A. V. Orlov, “The Effect Of Layer Thickness at Selective Laser Melting,” *Procedia Engineering,* vol. 174, pp. 126-134, 2017.

[205] M. Averyanova, P. Bertrand and B. Verquin, “Effect of Initial Powder Properties On Final Microstructure and Mechanical Properties of Parts Manufactured by Selective Laser Melting,” *Proceedings of teh 21st International DAAAM Symposium,* vol. 21, no. 1, 2010.

[206] W.-C. Huang, C.-S. Chuang, C.-C. Lin, C.-H. Wu, D.-Y. Lin, S.-H. Liu, W.-P. Tseng and J.-B. Horng, “Microstructure-Controllable Laser Additive Manufacturing Process for Metal Products,” *Physics Procedia of the 8th International Conference on Photonic Technology,* vol. 56, pp. 58-63, 2014.

[207] Y. Bai, Y. Yang, Z. Xiao, M. Zhang and D. Wang, “Process Optimization and Mechanical Property Evolution of AlSiMg0.75 by Selective Laser Melting,” *Materials and Design,* 2017.

[208] G. A. Edwards, K. Stiller, G. L. Dunlop and C. Couper, “The Precipitation Sequence in Al-Mg-Si Alloys,” *Acta Materialia,* vol. 46, no. 11, pp. 3893-3904, 1998.

[209] M. Liu, Z. Wu, R. Yang, J. Wei, Y. Yu, P. C. Skaret and H. J. Roven, “DSC analyses of static and dynamic precipitation of an Al-Mg-Si-Cu aluminium alloy,” *Progress in Natural Science Materials International,* vol. 25, pp. 153-158, 2015.

[210] X.-b. Fan, Z.-b. He, W.-x. Zhou and S.-J. Yuan, “Formability adn Strengthening Mechanism of Solution Treated Al-Mg-Si Alloy Sheet Under Hot Stamping Conditions,” *Journal of Materials Processing Technology,* vol. 228, no. February, pp. 179-185, 2016.

[211] T. Marlaud, A. Deschamps, F. Bley, W. Lefebvre and B. Baroux, “Influence of Alloy Composition and Heat Treatment on Precipitate Composition in Al-Zn-Mg-Cu Alloys,” *Acta Materialia,* vol. 58, no. 1, pp. 248-260, 2010.

[212] M. Tang and C. P. Pistorius, “Oxides, porosity and fatigue performance of AlSi10Mg parts produced by selective laser melting,” *International Journal of Fatigue,* 2016.

[213] T. Kimura, T. Nakamoto, M. Mizuno and H. Araki, “Effect of Silicon Content on Densification, Mechanical and Thermal Properties of Al-xSi Binary Alloys Fabricated Using Selective Laser Melting,” *Materials Science and Engineering: A,* vol. 682, pp. 593-602, 2017.

[214] J. H. Martin, B. D. Yahata, J. M. Hundley, J. A. Mayer, T. A. Schaedler and T. M. Pollock, “3D Prnting of High Strength Aluminium Alloys,” *Nature,* vol. 549, p. 365, 2017.

[215] N. T. Aboulkhair, I. Maskery, C. Tuck, I. Ashcroft and N. M. Everitt, “The Microstructure and Mechanical Properties of Selectively Laser Melted AlSi10Mg: The Effect of a Conventional T6-Heat Treatment,” *Materials Science and Engineering: A,* vol. 667, pp. 139-146, 2016.

[216] L. Girelli, M. Tocci, L. Montesano, M. Gelfi and A. Pola, “Optimization of Heat Treatment Parameters for Additive Manufacturing and Gravity Casting AlSi10Mg Alloy,” *Materials Science and Engineering,* vol. 264, 2017.

[217] K. Kempen, L. Thijs, J. van Humbeeck and J. P. Kruth, “Mechanical Properties of AlSi10Mg produced by Selective Laser Melting,” *Physics Procedia,* vol. 39, pp. 439 - 446, 2012.

[218] K. G. Prashantha, S. Scudino, H. J. Klauss, K. B. Surreddi, L. Löber, Z. Wang, A. K. Chaubey, U. Kühn and J. Eckert, “Microstructure and Mechanical Properties of Al–12Si Produced by Selective Laser Melting: Effect of Heat Treatment,” *Materials Science And Engineering,* vol. 590, pp. 153 - 160, 2014.

[219] W. Li, S. Li, J. Liu, A. Zhang, Y. Zhou, W. Qingsong, C. Yan and Y. Shi, “Effect of Heat Treatment on AlSi10Mg Alloy Fabricated by Selective Laser Melting: Microstructure Evolution, Mechanical Properties and Fracture Mechanism,” *Materials Science & Engineering A,* vol. 663, pp. 116-125, 2016.

[220] M. C. H. Karg, B. Ahuja, S. Wiesenmayer, S. V. Kuryntsev and M. Schmidt, “Effects of Process Conditions on the Mechanical Behaviour of Aluminium Wrought Alloy EN AW-2219 (AlCu6Mn) Additively Manufactured by Laser Beam Melting in Powder Bed,” *Micromachines,* vol. 8, p. 23, 2017.

[221] P. Wang, C. Gammer, F. Brenne, K. G. Prashanth, R. G. Mendes, M. H. Rummeli, T. Gemming, J. Eckert and S. Scudino, “Microstructure and Mechanical Properties of a Heat-treatable Al-3.5Cu-1.5Mg-1Si Alloy Produced by Selective Laser Melting,” *Materials Science & Engineering A,* vol. 711, pp. 562-570, 2018.

[222] P. Skalicky, D. Koutny, L. Pantelejev and D. Palousek, “Processing of Aluminium Alloy En AW 7075 Using Selective Laser Melting: Initial Study,” *58th International Conference of Machine Design Departments,* 2017.

[223] APWorks, “APWORKS and TOYAL will collaborate on the production, distribution and further development of Scalmalloy® in the future,” 24 November 2017. [Online]. Available: http://www.apworks.de/blog/toyal-partnerschaft/. [Accessed 7 February 2018].

[224] A. B. Spieings, K. Dawson, T. Heeling, P. J. Uggowitzer, R. Schaublin, F. Palm and K. Wegener, “Microstructural Features of Sc- and Zr- Modified Al-Mg Alloys Processed by Selective Laser Melting,” *Materials and Design,* vol. 115, pp. 52-63, 2017.

[225] R. Li, M. Wang, T. Yuan, B. Song, C. Chen, K. Zhao and P. Cao, “Selective Laser Melting of a Novel Sc and Zr Modified Al-6.2 Mg Alloy: Processing, Microstructure, and Properties,” *Powder Technology,* vol. 319, pp. 117-128, 2017.

[226] J. R. Croteau, S. Griffiths, M. D. Rossell, C. Leinenbach, C. Kenel, V. Jansen, D. N. Seidman, D. C. Dunand and N. Q. Vo, “Microstructure and mechanical properties of Al-Mg-Zr alloys processed by selective laser melting,” *Acta Materialia,* vol. 153, no. July, pp. 35-44, 2018.

[227] Z. Tang, T. Seefeld and F. Vollertsen, “Grain Refinement by Laser Welding of AA5083 with Addition of Ti/B,” *Physics Procedia,* vol. 12, pp. 123-133, 2011.

[228] B. Vrancken, R. Wauthle, J. P. Kruth and J. Van Humbeeck, “Study of the Influence of Material Properties on Residual Stress in Selective Laser Melting,” *SFF Symposium,* 2013.

[229] P. Mercelis and J.-P. Kruth, “Residual Stresses in Selective Laser Sintering and Selective Laser Melting,” *Rapid Prototyping Journal,* vol. 12, no. 5, pp. 254-265, 2006.

[230] A. H. Nickel, D. M. Barnett and F. B. Prinz, “Thermal Stresses and Deposition Patterns in Layered Manufacturing,” *Materials Science and Engineering A,* vol. 317, pp. 59-64, 2001.

[231] T. Qi, H. Zhu, H. Zhang, J. Yin, L. Ke and X. Zeng, “Selective Laser Melting of Al7050 Powder: Melting Mode Transition and Comparison of the Characteristics Between the Keyhole and Conduction Mode,” *Materials and Design,* vol. 135, pp. 257-266, 2017.

[232] S. P. Edwardson, J. Griffiths, G. Dearden and K. G. Watkins, “Towards Controlled Three-Dimensional Laser Forming,” *Lasers in Engineering,* vol. 22, pp. 393-399, 2011.

[233] B. Vrancken, Study of Residual Stresses in Selective Laser Melting, PhD Thesis ed., KU Leuven, 2016.

[234] T. Mishurova, S. Cabeza, K. Artzt, J. Haubrich, M. Klaus, C. Genzel, G. Requena and G. Bruno, “An Assessment of Subsurface Residual Stress Analysis in SLM Ti-6Al-4V,” *Materials,* vol. 10, p. 348, 2017.

[235] B. Hu and I. M. Richardson, “Mechanism and Possible Solution for Transverse Solidification Cracking in Laser Welding of High Strength Aluminium Alloys,” *Materials Science and Engineering A,* vol. 429, pp. 287-294, 2006.

[236] K. Kempen, B. Vrancken, S. Buls, L. Thijs, J. Van Humbeeck and J. P. Kruth, “Selective Laser Melting of Crack-Free High Density M2 High Speed Steel Parts by Baseplate Preheating,” *Journal of Manufacturing Science and Engineering,* vol. 136, 2014.

[237] D. Koutny, D. Palousek, L. Pantelejev, C. Hoeller, R. Pichler, L. Tesicky and J. Kaiser, “Influence of Scanning Strategies on Processing of Aluminum Alloy EN AW 2618 Using Selective Laser Melting,” *Materials,* vol. 11, pp. 298-315, 2018.

[238] S. Catchpole-Smith, N. Aboulkhair, L. Parry, C. Tuck, I. A. Ashcroft and A. Clare, “Fractal Scan Strategy for Selective Laser Melting of "Unweldable" Nickel Superalloys,” *Additive Manufacturing,* vol. 15, pp. 113-122, 2017.

[239] A. Salmi, E. Atzeni, L. Iuliano and M. Galati, “Experimental Analysis of Residual Stresses on AlSi10Mg Parts Produced by Means of Selective Laser Melting (SLM),” *Procedia CIRP,* vol. 62, pp. 458-463, 2017.

[240] M. Shiomi, K. Osakada, K. Nakamura, T. Yamashita and F. Abe, “Residual Stress within Metallic Model made by Selective Laser Melting Process,” *CIRP Annals - Manufacturing Technology,* vol. 53, no. 1, pp. 195-198, 2004.

[241] E. Cicala, G. Duffet, H. Andrzejewski, D. Grevey and S. Ignat, “Hot Cracking in Al-Mg-Si Alloy Laser Welding - Operating Parameters and Their Effects,” *Materials Science and Engineering A,* vol. 395, pp. 1-9, 2005.

[242] S. Jansen, Generative Fertigung von konturnah temperierten Werkzeugen mittels Selective Laser Melting, PhD Thesis ed., Aachen University, 2014.

[243] M. F. Zaeh and G. Branner, “Investigations on Residual Stresses and Deforations in Selective Laser Melting,” *Production Engineering,* vol. 4, no. 1, pp. 35-45, 2010.

[244] J.-P. Kruth, J. Deckers, E. Yasa and R. Wauthle, “Assessing and Comparing Influencing Factors of Residual Stresses in Selective Laser Melting using a Novel Analysis Method,” *Proceedings of the Institute of Mechanical Engineers, Part B: Jurnal of Engineering Manufacture,* vol. 226, no. 6, pp. 980-991, 2012.

[245] H. Ali, H. Ghadbeigi and K. Mumtaz, “Effect of Scanning Strategies on Residual Stress and Mechanical Properties of Selective Laser Melted Ti6Al4V,” *Materials Science & Engineering A,* vol. 712, pp. 175-187, 2018.

[246] E. Yasa, J. Deckers, T. Craeghs, M. Badrossamay and J.-P. Kruth, “Investigation on Occurence of Elevated Edges in Selective Laser Melting,” *International Solid Freeform Fabrication Symposium,* pp. 673 - 685, 2009.

[247] Y. P. Yang, P. Dong, J. Zhang and X. Tian, “A Hot-Crack Mitigation Technique for Welding High-Strength Aluminium Alloy,” *Welding Journal,* p. 79, 2000.

[248] T. Heeling and K. Wegener, “The Effect of Multi-Beam Strategies on Selective Laser Melting of Stainless Steel 316L,” *Additive Maufacturing,* vol. 22, pp. 334-342, 2018.

[249] S. Siddique, M. Imran, E. Wycisk, C. Emmelmann and F. Walther, “Influence of Process-Induced Microstructure and Imperfections on Mechanical Properties of AlSi12 Processed by Selective Laser Melting,” *Journal of Materials Processing Technology,* vol. 221, pp. 205-213, 2015.

[250] T. Breczko, “X-Ray Measurement of Residual Stress,” *Wear,* vol. 82, no. 1, pp. 27-35, 1982.

[251] T. Pfaller, “Unlocking Aluminium Welding: To Successfully Weld 6000 Series Aluminium, It's Important To Understand All of the Key Aspect,” [Online]. Available: http://weldingproductivity.com/article/unlocking-aluminum-welding/. [Accessed 28 May 2018].

[252] M. J. Cieslak and P. W. Fuersbach, “On The Weldability,Composition, and Hardness of Pulsed and Continuous Nd:YAG LaserWelds in Aluminium Alloys 6061, 5456 and 5086,” *Metallurgical Transactions,* vol. 19, no. B, pp. 319-329, 1988.

[253] W. I. Pumphrey and P. H. Jennings, “A Consideration of the Nature of Brittleness and Temperature Above the Solidus in Castings and Welds in Aluminum Alloys,” *Journal of International Metals,* vol. 75, pp. 235-256, 1948.

[254] W. S. Pellini, “Strain Theory of Hot Tearing,” *Foundry,* vol. 80, pp. 125-199, 1952.

[255] J. C. Borland, “Generalized Theory of Super-Solidus Cracking in Welds and Casting,” *Welding Research,* vol. 7, no. 8, pp. 508-512, 1954.

[256] S. Lin, A Study of Hot Tearing In Wrought Aluminium Alloys, Université du Québec à Chicoutimi, 1999.

[257] C. Cross, “On the Origin of Weld Solidification Cracking,” in *Hot Cracking Phenomena in Welds*, H. Herold, Ed., Berlin, Springer-Verlag, 2005, pp. 3-18.

[258] X. Cao, W. Wallace, J. P. Immarigeon and C. Poon, “Research adn Progressin Laser Welding of Wrought Aluminium Alloys. II. Metallurgical Microstructures, Defects, and Mechanical Properties,” *Materials and Manufacturing Processes,* vol. 18, no. 1, pp. 23-49, 2003.

[259] CES, 2014.

[260] P. Kah, J. Martikainen, E. Hitunen, F. Brhane and V. Karkhin, “Hot Cracking Susceptibility of Wrought 6005 and 6082 Aluminium Alloys,” in *Hot Cracking Phenomena in Welds III*, Berlin, Springer-Verlag Berlin Heidelberg, 2011, pp. 59-69.

[261] Alcotec, “Weld Cracking Problem Using 6063-T6 Sheet Material,” 2015. [Online]. Available: http://www.alcotec.com/us/en/education/knowledge/qa/Weld-crackling-problem-using-6061-T6-sheet-material.cfm. [Accessed 28 May 2018].

[262] C. E. Cross, “On The Origin of Weld Solidification Cracking,” in *Hot Cracking Phenomena in Welds*, Berlin, Springer-Verlag Berlin Heidelberg, 2005, pp. 3-18.

[263] H. Yunija, R. H. Frost, D. L. Olson and G. R. Edwards, “Grain Refinement of Aluminium Weld Metal,” *Welding Journal,* vol. 68, no. 7, pp. 280-289, 1989.

[264] S. Kou, “A Criterion for Cracking During Solidification,” *Acta Materialia,* vol. 88, pp. 336-374, 2015.

[265] F. Malek Ghaini, M. Sheikhi, M. J. Torkamany and J. Sabbaghzadeh, “The Relation Between Liquation adn Solidification Cracks in Pulsed Laser Welding of 2024 Aluminium Alloy,” *Materials Science and Engineering A,* vol. 519, pp. 167-171, 2009.

[266] T. Soysal and S. Kou, “A Simple Test for Assessing Solidification Cracking Susceptibility and Checking Validity for Susceptibility Prediction,” *Acta Materialia,* vol. 143, pp. 181-197, 2018.

[267] C. Huang and S. Kou, “Liquation Cracking in Full-Penetration Al-Cu Weld,” *Welding Research,* pp. 50-58, 2004.

[268] S. Li and D. Apelian, “Hot Tearing of Aluminum Alloys A Critical Literature Review,” *International Journal of Metalcastings,* vol. 5, no. 1, pp. 23-40, 2011.

[269] N. Coniglio, C. E. Cross, T. Michael and M. Lammers, “Defining a Critical Weld Dilution to Avoid Solidification Cracking in Aluminium,” *Welding Research,* vol. 87, no. September, pp. 237-247, 2008.

[270] L. Abbaschian and M. S. F. d. Lima, “Cracking Susceptibility of Aluminium Alloys During Laser Welding,” *Materials Research,* vol. 6, no. 2, pp. 273-278, 2003.

[271] B. Kim, N. Kang, W. Oh, J. Kim, Y. Kim and Y. Pari, “Effects of Weaving Laser on Weld Microstructure and Crack for Al 6k21-T4 Alloy,” *Journal of Materials Science & Technology,* vol. 27, no. 1, pp. 93-96, 2011.

[272] K.-D. Choi, Y.-N. Ahn and C. Kim, “Weld Strength Improvement for Al Alloy by Using Laser Weaving Method,” *Journal of Laser Applications,* vol. 22, no. 3, pp. 116-119, 2010.

[273] J. Schindelin, I. Arganda-Carreras, E. Frise, V. Kaynig, M. Longair, T. Pietzsch, S. Preibisch, C. Rueben, S. Saalfeld, B. Schmid, J.-Y. Tinevez, D. J. White, V. Hartenstein, K. Eliceiri, P. Tomancak and A. Cardona, “Fiji: An Open-Source Platform for Biological-Image Analysis,” *Nature Methods,* vol. 9, pp. 676-682, 2012.

[274] G. E. Bean, D. B. Witkins, T. D. McLouth, D. N. Patel and R. J. Zaldivar, “Effect of Laser Focus Shift on Surface Quality and Density of Inconel 718 Parts Produced via Selective Laser Melting,” *Additive Manufacturing,* vol. 22, pp. 207-215, 2018.

[275] K. Kanaya and S. Okayama, “Penetration and Energy Loss Theory of Electrons in Solid Targets,” *Journal of Physics D: Applied Physics,* vol. 5, no. April, pp. 43-58, 1971.

[276] Claudionico, *Diagram illustrating the phenomena resulting from the interaction of highly energetic electrons with matter,* Wiki Commons, 2013.

[277] L. F. Pease and W. G. West, Fundamentals of Powder Metallurgy, Princeton, N.J., USA: Metal Powder Industries Federation, 2002.

[278] D. Barling, D. A. Morton and K. Hapgood, “Pharmaceutical Dry Powder Blending and Scale-up: Maintaining Equivalent Mixing Conditions Using a Coloured Tracer Powder,” *Powder Technology,* Vols. 270, Part B, no. January, pp. 461-469, 2015.

[279] Powder & Bulk Solids, “Mixing & Blending,” 7 June 2011. [Online]. Available: https://www.powderbulksolids.com/article/mixing-blending-3. [Accessed 11 12 2018].

[280] ASTM F3049 - 14, “Standard Guide for Characterizing Properties of Metal Powders Used for Additive Manufacturing Processes,” 2014.

[281] H. Maleki, F. Ebrahimi and E. N. Oskoee, “The Angle of Repose of Sperical Grains in Granular Hele-Shaw Cells: A Molecular Dynamics Study,” *Journal of Statistical Mechanics: Theory and Experiment,* vol. 2008, no. April, 2008.

[282] BS 4140-9, “Methods of test for Aluminium Oxide,” in *Measurement of the Angle of Repose*, British Standards Online, 1986.

[283] ASTM B212-99, “Standard Test Method for Apparent Density of Free-Flowing Metal Powders Using the Hall Flowmeter Funnel,” ASTM Standards, 1999.

[284] Y. Liu, J. Zhang, Z. Pang and W. Wu, “Investigation Into The Influence of Laser Energy Input on Selective LAser Melting Thin-Walled Parts by Responsese Surface,” *Optics and Lasers in Engineering,* vol. 103, pp. 34-45, 2018.

[285] V. S. Sufiiarov, A. A. Popovich, E. V. Borisov, I. A. Polozov, D. V. Masaylo and A. V. Orlov, “The Effect Of Layer Thicness at Selective Laser Melting,” *Procedia Engineering,* vol. 174, pp. 126-134, 2017.

[286] NIST/SEMATECH, “e-Handbook of Statistical Methods,” 2012. [Online]. Available: https://www.itl.nist.gov/div898/handbook/. [Accessed 12 May 2018].

[287] A. B. Spierings, M. Schneider and R. Eggenberger, “Comparison of Denisty Measurement Techniques for Additive Manufacturing Metallic Parts,” *Rapid Prototyping Journal,* vol. 17, no. 5, pp. 380-386, 2011.

[288] Micromeritics, “Gas Pycnometry Volume and Density,” 2018. [Online]. Available: https://micromeriticsusa.wistia.com/medias/84zzd0ssk4. [Accessed 15 May 2018].

[289] M. Ameli, B. Agnewa, P. S. Leung, B. Nga, C. J. Sutcliffe, J. Singh and R. McGlen, “A Novel Method for Manufacturing Sintered Aluminium Heat Pipes (SAHP),” *Applied Thermal Engineering,* vol. 52, pp. 498 - 504, 2013.

[290] L. Reimer, Scanning Electron Microscopy: Physics of Image Formation and Microanalysis, 2nd ed., Berin: Springer-Verlag, 1998.

[291] C. E. Roberts, D. Bourell, T. Watt and J. Cohen, “A Novel Processing Approach for Additive Manufacturing of Commercial Aluminium Alloys,” *Physics Procedia: 9th International Conference on Photonic Technologies,* vol. 83, pp. 909-917, 2016.